

17554

NATIONAL LIBRARY
OTTAWA



CANADA

BIBLIOTHÈQUE NATIONALE
OTTAWA

NAME OF AUTHOR..... *MARIE PETRA HRON*
TITLE OF THESIS..... *WAVES IN INHOMOGENEOUS
MEDIA*
UNIVERSITY..... *UNIVERSITY OF ALBERTA*
DEGREE FOR WHICH THESIS WAS PRESENTED..... *Ph.D.*
YEAR THIS DEGREE GRANTED..... *1973*

Permission is hereby granted to THE NATIONAL LIBRARY
OF CANADA to microfilm this thesis and to lend or sell copies
of the film.

The author reserves other publication rights, and
neither the thesis nor extensive extracts from it may be
printed or otherwise reproduced without the author's
written permission.

(Signed)..... *Marie Hron*

PERMANENT ADDRESS:

10725-79 avenue
Edmonton
Alberta

DATED..... *June 7*..... 1973

THE UNIVERSITY OF ALBERTA

WAVES IN INHOMOGENEOUS MEDIA

by



MARIE PETRA HRON

A THESIS

SUBMITTED TO THE FACULTY OF GRADUATE STUDIES AND RESEARCH
IN PARTIAL FULFILLMENT OF THE REQUIREMENTS FOR THE DEGREE
OF DOCTOR OF PHILOSOPHY

DEPARTMENT OF PHYSICS

EDMONTON, ALBERTA

FALL, 1973

THE UNIVERSITY OF ALBERTA

FACULTY OF GRADUATE STUDIES AND RESEARCH

The undersigned certify that they have read, and recommend to the Faculty of Graduate Studies and Research, for acceptance, a thesis entitled WAVES IN INHOMOGENEOUS MEDIA submitted by Marie Petra Hron in partial fulfillment of the requirements for the degree of Doctor of Philosophy.

C. H. Chapman

Supervisor

E. R. Kardar

R. J. D. Fitz

A. S. Coppi

Lore Johnson

External Examiner

Date May 29, 1973

ABSTRACT

The waves propagating in media with transition layers are investigated theoretically with application to the propagation of seismic waves in the Earth's crust and the upper mantle. The propagation of pressure perturbation from a point source in a fluid is studied in both the frequency and time domain. The problem is solved in the flat geometry under the assumption that the earth-flattening transformation can be used to transform the spherical geometry into the flat geometry.

When the monotonic velocity transition is broad the caustics are formed by the focussing of rays due to the rapid change in the velocity gradient. In such a case a triplication is formed on the travel-time curve and the wave propagation in the neighbourhood of the endpoints is studied. Numerical evaluation of the response of the medium shows that at high frequencies the decay into the region beyond the caustic is large and that low frequency waves carry the significant amount of energy. The amplitude maximum is shifted from the endpoint into the illuminated region due to constructive interference of the two arriving waves.

If the monotonic transition is thin the partial reflection occurs at sub-critical angles of incidence and the head wave arises at the critical incidence. They are both

effected by the thickness of the transition: as the transition becomes thinner, they behave more like sub-critical reflection and head waves from sharp velocity transition.

When the transition layer has a velocity maximum the amplitudes of the waves propagating along the velocity reversal decay exponentially with distance. This rapid decrease of the amplitude causes a "shadow" whose properties are very different from a "true" shadow due to an abrupt velocity decrease. The first is frequency independent while the other depends on frequency as $\exp(-a\omega^{1/3})$.

The numerical results for the monotonic velocity transition are compared to the results given by the complete and partial ray expansions for medium with homogeneous layers. The results suggest that if a good approximation of the inhomogeneous medium by a stack of homogeneous layers is required the number of layers must be very large. The error of the partial ray expansion with respect to the exact solution depends on the choice of rays considered. For large number of layers the rays with multiple reflections must be included in the expansion in order to obtain satisfactory results.

ACKNOWLEDGEMENTS

I am very grateful to my supervisor, Dr. C. H. Chapman for the advice, instruction and the encouragement he provided throughout this work.

I am indebted to Drs. J. Bennett and F. Nyland who read the manuscript and suggested several improvements. I also had many useful discussions with my fellow student, E. Waddington.

My husband, Franta, helped me with many problems encountered during my work. He also showed remarkable patience and understanding, especially throughout the last few arduous months.

Mrs. Lee Cech has helped immensely through her prompt and efficient typing.

I am grateful to the National Research Council of Canada for providing a Postgraduate Scholarship during the course of my doctoral studies.

TABLE OF CONTENTS

	Page
CHAPTER 1 INTRODUCTION	1
CHAPTER 2 BASIC EQUATIONS	11
2.1 Equations of motion	11
2.2 The coordinate transformations	13
2.3 The source	16
2.4 The response integral	20
CHAPTER 3 SOLUTION OF THE WAVE EQUATION BY EPSTEIN'S METHOD	23
3.1 Statement of the problem	23
3.2 Compatibility of the wave and the hypergeometric equations	27
CHAPTER 4 CAUSTICS AND HEAD WAVES DUE TO MONOTONIC VELOCITY TRANSITIONS	40
4.1 The reflection coefficient	40
4.2 The WKBJ reflection coefficient	52
4.3 Asymptotic behaviour of the response integral	61
4.4 Synthetic seismograms	90

	Page
CHAPTER 5 DIFFRACTION AT THE VELOCITY REVERSAL	121
5.1 The reflection coefficient for velocity reversal	122
5.2 The response integral	139
5.3 Synthetic seismograms	149
CHAPTER 6 CONVERGENCE OF THE RAY EXPANSION	153
6.1 Fundamental solution	154
6.2 The numerical solution of the wave equation	166
6.3 Convergence of the ray expansion	179
CONCLUSIONS	197
BIBLIOGRAPHY	200
APPENDIX A TRANSCENDENTAL FUNCTIONS	207
A.1 Hypergeometric functions	207
A.2 Airy functions and Stokes phenomenon	213
APPENDIX B VALIDITY OF THE REFLECTION COEFFICIENT	221
APPENDIX C CONVERGENCE OF THE RESPONSE INTEGRALS	225
APPENDIX D ALGORITHMS FOR SPECIAL FUNCTIONS NEEDED FOR EVALUATION OF THE RESPONSE INTEGRAL	232
D.1 Complex gamma function	232
D.2 Hankel function of the zeroth order	234

LIST OF TABLES

Table		Page
4.1	Influence of density variation on velocity profile in Model X	96
4.2	Influence of density variation on velocity profile in Model IV	97
4.3	Influence of density variation on velocity profile in Model V	98
6.1	The percentage error of the complete ray expansion for Model IV	171
6.2	The percentage error of the partial ray expansion for Model IV	177
6.3	The number of distinct ways in which M balls can be distributed into J-1 pockets allowing at most three balls per pocket (Eisen)	185
6.4	The number of distinct ways in which M balls can be distributed into J-1 pockets allowing at most two balls in the first and third pockets, three balls in the second pocket and four balls in the fourth pocket	187

LIST OF FIGURES

Figure		Page
1.1	Velocity structure of compressional waves in the upper mantle (Johnson)	2
1.2	The triplication and caustics due to the broad velocity transition	7
1.3	The partial reflection and head wave from a narrow velocity transition	8
3.1	The Epstein profiles	24
3.2	The WKBJ solutions in the medium with velocity transition	26
3.3	Conformal mapping - $\xi = e^z$	29
3.4	The analytic continuation interpreted physically as reflection-transmission law	33
3.5	The reflection laws for incidence from above and below the interface	35
4.1	The partial reflections and head waves near the critical point for monotonic velocity increase	41
4.2a	The poles on the (++) Riemann sheet of the complex κ plane	44
4.2b	The poles on the (+-) Riemann sheet of the complex κ plane	45
4.3a	The poles on the (-+) Riemann sheet of the complex κ plane for frequency $\omega_3 > \omega > \omega_2$	46
4.3b	The poles on the (--) Riemann sheet of the complex κ plane for frequency $\omega_3 > \omega > \omega_2$	47
4.4	The complex ζ plane with the branch cut integration for evaluation of the WKBJ reflection coefficient (Chapman)	53

Figure		Page
4.5	The complex ζ plane for κ complex	56
4.6	The Stokes diagrams describing the behaviour of the WKBJ solutions	57
4.7	The complex ζ and q planes showing the contours of integration used in the evaluation of the WKBJ reflection coefficient for Epstein profile (Budden)	59
4.8	Saddle points in the complex κ plane for a broad velocity transition	64
4.9	Saddle points in the complex κ plane for a narrow velocity transition	67
4.10	The horizontal wavenumber versus the horizontal distance	71
4.11	The amplitude curves near the caustic C ($\theta_C = 10^\circ 20'$)	76
4.12	The amplitude curves near the critical point ($X_C = 60.5$ km)	78
4.13	The amplitude curves near the critical point ($X_C = 67.8$ km)	79
4.14	The de Hoop contour in the complex p plane	85
4.15	The amplitude of the head wave at different ranges beyond the critical point for .2 km transition zone at 20 km	87
4.16	The amplitude of the head wave at different ranges beyond the critical point for 1.6 km transition zone at 20 km	88
4.17	The effect of the earth-flattening transformation on the ray path	92
4.18	The effect of the density variation on the velocity profile in Model X	95

Figure		Page
4.19	Contour map of the modulus of the integrand for $\theta = 10^{\circ}25'$ (1)	100
4.20	Contour map of the phase of the integrand for $\theta = 10^{\circ}25'$	101
4.21	Contour map of the modulus of the integrand for $\theta = 10^{\circ}25'$ (2)	102
4.22	The amplitude curves near the caustic B ($\theta_B = 21^{\circ}$)	107
4.23	The contour of integration in the complex k plane when the saddle points are well separated	109
4.24	The combined spectrum of the critically damped seismometer and the unit step function source	110
4.25	The response of the critically damped seismometer to the unit step function source	111
4.26	The synthetic seismograms for Model X at ranges near the caustic C	114
4.27	The synthetic seismograms for Model X at ranges near the caustic B	115
4.28	The synthetic seismograms for Model IV at ranges near the critical point	116
4.29	The synthetic seismograms for Model V at ranges near the critical point	117
5.1	The travel-time curve and the rays in the medium with the velocity reversal	124
5.2	The dependence of the modulus of the reflection coefficient on the effective thickness of the "sech" layer	127
5.3	The parabolic velocity profile	128

Figure		Page
5.4	The variation of the modulus of the reflection coefficient with frequency for parabolic layers of different effective thickness (Chessell)	130
5.5a	The high frequency positions of the poles $2^{\kappa} n$	133
5.5b	The high frequency positions of the poles $3^{\kappa} n$	134
5.6a	The poles' positions on the top Riemann sheet of the complex κ plane for low frequencies	135
5.6b	The poles' positions on the bottom Riemann sheet of the complex κ plane for low frequencies	136
5.7	The steepest descent path in the complex κ plane for large horizontal distances	143
5.8	The amplitude curves evaluated numerically for the velocity reversal	144
5.9	The synthetic seismograms for the Model II (1)	150
5.10	The synthetic seismograms for the Model II (2)	151
6.1	The stratified medium of homogeneous layers	156
6.2	Group of kinematic analogues	161
6.3	Groups of dynamic analogues	163
6.4	The unconverted ray expansion	164
6.5	Plane waves propagating in the layered medium	174
6.6	Percentage error of the complete and partial ray expansions	178

Figure		Page
6.7	Some of the dynamic analogues in the group of kinematic analogues $N_k(2,2,2)$	191
6.8	Schematic diagram of the behaviour of $ A_{\mathcal{M}} $, $\chi(N, M)$ and $ \chi_{\mathcal{M}} $	193
A.1	The complex s plane showing contour for Barnes integral	210
A.2	Airy functions for real values of χ (Budden)	214
A.3	The complex y plane (Budden)	217
A.4	The complex y plane with Stokes lines (S) and anti-Stokes' lines of the Airy function (Budden)	218
A.5	Stokes diagram for the functions $A_1(\chi)$ and $B_1(\chi)$ (Budden)	220

CHAPTER 1 INTRODUCTION

Improved coverage by stations of the USCGS world-wide network has provided better data in the last decade. Their processing has lead to more accurate estimates of elastic wave velocities and density within the Earth. All the recent models (Johnson, 1967; Julian and Anderson, 1968, for example) show remarkable agreement with the classical models of Jeffreys and Bullen (1940) and Gutenberg (1958) except at regions of high velocity gradients or low velocity channels (Figure 1.1). All these anomalous regions in the velocity structure are characterised by discontinuities or reversals in the travel-time curves. Increased resolution of these curves is the basis for better interpretation and leads to better understanding of the Earth's interior. This thesis studies theoretically a number of phenomena displayed by waves propagating in media with velocity transitions.

The first models of the velocity structure within the Earth were derived by simple geometrical ray theory (Bullen, 1963; p. 109). It solves the problem of wave propagation when energy propagates within a ray tube without leaking through its walls. The vector of energy flux is normal to the wave front. The energy propagation cannot be explained so simply for many signals. For example the high velocity gradients in the upper mantle give rise to triplications on

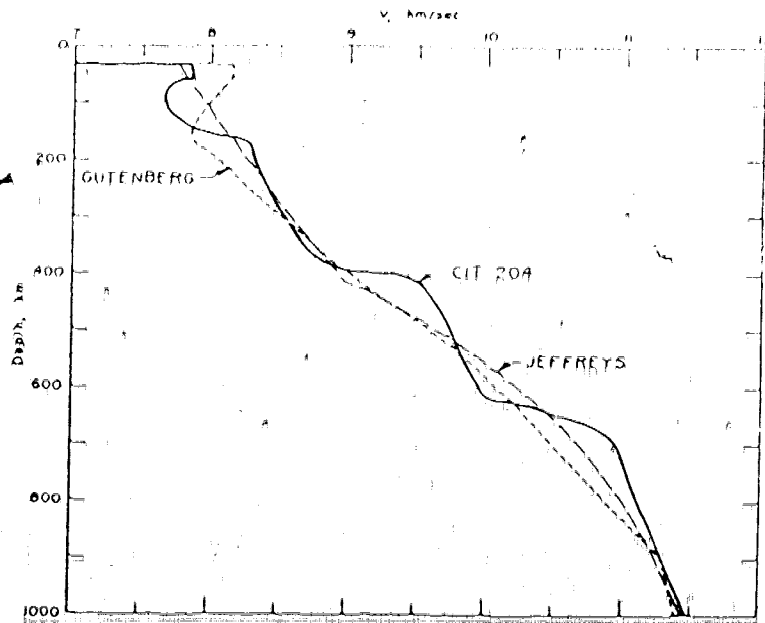


Figure 1.1 Velocity structure of compressional waves in the upper mantle (from Johnson, 1967).

the travel-time curves at approximately 15° and 20° . The later arrivals were first carefully studied by Johnson (1967) and their interpretation lead to model CIT 204 Fig. 1.1. The ray tube on the caustic has a zero cross-section caused by focussing of the rays. Therefore the simple assumption about propagation of energy fails. The wave propagation in the region of the caustic was first studied by Jeffreys (1939) in connection with the PKP caustic. Other signals for which the geometrical ray theory is inapplicable are head waves in the vicinity of the critical angle. These were first studied by Cagniard (1939) and recently Cerveny and Ravindra (1971) published an excellent book that studies head waves in great detail. Diffraction signals cannot be explained by geometrical ray theory either (Knopoff and Gilbert, 1961; Alexander and Phinney, 1966; Phinney and Cathles, 1969 and others). In all these cases the wave equations that describe the motion of the medium have to be solved exactly in the frequency range needed as the response is frequency dependent. The geometrical ray theory forms the high frequency approximation.

The solution must satisfy the source condition, the boundary conditions and the radiation conditions. This is equivalent to finding a reflection coefficient. The original equation is usually transformed to one variable. The transformation is in effect a decomposition of a spherical or

cylindrical wave into plane waves which are solutions of simpler differential equations. The wave equation for one variable must be solved and the reflection coefficient found. But even the one-dimensional equation can be solved analytically for only a few models. For more complicated velocity structures numerical methods of solution must be employed (Chapman, 1969; Müller, 1970; Chapman and Phinney, 1972). With the great development of powerful computers the importance of analytic solutions seems to have faded in recent years. The numerical solutions, however, carry with them a heavy computing penalty if we want to achieve the necessary accuracy. It seems useful to reinvestigate existing solutions and look to other fields of theoretical physics, if problems solved there are relevant to elastic wave propagation. Analytic solutions are still an indispensable part of research in theoretical seismology. However limited the model may appear with respect to the Earth's structure the results obtained often prove themselves to be very valuable.

When the reflection coefficient has been found, the seismic response of any medium is obtained as a product of elementary waves that represent the source and the reflection coefficient. The complete solution which covers all frequencies can sometimes be obtained exactly in analytic closed form. That is the case when the reflection coefficient is independent

of frequency and the Cagniard-de Hoop method can be used (Cagniard, 1939; de Hoop, 1960). Gilbert and Helmberger (1972) expanded the spherical reflection coefficient into an asymptotic, frequency independent form in order to obtain solution for response of a layered sphere in time domain. Müller (1970) and Helmberger and Wiggins (1971) applied an earth-flattening approximation to the spherical model and then applied the exact Cagniard-de Hoop method to the approximate model of plane layers. But generally the reflection coefficient is frequency dependent and the response of the medium in the frequency domain must be found first. The time domain response can be obtained by inverse Fourier transformation. In many cases the results in frequency domain are more valuable as seismological data are usually analysed in the frequency domain.

The small family of models for which the reflection coefficient has been found includes the homogeneous layers, linear transition layers (Gupta, 1966; Nakamura, 1964; Ward, 1972), exponential and parabolic layers (Merzer, 1971; Rydbeck, 1943) and Epstein layers (Epstein, 1930; Rawer, 1939; Lang and Shmoys, 1968; Phinney, 1970). Budden (1961) and Brekhovskikh (1960) summarize some of these results. Linear layers have discontinuities in velocity gradient which may not be realistic. Merzer's study is concerned only with head

waves and studies the variation of their amplitudes with frequency, layer thickness and shape of the transition. The Epstein models offer a wider range of applicability. We can model a region of high velocity gradient that gives rise to the triplication on the travel-time curve (Figure 1.2) or a narrow transition for investigation of the head wave (Figure 1.3). We have already mentioned that the classical ray theory cannot describe the energy propagation in the neighbourhood of the caustics and around the critical point. Furthermore if the transition is continuous it cannot explain any sub-critical or partial reflection. Epstein (1930) and Phinney (1970) studied the modulus of the reflection coefficient to obtain an estimate of the amplitude of the partial reflection. The modulus of the reflection coefficient itself, however, cannot give a good picture about energy propagation when the incident wave interacts with the strong velocity gradient. That can only be studied using the spectral amplitudes and impulse response of the model. A principle contribution of this work is their evaluation and investigation (Chapter 4).

Another velocity variation we can study is the velocity reversal which does not cause any discontinuity on the travel-time curve. Nevertheless, at large ranges the signals carry very little energy due to large geometrical

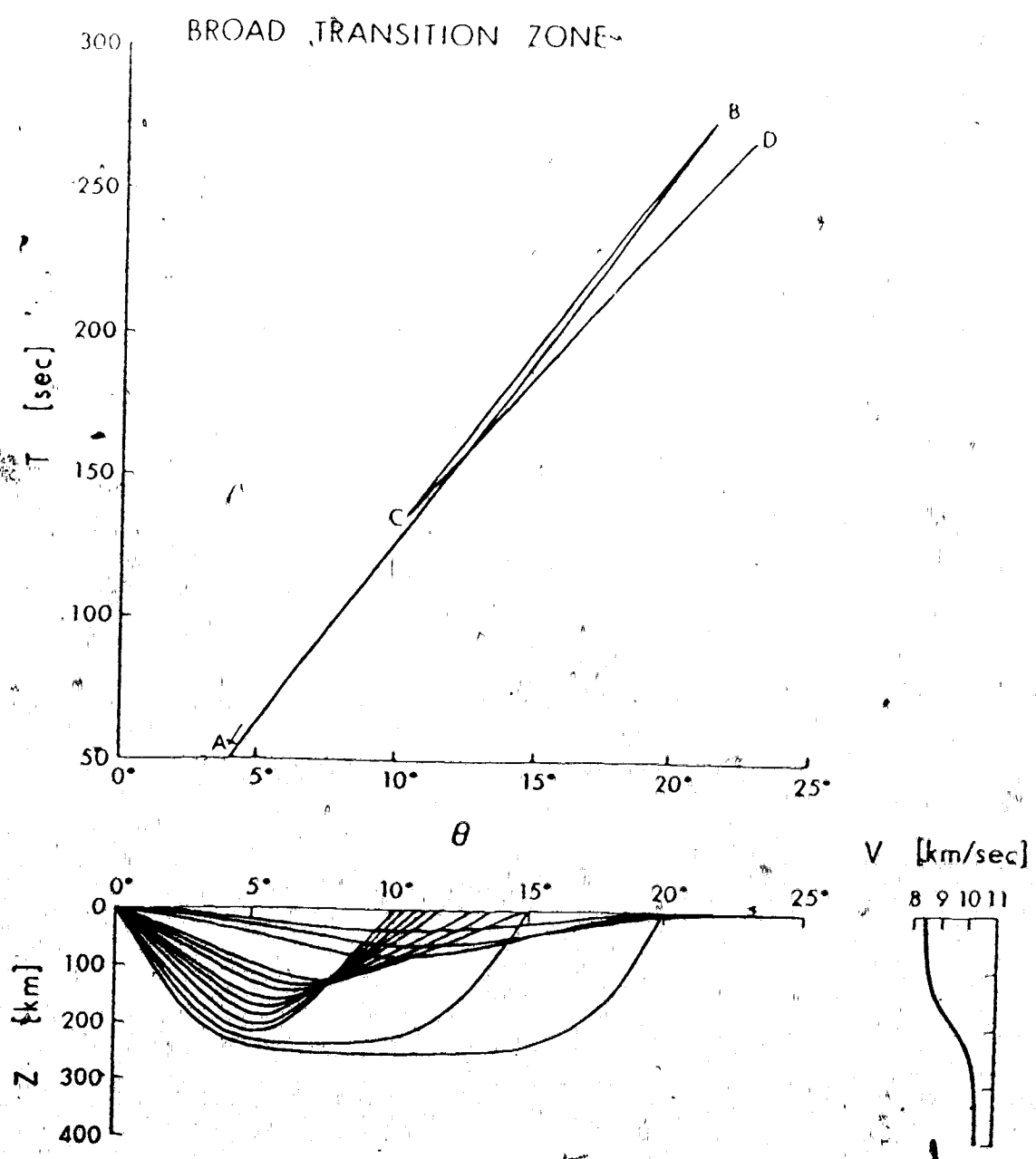


Figure 1.2. The triplication and caustics due to the broad velocity transition.

0.2 km transition zone at 20 km

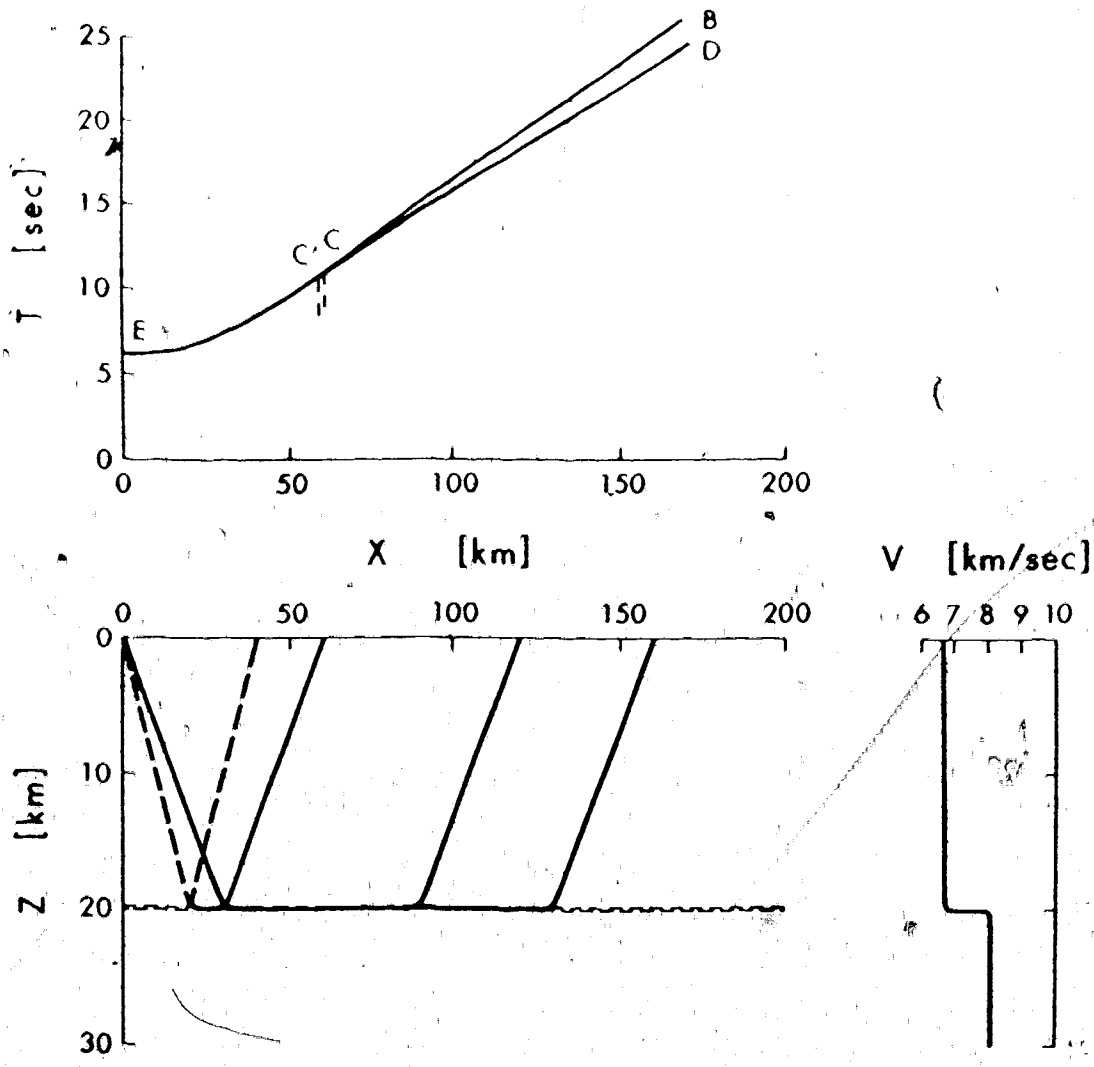


Figure 1.3 The partial reflection and head wave from a narrow velocity transition.

spreading along the wave path. The low frequency signals leak through the velocity barrier. The "shadow" caused by velocity reversal has not been studied and the results can be useful for investigation of the upper part of the low velocity channel and the region D" at the base of the mantle. The nature of "shadow" caused by this velocity structure is basically very different from a true shadow formed by an interface with velocity decrease. The interface shadow has a frequency dependent diffracted signal (Scholte, 1956; Duwalo and Jacobs, 1959; Chapman, 1969; Chapman and Phinney, 1972, and others) whereas the reversal "shadow" is independent of frequency. The discussion of the results for the reversal and the interface shadows is presented in Chapter 5.

We have already mentioned that solution for wave propagation in inhomogeneous media can be obtained by numerical solution of the wave equation and that this requires sophisticated high-speed computers. Approximation of such media by a stack of homogeneous layers has often been used to solve the problem approximately. Solution for propagation of plane waves in a layered medium was found by Thomson (1950) and Haskell (1953). Cisternas et al. (1973) showed that such solution can be written as an infinite series where each term represents one ray, i.e. we can say that the exact solution is equivalent to the "complete" ray expansion. In

practise only a "partial" ray expansion is used, i.e. only the rays with greatest amplitude are considered in evaluation of the response of the medium (Müller, 1970; Hron, 1971). The rest of the series is neglected under the assumption that the series is convergent. The convergence has not been proved to date, and we will investigate it in Chapter 6. The estimate of the error introduced by the approximation of the inhomogeneous medium by stratified medium of homogeneous layers can be obtained by comparison of the complete ray expansion with the exact solution (analytic, when exists, or numerical). In spite of growing importance of partial ray expansion for theoretical seismology (Gilbert and Helmberger, 1972; Waddington, 1973) very little is known about the error introduced by using it in place of the complete ray expansion. From this point of view the study presented in Chapter 6 can be regarded as a contribution to the solution of this complex problem.

CHAPTER 2 BASIC EQUATIONS

2.1 Equations of motion

The displacement equation of elastic motion may be found from the equation of conservation of momentum:

$$\rho(\underline{x}) \frac{\partial^2 \underline{u}}{\partial t^2} = \nabla \cdot \underline{\underline{\sigma}} + \rho(\underline{x}) \underline{f} \quad (2.1)$$

where $\underline{u}(\underline{x}, t)$ is infinitesimal elastic displacement, $\rho(\underline{x})$ is the density and $\underline{\underline{\sigma}}(\underline{x})$ is the stress tensor. $\underline{f}(\underline{x})$ is the applied force per unit mass acting at \underline{x} . Richards (1971) has introduced a potential representation of the displacement \underline{u} at $\underline{x} = (r, \theta, \phi)$

$$\underline{u}(\underline{x}, t) = \frac{1}{g} \left\{ \nabla \left(g \frac{P}{\rho^{1/2}} \right) + \nabla \times \nabla \times \left(r g \frac{S}{\rho^{1/2}} \underline{e}_r \right) + \nabla \times \left(r \frac{T}{\mu^{1/2}} \underline{e}_r \right) \right\} \quad (2.2)$$

which provides the correct separation in spherically inhomogeneous media. The density $\rho(r)$ and shear modulus $\mu(r)$ are functions of radius and so is the scalar function $g(r)$. The potentials $P(\underline{x}, t)$, $S(\underline{x}, t)$ and $T(\underline{x}, t)$ can be considered as representing P, SV and SH wave motion in the high frequency limit. When (2.2) is substituted into (2.1) and $\underline{f}(\underline{x}, t)$ is represented similarly, a second order differential equation for $T(\underline{x}, t)$ plus two coupled second order differential equations

for $P(\underline{x},t)$ and $S(\underline{x},t)$ are obtained. At high frequencies or when the medium is nearly homogeneous the coupling terms are small. Thus, at high frequencies we have three Helmholtz wave equations for P, SV and SH wave motion separately. Their solution can be used as approximate solutions for P and SV waves and are exact for SH waves. We know from observations that the frequency range where P and SV waves are clearly distinguishable is quite wide. Thus the solutions of the Helmholtz equation are of great importance.

We shall study motion in a fluid whose parameters vary smoothly with depth. We shall solve the problem by Epstein's method (Epstein, 1930) for pressure P rather than for potential $P\rho^{-\frac{1}{2}}$. The density variation will be included in the solution. In Richard's formulation, the Helmholtz equation for potential $P\rho^{-\frac{1}{2}}$ is valid only under the assumption of small density variations with respect to the wavenumber (Hill, 1971). This condition is violated for a discontinuity in density and, therefore, other methods of solutions must be employed in this case (Brekhovskikh, 1960; p. 171). The solutions for pressure P has no such disadvantage and is applicable to the decoupled P-SV motion or SH motion subject to the aforementioned constraints.

Pressure in the fluid is given by

$$P(\underline{x},t) = -K(z)\nabla \cdot \underline{u}(\underline{x},t) \quad (2.3)$$

and the equation of motion by

$$\rho(z) \frac{\partial^2 \underline{u}}{\partial t^2} = - \nabla P(\underline{x}, t) \quad (2.4)$$

$K(z)$ and $\rho(z)$ are coefficient of incompressibility and density, respectively. $\underline{u}(\underline{x}, t)$ is the displacement at $\underline{x}(r, \phi, z)$ and $P(\underline{x}, t)$ is the pressure. We assume that the source and the solution are azimuthally symmetric. In cylindrical coordinates (r, ϕ, z) this means that $\frac{\partial}{\partial \phi} = 0$. In practice this is not a serious limitation as the frequency range of the acoustic waves of interest to us is such that lateral inhomogeneities would effect the propagation very little.

If we eliminate $\underline{u} = \underline{u}(r, \phi, z, t)$ in (2.4) we get

$$\frac{1}{v^2} \cdot \frac{\partial^2 P}{\partial t^2} = \rho(z) \nabla \cdot \left(\frac{1}{\rho(z)} \cdot \nabla P \right) \quad (2.5)$$

where $v(z) = \sqrt{\frac{K(z)}{\rho(z)}}$ is the velocity of acoustic pressure perturbations. Equation (2.5) is a second order differential equation and in order to solve such an equation analytically we must transform the variables.

2.2 The coordinate transformations

First, equation (2.5) is Fourier transformed with respect to time, i.e.

$$f(t) = \frac{1}{2\pi} \int_{-\infty}^{+\infty} e^{-i\omega t} \cdot \int_{-\infty}^{+\infty} f(t') e^{i\omega t'} dt' d\omega = \frac{1}{2\pi} \int_{-\infty}^{+\infty} \tilde{F}(\omega) e^{-i\omega t} d\omega \quad (2.6)$$

The Fourier transformation is denoted by curly tilde. f denotes any function of t . Further, the finite Fourier transform with respect to the angle ϕ is used, i.e.,

$$f(\phi) = \frac{1}{2\pi} \sum_{\ell=-\infty}^{+\infty} e^{i\ell\phi} \int_0^{2\pi} f(\phi') e^{i\ell\phi'} d\phi' = \frac{1}{2\pi} \sum_{\ell=-\infty}^{+\infty} \hat{f}(\ell) e^{i\ell\phi} \quad (2.7)$$

The finite Fourier transform is denoted by capped tilde. Since $f(\phi)$ must be a single valued function of ϕ , ℓ must be an integer. In our case of azimuthal symmetry $\ell = 0$ is the only non-zero term. The Hankel transform or the Fourier-Bessel transform with respect to r is used, i.e.,

$$f(r) = \int_0^{\infty} \kappa J_{\ell}(\kappa r) \int_0^{\infty} r' f(r') J_{\ell}(\kappa r') dr' d\kappa = \int_0^{\infty} \hat{f}(\kappa) J_{\ell}(\kappa r) d\kappa \quad (2.8)$$

The Hankel transform is denoted by double capped tilde.

We also define the Laplace transformation of time

$$f(t) = \frac{1}{2\pi i} \int_{-i\infty}^{+i\infty} e^{st} \int_0^{\infty} f(t') e^{-st'} dt' ds = \frac{1}{2\pi i} \int_{-i\infty}^{+i\infty} f(s) e^{st} ds \quad (2.9)$$

When Laplace transformation is used to transform time t , the Laplace-Bessel transform is used to transform r .

$$\begin{aligned} f(r) &= \frac{s^2}{\pi} \operatorname{Im} \int_{-i\infty}^{+i\infty} p K_{\ell}(spr) \int_0^{\infty} r' I_{\ell}(spr') f(r') dr' dp = \\ &= \frac{s^2}{\pi} \operatorname{Im} \int_{-i\infty}^{+i\infty} p \hat{f}(p) K_{\ell}(spr) dp \end{aligned} \quad (2.10)$$

$K_{\ell}(spr)$ and $I_{\ell}(spr')$ are the modified Bessel functions. The equivalence of the Laplace-Bessel and Fourier-Bessel transformations is evident if we change the variables $s = -i\omega$ and $isp = \kappa$ and convert the modified Bessel functions to $I_{\ell}(spr)$ and $K_{\ell}(spr)$ to $J_{\ell}(\kappa r)$. The relationship between the transformed functions is

$$\hat{f}(p) = e^{-i\ell \frac{\pi}{2}} \hat{f}(\kappa) \quad (2.11)$$

2.3 The source

Let us consider a point pressure source $P_s(t)$ residing at $r = 0, z = z_s$ where the medium varies slowly. The homogeneous equation (2.5) is replaced by

$$\rho(z) \nabla \cdot \left(\frac{1}{\rho(z)} \nabla P \right) - \frac{1}{v^2} \frac{\partial^2 P}{\partial t^2} = \frac{2}{r} P_s(t) \delta(r) \delta(z - z_s) \quad (2.12)$$

After transforming the equation (2.12) with respect to t, ϕ, r we get the following equation for transformed pressure $\hat{P} = \hat{P}(\omega, \kappa, \ell, z)$

$$\rho(z) \frac{d}{dz} \left(\frac{1}{\rho(z)} \frac{d\hat{P}}{dz} \right) + \left(\frac{\omega^2}{v^2} - \kappa^2 \right) \hat{P} = \hat{P}_s(\omega) \delta(z - z_s) \quad (2.13)$$

for $\ell = 0$, and equal to zero for $\ell \neq 0$. $k = \frac{\omega}{v}$ is the wavenumber, $\kappa = k \cdot \sin \theta$ is the horizontal wavenumber and $Q = \left(\frac{\omega^2}{v^2} - \kappa^2 \right)^{1/2} = k \cdot \cos \theta$ is the vertical wavenumber. The Riemann surface $\text{Im } Q > 0$ is the "physical" Riemann sheet. This choice is bound to our choice of the Fourier transform. It assumes the time dependence of the wave being $e^{-i\omega t}$ rather than $e^{i\omega t}$ which has often been used in earlier works on elastic wave propagation. Our choice makes the physical identification of solutions easier as we shall see in the next chapter.

The ultimate aim of the transformations is to describe the motion by a one-dimensional wave equation which can be solved for several velocity-depth structures. We introduce a new variable ζ that will measure depth in terms of density changes with depth:

$$\zeta = \int_{z_0}^z \frac{\rho(z)}{\rho_0} dz \quad (2.14)$$

$\rho_0 = \rho(z_0)$ is a constant value (Phinney, 1970). We can see that for constant density ζ and $(z-z_0)$ are identical. The equation (2.13) becomes

$$\frac{d^2 \hat{P}}{d\zeta^2} + q^2 \hat{P} = \frac{\rho_0}{\rho(\zeta)} P_s(\omega) \delta(\zeta - \zeta_s) \quad (2.15)$$

$q = \frac{\rho_0}{\rho(\zeta)} Q$ can be interpreted as a vertical wavenumber that includes the change of density.

The homogeneous part of the equation (2.15) is the one-dimensional wave equation. If the velocity-depth dependence is such that an analytic solution can be found, the solution of the equation with the source is easy to find. The homogeneous equation has two independent solutions and every linear combination of these is a solution too.

The equation (2.15) has two approximate WKBJ solutions

$$\hat{P}_{1,2}(\zeta) \sim \frac{1}{q^{1/2}} e^{\pm i \int^{\zeta} q d\zeta} \quad (2.16)$$

except in regions of high velocity gradient, where $q(\zeta)$ varies rapidly, or near the turning point ζ_T , where $q(\zeta_T) = 0$ (Morse and Feshbach, 1953; p. 1094). The factor $q^{-1/2}$ in the WKBJ solution is such that the energy flux $P \cdot \underline{v}$ remains constant in the vertical direction. Mathematically, the validity of the WKBJ solutions is explained in great detail in Budden (1961; p. 133).

The source lies in a region where parameters of the medium vary slowly and the two independent WKBJ solutions $\hat{P}_1(\zeta)$ and $\hat{P}_2(\zeta)$ represent waves travelling in positive and negative directions, respectively. We expect that the signal propagates along the same path from the source to the receiver as if it propagated from the receiver to the source. Hence the particular solution of (2.15) must be symmetrical with respect to ζ and ζ_s . Such a solution is

$$\hat{P}_s(\zeta, \zeta_s) = D \hat{P}_1(\zeta_{<}) \cdot \hat{P}_2(\zeta_{>}) \quad (2.17)$$

where $\zeta_{<}$ is the lesser of (ζ, ζ_s) and $\zeta_{>}$ is the greater of (ζ, ζ_s) . This is a standard method used in electromagnetic field theory to find Green's functions (Jackson, 1965; p. 84).

The constant factor D is implied by (2.15):

$$\int_{\zeta_s - \epsilon}^{\zeta_s + \epsilon} \left(\frac{d^2 \hat{P}_s}{d\zeta^2} + q^2 \hat{P}_s \right) d\zeta = \frac{\rho_0}{\rho(\zeta_s)} \hat{P}_s(\omega) \quad \diamond$$

where $\epsilon > 0$ is an arbitrary real number. From the limiting case where $\epsilon \rightarrow 0$ we obtain

$$D = \frac{\frac{\rho_0}{\rho_s} \hat{P}_s(\omega)}{W(\hat{P}_1(\zeta_s), \hat{P}_2(\zeta_s))} \quad (2.18)$$

where $W(\hat{P}_1(\zeta_s), \hat{P}_2(\zeta_s))$ is the Wronskian. In homogeneous medium, \hat{P}_1 and \hat{P}_2 are the exact solutions of the wave equation and the result (2.17) together with (2.18) is equivalent to solutions obtained by other methods (Ewing et al., 1957; p. 19; Chapman and Phinney, 1972). Richards (1970) has shown that in slightly homogeneous medium the Wronskian can be obtained from the approximate solutions valid in the source region. Thus the particular solution may be written as

$$\hat{P}_s(\zeta, \zeta_s) = \frac{1}{2} \tau \cdot \frac{\rho_0}{\rho_s} \cdot \hat{P}_s(\omega) \hat{P}_1(\zeta_<) \hat{P}_2(\zeta_>) \quad (2.19)$$

The general problem of a source in inhomogeneous medium is a complicated one. Effects of both the point source and the

inhomogeneous medium exist together and complicate the solution. Ward (1973) used the principle of seismic reciprocity to solve a problem reciprocal to a problem of a point source near or within a linear transition layer. In the reciprocal problem the effects of a point source and the medium are separated and the solution is relatively easy to find. In the problems discussed here the source is always in the nearly homogeneous part of the model and we shall use (2.19).

2.4 The response integral

The source solution (2.19) represents waves travelling away from the source in both positive and negative ζ directions. We are going to study the waves reflected by an anomalous region below the source. Therefore only the downward travelling solution will be considered:

$$\hat{P}_s = \frac{1}{2} \cdot \frac{\rho_o}{\rho_s} \cdot P_s(\omega) \hat{P}_1(\zeta) \hat{P}_2(\zeta_s) \quad (2.20)$$

Its amplitude at the source is

$$\frac{1}{2} \cdot \frac{\rho_o}{\rho_s} P_s(\omega) \hat{P}_1(\zeta_s) \hat{P}_2(\zeta_s) \quad (2.21)$$

While propagating downwards this wave changes by interaction with the medium. If reflected by the anomalous region, it propagates upwards towards the receiver ζ_r , if transmitted, it continues to propagate downwards. Therefore, there are two waves above the transition, the incident and the reflected waves, while there is only the transmitted wave below the transition. The generalized reflection coefficient $R(\zeta_s, \zeta_r, \kappa)$ is a result of these boundary conditions and thus it describes the response of the medium. Hence the transformed pressure response is

$$P(\omega, r, \zeta_r) = \frac{1}{2} \cdot \frac{\rho_o}{\rho_s} P_s(\omega) \int_0^{\infty} \hat{P}_1(\zeta_s) \hat{P}_2(\zeta_s) R(\zeta_s, \zeta_r, \kappa) J_0(\kappa r) \kappa d\kappa \quad (2.22)$$

The result of (2.22) is standard in seismology and has been used by many authors e.g. Ewing et al. (1957, p. 94) and Chapman and Phinney (1972). The reflection coefficient $R(\zeta_s, \zeta_r, \kappa)$ will be determined in the next chapter from the exact solutions of (2.15) for Epstein velocity structures. Then the response integral (2.22) can be evaluated asymptotically or numerically. Both methods are equally important in the theoretical investigation of spectral amplitudes. The first, while of limited range of validity, indicates the most efficient way of performing the numerical integra-

tion in the complex κ plane. It also determines the correct asymptotic behaviour of the numerical results. The numerical method, while valid in the entire frequency range needed for computation of synthetic seismograms, demands sophisticated computers and is still rather costly. Richards (1973) suggested a middle way between the two. His approach involves the numerical integration of (2.22) but the solutions used are the WKBJ solutions rather than exact wave solutions. It contains the higher order terms of the second order saddle point method but ignores the higher order terms of the wave solution. For the problems we shall consider the wave solutions are simple analytic functions so we need not resort to this approximation.

CHAPTER 3 SOLUTION OF THE WAVE EQUATION BY EPSTEIN'S METHOD

In the previous chapter the equations of motion were established and reduced to the one-dimensional wave equation. We are going to investigate the wave propagation in media with continuous velocity transitions. The non-geometrical effects at caustics, critical points and shadow can be studied for the Epstein velocity structures (Fig. 3.1). We demonstrate here the method of circuit relations first used by Epstein (1930). His approach was discussed later in books by Budden (1961, p. 369), Brekhovskikh (1960, p. 172) and its application to seismic waves is due to Phinney (1970).

3.1 Statement of the problem

We will assume that the velocity-depth structure is one of those drawn in Fig. 3.1. The transition zone is centered around $z = 0$ where the velocity is v_0 . Its thickness is measured by factor σ so that $\xi = \frac{z}{\sigma}$. The transition zone grades smoothly into homogeneous half-spaces above and below the anomalous region and velocity there approaches constant values v_1 and v_2 , respectively. Thus we expect that in these regions the downwards and upwards travelling waves can be distinguished. This is an important property of our medium as it will help us identify the right solutions as waves

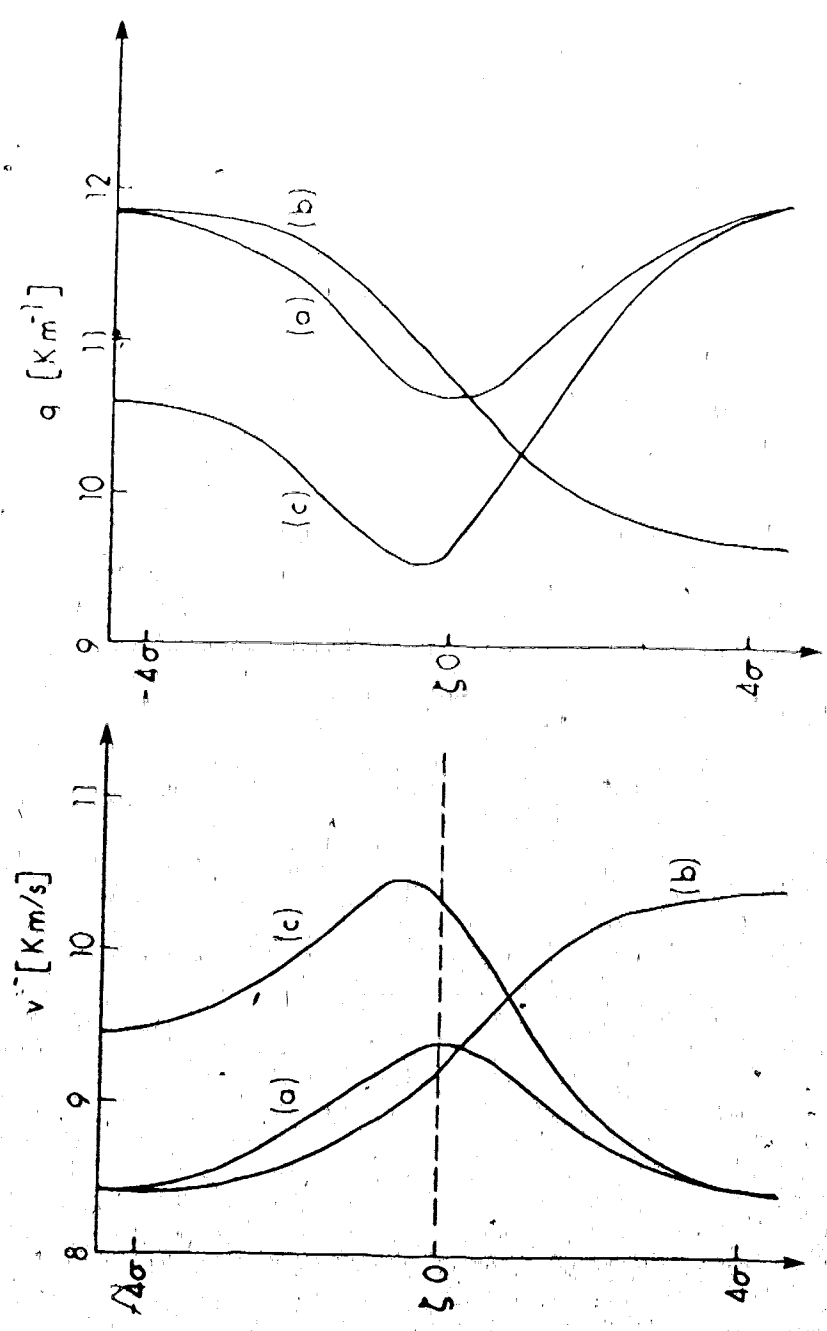


Figure 3.1 Epstein profiles. Curves of q are for vertical incidence ($\sin \theta = 0$) for $\omega = 10$. Curve (a) is for $v_1 = v_2 = 8.4 \text{ km/s}$, $v_0 = 9.4 \text{ km/s}$; curve (b) is the monotonic velocity transition from $v_1 = 8.4 \text{ km/s}$ to $v_2 = 10.4 \text{ km/s}$; in curve (c) $v_1 = 9.4 \text{ km/s}$, $v_2 = 8.4 \text{ km/s}$, $v_0 = 10.4 \text{ km/s}$.

incident, reflected and transmitted through the anomalous region.

With the new variable for depth $z = \frac{\zeta}{\sigma}$ the equation to solve is

$$\frac{d^2 \hat{P}}{dz^2} + \sigma^2 q^2(z) \hat{P} = 0 \quad (3.1)$$

This equation has two approximate WKBJ solutions (2.16) which represent two waves travelling in the opposite directions and are valid in the regions above and below the anomalous region. We assume the source placed above the transition i.e. no wave travelling in the negative z direction exists far below the transition (Fig. 3.2). The solution that satisfies this boundary condition is

$$\hat{P}(\omega, \kappa, z) \sim \frac{1}{\sqrt{\sigma q}} \left(e^{i\sigma \int z q dz} + R e^{-i\sigma \int z q dz} \right) \quad \text{for } 0 \gg z$$

$$\hat{P}(\omega, \kappa, z) \sim \frac{1}{\sqrt{\sigma q}} T e^{i\sigma \int z q dz} \quad \text{for } 0 < z$$

(3.2)

and every exact solution of (3.1) must asymptotically approach to (3.2). Coefficients R and T are the reflection and transmission coefficients. It is therefore essential to find the

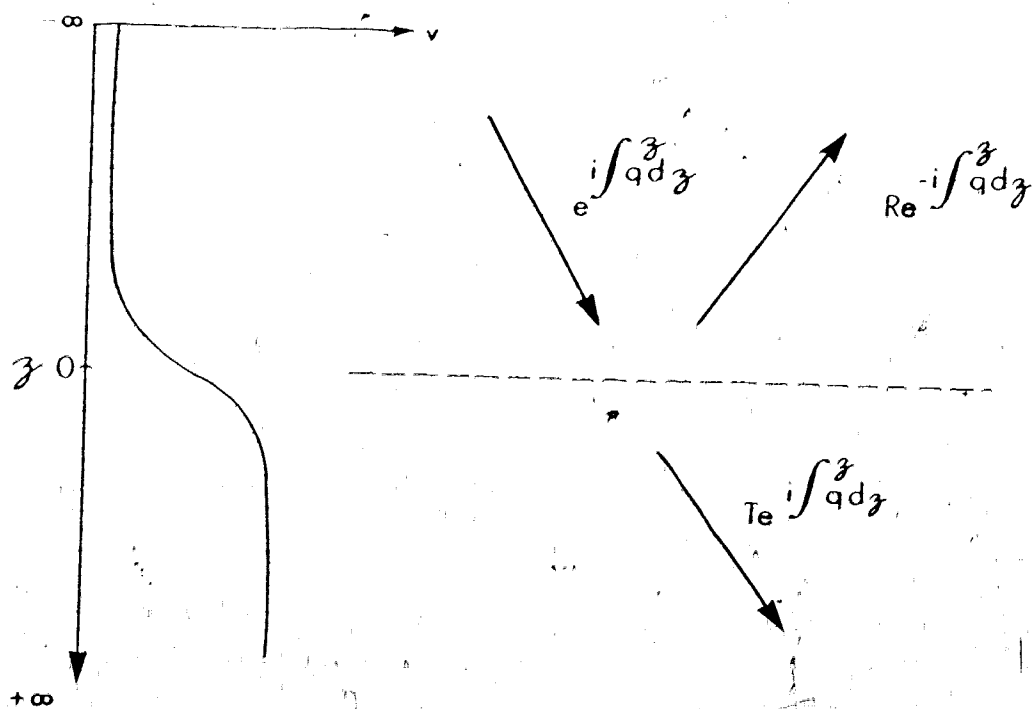


Figure 3.2 The WKB solutions in the medium with velocity transition.

relationship between the field in the region of incidence and the field in the region of transmission. Mathematically this is equivalent to determining the correct analytic continuation of these asymptotic solutions outside the range of their validity.

Epstein's method shows how the solutions above and below the transition can be matched and the correct reflection and transmission coefficients found.

3.2 Compatibility of the wave and the hypergeometric equations

Epstein (1930) showed that the hypergeometric equation

$$\xi(1-\xi) \frac{d^2 \phi}{d\xi^2} + (c - (a+b+1)\xi) \frac{d\phi}{d\xi} - a b \phi = 0 \quad (3.3)$$

is equivalent to the wave equation

$$\frac{d^2 \psi}{d\beta^2} + h^2 \psi = 0 \quad (3.4)$$

if

$$-\xi = e^\beta \quad (3.5)$$

$$\phi = \psi(\beta) e^{-\frac{1}{2}(c-1)\beta} (1 + e^\beta)^{-d} \quad d = \frac{1}{2}((a+b) - (c-1)) \quad (3.6)$$

and

$$\begin{aligned}
 h^2 &= \frac{(c-1)^2}{4} + \frac{(c-1)^2 - (a-b)^2}{4(e^{\beta}+1)} e^{\beta} + \frac{(a+b-c-1)(a+b-c+1)}{4(e^{\beta}+1)^2} e^{\beta} \\
 &= r_1 + (r_2 - r_1) \frac{e^{\beta}}{(e^{\beta}+1)} + r_3 \frac{e^{\beta}}{(e^{\beta}+1)^2} \quad (3.7)
 \end{aligned}$$

The hypergeometric equation has three singularities, $\xi_1 = 0$, $\xi_2 = 1$, $\xi_3 = \infty$. The change of variables (3.5) maps the inside of the unit circle in ξ plane on the left-hand half plane of β . The outside of the unit circle in ξ plane maps into the right hand half-plane of β (Fig. 3.3).

The solutions Φ_1 ($i = 1, 2, 3, 4, 5, 6$) are all in terms of hypergeometric series of type

$$F(a, b; c; \xi) = \sum_{n=0}^{\infty} \frac{(a)_n (b)_n}{(c)_n n!} \xi^n \quad (a)_n = \frac{\Gamma(a+n)}{\Gamma(a)} \quad (3.8)$$

and are all defined in Appendix A.1. They are valid only in those regions of ξ plane where the series are convergent. If we map these into β plane we have the following solutions of (3.4):

For $\beta < 0$

$$\Psi_1(\beta) = F(a, b; c; -e^{\beta}) e^{\frac{1}{2}(c-1)\beta} (1 + e^{\beta})^d$$

$$\Psi_2(\beta) = F(a-c+1, b-c+1; 2-c; -e^{\beta}) e^{-\frac{1}{2}(c-1)\beta} (1 + e^{\beta})^d$$

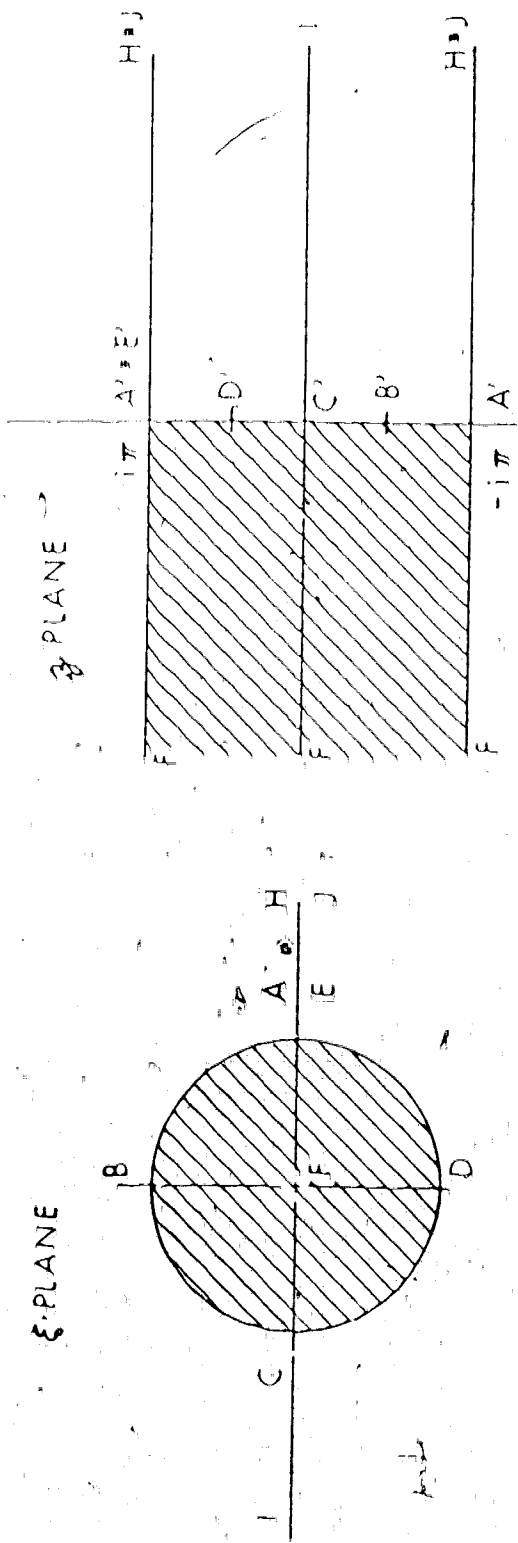


Figure 3.3 Conformal mapping $z = e^{-\zeta}$

For $\beta = 0$

$$\Psi_3(\beta) = F(a, b; a+b+1-c; 1+e^\beta) e^{\frac{1}{2}(c-1)\beta} (1+e^\beta)^d.$$

$$\Psi_4(\beta) = F(c-b, c-a; c-a-b+1; 1+e^\beta) e^{\frac{1}{2}(c-1)\beta} (1+e^\beta)^{c-a-b+d}$$

(3.9)

For $\beta > 0$

$$\Psi_5(\beta) = F(b, b-c+1; b-a+1; -e^{-\beta}) e^{\frac{1}{2}(a-b)\beta} (1+e^{-\beta})^d$$

$$\Psi_6(\beta) = F(a, a-c+1; a-b+1; -e^{-\beta}) e^{-\frac{1}{2}(a-b)\beta} (1+e^{-\beta})^d.$$

Outside the region of convergence of the series, each of the solutions can be analytically continued into the rest of the β plane. The solution is then expressed as a linear combination of the two series solution convergent in that region. The analytic continuation is possible because an integral solution of (3.3) exists that is valid throughout the ξ plane with exception of the singularities, ξ_1 , ξ_2 and ξ_3 (Appendix A.1). The relationship between the solution in different regions of the convergence is given by their analytic continuation can be written in a simple matrix form:

$$i\phi = \sum_{j=1}^3 A_{ij} \phi_j \quad \begin{array}{l} i \neq j \\ i, j = 1, 2, 3 \end{array} \quad (3.10)$$

Φ_{1-} is a 2×1 vector of two independent solutions in the region of convergence around ξ_1 . ${}_{11}^A$ is a 2×2 matrix of analytic continuation from region ξ_1 to region ξ_j (Appendix A.1).

We are looking for solutions of equation (3.4). These are connected to the solutions of (3.3) by (3.6). Therefore the same matrix relationship as (3.10) is valid for solutions Ψ_{1-} . Ψ_{1-} is a vector of two independent solutions in regions of convergence around β_1 ($\beta_1 = -\infty$, $\beta_2 = 0$, $\beta_3 = +\infty$). By inspection of the asymptotic solutions (3.2) we conclude we need the following relationship:

$$\begin{pmatrix} \Psi_5 \\ \Psi_6 \end{pmatrix} = \begin{pmatrix} A_{51} & A_{52} \\ A_{61} & A_{62} \end{pmatrix} \cdot \begin{pmatrix} \Psi_1 \\ \Psi_2 \end{pmatrix} \quad (3.11)$$

The matrix is the continuation matrix ${}_{31}^A$ given by (A.1.11)

$${}_{31}^A = \begin{pmatrix} \frac{\Gamma(1-c)\Gamma(1+b-a)}{\Gamma(1-a)\Gamma(1+b-c)} & \frac{\Gamma(c-1)\Gamma(1+b-a)}{\Gamma(c-a)\Gamma(b)} \\ \frac{\Gamma(1-c)\Gamma(1+a-b)}{\Gamma(1-b)\Gamma(1+a-c)} & \frac{\Gamma(c-1)\Gamma(1+a-b)}{\Gamma(c-b)\Gamma(a)} \end{pmatrix} \quad (3.12)$$

If the solution $\Psi(\beta)$ for $\beta > 0$ is given by Ψ_5 or Ψ_6 and for $\beta < 0$ by the linear combination of Ψ_1 and Ψ_2 prescribed by the matrix of analytical continuation ${}_{31}^A$ we can be sure we have chosen the right solution. Identification of Ψ_1 , Ψ_2 and

Ψ_5 or Ψ_6 as incident, reflected and transmitted waves depends on the choice of $\text{Im}(c-1)$. If $\text{Im}(c-1) > 0$, the leading term in Ψ_1 (3.9) gives the wave travelling in the positive z direction and in our problem Ψ_1 is an incident wave. Ψ_2 represents the wave travelling in the negative z direction i.e. the reflected wave. If $\text{Im}(c-1) < 0$ the directions of propagation of Ψ_1 and Ψ_2 would be interchanged and Ψ_2 would represent incident wave while Ψ_1 would be the reflected one. The sign of $\text{Im}(a-b)$ which determines the wave propagation for $z > 0$ has to be taken in agreement with the sign of $\text{Im}(c-1)$. In case of constant velocity throughout the medium the wave travels without change. Therefore, if $\text{Im}(c-1) > 0$ it is Ψ_5 that represents the transmitted wave. Ψ_6 represents the transmitted wave if $\text{Im}(c-1) < 0$ (Fig. 3.4a,b).

The matrix of analytic continuation represents the law of reflection when the incident wave propagates from $-\infty$. The inverse matrix ${}_{13}A = {}_{31}A^{-1}$ represents the law of reflection should the incident wave propagate from $+\infty$ (Fig. 3.4c,d). There is, however, a better way or more common way to write the reflection law once we choose the sign of $\text{Im}(c-1)$. The equation (3.11) represents two physical problems that never arise at the same time. This is due to ambiguity in sign of $\text{Im}(c-1)$. Once that is chosen, one of the equations in (3.11) has no physical meaning. The same is true should the

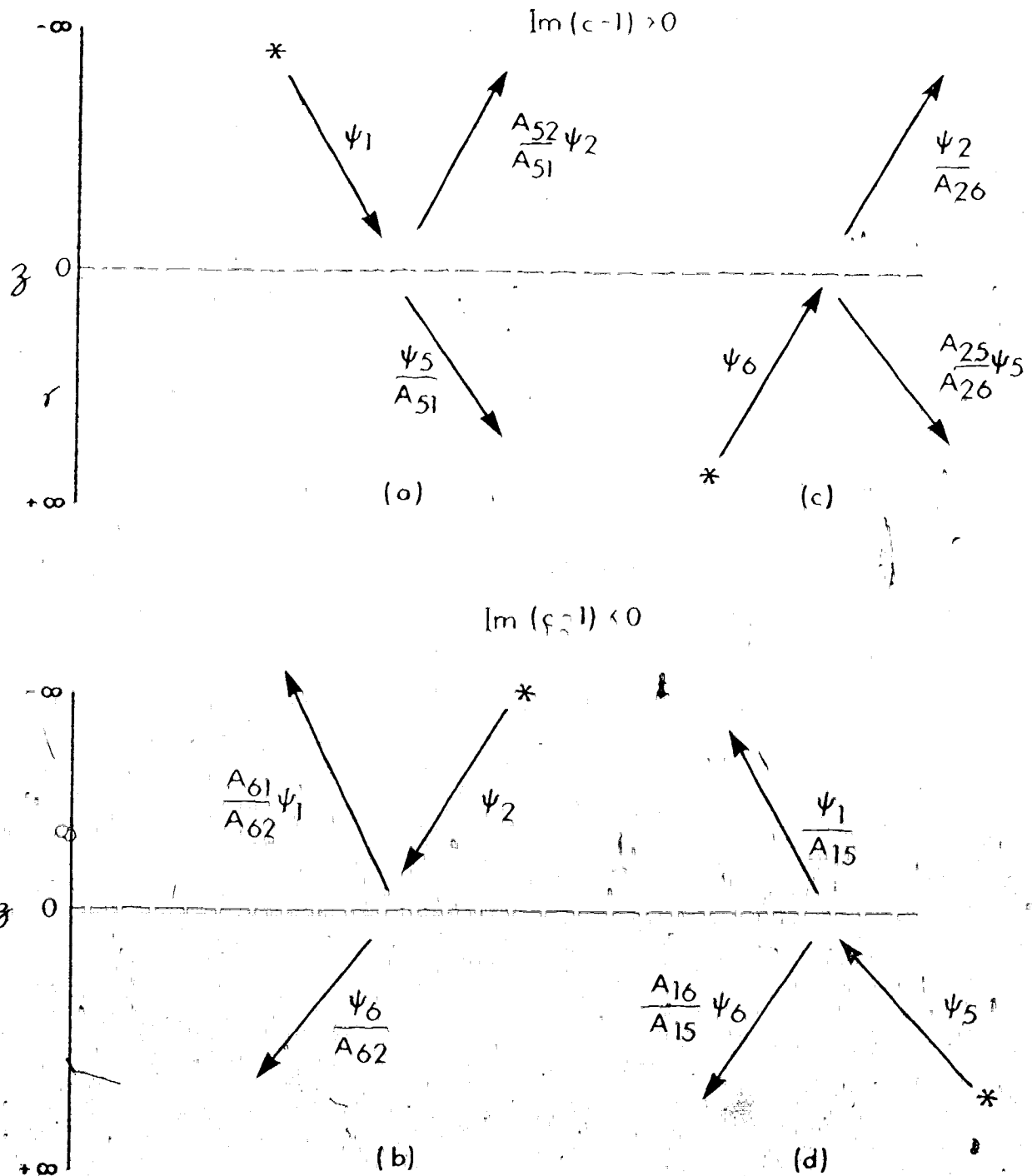


Figure 3.4 Analytic continuation interpreted physically as reflection-transmission law.

source be positioned at $+\infty$.

For $\text{Im}(c-1) > 0$ and $\text{Im}(a-b) > 0$ we can write

$$-\begin{pmatrix} \Psi_1 \\ \Psi_6 \end{pmatrix} = \begin{pmatrix} S_{11} & S_{12} \\ S_{21} & S_{22} \end{pmatrix} \begin{pmatrix} \Psi_2 \\ \Psi_5 \end{pmatrix} \quad (3.13)$$

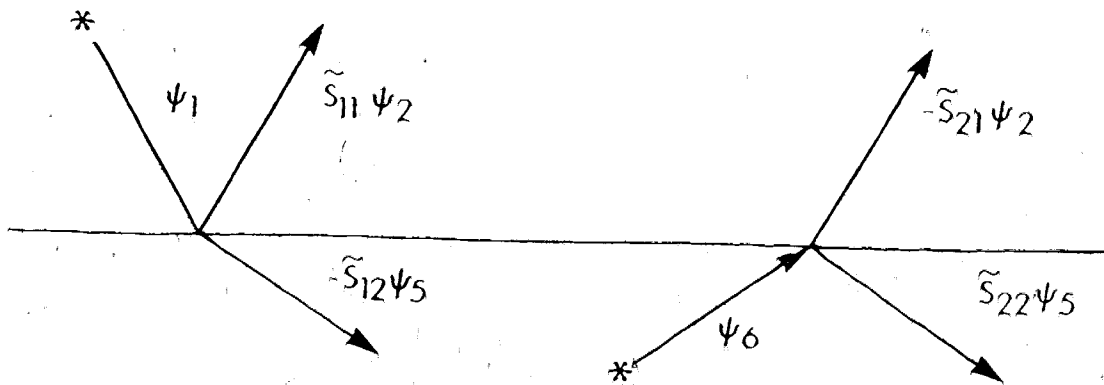
$$\text{where } S_{11} = -\frac{A_{52}}{A_{51}} \quad S_{12} = -\frac{1}{A_{51}}$$

$$S_{21} = -\frac{\det_{31} A}{A_{51}} \quad S_{22} = -\frac{A_{61}}{A_{51}}$$

$$\det_{31} A = \frac{a-b}{c-1}$$

The vector on the L.H.S. represents waves travelling towards the transition i.e. incident waves from above and below. The vector on the R.H.S. represents the waves travelling away from the transition after reflection or transmission (Fig. 3.5). The diagonal terms of the matrix \underline{S} are the reflection coefficients, the off-diagonal terms are the transmission coefficients. We will show that suitable normalization of the vectors with respect to constant energy flux in the z -direction will yield identical transmission coefficients in both directions. Then the matrix \underline{S} is symmetrical. We have found a new formulation of our problem which is analogous to that used commonly in seismology (see for example Chapman, 1971, unpublished lectures).

MEDIUM 1



MEDIUM 2

Figure 3.5 Reflection laws for incidence from above and below the interface.

for Physics 521). It must be used with care, however, as all the reflection and transmission coefficients are valid in far regions. The field

$$\Psi(z) = \Psi_1(z) + \frac{\Gamma(c-1)\Gamma(1-a)\Gamma(1+b-c)}{\Gamma(c-a)\Gamma(b)\Gamma(1-c)} \Psi_2(z) \quad (3.14)$$

is valid throughout the region above the transition i.e. for $z < 0$ without restriction. The field

$$\Psi(z) = \frac{\Gamma(1-a) \cdot \Gamma(1+b-c)}{\Gamma(1+b-a)\Gamma(1-c)} \Psi_5(z) \quad (3.15)$$

is also valid for $z > 0$ with no constraints. The reflection coefficient

$$R(z_s, z_r) = \frac{\Gamma(c-1)\Gamma(1-a)\Gamma(1+b-c)}{\Gamma(c-a)\Gamma(b)\Gamma(1-c)} \cdot \frac{\Psi_2(z_r)}{\Psi_1(z_s)} \quad (3.16)$$

and the transmission coefficient

$$T(z_s, z_t) = \frac{\Gamma(1-a)\Gamma(1+b-c)}{\Gamma(1+b-a)\Gamma(1-c)} \cdot \frac{\Psi_5(z_t)}{\Psi_1(z_s)} \quad (3.17)$$

however, are valid only in regions where we can be sure that Ψ_1 , Ψ_2 and Ψ_5 represent waves incident, reflected and transmitted, respectively. And this is only in the region where medium is nearly homogeneous. Throughout this work we have found that the reflection coefficient and transmission

coefficients are accurate enough for frequency range and thicknesses considered. Comparison of the leading terms in the solution with the next terms gives the estimate of the error (Appendix B).

To apply these results to equation (3.1) we must assign suitable physical meaning to constants a , b , c . Equations (3.1) and (3.4) are equivalent if $oq = h$. Solutions (3.14) and (3.2) of the equations (3.4) and (3.1) must be equivalent. By inspection of (3.2) and (3.14) we get

$$\begin{aligned} c-1 &= 2i\sigma q_1 = 1S \frac{\rho_0}{\rho_1} \cos \theta_1 = 2i\sigma \frac{\rho_0}{\rho_1} \left(\frac{\omega^2}{v_1^2} - \kappa^2 \right)^{\frac{1}{2}} \\ a-b &= 2i\sigma q_2 = 1S \frac{\rho_0}{\rho_2} \left(\frac{v_1^2}{v_2^2} - \sin^2 \theta_1 \right)^{\frac{1}{2}} = 2i\sigma \frac{\rho_0}{\rho_2} \left(\frac{\omega^2}{v_2^2} - \kappa^2 \right)^{\frac{1}{2}} \end{aligned} \quad (3.18)$$

where S is the effective thickness

$$S = \frac{2\pi}{\lambda_1} \cdot 2\sigma = \frac{\omega}{v_1} \cdot 2\sigma$$

From $\sigma^2 q_0^2 = h^2(0)$ we obtain

$$a+b-c = \pm 2\gamma = \pm \left(1 + 16\sigma^2 (q_0^2 - \frac{1}{2}(q_1^2 + q_2^2)) \right)^{\frac{1}{2}} \quad (3.18a)$$

The sign is arbitrary and each gives the identical reflection and transmission coefficients (Appendix B). The analytic

expression for vertical wavenumber for the Epstein models is

$$q^2(\beta) = q_1^2 - (q_1^2 - q_2^2) \frac{e^\beta}{(e^\beta + 1)} + 4(q_0^2 - \frac{1}{2}(q_1^2 + q_2^2)) \frac{e^\beta}{(e^\beta + 1)^2} \quad (3.19)$$

and its form is shown in Fig. 3.1 for various values of v_1 , v_2 and v_0 . The law of reflection with normalization of solutions to preserve constant energy flux in β direction is

$$\begin{pmatrix} \psi_1 \\ \frac{1}{q_1} \\ \frac{1}{2} \\ \psi_6 \\ \frac{1}{q_2} \\ \frac{1}{2} \end{pmatrix} = \begin{pmatrix} S_{11} & S_{12} \\ S_{21} & S_{22} \end{pmatrix} \begin{pmatrix} \psi_2 \\ \frac{1}{q_1} \\ \frac{1}{2} \\ \psi_5 \\ \frac{1}{q_2} \\ \frac{1}{2} \end{pmatrix} \quad (3.20)$$

where matrix \underline{S} is symmetrical with elements

$$S_{11} = \frac{\Gamma(1+2i\sigma q_1) \Gamma(\frac{1}{2}-\gamma-i\sigma(q_1+q_2)) \Gamma(\frac{1}{2}+\gamma-i\sigma(q_1+q_2))}{\Gamma(1-2i\sigma q_1) \Gamma(\frac{1}{2}+\gamma+i\sigma(q_1-q_2)) \Gamma(\frac{1}{2}+\gamma+i\sigma(q_1-q_2))}$$

$$S_{12} = -\frac{q_2}{q_1} \cdot \frac{\Gamma(\frac{1}{2}-\gamma-i\sigma(q_1+q_2)) \Gamma(\frac{1}{2}+\gamma-i\sigma(q_1+q_2))}{\Gamma(1-2i\sigma q_2) \Gamma(-2i\sigma q_1)} = S_{21}$$

$$S_{22} = \frac{\Gamma(1+2i\sigma q_2)}{\Gamma(1-2i\sigma q_2)} \cdot \frac{\Gamma(\frac{1}{2}-\gamma-i\sigma(q_1+q_2)) \Gamma(\frac{1}{2}+\gamma-i\sigma(q_1+q_2))}{\Gamma(\frac{1}{2}-\gamma+i\sigma(q_1-q_2)) \Gamma(\frac{1}{2}+\gamma+i\sigma(q_1-q_2))}$$

If we use the asymptotic expressions for $\Psi_1(z_s)$ and $\Psi_2(z_r)$ in (3.16) we obtain the following reflection coefficient:

$$R(z_s, z_r) = S_{11} e^{-i\sigma(q_s z_s + q_r z_r)}, \quad z_s < 0, z_r < 0 \quad (3.22)$$

where $q_s = \frac{\rho_o}{\rho_s} \left(\frac{\omega^2}{v_s^2} - \kappa^2 \right)^{1/2}$ and $q_r = \frac{\rho_o}{\rho_r} \left(\frac{\omega^2}{v_r^2} - \kappa^2 \right)^{1/2}$.

The term in the exponent gives the change of the phase of the wave on its path from the source to the receiver. Using asymptotic expressions for $\Psi_1(z_s)$ and $\Psi_5(z_t)$ in (3.17) we get the transmission coefficient

$$T(z_s, z_t) = -S_{12} e^{-i\sigma(q_s z_s - q_t z_t)} \quad (3.23)$$

where $q_t = \frac{\rho_o}{\rho_t} \left(\frac{\omega^2}{v_t^2} - \kappa^2 \right)^{1/2}$.

The reflection coefficient (3.22) will be used for evaluation of the pressure response (2.22) for the monotonic velocity transition (Chapter 4) and for the velocity reversal (Chapter 5).

CHAPTER 4 CAUSTICS AND HEAD WAVES DUE TO MONOTONIC
VELOCITY TRANSITIONS

4.1 The reflection coefficient

For the monotonic velocity transition in Figures 1.2, 1.3 and 4.1 $q_0^2 = \frac{1}{2}(q_1^2 + q_2^2)$ and the vertical wavenumber is given by

$$q^2(\zeta) = \frac{1}{2}(q_1^2 + q_2^2) - \frac{1}{2}(q_1^2 - q_2^2) \tanh \frac{\zeta}{2\sigma} \quad (4.1)$$

The reflection coefficient (3.22) becomes

$$R(\zeta_S, \zeta_T, \kappa) = \frac{q_1 - q_2}{q_1 + q_2} \cdot \frac{\Gamma(1 + 2i\sigma q_1)}{\Gamma(1 - 2i\sigma q_1)} \cdot \frac{\Gamma^2(1 - i\sigma(q_1 + q_2)) e^{-i(q_S \zeta_S + q_T \zeta_T)}}{\Gamma^2(1 + i\sigma(q_1 - q_2))} \quad (4.2)$$

The reflection coefficient (4.2) was studied by Epstein (1930), Rawer (1939) and Phinney (1970), although they only studied its modulus and not the full wave response. The term $\Gamma(1 + 2i\sigma q_1)/\Gamma(1 - 2i\sigma q_1)$ effects only the phase change that occurs during the reflection. When attenuation is not considered $q^2(\zeta)$ is real. For angles of emergence less than the critical angle $\theta_c = \sin^{-1} \frac{v_1}{v_2}$, the vertical wavenumber below the transition is real and partial reflection occurs. In this case

1.6 km transition zone at 20 km

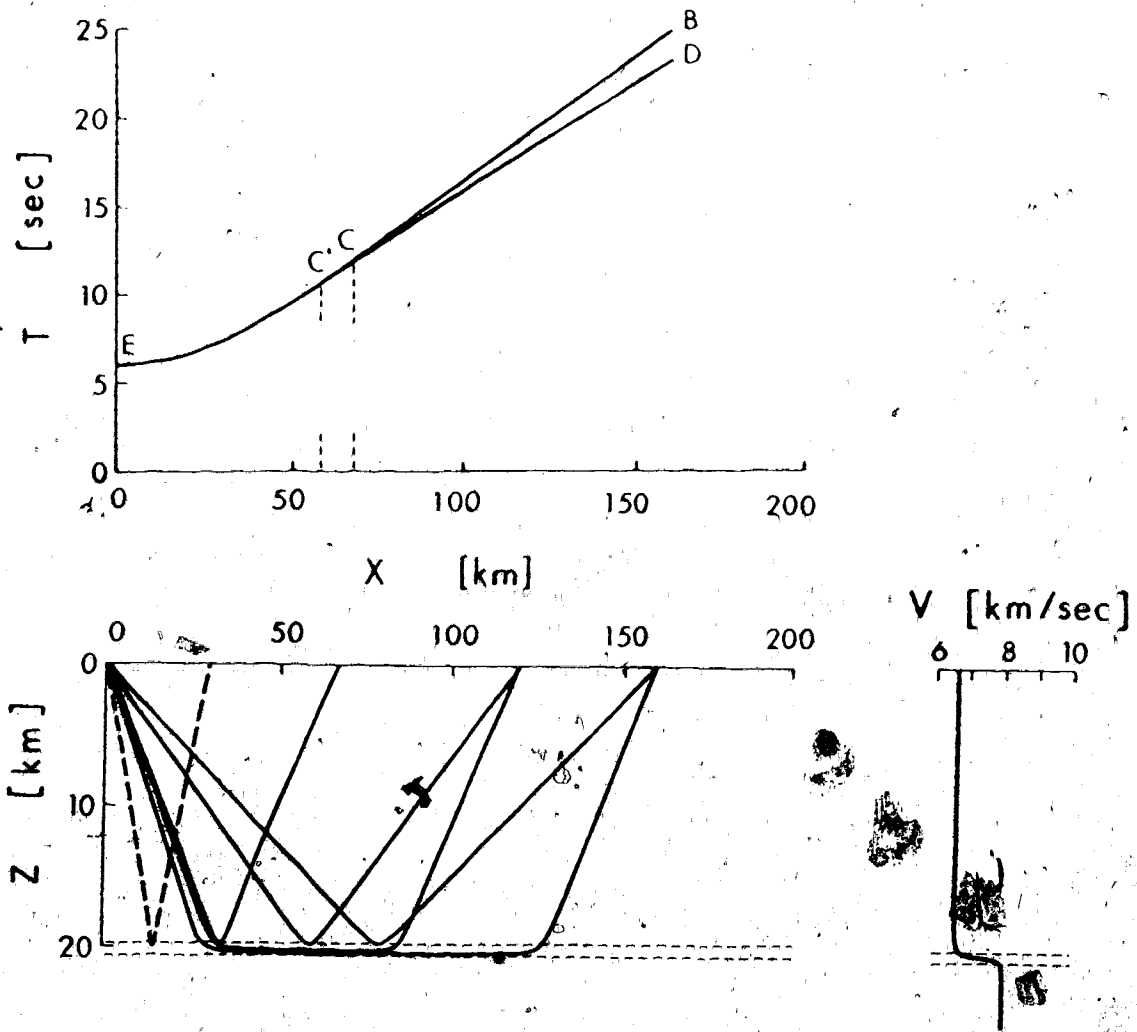


Figure 4.1 The partial reflections and head waves near the critical point for monotonic velocity increase.

$$|R| = \frac{\sinh(\pi\sigma(q_1 - q_2))}{\sinh(\pi\sigma(q_1 + q_2))} \quad (4.3)$$

At sub-critical angles the partial reflection depends on the effective thickness S (3.18). The reflection and transmission through the medium depend on the absolute thickness of the layer 0 as well as the wavelength of the propagating wave and the effective thickness S includes both effects. If S is small the reflection is nearly as strong as the sub-critical reflection for the sharp velocity increase from v_1 to v_2 . Then the reflection coefficient is the well-known Fresnel formula

$$|R| = \frac{q_1 - q_2}{q_1 + q_2} \quad (4.4)$$

In this case the reflection coefficient is independent of frequency and the Cagniard-de Hoop method may be used for evaluation of the response integral (Cagniard, 1962; de Hoop, 1960).

If the effective thickness is large the nature of the partial reflection is changed. The partial reflection, which is quite strong at near-vertical angles when the transition is thin becomes very weak for thick transitions with triplications (Figure 1.2). Most of the energy is transmitted through the transition and only in the neighbourhood of the

cusps some energy returns. The decay of the modulus of the reflection coefficient into the region before the critical point is given by

$$|R| = e^{-\pi S \frac{\rho_0}{\rho_2} \left(\frac{v_1^2}{2} - \sqrt{1 - n^2} \right)^{1/2}} \quad (4.5)$$

For angles of emergence from the source exceeding the critical angle, $|R| = 1$ and total reflection occurs whether or not the transition zone is thin or thick. Thus the reflection coefficient (4.2) gives the phase change along the wave path.

The study of the analytic behaviour of the reflection coefficient is necessary for the evaluation of the response integral (2.22). Only perfect understanding of the reflection coefficient in the complex plane of the horizontal wavenumber κ enables us to perform the evaluation of the response integral efficiently.

The reflection coefficient (4.2) has eight branch points $\pm \kappa_1 = \pm \frac{\omega}{v_1}$, $\pm \kappa_2 = \pm \frac{\omega}{v_2}$, $\pm \kappa_s = \pm \frac{\omega}{v_s}$ and $\pm \kappa_r = \pm \frac{\omega}{v_r}$ due to zeros of the vertical wavenumbers q_1 , q_2 , q_s and q_r (3.18) and (3.22), respectively. The complex κ plane has, therefore, sixteen Riemann surfaces separated by branch cuts but only four are important in our discussion (Figures 4.2 and 4.3). The twelve remaining sheets need never be considered. In our problem the best choice of branch cuts are lines $\pm \kappa_p$,

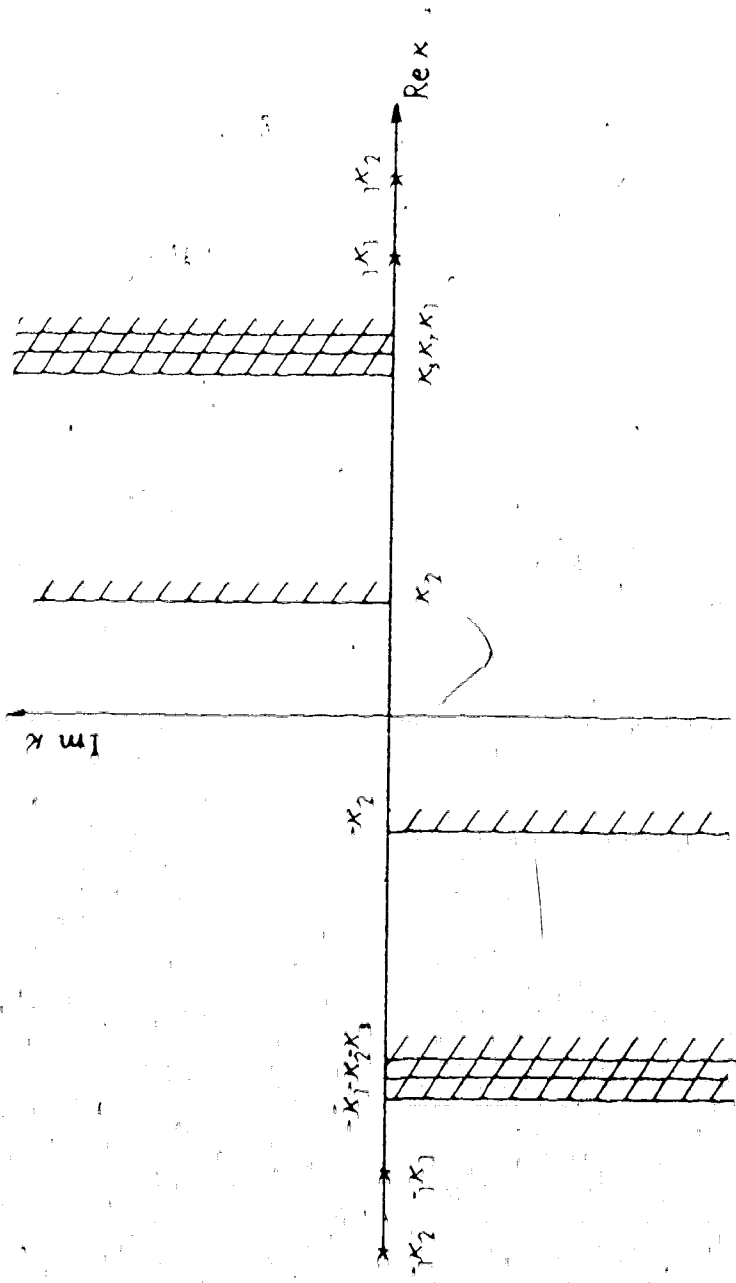


Figure 4.2a The poles on (++) Riemann sheet of the complex x plane.

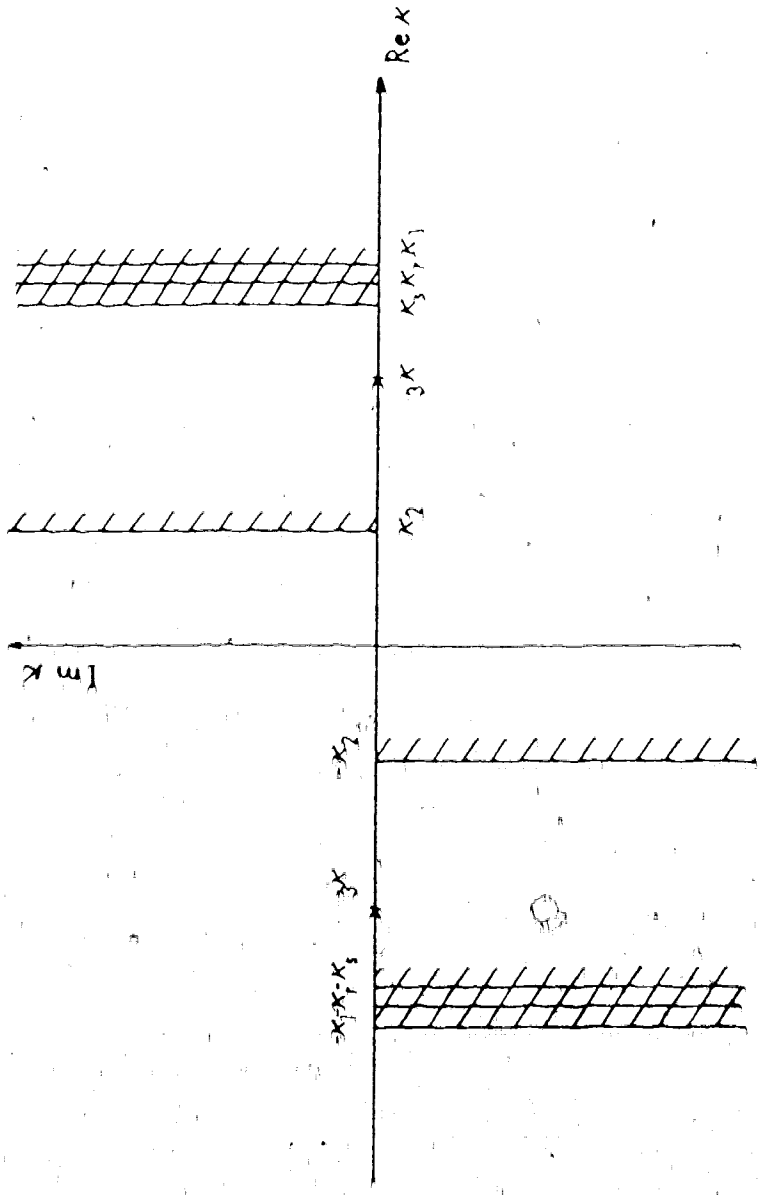


Figure 4.2b The poles on (+-) Riemann sheet of the complex x plane.

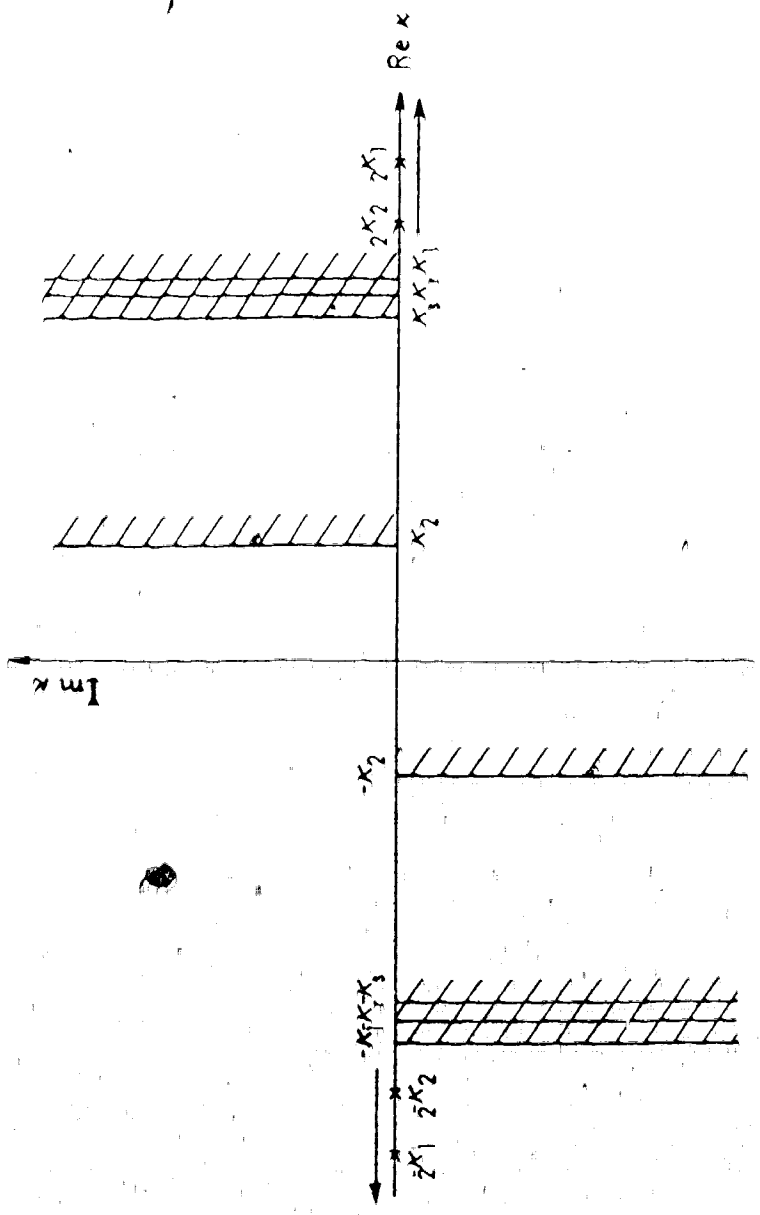


Figure 4.3a The poles on $(-+)$ Riemann sheet of the complex k plane for frequency $\omega_3 > \omega > \omega_2$. The arrows indicate the direction of the movement of poles as frequency increases.

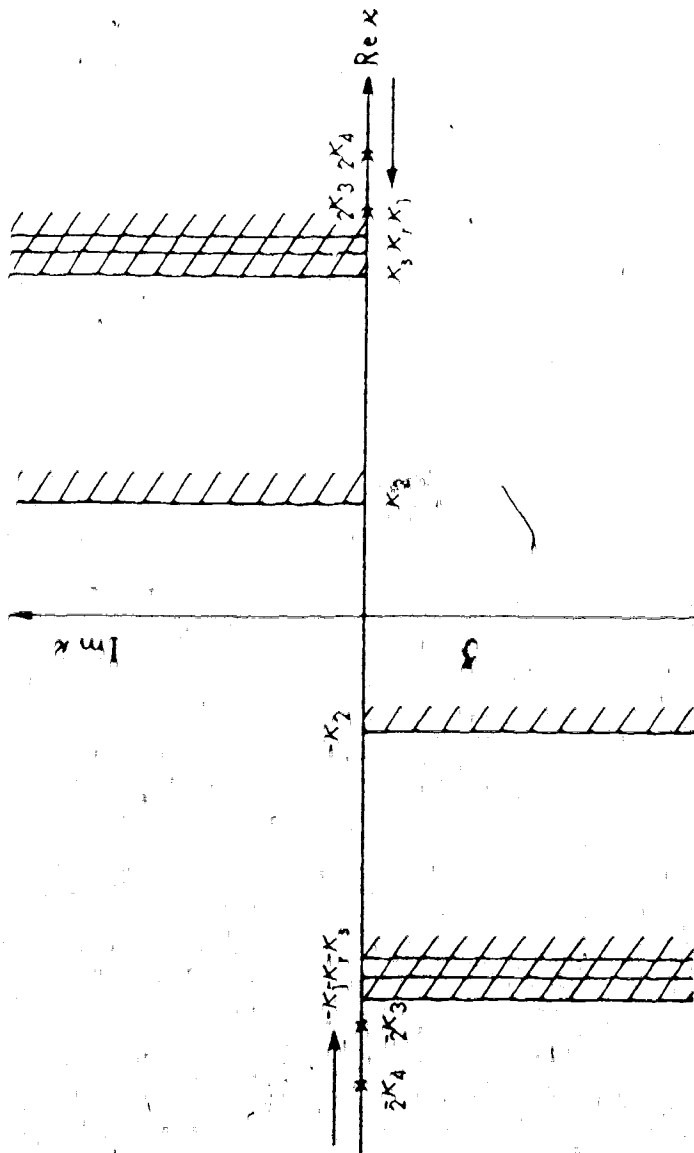


Figure 4.3b The poles on (--) Riemann sheet of the complex x plane for frequency $\omega_3 > \omega > \omega_2$. The arrows indicate the direction of the movement of poles as frequency increases.

$+k_p + i\omega$, $-k_p - i\omega$, $-k_p$, where $p = 1, 2, s$ or r . The branch cuts from k_1 , k_s and k_r to $-k_1$, $-k_s$, $-k_r$, respectively, are very close together and when speaking about the top sheet of q_1 we implicitly assume also top sheet of q_s and q_r . The bottom sheet of q_1 is also assumed to be a bottom sheet of q_s and q_r . The notation $(++)$ sheet has been used by several authors including Phinney (1961) and Gilbert and Laster (1962). Their definition is slightly different from ours which suits our problem best (Appendix C). The $(++)$ indicates the signs of the imaginary parts of q_2 and q_1 , respectively. The $(++)$ sheet is sometimes referred to as the "top" or "upper" Riemann sheet in this thesis.

The reflection coefficient has poles at the poles of the gamma functions in the numerator of (4.2). The contribution from poles of reflection coefficients often has important physical interpretation. For example; Lamb (1904) interpreted the residue at the pole of the reflection coefficient in a homogeneous half-space as the Rayleigh wave. Pekeris (1948) interpreted normal modes, i.e. waves due to interference within layers of a layered medium, as contributions from poles of the reflection coefficients. Phinney (1961), Gilbert and Laster (1962) and Chapman (1972) have shown how poles on other Riemann sheets may cause separate arrivals or modify geometrical ray arrivals from the top sheet. We must therefore

Investigate all the poles of the reflection coefficient. There are three characteristic or secular equations which determine the position of poles in our problem:

$$2i\sigma q_1 = -n \quad n = 1, 2, 3, \dots \quad (4.6a)$$

$$i\sigma(q_1 + q_2) = n \quad n = 1, 2, 3, \dots \quad (4.6b)$$

$$q_1 + q_2 = 0 \quad (4.6c)$$

The first secular equation gives poles on the top Riemann sheet. They lie on the real axis "beyond" the branch points $\pm \kappa_1$ (Fig. 4.2a)

$$\pm i \kappa_n = \pm \left(\frac{\omega^2}{v_1^2} + \frac{n^2 \rho_1^2}{4\sigma^2 \rho_0^2} \right)^{1/2} \quad (4.7)$$

The signals arising from their contribution decay exponentially in the vertical direction and propagate with phase velocity smaller than v_1 :

$$c = v_1 \left(1 + \frac{1}{\kappa_1^2} \cdot \frac{n^2}{4\sigma^2} \cdot \frac{\rho_1^2}{\rho_0^2} \right)^{-1/2}$$

We are mainly interested in waves propagating with phase velocities between v_1 and v_2 i.e. arriving earlier than signals arising from the pole's contribution.

The secular equation (4.6b) gives sets of poles either on $(-+)$ or on $(--)$ sheet. We will treat here only the case of constant density as the algebra is simpler and overall conclusions are analogous. The poles on $(-+)$, $(+-)$ and $(--)$ sheets must be investigated as they sometimes contribute signals called "leaking" modes. In contrast to signals arising from poles $\pm \kappa_n$, which decay with depth, signals arising from poles on other sheets grow exponentially with depth. The energy "leaks" into the lower medium. The "leaking" modes arise from poles that are within certain neighbourhood of a branch point and, therefore, influence the reflection coefficient on the top Riemann sheet (Chapman, 1972). In our problem, the poles

$$\pm 2\kappa_n = \pm \left\{ \frac{1}{2} \left(\frac{\omega^2}{v_1^2} + \frac{\omega^2}{v_2^2} \right) + \frac{n^2}{4\sigma^2} + \frac{\sigma^2}{4n^2} \left(\frac{\omega^2}{v_1^2} - \frac{\omega^2}{v_2^2} \right)^2 \right\}^{1/2} \quad (4.8)$$

would have to approach the branch points $\pm \kappa_2$ to cause such effect. This is very unlikely as the poles lie always on the real axis "beyond" the branch points $\pm \kappa_1$ (Fig. 4.3).

At low frequencies all poles lie on the $(--)$ Riemann sheet.

The zero frequency position is

$$\pm 2\kappa_n^0 = \pm \frac{n}{2\sigma} \quad n = 1, 2, \dots$$

As frequency increases the poles move towards the branch points and a cutoff frequency exists for each order n when $\pm 2\kappa_n$ appear at the branch points $\pm\kappa_1$ and pass from $(--)$ on $(-+)$ sheet:

$$\omega_n = \frac{n}{0} \left(\frac{1}{v_1} - \frac{1}{v_2} \right)^{-\frac{1}{2}}$$

For higher frequencies the poles $\pm 2\kappa_n$ move away from the branch points on the $(-+)$ sheet (Fig. 4.3a). Thus the two sets of poles $\pm 2\kappa_n$ will not become important when evaluating the response integral (2.22).

The roots of equation (4.6c) give poles analogous to those in two fluid half-spaces, Gilbert (1964). They lie on the real or imaginary axis of $(-+)$ and $(+-)$ sheets:

$$\pm 3\kappa = \pm \frac{\omega}{v_1} \left\{ \frac{\rho_1 v_2^2}{2 v_1^2} \right. \\ \left. 1 - \frac{\rho_1}{\rho_2} \right\} \quad (4.9)$$

Depending on the parameters ρ_1 , ρ_2 and v_1 , v_2 , the poles can contribute to signals propagating along the thin transition. We are interested in the propagation at the receiver point well above the transition and the contribution of these pulses is negligible there.

We can conclude the investigation of poles by saying that for the monotonic velocity transition, the signals arising from poles' contribution arrive at later times than those we are going to study.

4.2 The WKBJ reflection coefficient

In Chapter 3 the reflection coefficient for Epstein models was established by solving the wave equation (3.1) exactly. The approximate WKBJ reflection coefficient can be obtained from the WKBJ solutions (3.2) and it is given by the well known "phase-integral" formula

$$R(\zeta_s, \zeta_T, \kappa) = -1 e^{i \int_{\zeta_s}^{\zeta_T} q d\zeta} \quad (4.10)$$

(Budden, 1961; p. 329). The integral in the exponent may be regarded as a line integral in the complex ζ plane around the branch cut given by $\text{Im } q(\zeta) = 0$ (Fig. 4.4). ζ_T is the turning point of the ray and the formula (4.10) can be deduced by solving the wave equation in its neighbourhood. The WKBJ solutions break down in this region and must be replaced by solutions valid there. For linear behaviour of q^2

$$q^2 = -q_0^2 (\zeta - \zeta_T) \quad (4.11)$$

the wave propagation in the vicinity of the turning point is

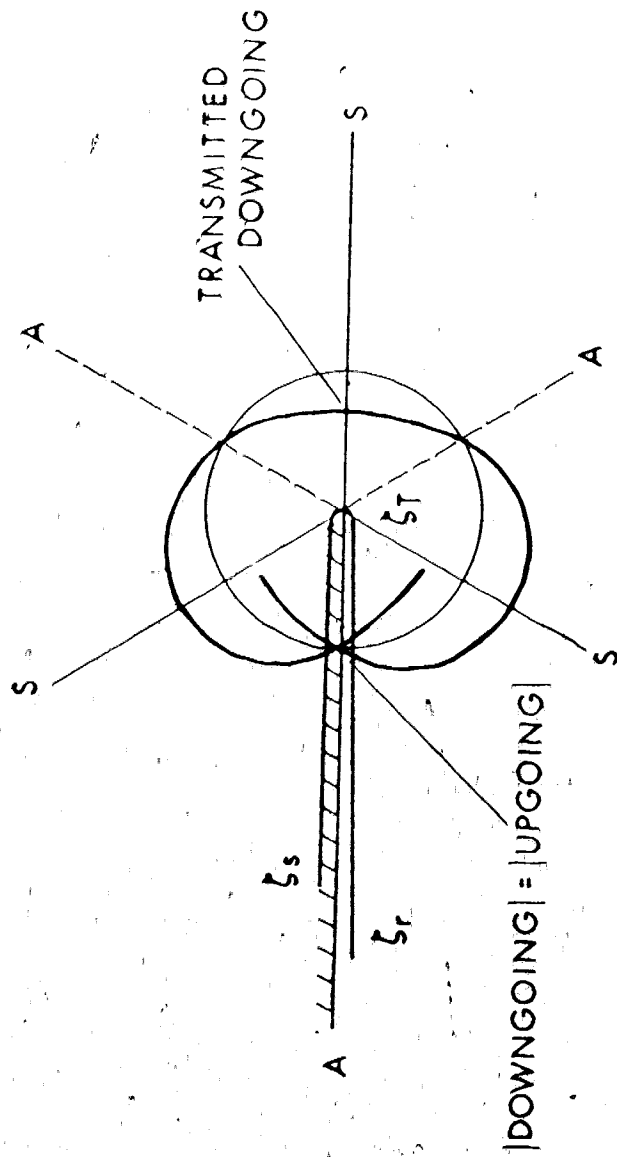


Figure 4.4 Complex ζ plane with the branch cut integration for evaluation of the WKBJ reflection coefficient. The Stokes diagram of the $Ai(\chi)$ describes the behaviour of the solutions above and below the turning point ζ_t . The asymptotic term for $Ai(\chi)$ is indicated by heavy line for $\arg \chi$ not $|\chi|$. When inside the circle the term is subdominant and when outside dominant (From Chapman, 1972).

described by Stokes equation

$$\frac{d^2 \hat{P}}{d\chi^2} - \chi \hat{P} = 0 \quad (4.12)$$

where

$$\chi = q_0^{2/3} (\zeta - \zeta_T)$$

Solutions to this equation are any independent combination

of Airy functions $Ai(\chi)$, $Bi(\chi)$, $Ai(\chi e^{\frac{2\pi i}{3}})$ or $Ai(\chi e^{-\frac{2\pi i}{3}})$. (See Appendix A.2). The WKBJ reflection coefficient (4.10) is

implied by the formula (A.2.2) if we assume $|\chi|$ large. Then

$Ai(\chi e^{\frac{2\pi i}{3}})$ and $Ai(\chi e^{-\frac{2\pi i}{3}})$ represent waves travelling downwards and upwards in regions above the turning point. In the region below the turning point $Ai(\chi)$ describes the evanescent wave.

The WKBJ solutions for real and imaginary wave-number q represent either oscillatory or exponential solutions. They remain valid for complex wavenumbers (Budden, 1961; p. 437).

This will occur in the response integral (2.22) when the stationary phase point corresponding to the ray is off the

real axis in the complex κ plane. The vertical wavenumber

$q = \left(\frac{\omega^2}{v^2} - \kappa^2\right)^{1/2}$ cannot have zero for complex κ unless the

velocity $v = v(\zeta)$ is analytically continued to the complex

ζ plane. Then a complex depth ζ_T exists so that $q(\zeta_T) = 0$.

The Stokes lines, which for real ζ_T agreed with the Stokes

lines of the Airy functions, (see Appendix A.2), are moved in the complex ζ plane. If we define

$$\alpha = \int_{\zeta_T}^{\zeta_S} q \, d\zeta \quad (4.13)$$

the Stokes lines are defined by $\text{Re } \alpha = 0$ and the anti-Stokes lines by $\text{Im } \alpha = 0$. For complex wavenumber κ they start at complex depth ζ_T , $q(\zeta_T) = 0$. If $\text{Im } \kappa > 0$ then $\text{Im } \zeta_T < 0$ as follows from the Cauchy-Riemann conditions (Fig. 4.5b). Both the downward and upward travelling solutions are dominant on the real ζ axis (Fig. 4.6b), i.e. exponentially growing in their direction of propagation. If $\text{Im } \kappa < 0$ then $\text{Im } \zeta_T > 0$ and both solutions are now subdominant on the real ζ axis, and, therefore, they both decay in their direction of propagation (Fig. 4.6a). This case also corresponds to the physical problem of absorption when the wave is partly attenuated in the medium. Ewing et al. (1957, p. 272) showed that attenuation can be theoretically expressed using complex wave velocities. Thus for real wavenumber κ the Fig. 4.5a applies to this case. If the wavenumber κ is complex, the presence of attenuation reduces $\text{Im } \zeta_T$. Effectively, it decreases the exponential growth of WKBJ solutions if $\text{Im } \kappa > 0$ and increases their exponential decay if $\text{Im } \kappa < 0$ (Heading, 1962; p. 75).

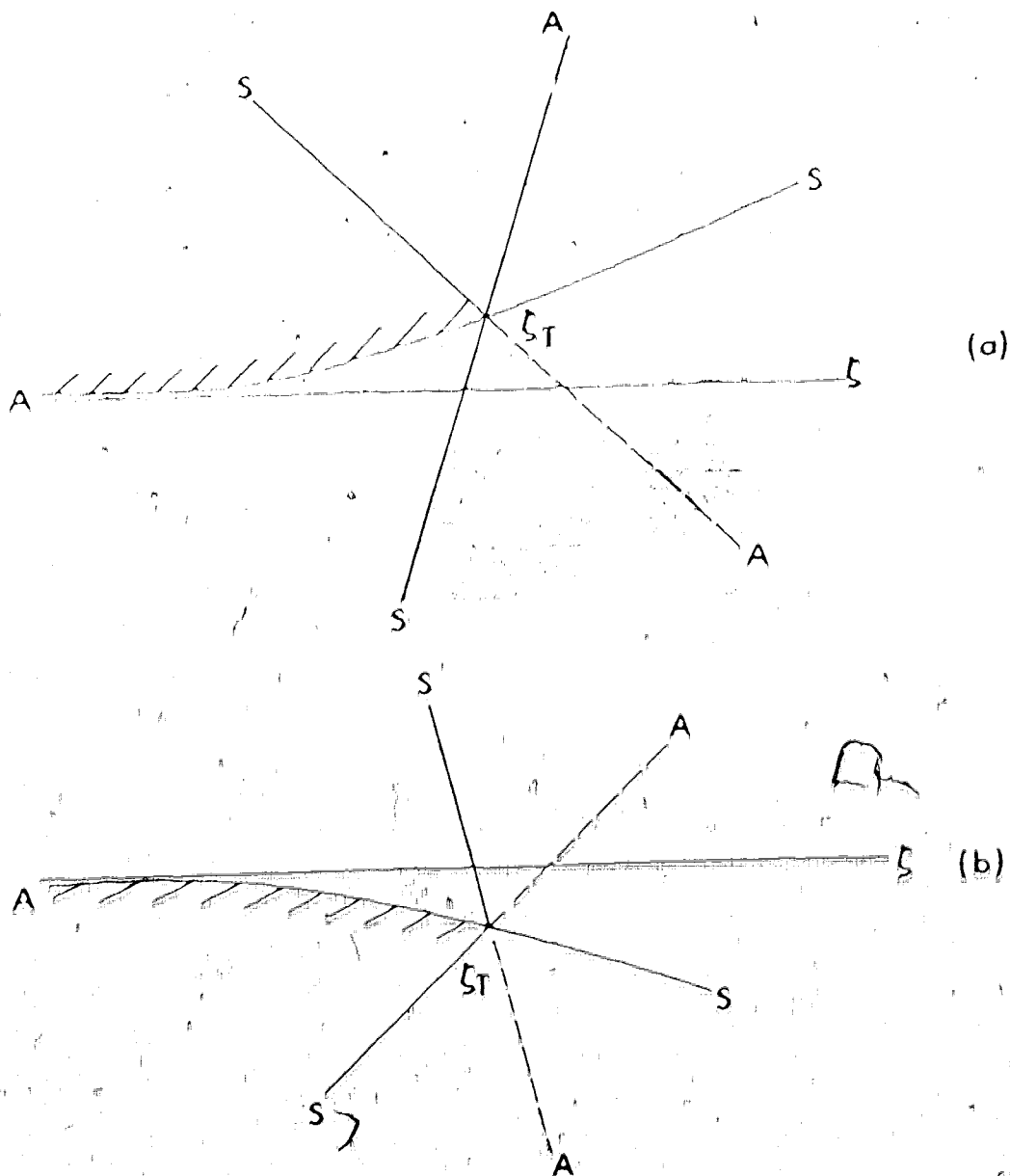


Figure 4.5 The complex ζ plane for κ complex
 (a) $\text{Im } \kappa < 0$, (b) $\text{Im } \kappa > 0$. The
 Stokes (S) and anti-Stokes (A) lines
 are also indicated.

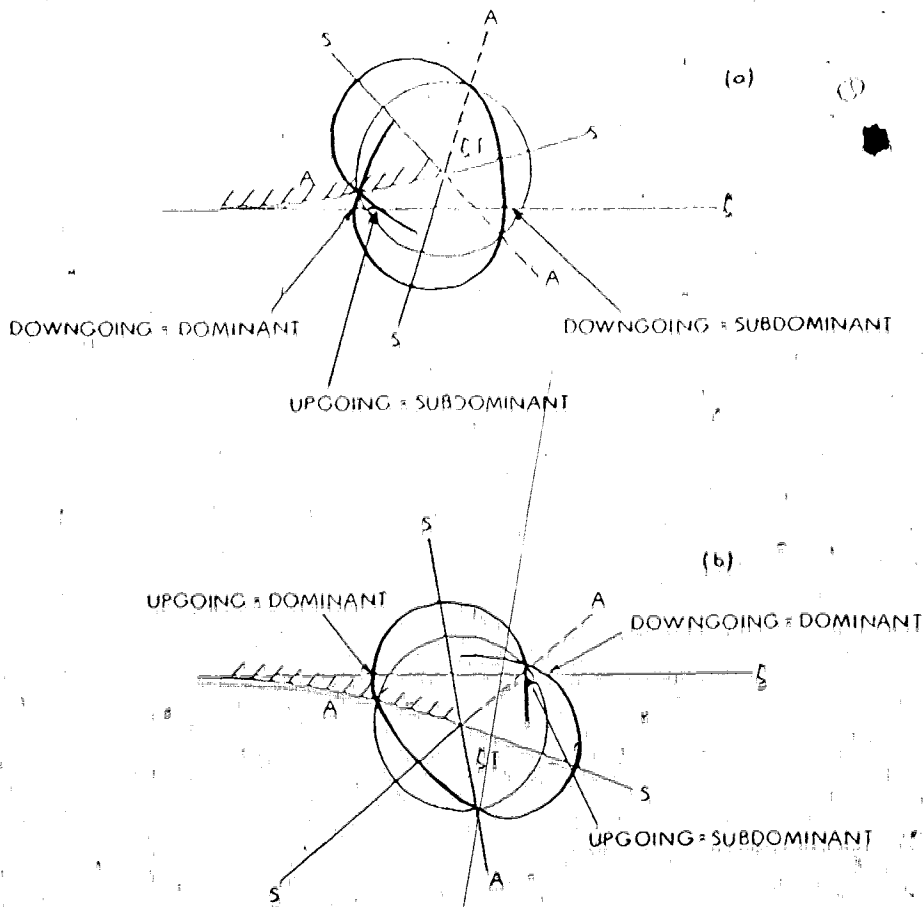


Figure 4.6 The Stokes diagrams describing the behaviour of the WKB solutions. (a) for $\text{Im } \zeta_T > 0$, (b) for $\text{Im } \zeta_T < 0$. When inside the circle the heavy line indicates the subdominant solution and when outside the dominant.

The approximate reflection coefficient for the monotonic velocity increase can be derived from the phase integral result (4.10). The vertical wavenumber

$$q(\zeta) = \left(\frac{1}{2}(q_1^2 + q_2^2) - \frac{1}{2}(q_1^2 - q_2^2) \tanh \frac{\zeta}{2\sigma} \right)^{1/2} \quad (4.14)$$

has branch points at $q = 0$ and $q = \infty$

$$\begin{aligned} \zeta_j &= 2\sigma \left\{ \operatorname{arctanh} \left(\frac{q_1^2 + q_2^2}{q_1^2 - q_2^2} \right) + i(2j + 1) \frac{\pi}{2} \right\} \\ \infty \zeta_j &= i \cdot 2\sigma(j + 1) \frac{\pi}{2}, \quad j = 0, \pm 1, \pm 2, \dots \end{aligned} \quad (4.15)$$

respectively (Fig. 4.7, Budden, 1961; p. 448).

From analogy with the linear behaviour of $q^2(\zeta)$ we expect that one of the branch points $q(\zeta_j) = 0$ above the real ζ axis must be considered for evaluation of the phase integral. We perform the integration along the branch cut $\operatorname{Im} q = 0$ starting at the source ζ_s , where $q(\zeta_s) = -q_1 + \epsilon_s$ and ending at the receiver ζ_r on the other Riemann sheet where $q(\zeta_r) = q_1 - \epsilon_r$. This is represented by curve C_1 in the complex ζ plane or complex q plane (Fig. 4.7). In the complex q plane the curve C_1 can be moved to our convenience, provided we take into account all singularities enclosed or

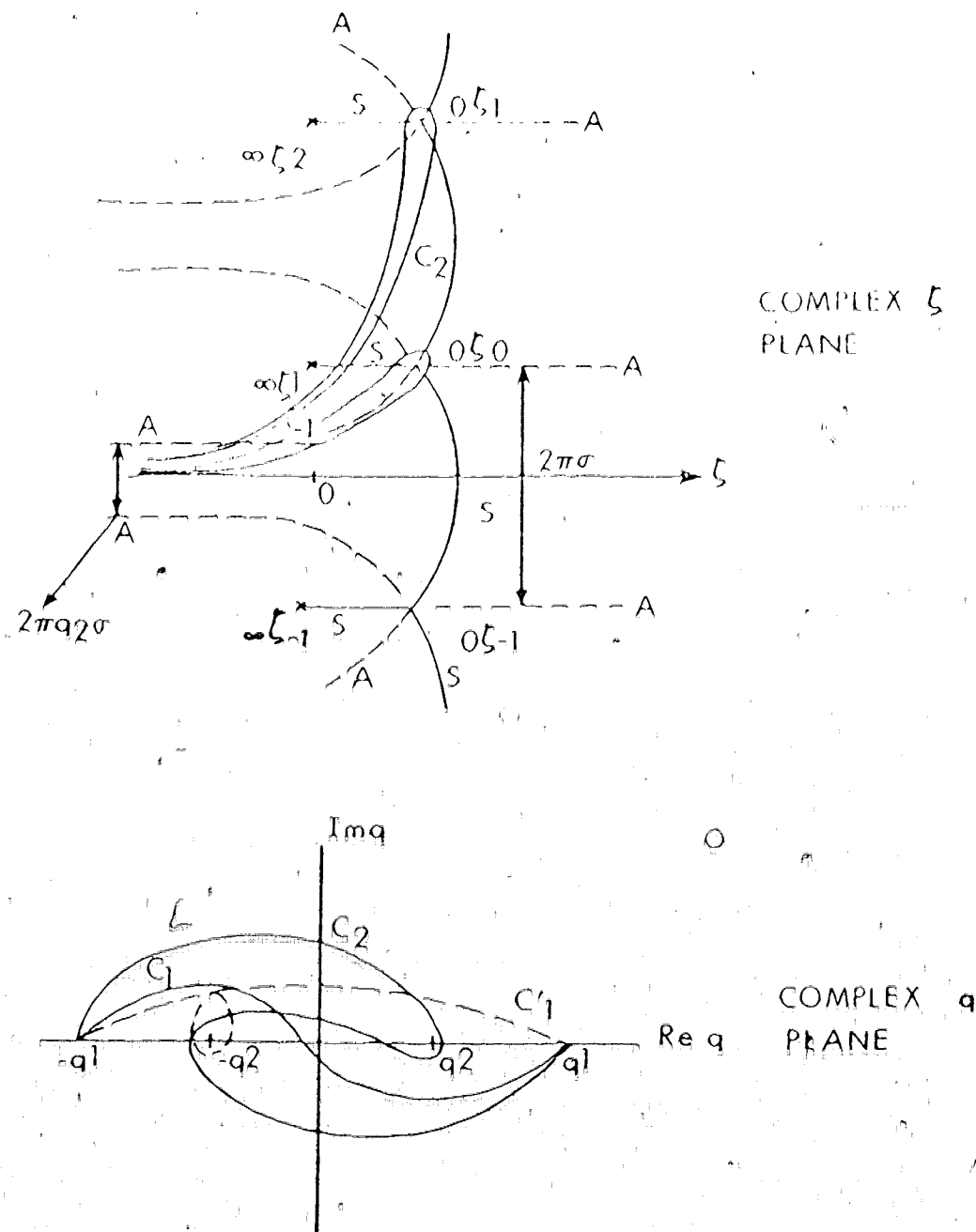


Figure 4.7. The complex ζ and q planes showing the contours of integration used in the evaluation of the WKBJ reflection coefficient for Epstein profile (Budden, 1961; p. 448 and 449).

crossed by the deformation of the contour. The best integration path in the q plane is C_1 because the integration is then very simple. For $\zeta_s = \zeta_r$ we get

$$\oint_{C_1} q d\zeta = 2\sigma \int_{-q_1}^{q_1} \left(\frac{q_1^2}{q_1^2 - q^2} + \frac{q_2^2}{q^2 - q_2^2} \right) dq + 2\pi i \operatorname{Res} \left(\frac{q_2^2}{q - q_2} \right)$$

and finally

$$\oint_{C_1} q d\zeta = 2\sigma q_1 \log \frac{4q_1^2}{q_1^2 - q_2^2} = 2\sigma q_2 \log \frac{q_1 + q_2}{q_2 - q_1} = 2q_1 \zeta_s \quad (4.16)$$

This result obtained from the phase integral is identical to the approximation of the exact reflection coefficient (4.2) for large effective thickness. Then we may use the Stirling approximation for gamma functions (C.11) and

$$R(\zeta_s, \zeta_r, \kappa) \approx -1 e^{i\phi(\kappa)} \quad (4.17)$$

where

$$\phi(\kappa) = \oint_{C_1} q d\zeta \quad \text{for} \quad \zeta_s = \zeta_r$$

The phase $\phi(k)$ is real for angles of emergence from the source greater than critical. The phase change $\frac{\pi}{2}$ is in agreement with the phase change due to total reflection. The two logarithmic terms can be interpreted as phase change due to the transition layer and $2q_1 \zeta_s$ is the usual phase change along the wave path.

The fact that the WKBJ reflection coefficient agrees with the high frequency approximation of the exact reflection coefficient justifies the choice of the branch point ζ_0 for evaluation of the phase integral. The branch point ζ_1 , for example, would give a wrong constant of integration due to encircling both poles $q = q_2$ and $q = -q_2$ (see curve C_2 in ζ and q planes in Fig. 4.7). The singularities must be well separated so that they do not influence the evaluation of the integral. This requirement, however, is implicitly satisfied as the WKBJ solutions are valid in slowly varying media i.e. in our case broad transitions. More detailed description of phase-integral method may be found in Budden (1961, p. 437) and Heading (1962).

4.3 Asymptotic behaviour of the response integral

For the monotonic velocity transition the response integral (2.22) is

$$P(\omega, r, \zeta_r) = \frac{i}{4} \cdot \frac{\rho_0}{\rho_s} P_s(\omega) \int_{-\infty}^{+\infty} R(\zeta_s, \zeta_r, k) H_0^{(1)}(kr) \frac{k}{q_s} dk \quad (4.18)$$

where $R(\zeta_s, \zeta_r, \kappa)$ is given by (4.2) (see Appendix C). The integral (4.18) can be evaluated approximately at high or low frequencies. These approximations will show the best way of performing the numerical contour integration in the κ plane in the entire frequency range.

At high frequencies the WKBJ reflection coefficient from the previous section may be used. If we use the approximate formula for $H_0^{(1)}(\kappa r)$ at large arguments (C.4) the response integral becomes

$$\begin{aligned}
 P(\omega, r, \zeta_r) &\approx \frac{P_s(\omega)}{2\sqrt{2\pi r}} \cdot \frac{\rho_o}{\rho_s} e^{-1\frac{\pi}{4}} \int_{-\infty}^{+\infty} e^{i\kappa r - 1} \int_{\zeta_s}^{\zeta_T} q d\zeta + 1 \int_{\zeta_T}^{\zeta_r} q d\zeta \cdot \frac{\kappa^{1/2}}{q_s} d\kappa \\
 &\approx \frac{P_s(\omega)}{2\sqrt{2\pi r}} \cdot \frac{\rho_o}{\rho_s} e^{-1\frac{\pi}{4}} \int_{-\infty}^{+\infty} e^{i\kappa r + 1\phi(\kappa)} \frac{\kappa^{1/2}}{q_s} d\kappa
 \end{aligned}
 \tag{4.19}$$

where

$$\phi(\kappa) = 2\sigma q_1 \log \frac{4q_1^2}{q_1 - q_2} - 2\sigma q_2 \log \frac{q_1 + q_2}{q_2 - q_1} - q_s \zeta_s - q_r \zeta_r
 \tag{4.20}$$

The integrand in (4.19) is oscillatory along the real κ axis and contribution from the integrand is significant only at points of stationary phase. The contour of integration along the real axis can be moved to pass through the stationary phase points (Fig. 4.8) and the integral evaluated approximately by the second order saddle point method (Morse and Feshbach, 1953; p. 440). The phase in (4.19) is

$$f(\kappa) = \kappa r - \int_{\zeta_s}^{\zeta_T} q \, d\zeta + \int_{\zeta_T}^{\zeta_r} q \, d\zeta = \kappa r + \phi(\kappa) \quad (4.21)$$

The stationary phase condition

$$\frac{df}{d\kappa} = r - \int_{\zeta_T}^{\zeta_s} \frac{\kappa}{q} \, d\zeta - \int_{\zeta_T}^{\zeta_r} \frac{\kappa}{q} \, d\zeta = r + \frac{d\phi}{d\kappa} = 0 \quad (4.22)$$

where

$$\begin{aligned} \frac{d\phi}{d\kappa} = & -2\sigma \frac{\rho_o^2}{\rho_1^2} \cdot \frac{\kappa}{q_1} \log \frac{4q_1^2}{q_1^2 - q_2^2} + 2\sigma \frac{\rho_o^2}{\rho_2^2} \cdot \frac{\kappa}{q_2} \log \frac{q_1 + q_2}{q_2 - q_1} + \frac{\rho_o^2}{\rho_s^2} \cdot \frac{\kappa}{q_s} \zeta_s + \\ & + \frac{\rho_o^2}{\rho_r^2} \cdot \frac{\kappa}{q_r} \zeta_r \end{aligned} \quad (4.23)$$

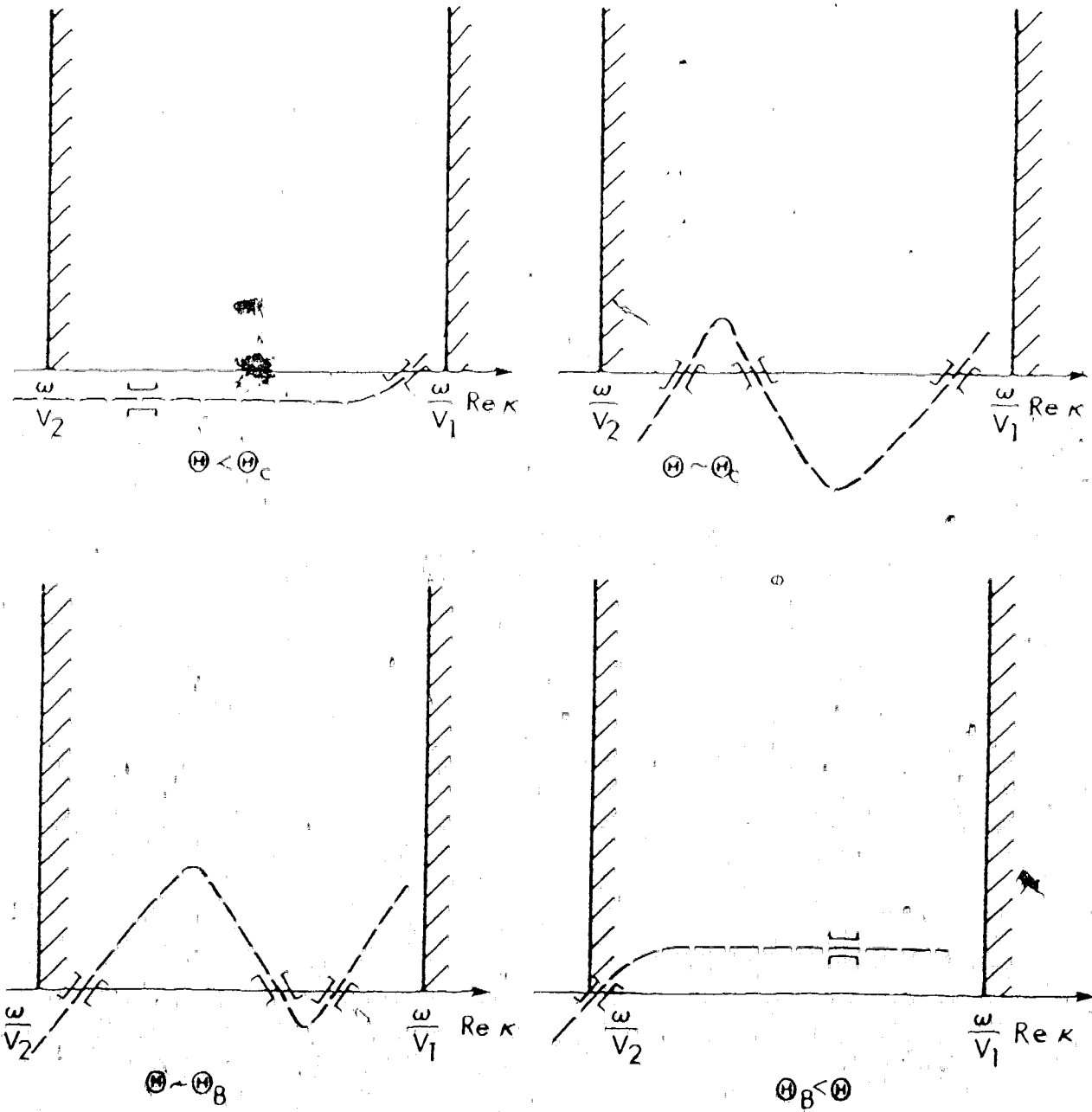


Figure 4.8 Saddle points in the complex κ plane for a broad velocity transition.

gives at least one saddle point on the real axis between κ_2 and κ_1 . z_T is the depth of the turning point of the ray represented by the saddle point and it is a function of κ . This, however, does not effect the result of the differentiation in (4.21) as $q'(z_T) = 0$. The result in (4.22) can be compared to the classical result given by Bullen (1963, p. 111). We just have to transform his result to flat geometry to get horizontal range $X(p) = r(\kappa)$ of the ray that bottomed at depth z_T .

$$X(p) = p \int_{z_T}^{z_s} \frac{dz}{(\eta^2 - p^2)^{1/2}} + p \int_{z_T}^{z_r} \frac{dz}{(\eta^2 - p^2)^{1/2}} \quad (4.24)$$

$p = \frac{\sin \theta}{v} = \frac{1}{c}$ is the ray parameter or horizontal slowness

$\eta = \frac{1}{v}$ is the slowness of the acoustic waves

$$\frac{\rho}{\rho_0} q = \omega(\eta^2 - p^2)^{1/2}, \quad \kappa = \frac{\omega}{v} \sin \theta = \omega p \quad \text{and} \quad \zeta = \int_{z_0}^z \frac{\rho(z)}{\rho_0} dz$$

For the monotonic velocity transition where the triplication occurs (Fig. 1.2), three saddle points exist on the real κ axis at ranges between O_C and O_B (Fig. 4.8). The saddle point close to $\frac{\omega}{v_2}$ represents the ray close to the critical,

the saddle point close to $\frac{\omega}{v_1}$ is the shallow ray and the saddle point in the middle is the ray reflected by the high velocity gradient. At ranges $0 > 0_B$ only the near-critical ray exists i.e. the saddle point close to $\frac{\omega}{v_2}$. At ranges $0 < 0_C$ only the shallow ray with a saddle point close to $\frac{\omega}{v_1}$ exists.

For narrow transition in Figure 4.1 the stationary phase condition gives two real saddle points at horizontal distances greater than the critical X_C (Fig. 4.9). They are the head wave and the reflected wave shown in Figure 4.1. The head wave is represented by a narrow saddle point that approaches the branch point $\frac{\omega}{v_2}$ as the transition gets thinner. Concurrently, the steepest descent path through this saddle point approaches the branch cut integral which is interpreted as a head wave in case of the sharp velocity increase (Cagniard, 1962).

The stationary phase condition (4.22) is a transcendental equation and must be solved numerically. The phase at the saddle point κ^* gives the arrival time of the ray

$$f(\kappa^*) = \int_{\zeta_T}^{\zeta_S} q(\kappa^*) d\zeta + \int_{\zeta_T}^{\zeta_R} q(\kappa^*) d\zeta + \kappa^* \cdot r(\kappa^*) = \omega T \quad (4.25)$$

Again, T agrees with the classical result given by Bullen (1963, p. 112)

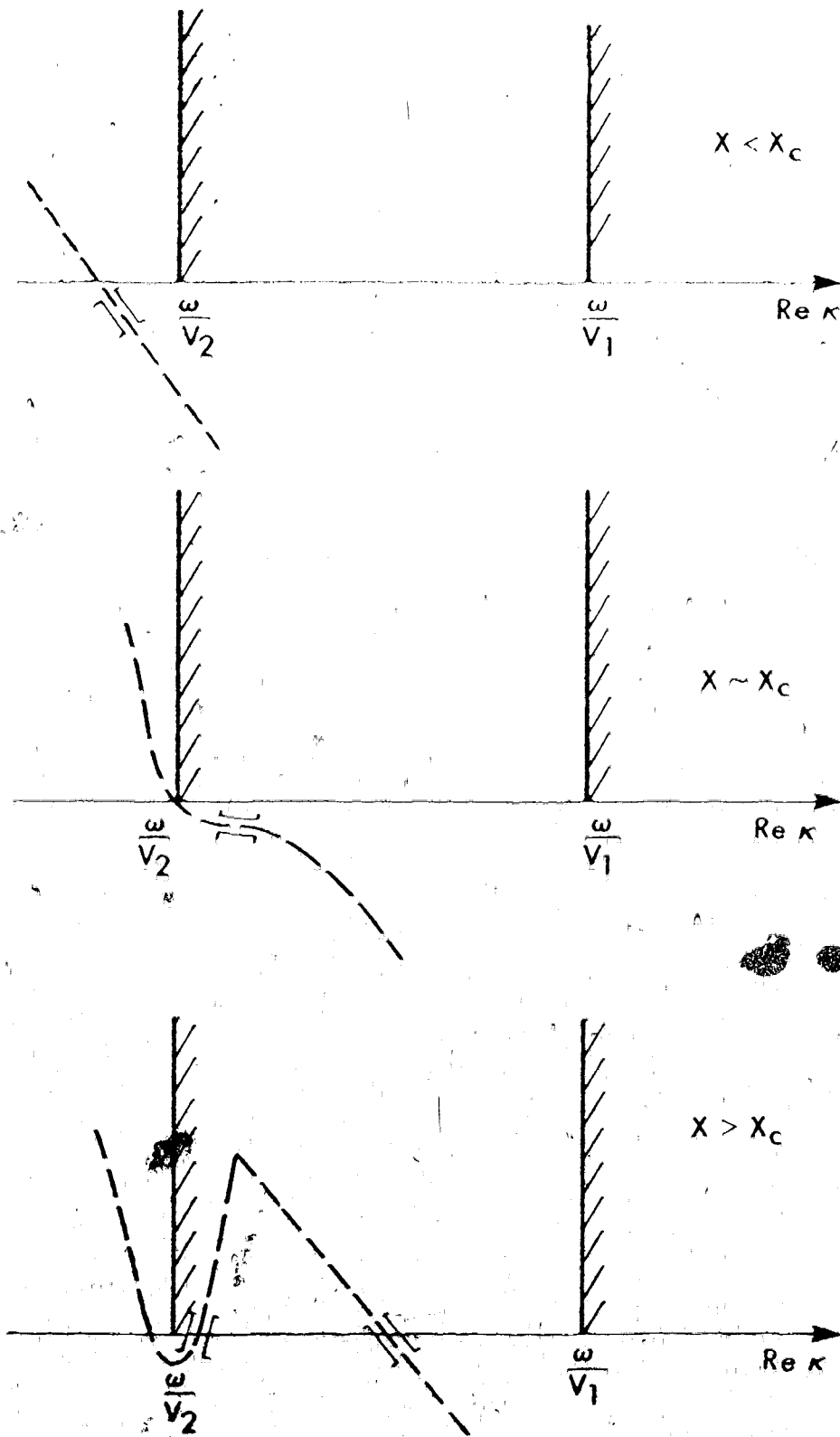


Figure 4.9 Saddle points in the complex κ plane for a narrow velocity transition.

$$T = p \cdot X(p) + \int_{z_T}^{z_S} (\eta^2 - p^2)^{1/2} dz + \int_{z_T}^{z_R} (\eta^2 - p^2)^{1/2} dz \quad (4.26)$$

The second derivative at the saddle point is

$$\left. \frac{d^2 \phi}{d\kappa^2} \right|_{\kappa^*} = - \left. \frac{dr(\kappa)}{d\kappa} \right|_{\kappa^*} = - \left. \frac{d^2 \phi}{d\kappa^2} \right|_{\kappa^*} \quad (4.27)$$

where

$$\begin{aligned} \left. \frac{d^2 \phi}{d\kappa^2} \right|_{\kappa^*} = & -2\sigma \frac{\rho_o^4}{\rho_1^4} \cdot \frac{\omega^2}{v_1^2} \frac{1}{q_1^3} \log \frac{4q_1^2}{2^2 q_1 - q_2^2} + 2\sigma \frac{\rho_o^4}{\rho_2^4} \frac{\omega^2}{v_2^2} \frac{1}{q_2^3} \log \frac{q_1 + q_2}{q_2 - q_1} + \\ & + \frac{\rho_o^4}{\rho_s^4} \frac{\omega^2}{v_s^2} \frac{1}{q_s^3} \zeta_s + \frac{\rho_o^4}{\rho_r^4} \frac{\omega^2}{v_r^2} \frac{1}{q_r^3} \zeta_r + \frac{4\sigma\kappa^2}{q_1(q_1^2 - q_2^2)} \\ & \cdot \frac{\rho_o^4}{2^2 \rho_1^2 \rho_2^2} \left(2 - \frac{\rho_1^2 q_1^2}{2^2 q_2^2} - \frac{\rho_2^2 q_2^2}{2^2 q_1^2} \right) \quad (4.28) \end{aligned}$$

The sign of $\left. \frac{d^2 \phi}{d\kappa^2} \right|_{\kappa^*}$ determines the direction of the saddle point and $\left| \frac{d^2 \phi}{d\kappa^2} \right|_{\kappa^*}^{-1/2}$ gives the amplitude of the ray. The forward

branches of the triplication AB and CD are due to rays that travel further in horizontal direction if they penetrate deeper into the medium. The saddle points are positioned at

angle $\frac{\pi}{4}$ with respect to the real κ axis since $\frac{dr}{d\kappa} < 0$. For these rays the second order saddle point evaluation gives

$$P(\omega, r, \zeta_r) = \frac{P_s(\omega)}{2\sqrt{2\pi}} \cdot \frac{\rho_o}{\rho_s} \cdot \frac{\kappa^{\frac{1}{2}} e^{i\omega T}}{q_s \left\{ r(\kappa) \left| \frac{dr}{d\kappa} \right| \right\}^{\frac{1}{2}}} \quad (4.29)$$

Thus there is no phase shift of the resulting response with respect to the source $P_s(t)$ and the amplitude is frequency independent. The factor $\left\{ r \left| \frac{dr}{d\kappa} \right| \right\}^{-\frac{1}{2}}$ represents the geometrical spreading of the ray tube along the ray path.

The rays of the reversed branch of the triplication arrive at shorter ranges if they penetrate the medium deeper. The same is true for the reflected branch in Figure 4.1. Thus the saddle point is situated at angle $-\frac{\pi}{4}$ towards the real κ axis since $\frac{dr}{d\kappa} > 0$. For these rays the pressure response is

$$P(\omega, r, \zeta_r) = -1 \frac{P_s(\omega)}{2\sqrt{2\pi}} \cdot \frac{\rho_o}{\rho_s} \cdot \frac{\kappa^{\frac{1}{2}} e^{i\omega T}}{q_s \left\{ r(\kappa) \left| \frac{dr}{d\kappa} \right| \right\}^{\frac{1}{2}}} \quad (4.30)$$

and they are shifted by $-\frac{\pi}{2}$ with respect to the source function $P_s(t)$. As frequency decreases the "geometrical" amplitudes (4.29) and (4.30) become poor approximations and (4.18) must be evaluated numerically.

The triplication has two cusps at B and C and the curve r vs. θ (i.e. $\frac{dT}{d\theta}$ vs. θ curve) has two reversals at $\frac{dr}{d\theta}|_r = 0$ (Fig. 4.10a). The travel time curve for narrow transition has a cusp at C which approaches the critical point of the sharp discontinuity as the transition becomes thinner. The r vs. X curve in Figure 4.10b has also a reversal at $\frac{dX}{dr} = \frac{dr}{dX}|_r = 0$. At all these points the second derivative of the phase (4.27) is zero and the second order saddle point method cannot be used. The saddle points approach each other at ranges close to θ_C , θ_B or X_C and separate evaluation of their contribution is not valid. However, the width of the saddle point is proportional to $|\frac{d^2 f}{dr^2}|^{-1/2}$ i.e. $\omega^{-1/2}$ and, therefore, at high frequency the separate evaluation remains valid at distances closer to $r(\bar{\kappa}) = \bar{r}$ (\bar{r} applied to either of θ_C , θ_B and X_C). The sign of the third derivative of the phase determines at which endpoint the reversal occurs.

$$\frac{d^3 f}{d\kappa^3} \Big|_{\bar{\kappa}_1} < 0 \text{ at the "near" endpoint} \quad (4.31)$$

$$\frac{d^3 f}{d\kappa^3} \Big|_{\bar{\kappa}_2} > 0 \text{ at the "far" endpoint}$$

where $-\frac{d^3 f}{d\kappa^3} = \frac{d^3 \phi}{d\kappa^3} = -6\sigma \frac{\omega^2}{v_1} \frac{\kappa}{q_1} \log \frac{4q_1^2}{2 - q_2} + \frac{\omega^2}{v_s} \frac{\kappa}{q_s} \zeta_s +$

$$+ \frac{\omega^2}{v_r} \frac{\kappa}{q_r} \zeta_r + 6\sigma \frac{\omega^2}{v_2} \frac{\kappa}{q_2} \log \frac{q_1 + q_2}{q_2 - q_1} + 40\kappa \left(\frac{1}{q_1} \left(\frac{\omega^2}{v_1} \frac{1}{q_1} - \frac{\omega^2}{v_2} \frac{1}{q_2} \right) - \frac{2}{q_1 q_2} \left(\frac{\omega^2}{v_1} - \frac{\omega^2}{v_2} \right) \left(1.5 \frac{\kappa^2}{q_1} + \frac{\omega^2}{\sqrt{2}} \frac{1}{q_2} \right) \right), \quad \rho = \text{const.} \quad (4.32)$$

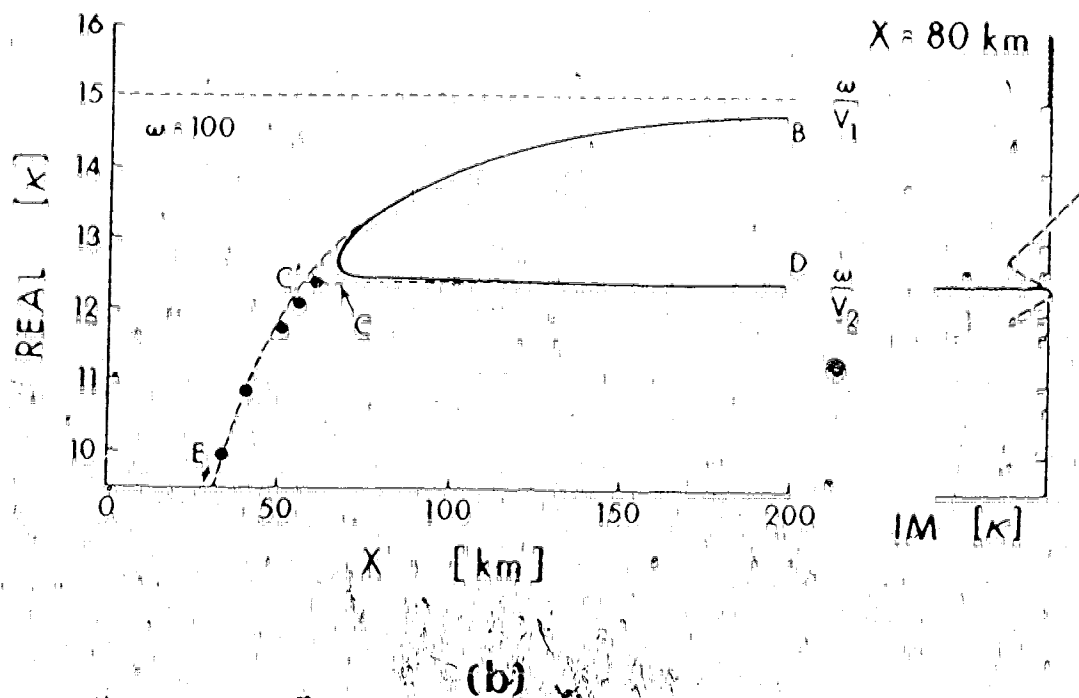
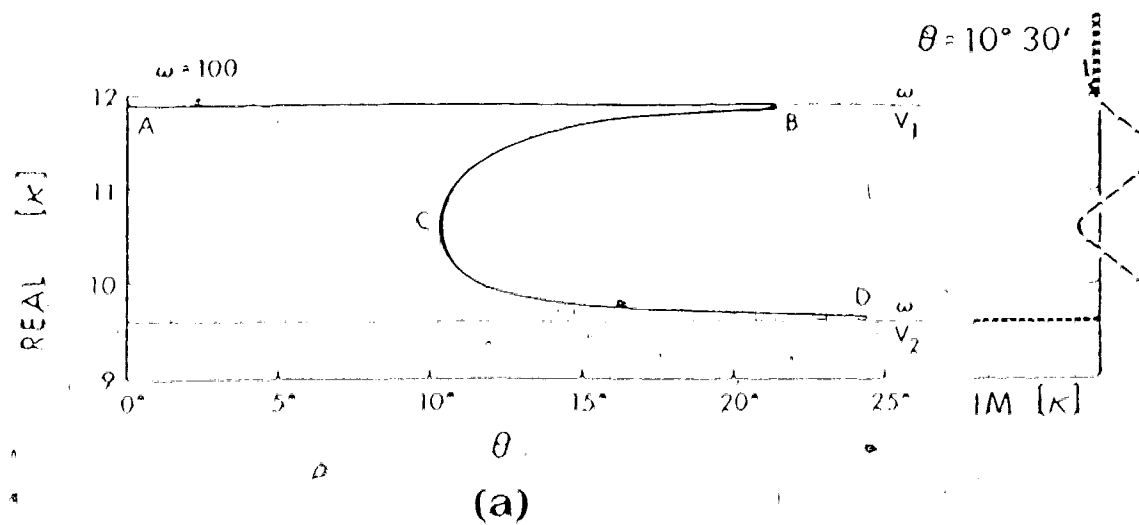


Figure 4.10 Horizontal wavenumber versus horizontal distance (a) for broad transition with triplication, (b) for narrow transition with head wave. The dots indicate the partial reflection.

When approaching the range r from the illuminated region two very similar waves arrive. They differ only slightly in their path-lengths and amplitudes, they interfere and cannot be separated. This is caused by focusing of rays into a caustic due to the change in velocity gradient. Other examples of caustics exist in seismology which are formed by focusing of rays due to geometry as, for example, the PKP caustic in the Earth's core. At the caustic the saddle points coalesce, and at ranges out of the illuminated region they separate again and move to complex positions in the κ plane. The steepest descent path passes now through one of these saddle points only (Figures 4.8 and 4.9) and its contribution gives partial reflection decaying rapidly away from the illuminated region. The stationary phase condition can still be solved for complex κ and the arrival time determined. The geometrical arrival time is essential for the synthesis of pulses discussed in the next section.

The response integral in the region of caustic can be evaluated by the third order saddle point method (Airy, 1838). The first term in the asymptotic series was used in seismology by Jeffreys (1939):

$$\int_{-\infty}^{+\infty} g(\kappa) e^{if(\kappa)} d\kappa = g(\bar{\kappa}) e^{if(\bar{\kappa})} \left(\frac{1}{2} \frac{d^3 f}{d\kappa^3} \bigg|_{\bar{\kappa}} \right)^{-1/3} A_1(\chi) \quad (4.33)$$

where

$$\chi = \frac{df}{dk} \Big|_{\bar{k}} - \left(\frac{1}{2} \frac{d^3 f}{dk^3} \Big|_{\bar{k}} \right)^{-1/3}$$

The definition of the Airy function $Ai(\chi)$ is in Appendix A.2.

The integral expression for Airy function (A.2.7) has two stationary points in region "before" the caustic ($\chi < 0$) which corresponds to the illuminated region:

$$\chi < 0 \quad y_{1,2} = \pm |\chi|^{1/2} \quad y \text{ real}$$

y_1 corresponds to the minimum of the phase i.e. to rays on branches AB or CD. y_2 represents the maximum phase saddle point i.e. rays of the reversed branch BC. The two saddle points give rays that arrive to the receiver in the illuminated region at different times. No real stationary point exists in regions "beyond" the caustic ($\chi > 0$) where no geometrical rays arrive. On the caustic ($\chi = 0$) the two saddle points y_1 and y_2 coalesce at the origin.

The phases at the saddle points before the caustic are

$$f(y_1) = f(\bar{k}) - \frac{2}{3} |\chi|^{3/2} \quad (4.34)$$

$$f(y_2) = f(\bar{k}) + \frac{2}{3} |\chi|^{3/2}$$

and

$$|\chi| = \left[\frac{3}{4} (f(y_2) - f(y_1)) \right]^{2/3}$$

We have obtained an expression for absolute value of the argument of the Airy function in (4.33). $\chi = 0$ corresponds to one of the geometrical endpoints of the triplication. Therefore if we know the phases of the two rays arriving at distance $r(r^*)$ in the illuminated region, we can calculate the integral at distance $r' = r(\bar{\kappa}) + r(\kappa) - r(r^*)$. The range r' is symmetrical to $r(r^*)$ with respect to $r(\bar{\kappa})$. We denote T_C and T_B the geometrical arrival times at $r(r_C)$ and $r(r_B)$, respectively. T_1 , T_2 and T_3 are arrival times corresponding to branches AB, BC and CD at range $r(r^*)$, respectively. The asymptotic expression for the pressure response near the caustic C is

$$P(\omega, r, c_r) = P_s(\omega) \frac{\rho_0}{\rho_s} \left(\frac{\pi}{2}\right)^{1/2} \frac{\kappa^{1/2}}{q_s} \left\{ \frac{1}{2} \left| \frac{d^2 r}{d\kappa^2} \right| \right\}^{-1/3} e^{i\omega T_C - i\frac{\pi}{4}} = i \frac{\pi}{3} \\ \cdot \text{Ai} \left(\pm \left[\frac{4}{3} \omega (T_2 - T_3) \right]^{2/3} \right) \quad (4.35)$$

T_2 and T_3 are arrival times at $r_>$, where $r_>$ is the greater of $(r, r_C + (r_C - r))$. Near the caustic B the response is

$$P(\omega, r, c_r) = P_s(\omega) \frac{\rho_0}{\rho_s} \left(\frac{\pi}{2}\right)^{1/2} \frac{\kappa^{1/2}}{q_s} \left\{ \frac{1}{2} \left| \frac{d^2 r}{d\kappa^2} \right| \right\}^{-1/3} e^{i\omega T_B - i\frac{\pi}{4}} \\ \cdot \text{Ai} \left(\pm \left[\frac{4}{3} \omega (T_2 - T_1) \right]^{2/3} \right) \quad (4.36)$$

T_2 and T_1 are arrival times at r_1 , where r_1 is the lesser of $(r, r_B + (\tau_B - r))$. The - and + signs correspond to response before and beyond the caustic, respectively. And $|\frac{d^2 r}{dr^2}|$ is given by (4.32).

The shift of the amplitude maximum from the geometrical endpoint $r(\bar{r})$ towards the illuminated region is shown in Figure 4.11. The peak of the constructive interference occurs before the caustic and causes the maximum amplitude. Figure 4.11 also shows the amplitude curves obtained from contour integration in the complex k plane. The agreement of the "exact" amplitude at $\omega = 20$ with the asymptotic amplitude (4.35) is very good. The exact amplitudes oscillate due to interference of the rays on branches BC and CD. Their geometrical amplitudes given by (4.30) and (4.29) are also indicated. The rays of the reversed branch BC are stronger and the amplitude curves oscillate around this value. Out from the illuminated region the amplitudes decrease rather quickly at high frequency. The contribution increases as frequency decreases and confirms the fact that partial reflection is enhanced at lower frequencies.

Results (4.35) and (4.36) based on the Jeffreys' evaluation of the first term in the asymptotic series are correct when the two interfering rays are identical or, in other words, the two approaching saddle points give identical

BROAD TRANSITION ZONE - NEAR END OF THE TRIPPLICATION

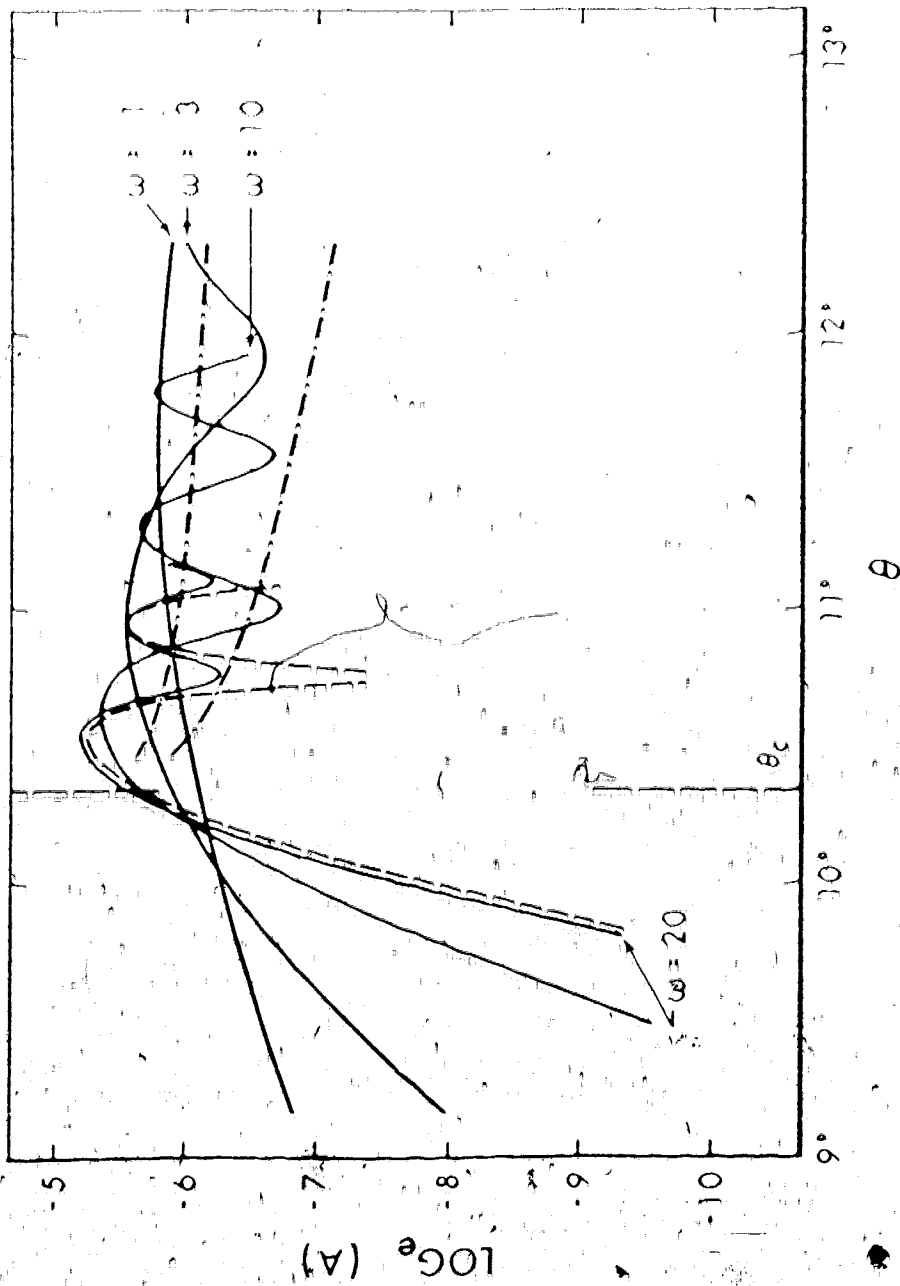


Figure 4.11 The amplitude curves near the caustic C ($\theta_c = 10^\circ 20'$) evaluated numerically for different frequencies (full lines). The geometrical amplitudes (chained lines) and the Airy function for $\omega = 20$ (broken line) are also indicated.

contribution when considered separately. Which means that the r vs. χ or θ curves are symmetrical around the reversals (Figure 4.10). This is the case of the broad transitions but as the transition becomes thinner the curve is distorted till it coincides with curves for sharp discontinuity. We expect this to happen as it indicates the transition from the caustic behaviour to the critical point behaviour. The departure from the Airy phase behaviour can be compared in Figures 4.12 and 4.13 which show the amplitude curves for two narrow transition thicknesses. For $\omega = 110$ the agreement is good for 1.6 km transition while at the same frequency for .2 km transition, the decay of the exact amplitude is slower. The partial reflection is stronger for thinner transition and results in enrichment of the amplitudes before the critical angle. In Figure 4.12 the high frequency behaviour given by the reflection coefficient (4.5) is indicated. It does not include the remaining terms in the integrand but its shape agrees well with the decay of amplitude at $\omega = 110$.

The higher order corrections to the Jeffreys' result (4.32) can be obtained from the further terms in the asymptotic series. These include differences between the interfering rays and were given by Chester et al. (1957) and Yanovskaya (1966):

0.2 km TRANSITION ZONE AT 20 km

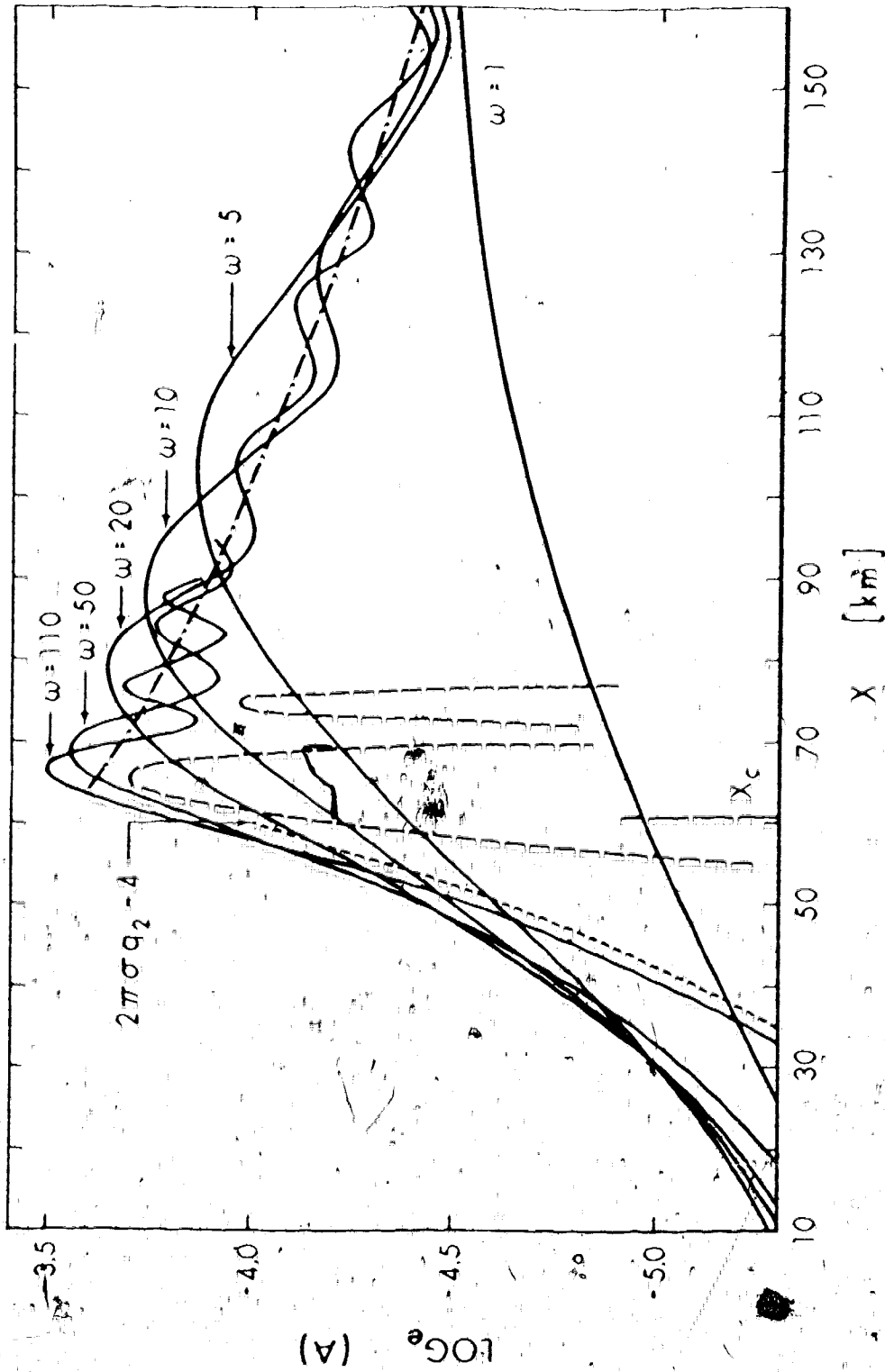


Figure 4.12 The amplitude curves near the critical point ($X_c = 60.5$ km) evaluated numerically for different frequencies (full lines). The geometrical amplitudes (chained line), the Airy function for $\omega = 100$ (broken line) and the exponential decay (fine broken line) are also indicated.

16 km TRANSITION ZONE AT 20 km

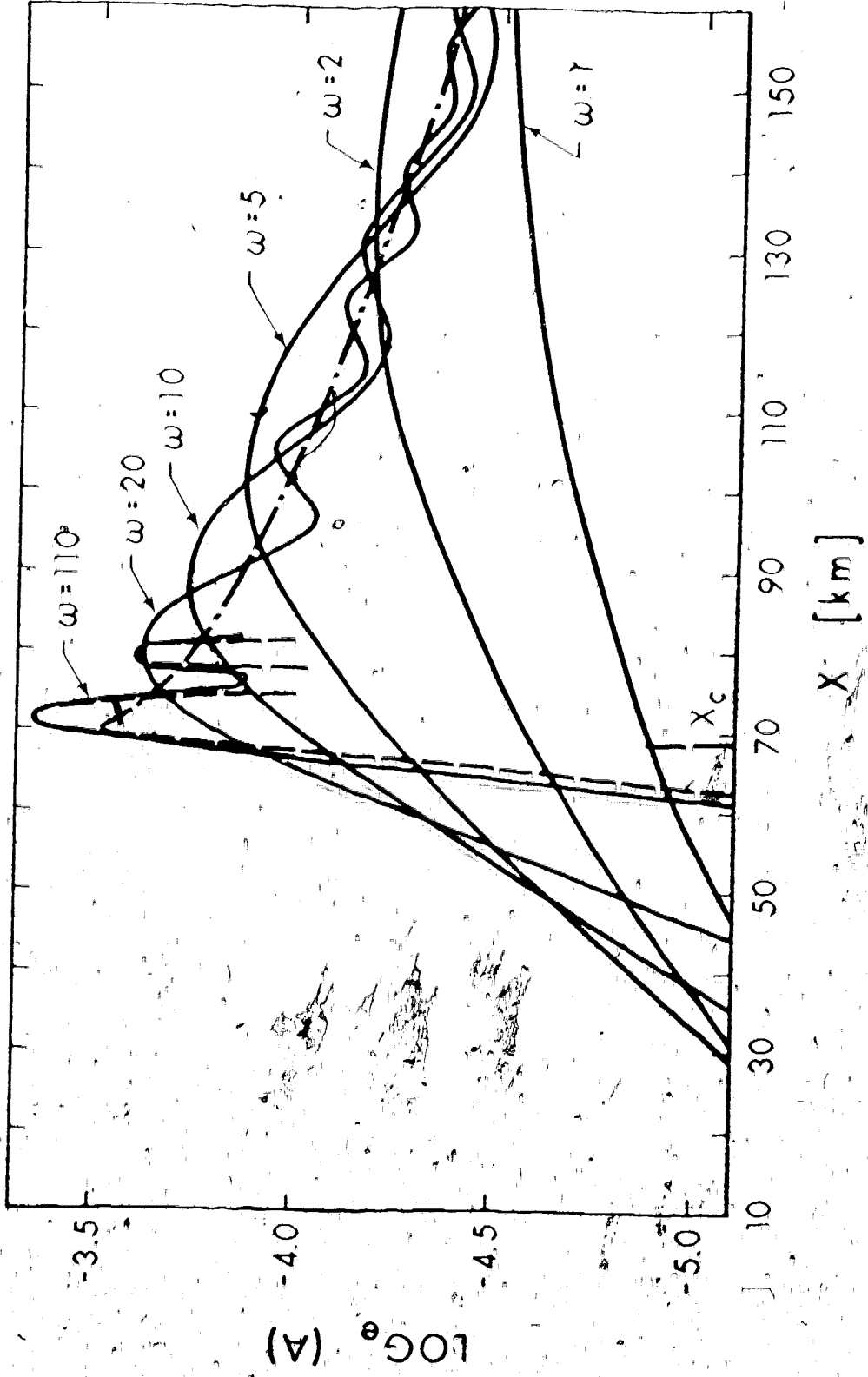


Figure 4.13 The amplitude curves near the critical point ($X_c = 67.8$ km) evaluated numerically for different frequencies (full lines). The geometrical amplitudes (chained line) and the Airy function for $\omega = 100$ (broken line) are also indicated.

The treatment of the caustic region described here is distinctly different from treatment of the shadow at the core of the Earth (Chapman and Phinney, 1972). The similarity of both problems suggested by the fact that two rays arrive simultaneously at the edge of the shadow, and at the far end of the triplication, is only superficial. In case of shadow the direct and reflected rays have different characteristics. The contribution from the direct ray remains finite as the shadow edge is approached while the reflected signal tends to zero.

In spite of the limitation of the previous results to high frequencies they are very useful. They show that the easiest way to perform the numerical integration in the complex k plane is by integration along the steepest descent path. They also give the geometrical arrival time indispensable for computation of synthetic seismograms. The geometrical amplitudes are also used to form part of the spectrum at the high frequency end. This is discussed in more detail in the next section.

At low frequencies a different approximation can be obtained. In section 4.1 we have shown that for thin transitions the reflection coefficient approaches the reflection coefficient for a discontinuous velocity increase (4.4). This is independent of frequency and in such cases the

Cagniard-de Hoop method of evaluation of the pressure response in the time domain is possible (Cagniard, 1962; de Hoop, 1960).

We shall investigate to what extent the method is applicable to our problem.

The gamma functions in the reflection coefficient (3.2) can be expanded in power series according to

$$\frac{1}{\Gamma(1+x)} = \sum_{k=0}^{\infty} a_k x^k \quad |x| < \infty \quad (4.37)$$

x is complex and $a_0 = 1$, $a_1 = .577216$, $a_2 = -.655878$ (see Abramowitz and Stegun (1965, p. 256)). This expansion gives a product of three power series in the numerator and denominator of the reflection coefficient. For $|x| \ll 1$ the series in the denominator can be expanded binomially. This restricts the validity of the following results to small thicknesses σ and low frequencies, i.e., to small values of the effective thickness S (3.18). In this case the reflection coefficient is

$$R(\zeta_s, \zeta_r, k) = \frac{q_1 - q_2}{q_1 + q_2} e^{-i q_1 (\zeta_s + \zeta_r)} (1 + 4(2a_2 - a_1^2) \sigma^2 q_1 q_2 + o(S^3)) \quad (4.38)$$

We assume $|\ell_s|, |\ell_r|$ and $|q_1| < 1, |q_2| < 1$. The first term reduces to the reflection coefficient between two fluid half-spaces with velocities and densities v_1, ρ_1 and v_2, ρ_2 . For use of Cagniard-de Hoop method the results have to be reformulated in terms of Laplace and Laplace-Bessel transforms (2.9) and (2.10). We were using the Fourier and the Hankel transformations as the inverse Fourier transform is easier to evaluate numerically. After the change of variables

$$-s = i\omega \quad sp = ik \quad -s\eta = -s\left(\frac{1}{v^2} - p^2\right) \quad \eta = 1 \frac{\rho}{\rho_0} q$$

the pressure response becomes

$$P(z_s, z_r, z_r) = \frac{s}{\pi} \int_{-\infty}^{+\infty} \frac{P_s(s)}{2} \operatorname{Im} \int_{-1}^{+1} R(z_s, z_r, sp) K_0(sp\eta) \frac{p}{\eta} dp \quad (4.39)$$

where for $z_r = z_s$

$$\begin{aligned} R(z_s, z_r, sp) &= \frac{\eta_1 \rho_2^{-\eta_2 \rho_1}}{\eta_1 \rho_2^{+\eta_2 \rho_1}} (1 - 4s^2 \sigma^2 (2a_2^2 - a_1^2)) \frac{\rho_0^2}{\rho_1 \rho_2} \eta_1 \eta_2 e^{-2s\eta_1(z_r - z_0)} \\ &= R_0 (1 + f_1(p)s^2) e^{-2s\eta_1(z_r - z_0)} \end{aligned} \quad (4.40)$$

The inversion into the time domain of the response integral (4.39) can be accomplished by method introduced by de Hoop (1960)

and used by Helmburger (1968). The paper by Helmburger is the best reference for details of the method used to find the results presented here. If we assume a Heaviside step function to be the source, i.e. $P_s(t) = H(t)$, the time pressure response is

$$(1) \text{ for } 0 < 0_c = \sin^{-1} \frac{v_1}{v_2}$$

$$P(t, r, z_r) = P_R(t, r, z_r) + \frac{d^2}{dt^2} (P_{1R}(t, r, z_r)) \quad (4.41)$$

$$(2) \text{ for } 0 > 0_c$$

$$P(t, r, z_r) = P_H(t_<, r, z_r) + P_R(t_>, r, z_r) + \frac{d^2}{dt^2} \{ P_{1H}(t_<, r, z_r) + P_{1R}(t_>, r, z_r) \} \quad (4.42)$$

where $t_<$ is the lesser of $(t, \frac{R}{v_1})$ and $t_>$ is the greater of $(t, \frac{R}{v_1})$, and $R = (r^2 + 4|z_r - z_o|^2)^{1/2}$

$$P_R(t, r, z_r) = \frac{1}{\pi} \int_{t_R}^t \frac{\text{Re} \left\{ \frac{p R_o}{(t-\tau + 2pr)^{1/2}} \right\}}{(t-\tau)^{1/2} \left(\tau^2 - \frac{R^2}{v_1^2} \right)^{1/2}} d\tau$$

$$P_H(t, r, z_r) = \frac{1}{\pi} \int_{t_H}^t \frac{p \sin 2\theta d\tau}{(t-\tau + 2pr)^{1/2} (t-\tau)^{1/2} \left(\frac{R^2}{v_1^2} - \tau^2 \right)^{1/2}} \quad (4.43)$$

where

$$\beta = \arctan \left(- \frac{|\eta_2| \rho_1}{\eta_1 \rho_2} \right)$$

$$\tau = \text{pr} + 2\eta_1 |z_r - z_o| \quad (4.44)$$

defines the so-called de Hoop contour in the p plane along which $\text{Im} \tau = 0$ (Figure 4.14). $P_R(t, r, z_r)$ represents the wave reflected from sharp velocity increase arriving at $t_R = \frac{R}{v_1}$. $P_H(t, r, z_r)$ is the head wave arising at critical incidence and propagating along the interface. Its arrival time is

$$t_H = \frac{r}{v_2} + \left(\frac{1}{v_2} - \frac{1}{v_1} \right)^{1/2} 2 |z_r - z_o| \quad (4.45)$$

The remaining terms in (4.40) and (4.41)

$$P_1'(t, r, z_r) = \frac{d^2}{dt^2} (P_{1R}(t, r, z_r)) \quad \text{for } 0 < \theta_c$$

$$P_1(t, r, z_r) = \frac{d^2}{dt^2} \{ P_{1H}(t, r, z_r) + R_{1R}(t, r, z_r) \} \quad \text{for } 0 > \theta_c$$

(4.46)

where

$$R_{1R} = \frac{1}{\pi} \cdot 4(a_1^2 - 2a_2) \sigma^2 \frac{\rho_o^2}{\rho_1 \rho_2} \int_{t_R}^t \frac{\text{Re} \left\{ \frac{\eta_1 \eta_2 \rho \cdot R_o}{(t-\tau + 2pr)^{1/2}} \right\}}{(t-\tau)^{1/2} \left(\tau^2 - \frac{R^2}{v_1^2} \right)^{1/2}} d\tau$$

$$P_{1H} = \frac{1}{\pi} \cdot 4(a_1^2 - 2a_2) \sigma^2 \frac{\rho_o^2}{\rho_1 \rho_2} \int_{t_H}^t \frac{\eta_1 |\eta_2| \rho \cos 2\beta}{(t-\tau + 2pr)^{1/2}} \frac{d\tau}{(t-\tau)^{1/2} \left(\frac{R^2}{v_1^2} - \tau^2 \right)^{1/2}}$$

(4.47)

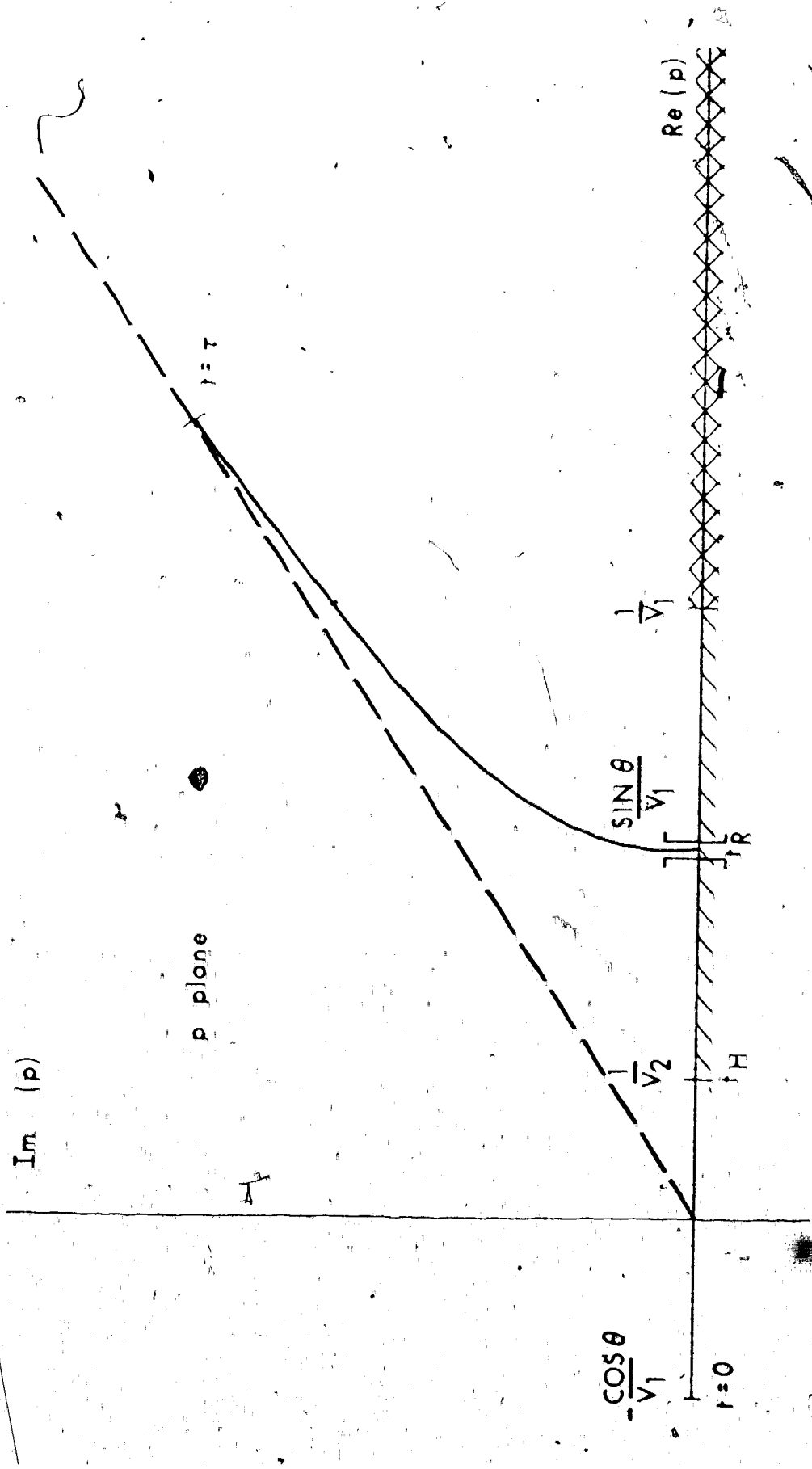


Figure 4.14 The de Hoop contour in the complex p plane.

are the corrections to the reflected wave and the head wave. They are due to finite thickness and continuity of the transition. In expressions (4.43) and (4.47) the parameter p is a function of t (Fig. 4.14) and all the integrals are just temporal convolutions that can be evaluated numerically. For computation of theoretical seismograms, this however is uneconomical, as the frequency range where the pulses are valid is very limited. The evaluation of the response in the frequency domain and the inverse Fourier transform are more practical and have wider ranges of applicability in our problem.

The amplitude for a head wave propagating along a velocity discontinuity is inversely proportional to frequency. Thus even if the velocity increase is continuous, we expect the amplitude behaviour of similar nature. For this purpose the amplitudes of the head wave were evaluated by contour integration and results are shown in Figures 4.15 and 4.16. We must distinguish two separate effects. One is the interference of the head wave with the reflected wave which changes the frequency dependence of the head wave within the interference zone (Cerveny, 1962). This explains why the amplitude-frequency dependence approaches to that of $\frac{1}{\omega}$ as epicentral distance increases. The other effect is that of transition thickness. For thinner transitions the head wave

0.2 km TRANSITION ZONE AT 20 km

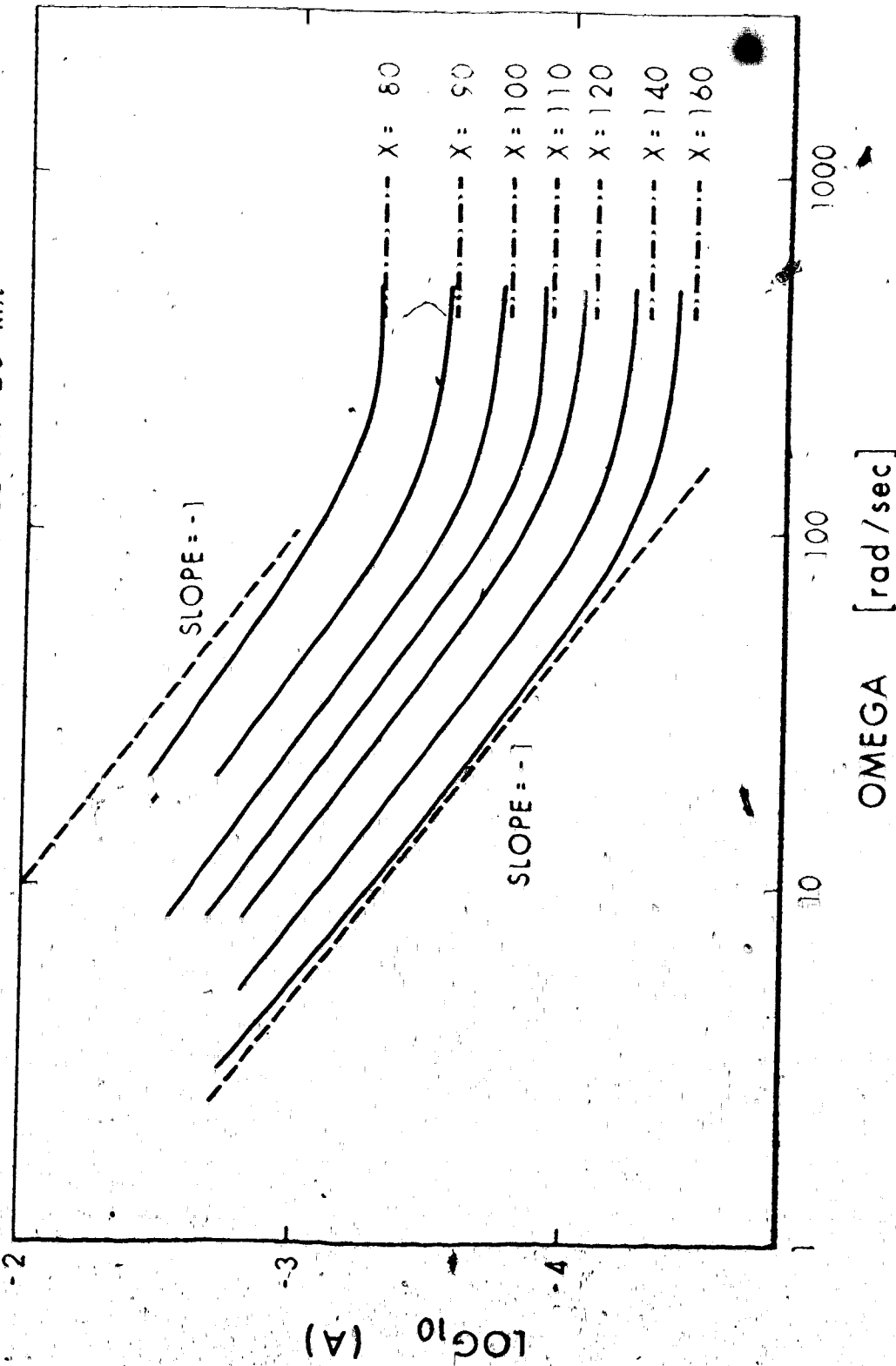


Figure 4.15. The amplitude of the head wave at different ranges beyond the critical point. (The chained lines indicate the geometrical amplitudes.)

1.6 km TRANSITION ZONE AT 20 km

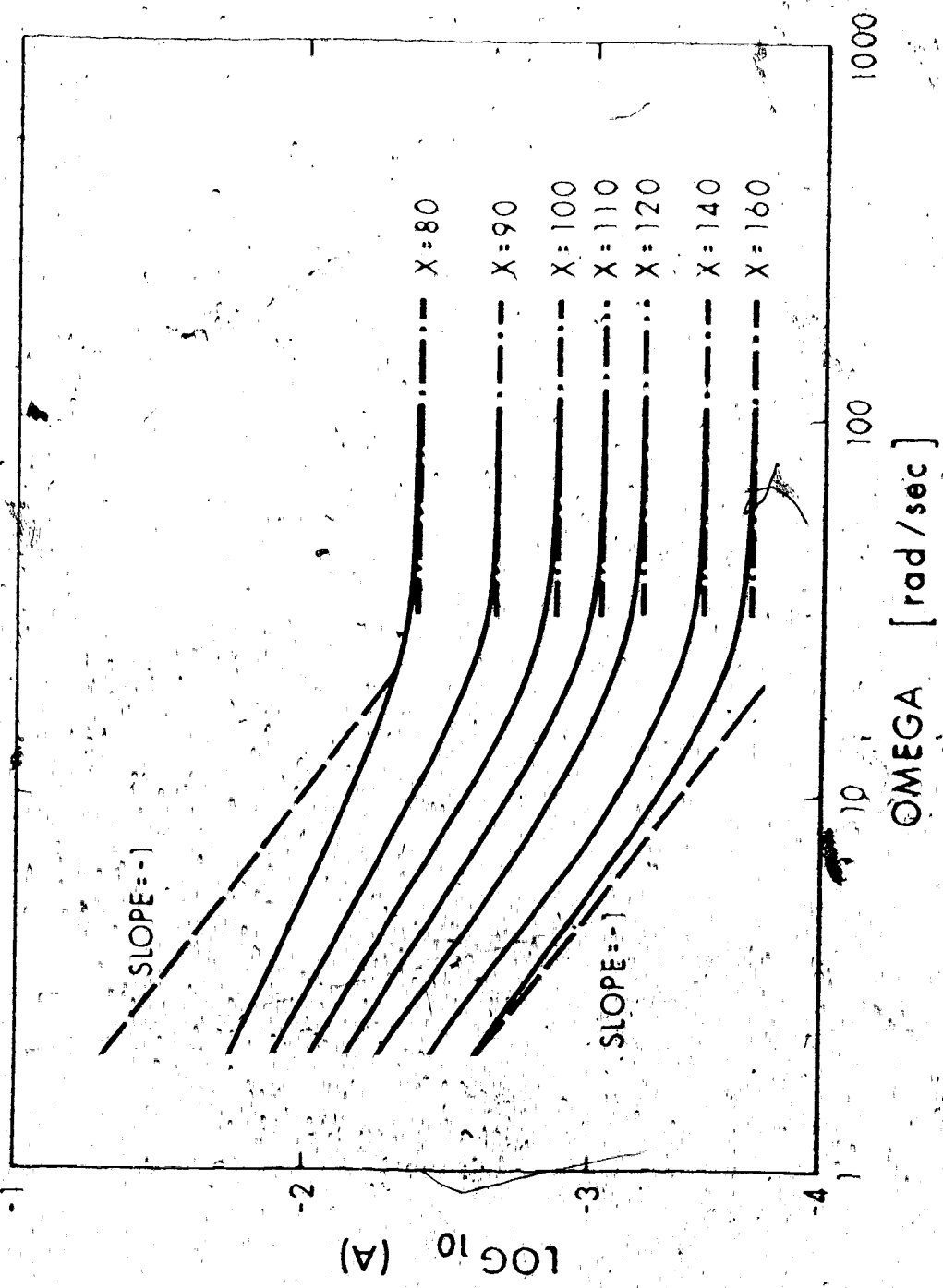


Figure 4.16 The amplitude of the head wave at different ranges beyond the critical point. (The chained lines indicate the geometrical amplitudes.)

is more like the "real" head wave at the velocity discontinuity and, therefore, its amplitude becomes inversely proportional to frequency as the transition thickness decreases. At high frequencies the amplitude approaches the geometrical amplitude (4.29) which is independent of frequency. This is another phenomenon that does not exist at sharp discontinuities while the amplitude is inversely proportional to frequency in the entire frequency range. Thus, whenever the velocity change has finite dimensions, a finite frequency exists at which the amplitude behaviour changes continuously from $\frac{1}{\omega}$ to 1. This frequency depends on the dimensions of the transition and with decreasing thickness it moves to higher frequencies. This is also well demonstrated in Figures 4.15 and 4.16. Equivalent results were obtained by Lang and Shmoys (1968) who studied analytically high frequency asymptotic approximation for the reflected field. Their approximation consists of two terms: the first is interpreted as a reflected wave for arbitrary transition thickness while the second represents a head wave when the wavelength is much greater than the transition thickness σ , and a reflected wave when the wavelength is much smaller than the transition thickness σ .

4.4 Synthetic seismograms

The results of the previous sections are not correct in application to wave propagation within the Earth if the transition is in great depth. Then the Earth's curvature cannot be neglected and the problem should be solved for spherical geometry. The earth-flattening transformation has been used by many authors (Müller, 1971; Hill, 1972; Helmberger, 1972) to obtain approximate solutions in flat geometry. The following transformation was used by Hill (1972) and applied to our problem:

$$\begin{aligned} r &= R - z \\ z &= R_r \log \frac{R}{R_r} \\ v_f(z) &= \frac{R_r}{R} v_s(R) \end{aligned} \quad (4.48)$$

where (R, θ, ϕ) are the spherical coordinates and R_r is some reference radius, in our case the radius of the receiver. $v_s(R)$ and $v_f(z)$ denote the velocities in spherical and flat geometry, respectively. Chapman (1973) showed that for a fluid the optimum transformation requires the following density transformation

$$\rho_f(z) = \frac{R_r}{R} \rho_s(R) \quad (4.48a)$$

where $\rho_s(R)$ and $\rho_f(z)$ are the densities in spherical and flat geometry, respectively. The earth-flattening transformation does not change the kinematic properties in the transformed model. The rays emerging at the same angle arrive at the same horizontal range at the same time. Thus the increased velocity in the flat model compensates for the longer ray path due to the depth transformation (Fig. 4.17). The dynamic properties, i.e. amplitudes do change and Müller (1971) showed that the ratios of the geometrical amplitude (4.29) to its equivalent in spherical geometry is

$$\frac{A_f}{A_s} = \left(\frac{\sin \theta}{\theta} \right)^{1/2}$$

Thus the amplitudes in the flat half-space are systematically smaller than those in a sphere.

Three models for monotonic velocity transition were chosen for calculation of synthetic seismograms.

Model X of broad velocity transition in Fig. 1.2:

$$\begin{aligned} v_{1f} &= 8.4 \text{ km/sec} & v_{1s} &\approx v_s(6200) = 8.4 \text{ km/s} \\ v_{2f} &= 10.4 \text{ km/sec} & v_{2s} &\approx v_s(5810) = 9.74 \text{ km/s} \\ \sigma &= 35 \\ z_o &= 180 \text{ km} \\ z_r &= z_s = 0 \text{ km} & R_r &= 6200 \text{ km/s} \\ \rho &= \text{constant} \end{aligned}$$

(4.49)

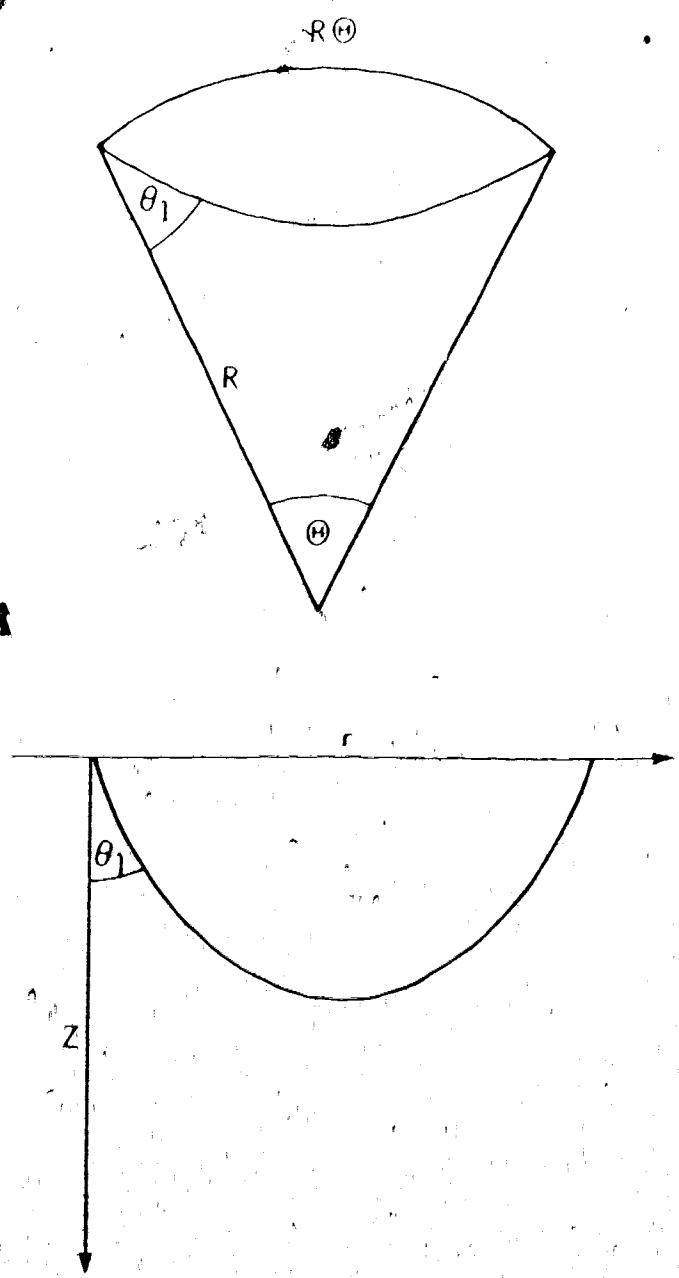


Figure 4.17 Effect of the earth-flattening transformation on the ray path.

The spherical velocities are close to values given by Johnson (1967) for the upper mantle transition at 400 km. The transition in model X is assumed to begin at $R = 6200$ km, i.e. below the low velocity zone.

Model IV of 1.6 km transition at 20 km in Fig. 4.1:

$$v_1 = 6.63 \text{ km/s}$$

$$v_2 = 8.05 \text{ km/s}$$

$$\sigma = .2$$

$$z_0 = 20 \text{ km/s}$$

$$z_s = z_r = 0 \text{ km}$$

$$\rho = \text{constant}$$

(4.50)

Model V of .2 km transition at 20 km in Fig. 1.3:

$$v_1 = 6.63 \text{ km/s}$$

$$v_2 = 8.05 \text{ km/s}$$

$$\sigma = .025$$

$$z_0 = 20 \text{ km/s}$$

$$z_s = z_r = 0 \text{ km}$$

$$\rho = \text{constant}$$

(4.51)

Velocities used in models IV and V are characteristic for the Earth's crust and the models differ only in the thickness of the transition.

The density was kept constant in all the models which is not a realistic assumption. Basically the change of density must be very similar to change of velocity. However, the assumption about density being constant is not a serious limitation. The density variation introduces a small asymmetry into the model due to stretching of the vertical coordinate. This is a result of transformation (2.14) and provided the Birch's relation for density change is valid

$$\rho = .328v + .613.$$

(Wang, 1972), the effect of density variation on model X is shown in Fig. 4.18 and in Table 4.1. For models IV and V the distorted models are displayed in Tables 4.2 and 4.3, respectively. We see that the difference between the original and the distorted models is very small.

For computation of synthetic seismograms the response integral (4.18) must be evaluated in wide range of frequencies. In a previous section the asymptotic pressure response was found in limited range of frequencies outside the limits of validity of the aforementioned results, the numerical integration must be done. This involves the calculation of the gamma function $\Gamma(z)$ and Hankel function $H_0^{(1)}(z)$ for complex arguments. Programs for these were written with algorithms based on formulae valid in different regions of complex z plane

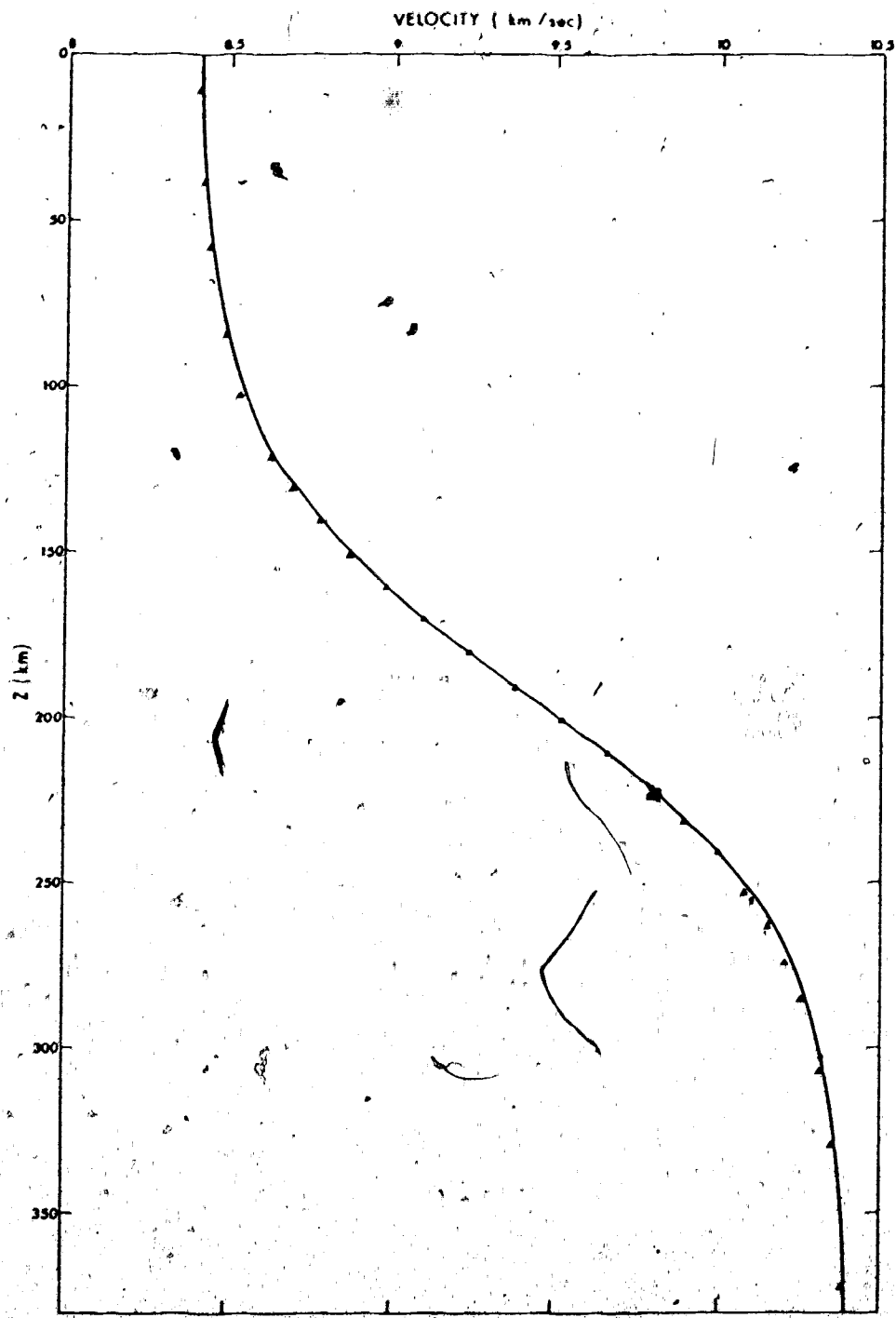


Figure 4.18 The effect of density variation on the velocity profile in Model X (full line). The triangles indicate the velocities in the model that includes density variation.

INFLUENCE OF DENSITY VARIATION ON
VELOCITY PROFILE IN MODEL X

Velocity v [km/s]	Original Coordinate $z-z_0$ [km]	Transformed Coordinate ζ [km]
8.41	-180	-169.8
8.42	-160	-151.3
8.43	-140	-132.8
8.45	-120	-114.2
8.48	-100	-95.6
8.54	-80	-76.9
8.63	-60	-58.1
8.78	-40	-39.1
8.98	-20	-19.8
9.24	0	0
9.52	20	20.3
9.79	40	41.0
10.00	60	62.2
10.15	80	83.7
10.25	100	105.4
10.31	120	127.3
10.35	140	149.3
10.37	160	171.3
10.38	180	193.3

Table 4.1

INFLUENCE OF DENSITY VARIATION ON
VELOCITY PROFILE IN MODEL IV

Velocity v [km/s]	Original Coordinate $z-z_0$ [km]	Transformed Coordinate ζ [km]
6.63	-20.	-18.69
6.63	-15.	-14.02
6.63	-10.	-9.35
6.63	-5.	-4.69
6.64	-1.	-0.95
6.71	-0.5	-0.49
7.24	0.	0.
7.91	0.5	0.52
8.04	1.	1.06
8.05	5.	5.42
8.05	10.	10.86
8.05	15.	16.31
8.05	20.	21.75

Table 4.2

INFLUENCE OF DENSITY VARIATION ON
VELOCITY PROFILE IN MODEL V

Velocity v [km/s]	Original Coordinate $z-z_0$ [km]	Transformed Coordinate ζ [km]
6.63	-20.	-18.67
6.63	-15.	-14.01
6.63	-10.	-9.34
6.63	-5.	-4.67
6.63	-1.	-0.94
6.63	.5	.47
6.65	.1	.096
6.76	.05	.049
7.24	.0	.0
7.83	.05	.052
8.02	.1	.106
8.05	.5	.54
8.05	1.	1.08
8.05	5.	5.43
8.05	10.	10.88
8.05	15.	16.33
8.05	20.	21.77

Table 4.3

(see Appendix D). It is easy to achieve accuracy comparable to that of other functions incorporated in the Fortran language.

Thus the main concern is about the efficiency and accuracy of the integration procedure. The analytic solutions of Section 4.3 showed that the integration contour can be moved to pass through the saddle points via the steepest descent path. The approximations are only good at high frequencies and they deteriorate as frequency decreases. To find a suitable contour in the complex κ plane, the integrand in (4.18) must be studied. Its analytic behaviour is studied using contour maps of logarithm of its modulus and phase (Fig. 4.19). The grid depends on frequency, widths of saddle points and steepness of the descent paths. For example: in case of the triplication, different grids are used in regions near to caustics at θ_C and θ_B (Fig. 4.19 and 4.21). The signals at caustic θ_B are weaker than signals at the caustic θ_C which results narrower saddle points in the first case. As low frequency end is approached the saddle point corresponding due to the rays of branch AB disappears, this is due to the source being placed in inhomogeneous medium: the high frequency waves at shallow angles encounter the small change in velocity gradient around the source and contribute to signals forming branch AB. The long period waves are not effected and, therefore they contribute very little to amplitudes of branch AB.

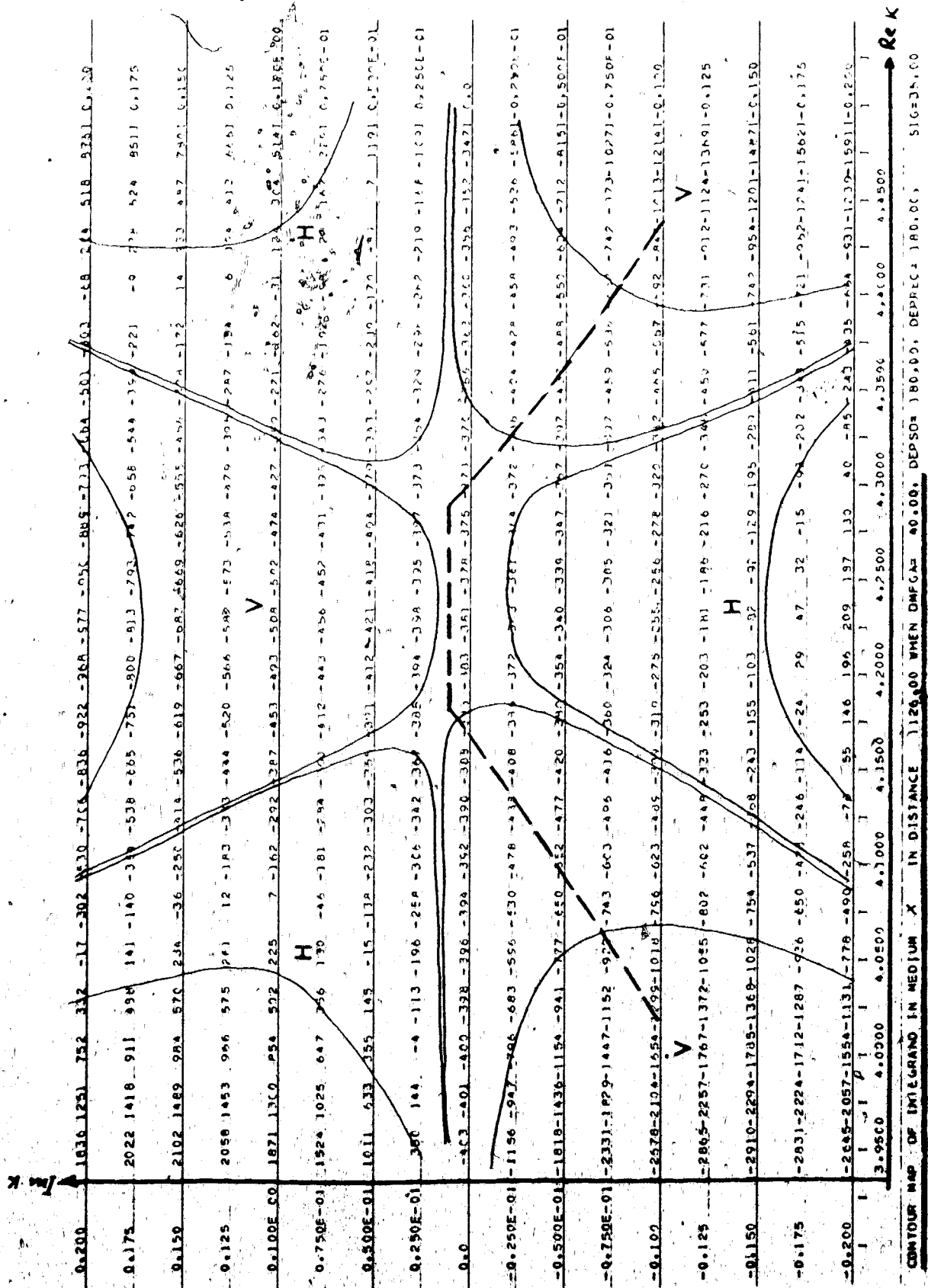


Figure 4.19. At $\theta = 10^\circ$ the modulus of the integrand is $e^{\pm 100}$ when the value on the map is ± 10000 . Valleys (V) and hills (H) are also indicated for saddle points near caustic C. The broken line is the integration contour.

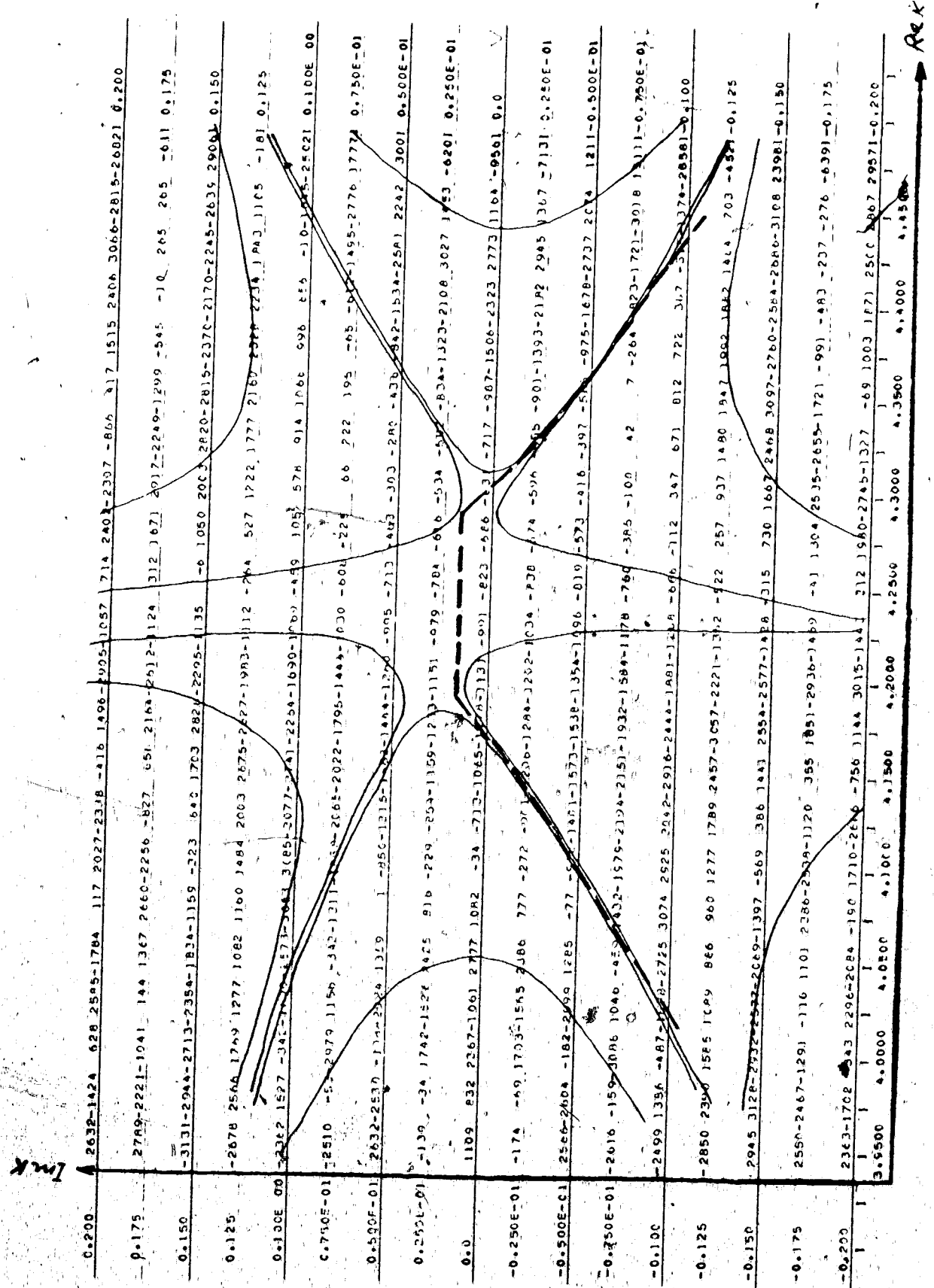


Figure 4.20 Contour map of the phase of the integrand at $\theta = 10^\circ 25'$, whose modulus is in Figure 4.19. The phase is $e^{i\phi}$ when the value on the map is ± 3142 . The broken line is the integration contour.

Rek

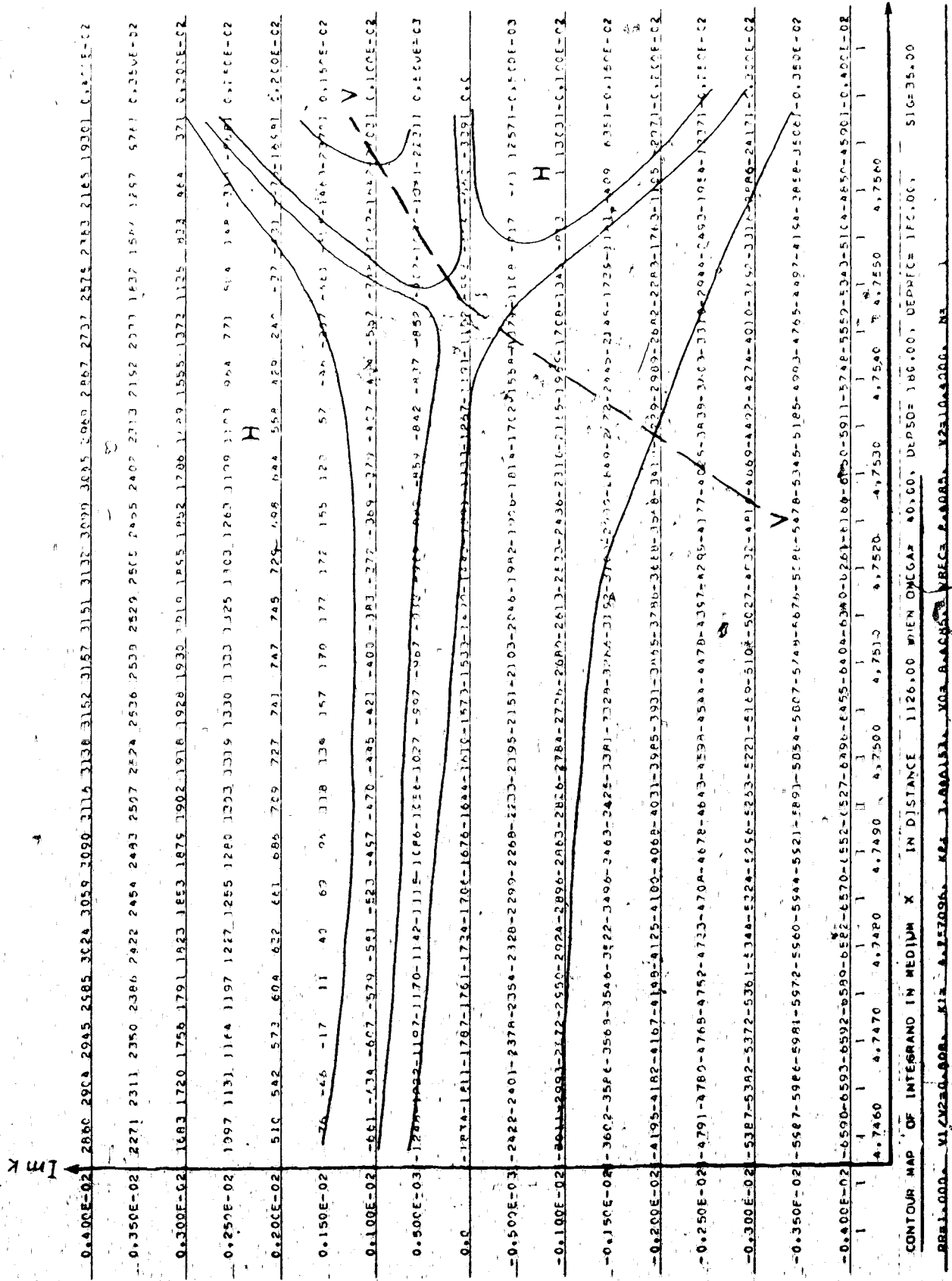


Figure 4.21 The saddle point representing the arrival on branch AB at $\theta = 10^\circ 25'$ is very narrow. The modulus of the integrand is $e^{\pm 1000}$ when the value on the map is ± 10000 . The broken line is the integration contour.

When the steepest descent path is found on the contour map it is approximated by straight line segments (Fig. 4.19). On the contour map of the phase in Fig. 4.20, these approximately follow the constant phase line. Thus the numerical integration can be performed accurately using one of the simplest numerical methods - the Simpson's method. If the contour were not along a line of constant phase, the oscillatory character of the integrand would make the integration extremely difficult. According to the Simpson's method (Abramowitz and Stegun, 1965; p. 886)

$$\int_{\kappa_j}^{\kappa_{j+1}} f(\omega, \kappa, r) d\kappa \approx \frac{1}{3} \Delta \kappa_j \{f_0 + 4f_1 + 2f_2 + \dots + 4f_{n-1} + f_n\} \quad (4.52)$$

where f_0, f_1, \dots, f_n are values of integrand at successive steps of interval $\langle \kappa_j, \kappa_{j+1} \rangle$. Rigorously, the step size should be evaluated from the error term in the Simpson's method. This is proportional to $f^{(iv)}(\kappa)$ because the Simpson's rule is correct to the second order, and it is rather tedious to evaluate the step size from it. Our integrand is a smoothly varying function along the path of integration and, therefore, the step size is simply estimated from the first derivative

$$\int_{-\Delta\kappa}^{\Delta\kappa} f(\kappa) d\kappa = \frac{1}{3}\Delta\kappa \{f(-\Delta\kappa) + 4f(0) + f(\Delta\kappa)\} - \frac{1}{90} f^{(iv)}(\xi_1) \Delta\kappa^5 \quad (4.53)$$

where $-\Delta\kappa \leq \xi_1 \leq \Delta\kappa$. If we assume that within $(-\Delta\kappa, \Delta\kappa)$, the integrand is an exponential function:

$$f(\kappa) = a \cdot e^{b\kappa}$$

the fractional error

$$\epsilon = \frac{f^{(iv)}(\xi_1) \Delta\kappa^5}{180f(\xi_2) \Delta\kappa} = \frac{1}{180} b^4 \Delta\kappa^4$$

Thus
$$|\Delta\kappa| = 3.7 \left| \frac{f(\kappa)}{f'(\kappa)} \right| \epsilon^{1/4} \quad (4.54)$$

For a fractional error $\epsilon = 10^{-4}$ we can take

$$|\Delta\kappa| = \left| \frac{f(\kappa)}{10f'(\kappa)} \right| \quad (4.55)$$

where factor 3.7 was ignored for safety. $\text{Arg}(\Delta\kappa)$ is chosen in the direction of the contour segment. This method has been used by Phinney and Cathles (1969) and Chapman and Phinney (1972). The first derivative in the denominator can be estimated by taking the gradient at the endpoints of the segment. The step size of two neighbouring segments is

evaluated and finally their minimum is chosen for integration:

$$|\Delta\kappa_j(r)| = \min\{|\Delta\kappa(\kappa_j, r)|, |\Delta\kappa(\kappa_{j+1}, r)|\} \quad (4.56)$$

where

$$|\Delta\kappa(\kappa_j, r)| = \left| \frac{f(\kappa_j, \omega, r) \delta\kappa}{10 [f(\kappa_j + \delta\kappa, \omega, r) - f(\kappa_j, \omega, r)]} \right|$$

Then

$$P(\omega, r, z_r) = \int_{-\infty}^{\kappa_1} f(\kappa, \omega, r) d\kappa + \sum_{j=1}^{j-1} \int_{\kappa_j}^{\kappa_{j+1}} f(\kappa, \omega, r) d\kappa + \int_{\kappa_J}^{\infty} f(\kappa, \omega, r) d\kappa \quad (4.57)$$

κ_1 and κ_J are chosen so that the integrals to infinity (which are deep in valleys) are small. Again assuming exponential decay their contribution can be estimated as

$$\int_{-\infty}^{\kappa_1} f(\kappa, \omega, r) d\kappa + \int_{\kappa_J}^{\infty} f(\kappa, \omega, r) d\kappa = \frac{f^2(\kappa_1, \omega, r)}{f'(\kappa_1, \omega, r)} - \frac{f^2(\kappa_J, \omega, r)}{f'(\kappa_J, \omega, r)}$$

(4.58)

The accuracy of the algorithm can be tested integrating around closed curves with or without singularities enclosed. All these trials proved to be within the required accuracy $\epsilon = 10^{-4}$.

But, even if the integration is performed by Simpson's rule, the amount of the computing time needed would be enormous, if further savings were not made. Many computations can be saved when one contour is used to evaluate the response at several ranges r . Only the Hankel function $H_0^{(1)}(\kappa r)$ is dependent on r and only these values have to be recalculated for every r . The rest of the integrand is stored and reused every time the response is computed for new r . The contour of integration is no longer the approximation of the steepest descent path, but if chosen with care, a useful range of integrals can be evaluated with no significant loss in accuracy. Usually, the contour is chosen to be a steepest descent path for r which is in the middle of the interval of r 's where the same contour is used. This is very efficient at low frequencies and in the neighbourhood of the caustics where the saddle points change their position slowly with changing r . In the illuminated region, the contour must be changed more often as the saddle points separate more and more rapidly, until a separate contribution from each has to be computed. The phase difference between the two rays is growing and interference becomes important and causes oscillation of the total amplitude (Fig. 4.22). The contour integral cannot be evaluated along the real axis between the saddle points. It must be taken into the valley

BROAD TRANSITION ZONE - FAR END OF THE TRIPLICATION

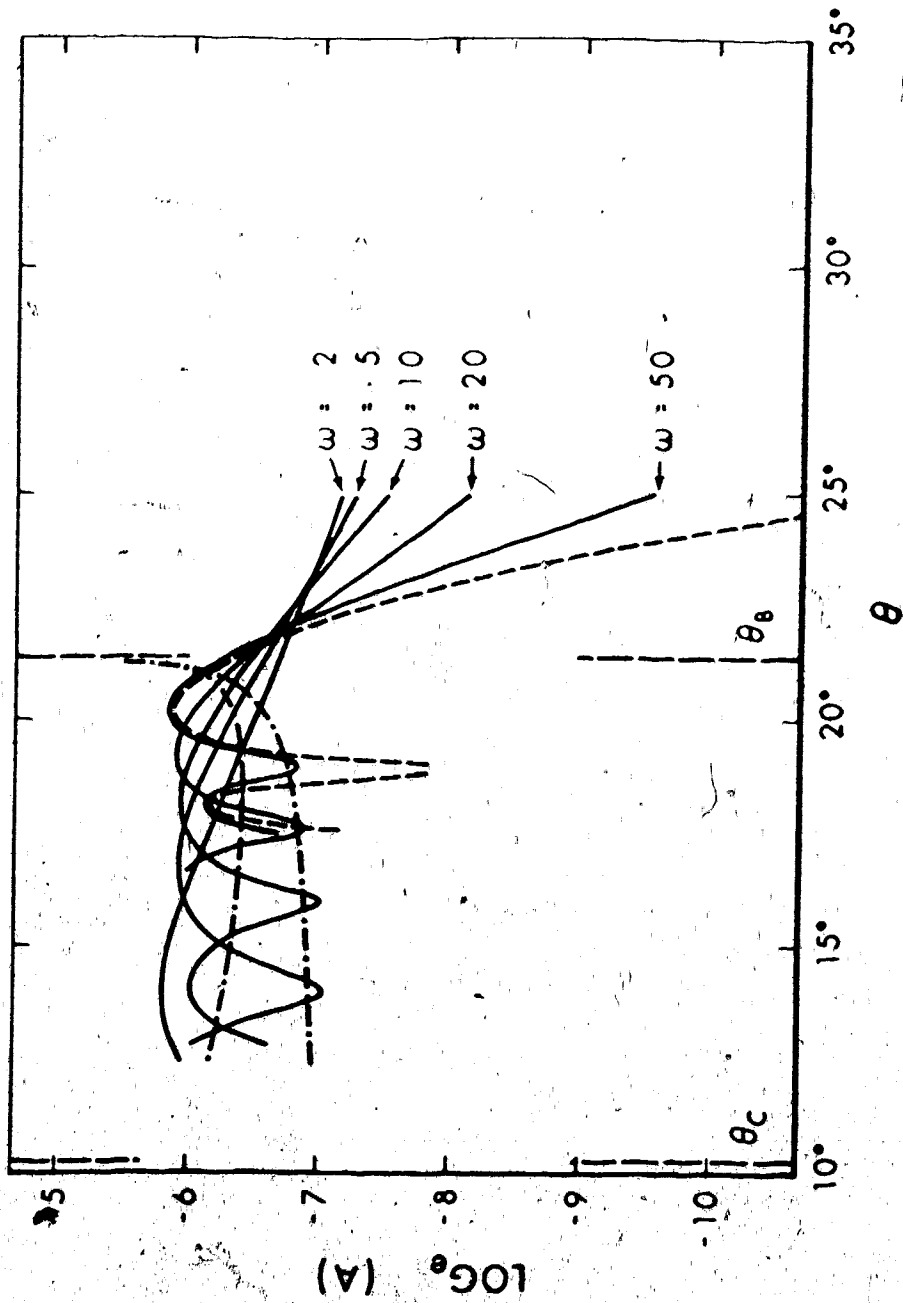


Figure 4.22 Amplitude curves near the caustic, $B(\theta_B = 21^\circ)$ evaluated numerically for different frequencies (full lines). The geometrical amplitudes (chained line) and the Airy function (broken line) are also indicated.

above or below the real axis which is common to both saddle points (Fig. 4.23). The Figure 4.22 showing the results of the contour integration is similar to those shown and discussed in the former section. In the illuminated region the reflected wave of the reverse branch BC is stronger and the amplitude oscillates^o about its geometrical amplitude (4.30).

For the synthesis of pulses in the time domain the method described by Chapman and Phinney (1972) was used. In order to synthesize theoretical seismograms, spectral values over a wide range of frequencies are needed. To limit the frequency range we have simulated a critically damped seismometer response with transfer function

$$\frac{\omega^3}{(\Omega_g^2 - \omega^2 - i\omega\Delta)(\omega_s^2 - \omega^2 - i\omega\delta)} \quad (4.59)$$

where Ω_g and ω_s are natural frequencies of the seismometer and galvanometer. For critical damping, $\delta = 2\omega_s$ and $\Delta = 2\Omega_g$. Although in period range used here ($T_s = .45$ sec, $T_g = 1.5$ sec) seismometers do not use galvanometers, the transfer function (4.59) still represents a band limited instrument.

The transfer function is convolved with the source of unit step function i.e. $P_s(t) = H(t)$. Their combined spectrum and the resultant seismogram are shown in Figures 4.24 and 4.25.

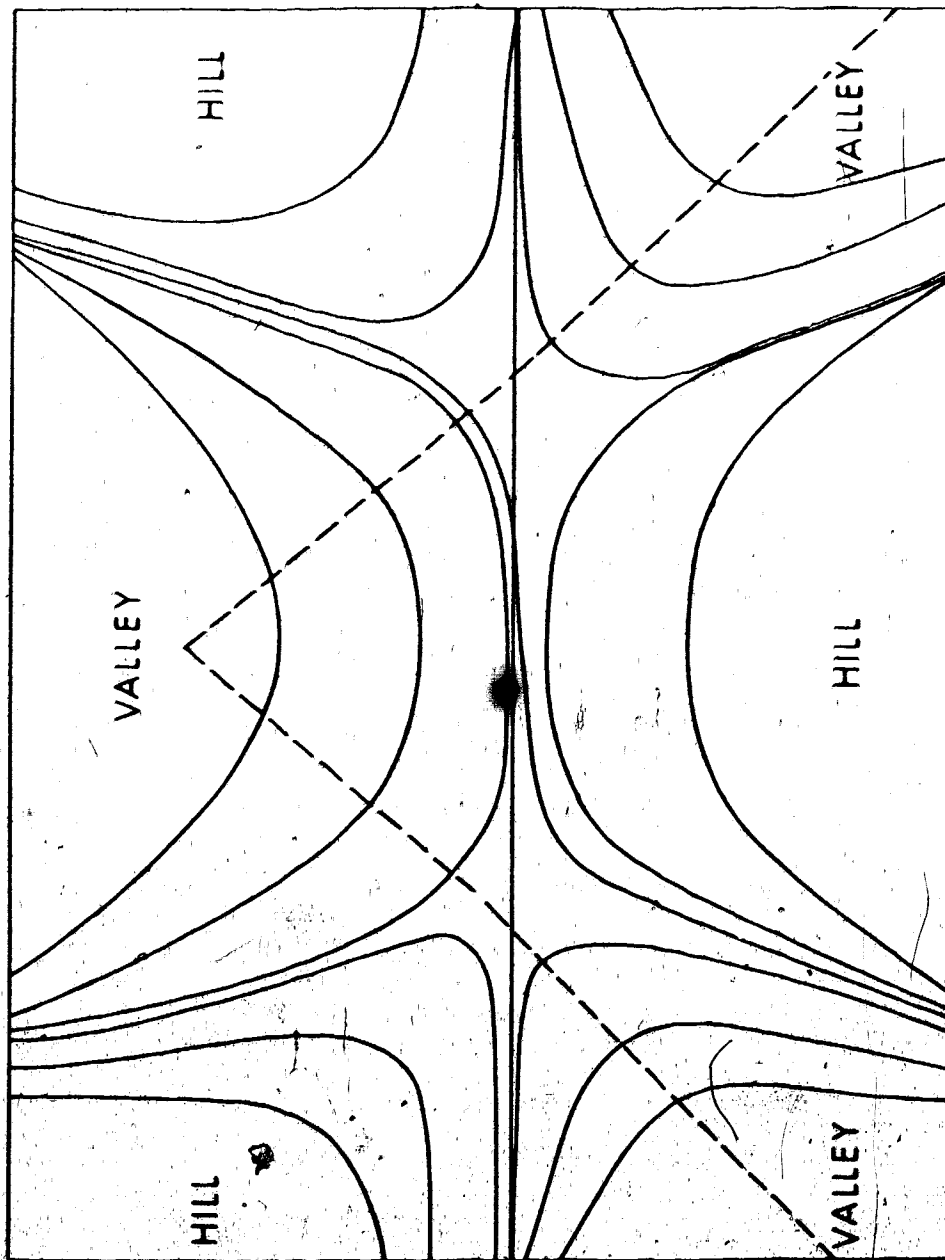


Figure 4.23 The contour of integration in the complex K plane when the saddle points are well separated (Diagrammatic).

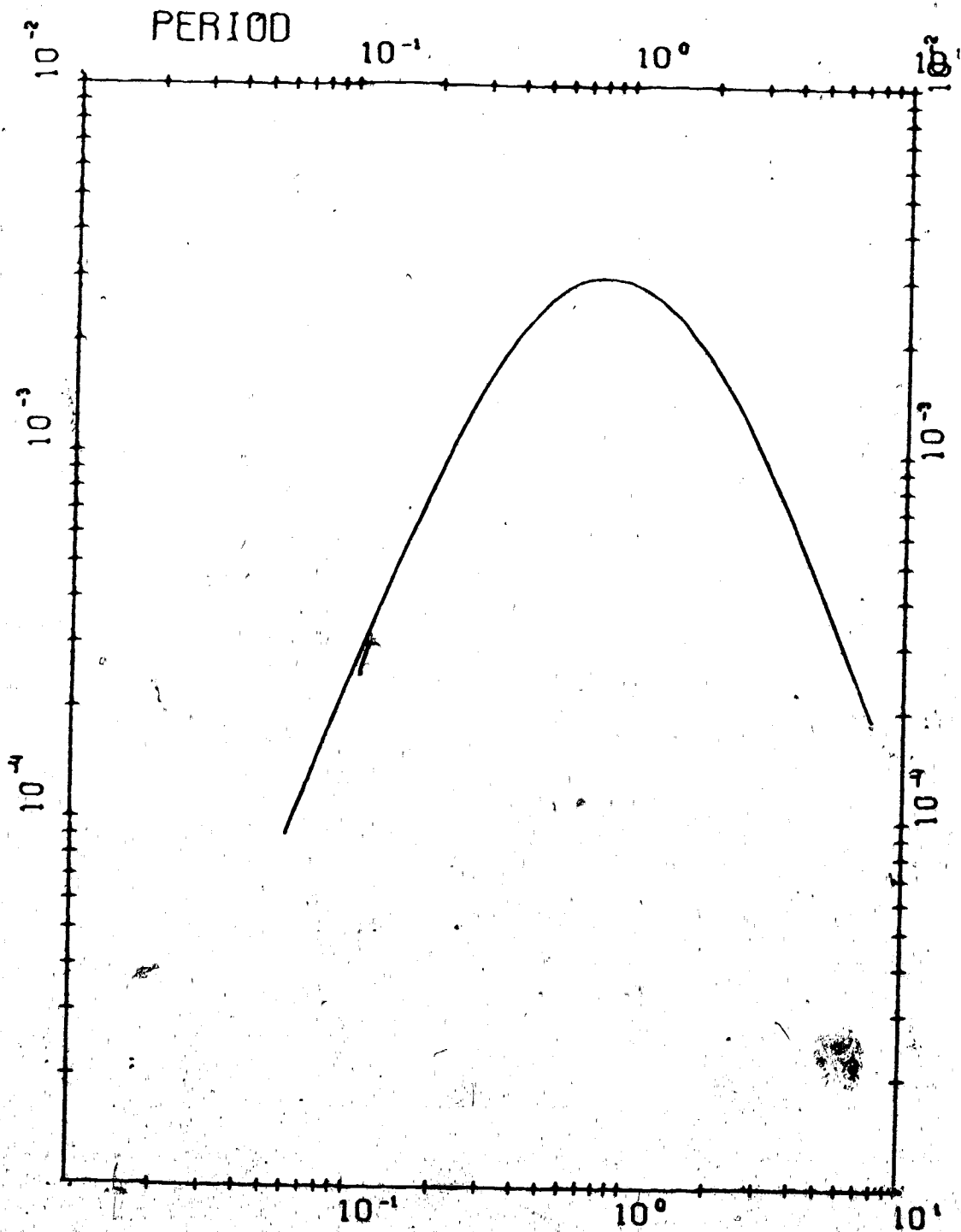


Figure 4.24 The combined spectrum of the critically damped seismometer and the unit step function source.

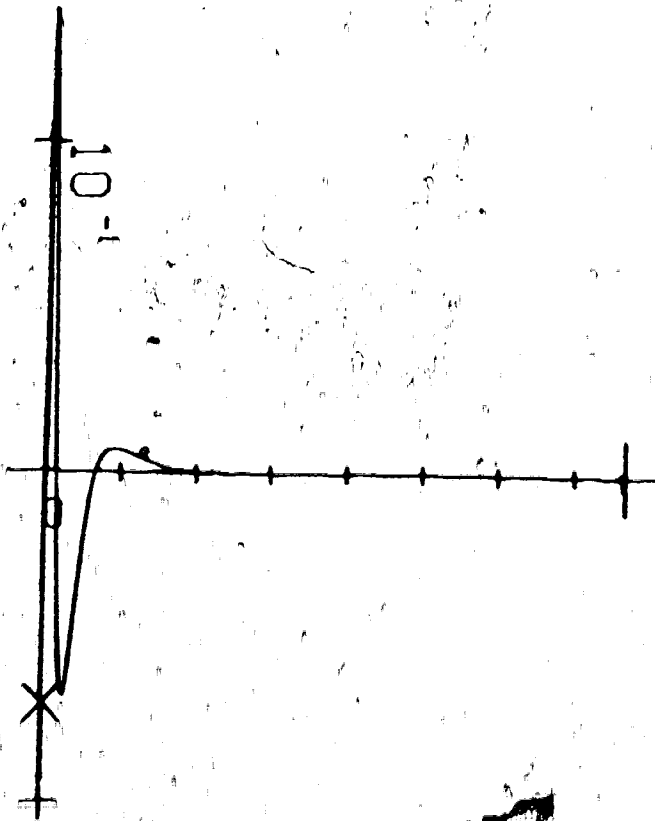


Figure 4.25 The response of the critically damped seismometer to the unit step function source. Marks on the time scale are every second.

The spectral amplitudes (4.29) and (4.30) are independent of frequency and, therefore, the pulses on forward branches of the travel-time curve have the same shape as in Figure 4.25. The pulses of the reversed branch will be shifted by $-\frac{\pi}{2}$, i.e. they are "allied" pulses to that in Figure 4.25.

The inverse Fourier transform (2.6) is evaluated using finite Fourier sum. Efficient programs, which use the algorithm for fast Fourier transform developed by Cooley and Tukey (1965), exist in Fortran and we only supply the spectral amplitudes. The spectral amplitudes calculated by evaluating the response integral (4.18) must be interpolated. $\hat{P}(\omega, r, \zeta_r)$ is complex and its modulus and phase must be interpolated separately. Where $\hat{P}(\omega, r, \zeta_r)$ is evaluated, the phase is a discontinuous function in the range $-\pi$ to π . The geometrical results can be used to remove the 2π ambiguity in the phase between various frequencies and ranges. From (4.21) and (4.23) we get

$$\frac{\partial f}{\partial r} = \kappa = \omega \cdot \frac{dT}{dr} \quad (4.60)$$

and

$$\frac{\partial f}{\partial \omega} = T$$

where $f(\kappa)$ is the continuous phase function. The equalities in (4.60) are valid only at high frequencies. At finite frequencies they can be replaced by approximate equalities.

As such they are used in the algorithm that forms continuous phase functions needed for interpolation. In the region before the caustic the arrival time is formed by solving the stationary phase condition (4.22) in complex κ plane. The arrival time is the real part of $\frac{f(\kappa)}{\omega}$. The same applies to regions before the critical point where the transition is thin. In this case, however, the times of arrival of sub-critical reflections from a sharp velocity increase can also be used, especially where the transition is very thin.

The theoretical seismograms evaluated using the transfer functions (4.59) with step function as a source are shown in Figures 4.26 to 4.29. They are normalized with respect to the maximum amplitude at caustic or at the critical point.

The seismograms in Figures 4.26 and 4.27 for pressure at the near and far ends of the triplication. The maximum amplitude at $10^{\circ}30'$ and at 20° is the Airy phase due to interference. The geometrical endpoints are at $10^{\circ}20'$ and 21° and as we move away from the illuminated region the signals decay rather quickly. The first pulse in both cases corresponds to the forward branches and is in phase with the source pulse. The pulses of the reverse branch BC are the allied pulses, shifted by $-\frac{\pi}{2}$ with respect to the first arrivals. The difference in phase can be clearly distinguished at ranges

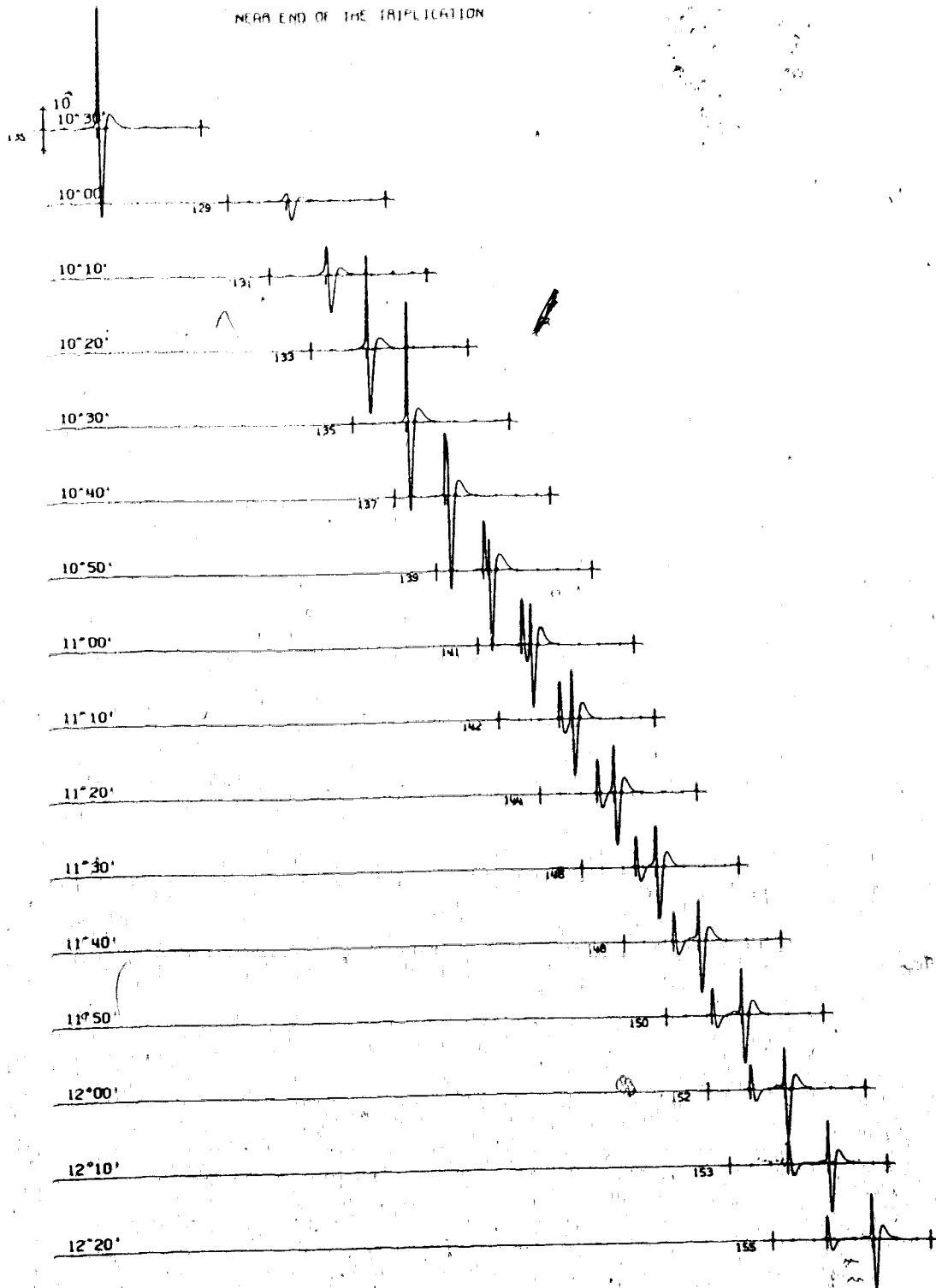


Figure 4.26 The synthetic seismograms for Model X at ranges near the caustic C. The marks on the time scale are every second. The geometrical arrival times are indicated by longer vertical marks.

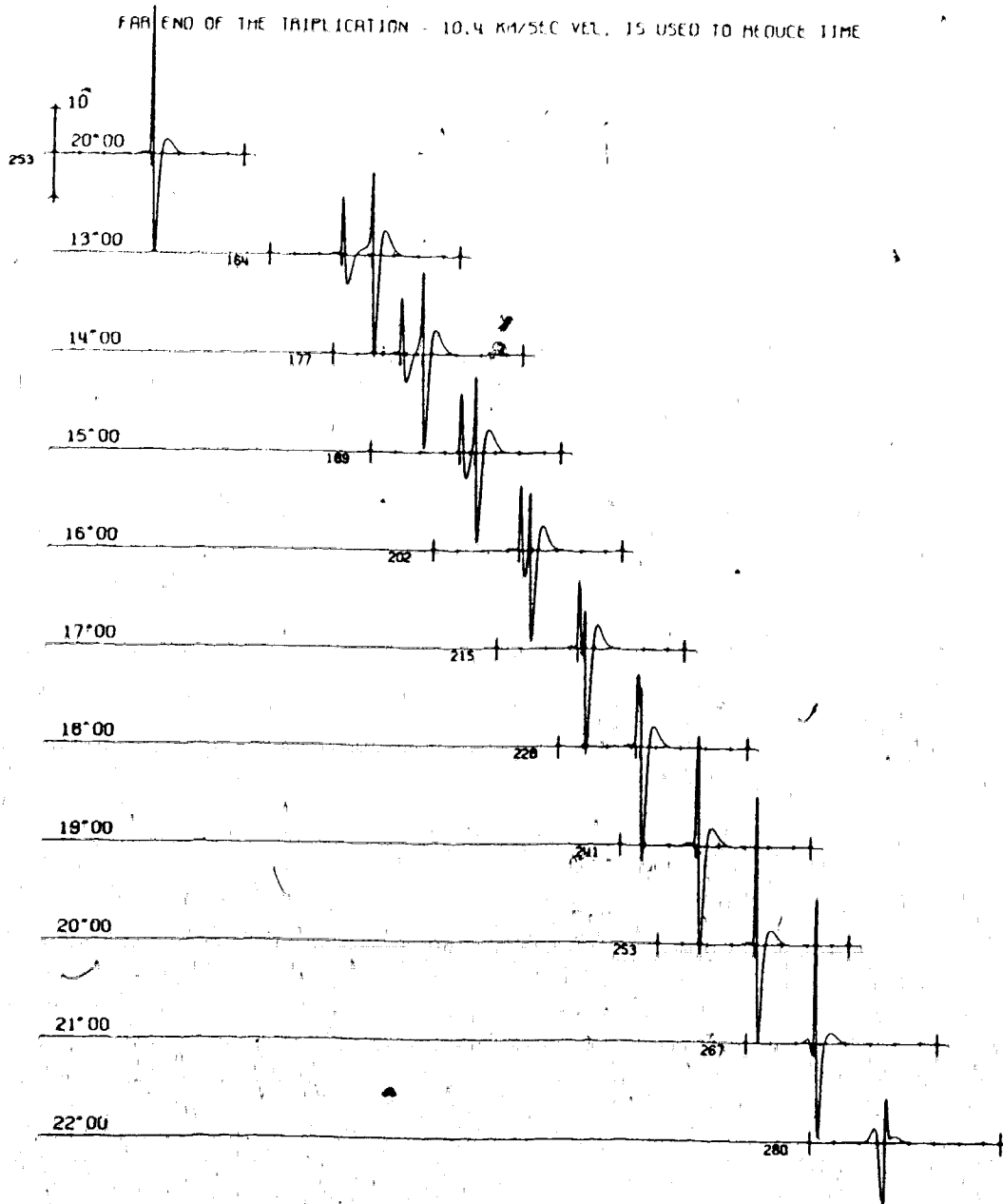


Figure 4.27 Synthetic seismograms for Model X at ranges near the caustic B. (Time scale as in Figure 4.26.)

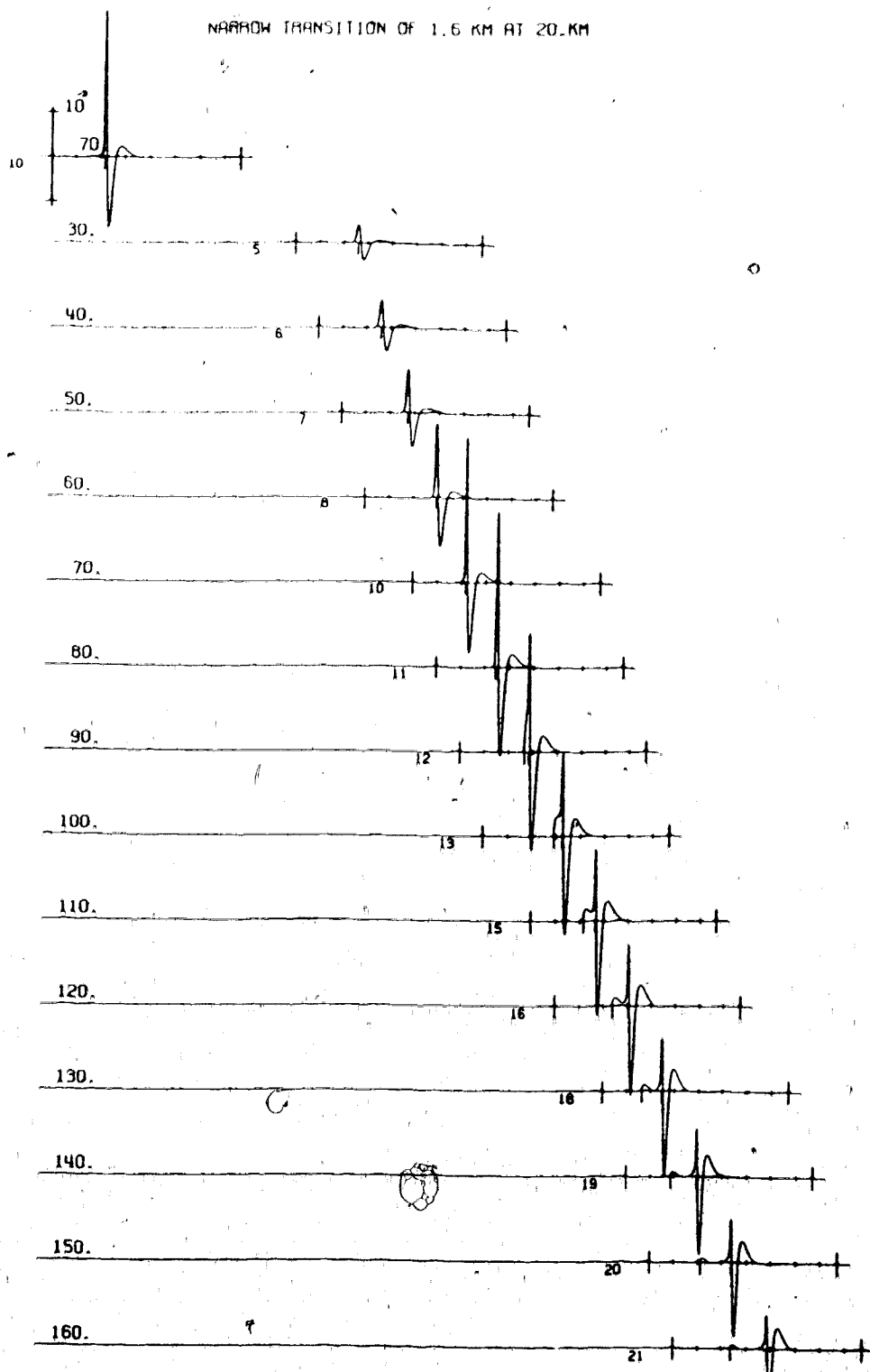


Figure 4.28 Synthetic seismograms for Model IV at ranges near the critical point. (Time scale as in Figure 4.26.)

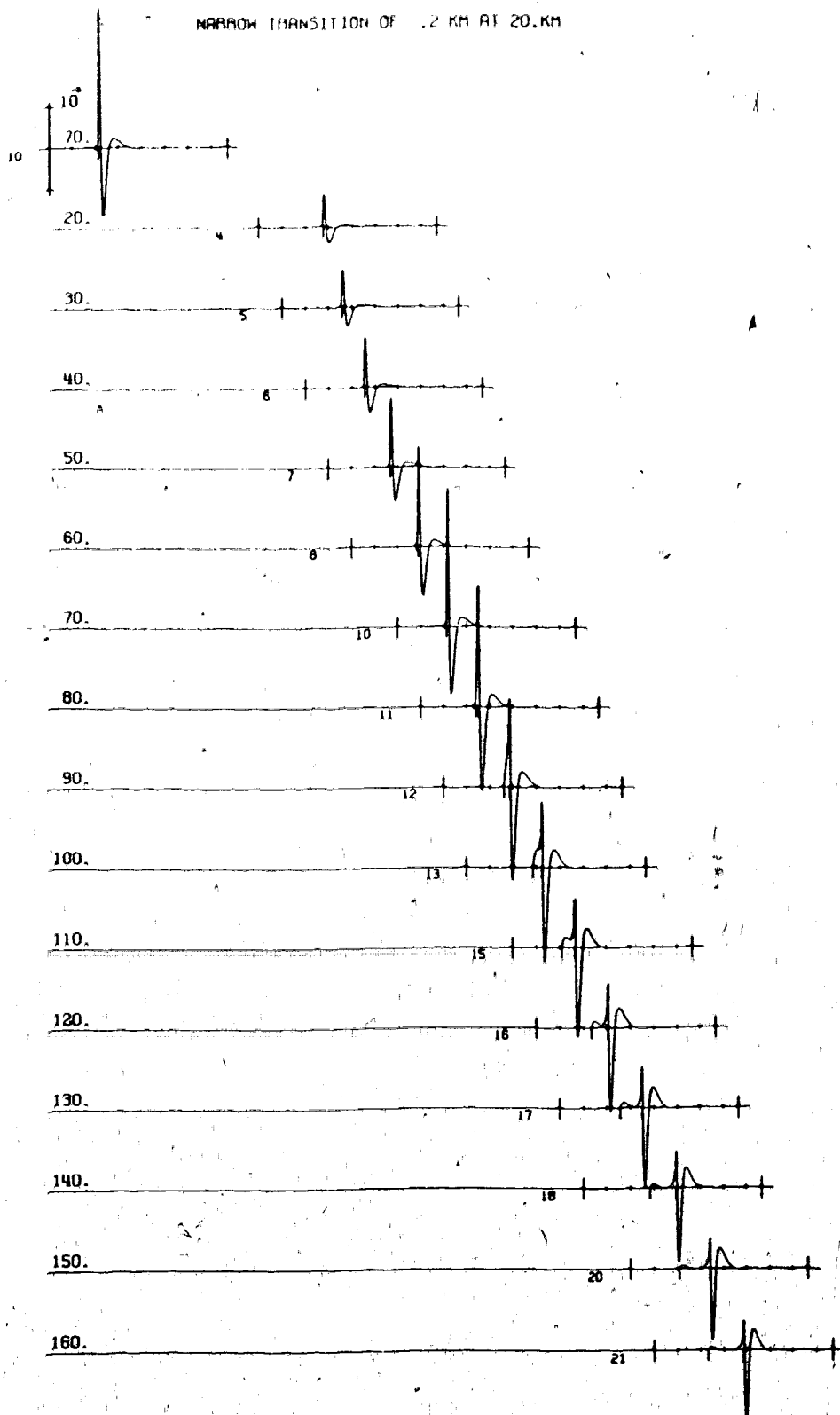


Figure 4.29 Synthetic seismograms for Model V at ranges near the critical point. (Time scale as in Figure 4.26.)

$12^{\circ}20'$ and 13° which are well inside the illuminated region. In this example, the response function (4.18) was calculated by numerical integration for 12 frequencies ranging from $\omega = .5$ rad/sec to $\omega = 60$ rad/sec. From $\omega = 60$ rad/sec to $\omega = 110$ rad/sec the geometrical values (4.29) and (4.30) were used. 12 spectral values were interpolated using cubic spline in order to obtain 128 spectral values between $\omega_1 \approx .82$ rad/sec and $\omega_N \approx 104.7$ rad/sec (Nyquist frequency) with step $\Delta\omega \approx .82$ rad/sec. These were used as input to the inverse Fourier transformation.

The seismograms in Figures 4.28 and 4.29 are for pressure in the neighbourhood of the critical point when the transition is thin. For both transitions the amplitudes are normalised with respect to amplitude at 70 km. For .2 km transition, this coincides with the maximum amplitude while for 1.6 km transition, maximum occurs at 80 km. This agrees with the shift of the critical points, $X_C = 60.5$ km and 67.8 km for .2 and 1.6 km transitions, respectively. In the region before the critical point, the seismograms show that partial reflection grows considerably as the transition becomes thinner. For .2 km transition, the signal at 20 km is quite strong while for 1.6 km transition it would barely show. Also their shape for the thinner transition appears to be more like the sub-critical reflection at sharp discontinuity. The partial

reflections are in phase with the source pulse which agrees with the fact that at sub-critical reflections, no phase change occurs. The amplitude maximum is due to interference of the reflected wave and head wave. Further beyond the critical range the two waves start to separate into first arriving head wave and later reflected wave. The reflected wave beyond the critical point is totally reflected and, therefore, shifted by $-\frac{\pi}{2}$ with respect to the source pulse. This is clearly observable at 150 km.

For calculation of the seismograms for thin transitions, the geometrical values (4.29) and (4.30) could not be used and the numerical evaluation of the pressure spectrum was performed at 17 frequencies between $\omega' = .5$ rad/sec and $\omega = 110$ rad/sec. Their interpolation was performed in the same manner as for the triplication.

The results presented in this section demonstrate that the numerical methods can be used efficiently to compute the spectral response and the synthetic seismograms. This should be an encouragement for their wider use in seismology. In application to the interpretation of data, the results for the response in the frequency domain are probably of greatest importance as the different properties are then easily seen and can be interpreted. Although results presented here were obtained for relatively simple models, some

of their basic features (behaviour near caustics and critical points) should be very similar to those which one would get even for more complex models. Furthermore these results can serve as calibration results for approximate methods. Their importance has increased considerably in recent years but the error estimates have always been very vague. These can only be evaluated rigorously if the approximations are compared to exact results.

CHAPTER 5 DIFFRACTION AT THE VELOCITY REVERSAL

Wave propagation in media with a monotonic velocity increase has been studied in the last chapter. The medium response was found and evaluated both exactly (or rather as accurately as is numerically required) and asymptotically (analytically). Triplications and critical points are not the only ambiguous regions for interpretation of travel-time curves. Problems also arise when a discontinuity is present such as the shadow due to the core-mantle interface or low velocity zone at the top of the mantle. The shadow is caused by a sudden decrease in velocity that may be abrupt or continuous. This information cannot be found easily from the travel-time curves. The boundary between the illuminated region and shadow zone is not sharp even for a first order discontinuity in velocity structure. The diffracted signals propagating along the interface bring considerable amount of energy beyond the shadow boundary. In case of a continuous velocity decrease the amplitude of the signals decrease with distance so rapidly that a shadow is observed too. The amplitude decay of these signals into the shadow is very different from the decay into the "true" shadow. Only after amplitude studies can the nature of the velocity structure, which causes the shadow, be revealed.

The diffracted signal caused by a first order discontinuity has been studied by many authors (Scholte, 1956; Phinney and Alexander, 1966; Teng and Richards, 1969; Chapman and Phinney, 1972) although the interpretation of data is still uncertain (Phinney and Alexander, 1969; Bolt, 1970). This probably reflects regional differences in the core-mantle interface but may be caused by a velocity reversal just above the interface (Bolt, 1970). No thorough treatment of the velocity reversal seems to have appeared in the literature. In particular the non-geometrical nature of the shadow and the decay rate of the signal does not appear to be fully appreciated (Bolt, 1972).

The present chapter studies the wave propagation in Epstein medium with velocity maximum (Epstein, 1930). The results are compared to those obtained earlier for a parabolic profile and sharp velocity decrease.

5.1 The reflection coefficient for velocity reversal

Some of the properties mentioned in this section were studied previously by Epstein (1930), Phinney (1970) and their summary may be found in Budden (1961, p. 380) or Brekhovskikh (1960, p. 185). Some are included for the sake of completeness, others are essential for discussion of the response integral which none of the aforementioned authors attempted.

For Epstein profile with velocity maximum v_0 and velocities above and below the transition v_1 (Fig. 5.1), the vertical wave number (3.17) becomes

$$q^2 = q_1^2 - (q_1^2 - q_0^2) \operatorname{sech}^2 \frac{\zeta}{2\sigma} \quad (5.1)$$

The reflection and transmission coefficients are

$$R(\zeta_s, \zeta_r, \kappa) = - \frac{\Gamma(1+2i\sigma q_1)}{\Gamma(1-2i\sigma q_1)} \cdot \frac{\Gamma(\frac{1}{2}-2i\sigma q_1-\gamma)}{\Gamma(\frac{1}{2}-\gamma)} \cdot \frac{\Gamma(\frac{1}{2}-2i\sigma q_1+\gamma)}{\Gamma(\frac{1}{2}+\gamma)} e^{-i(q_s \zeta_s + q_r \zeta_r)} \quad (5.2)$$

$$T(\zeta_s, \zeta_t, \kappa) = \frac{2i\sigma q_1 \Gamma(\frac{1}{2}-2i\sigma q_1-\gamma) \Gamma(\frac{1}{2}-2i\sigma q_1+\gamma)}{\Gamma^2(1-2i\sigma q_1)} e^{-i(q_s \zeta_s - q_r \zeta_t)} \quad (5.3)$$

where for ρ constant

$$\gamma = \left\{ \frac{1}{4} - 4\sigma^2 \frac{\omega^2}{v_1^2} \left(1 - \frac{v_1^2}{v_0^2}\right) \right\}^{\frac{1}{2}} = \left\{ \frac{1}{4} - S^2 \cos^2 \theta_c \right\}^{\frac{1}{2}} \quad (5.4)$$

and θ_c is the critical angle $\theta_c = \sin^{-1} \frac{v_1}{v_0}$. Instead of the absolute measure of the thickness of the layer σ , the effective thickness $S = \frac{2\pi}{\lambda_1} \cdot 2\sigma$ is introduced. The reflection and transmission coefficients depend on the thickness of the layer σ as well as the wavelength of the propagating wave and the effective thickness S includes both effects.

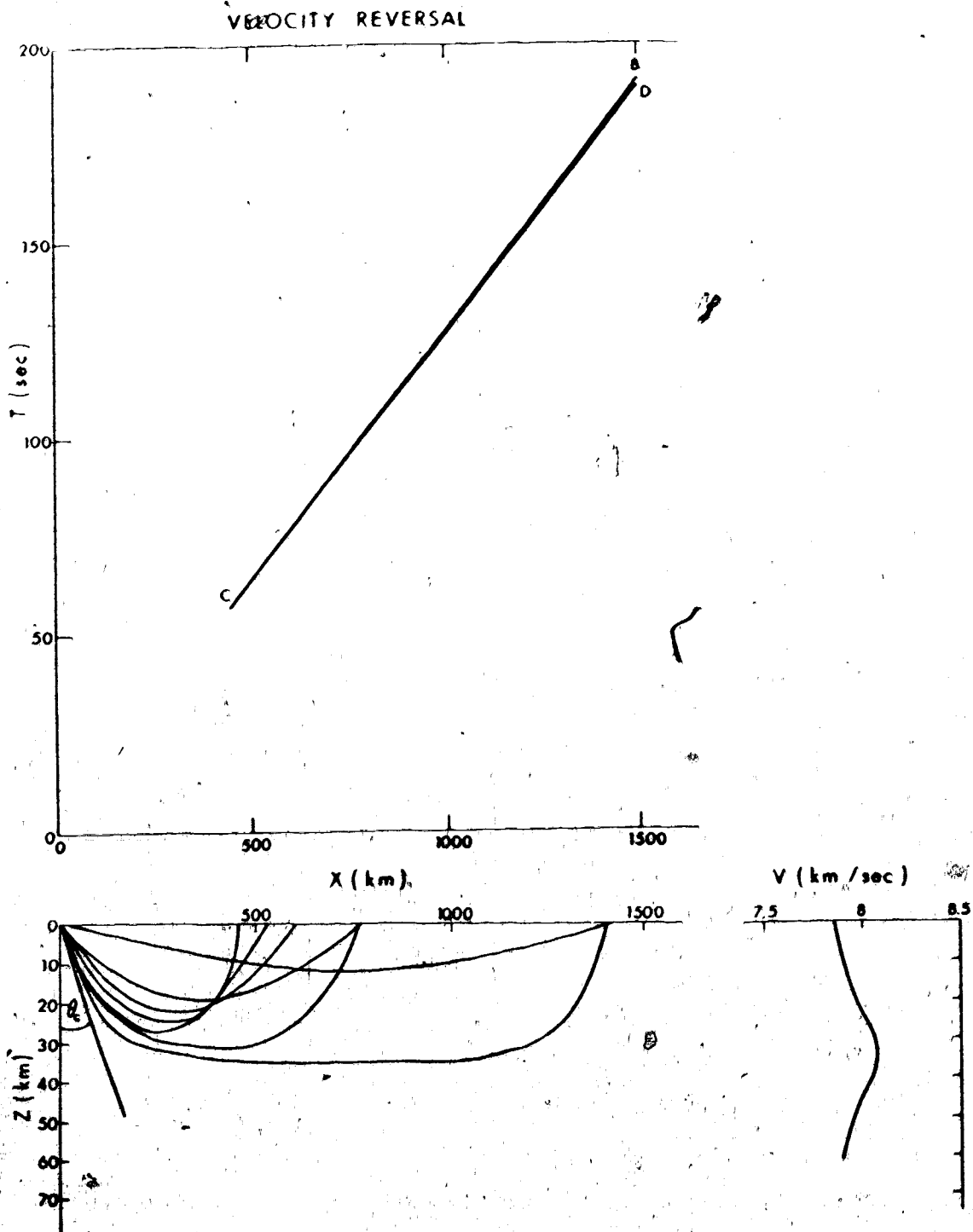


Figure 5.1 The travel-time curves and the rays propagating in the medium with velocity reversal.

The absolute values of the reflection and transmission coefficient are (Budden, 1961; p. 381)

$$|R| = \left\{ \frac{\cos 2\pi\gamma + 1}{\cos 2\pi\gamma + \cosh(2\pi S \cos \theta_1)} \right\}^{1/2} \quad (5.5)$$

$$|T| = \left\{ \frac{\cosh(2\pi S \cos \theta_1) - 1}{\cos 2\pi\gamma + \cosh(2\pi S \cos \theta_1)} \right\}^{1/2} \quad (5.6)$$

For thin layers or long wavelengths the effective thickness is small and the reflection is very weak.

$$S \rightarrow 0, \quad \gamma \rightarrow \frac{1}{2} \quad \text{and} \quad |R| \rightarrow 0 \\ |T| \rightarrow 1$$

For thick layers or short wavelengths when the effective thickness is large the amount of reflection depends on the emergent angle from the source θ_1 . (Brekhovskikh, 1960; p. 185)

$$S \rightarrow \infty, \quad \gamma = \frac{1}{2} \quad \text{and} \quad |R| \rightarrow 0, \quad |T| \rightarrow 1 \quad \text{if} \quad \sin \theta_1 < \frac{v_1}{v_0}$$

$$|R| = \frac{1}{\sqrt{2}}, \quad |T| = \frac{1}{\sqrt{2}} \quad \text{if} \quad \sin \theta_1 = \frac{v_1}{v_0}$$

$$|R| \rightarrow 1, \quad |T| \rightarrow 0 \quad \text{if} \quad \sin \theta_1 > \frac{v_1}{v_0}$$

At angles θ_1 less than critical most energy is transmitted while at angles of emergence greater than θ_c most energy is reflected. The range of angles when both, the reflection and the transmission, occur depends on the effective thickness (Fig. 5.2). The boundary between total transmission and total reflection is blurred by partial reflection at sub-critical angles and tunnelling effects at angles beyond critical. Both partial reflection and transmission by tunnelling increase as the effective thickness decrease.

$$\begin{aligned}
 |R| &\sim e^{-\pi S(\cos \theta_1 - \cos \theta_c)} & \theta_1 < \theta_c \\
 |T| &\sim e^{-\pi S(\cos \theta_c - \cos \theta_1)} & \theta_1 > \theta_c
 \end{aligned}
 \tag{5.7}$$

At this point it is desirable to point out the advantage of the Epstein profile over the parabolic profile in Fig. 5.3. The solutions of the wave equation for a parabolic velocity structure

$$v = v_0 + \frac{v_0''}{2} \cdot \zeta^2
 \tag{5.8}$$

can be expressed in terms of parabolic cylinder functions (Phinney, 1970). Then the reflection coefficient is

$$|R| = \frac{e^{\pi a^*}}{\sqrt{1 + e^{2\pi a^*}}}
 \tag{5.9}$$

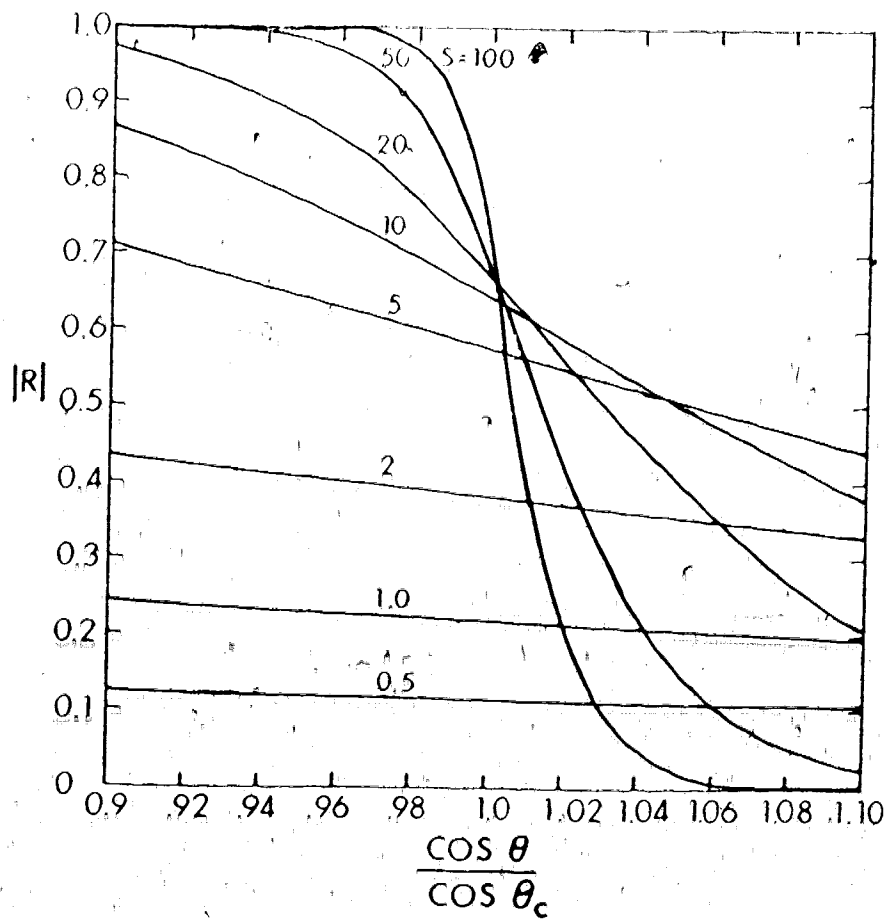


Figure 5.2 The dependence of the modulus of the reflection coefficient on the effective thickness of the "sech²" layer for $v_1 = v_2 = 7.83$ km/s, $v_0 = 8.05$ km/s.

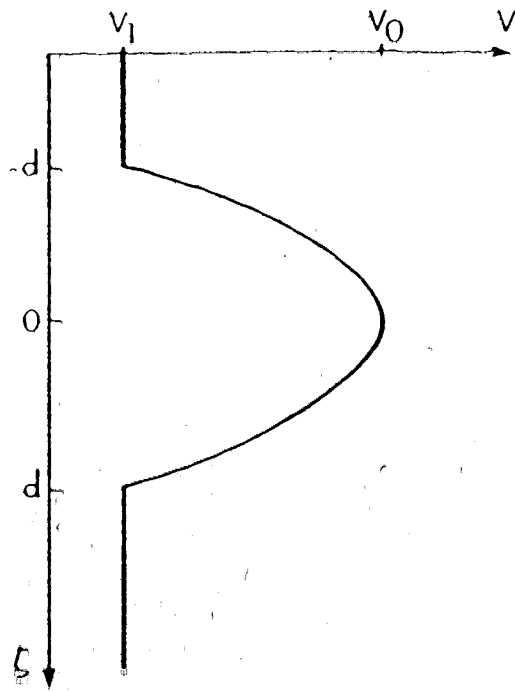


Figure 5.3 Parabolic velocity profile;

$$d = \left| \frac{2}{n} \right|^{1/2} v_0$$

where a^* is a complex conjugate of

$$a = \frac{1}{2} \cdot \frac{k^2(\bar{z})}{k_0} \cdot \left(\frac{v_0}{v_{ii}}\right)^{1/2} \left(\sin^2 \bar{\theta} - \frac{v^2(\bar{z})}{v_0^2}\right) \quad (5.10)$$

and $\sigma_p = \left|\frac{v_0}{v_{ii}}\right|^{1/2}$ is so-called half-thickness of the parabolic layer. The reflection coefficient (5.9) was first deduced by Rydbeck (1943) for propagation of waves in the ionosphere. It is evident that it does not give correct answers for thin layers ($\frac{\sigma_p}{\lambda} \rightarrow 0$) which is $R \sim 0$ rather than $R \sim \frac{1}{\sqrt{2}}$. This discrepancy is caused by discontinuities of the velocity gradient on the boundaries of the layer. Northover (1962) found a power series solution for thin parabolic layers which yields the correct reflection coefficient. His results were recently confirmed by Chesell (1971) who determined the reflection coefficient by exact numerical integration of the wave equation (Fig. 5.4). Northover (1962) criticizes the method of matching the solution above and below the transition zone in order to satisfy the boundary conditions. While partly justified in the case of the parabolic layer solved by Rydbeck (1943), his criticism does not apply to the Epstein models. The latter has no gradient discontinuity and no additional conditions have to be satisfied. The correct values of the reflection coefficient (5.5) at different limiting cases prove that the method of matching

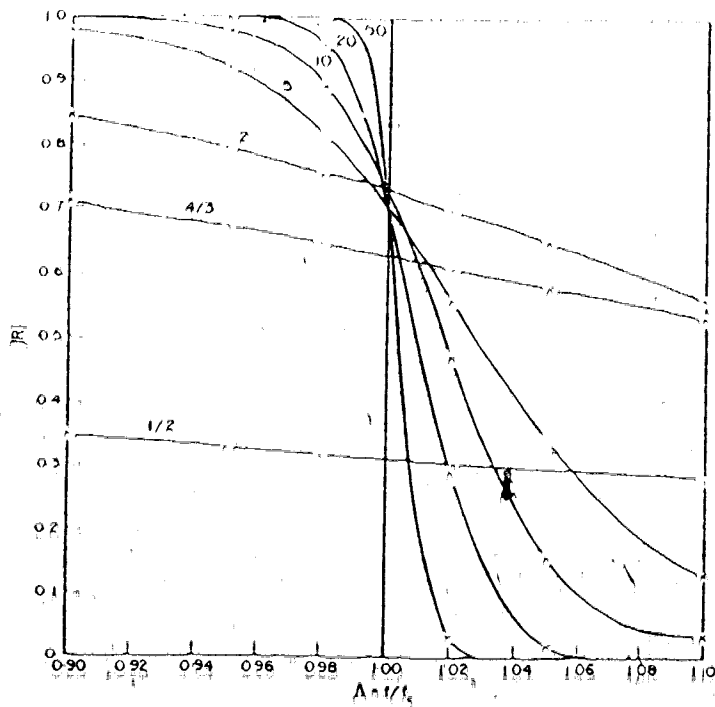


Figure 5.4 Variation of the modulus of the reflection coefficient with frequency for parabolic layers of different effective thickness $\mu = \frac{2\pi\sigma_p}{\lambda_c}$. f_c and λ_c are the critical frequency and wavelength of the ionospheric layer (from Chessell, 1971).

the solutions may be used in Epstein's problem. It can only be used in a limited range of frequencies and thicknesses for the parabolic layer. Subject to the aforementioned constraints the reflection coefficient (5.9) gives useful results.

In the complex κ plane the reflection coefficient (5.2) has three sets of poles due to the gamma functions and six branch points $\pm\kappa_1 = \pm\frac{\omega}{v_1}$, $\pm\kappa_s = \pm\frac{\omega}{v_s}$ and $\pm\kappa_r = \pm\frac{\omega}{v_r}$. Of total number eight only two of the Riemann surfaces are important in our discussions. The branch cuts from κ_p to $-\kappa_p$ via infinity, $p = 1, s$ or r , are very close to each other and the top (+) and the bottom (-) sheets of q_1 are taken in agreement with the convention introduced in Section 4.1.

The secular equations that determine the position of the poles are

$$2i\sigma q_1 = -n \quad n = 1, 2, 3, \dots \quad (a)$$

$$2i\sigma q_1 = n + \frac{1}{2} + \gamma \quad n = 0, 1, 2, 3, \dots \quad (b)$$

$$2i\sigma q_1 = n + \frac{1}{2} - \gamma \quad n = 0, 1, 2, 3, \dots \quad (c)$$

(5.11)

The sets of poles are given by (5.11a)

$$\pm \kappa_n = \pm \left(\frac{\omega^2}{v_1^2} + \frac{n^2}{4\sigma^2} \right)^{\frac{1}{2}} \quad (5.12)$$

are on the top Riemann sheet "beyond" the branch points $\pm \frac{\omega}{v_1}$. (Fig. 5.5a). The signals arising from the contribution of these poles propagate in horizontal direction and decay exponentially with depth. Their phase velocity

$$c = v_1 \left(1 + \frac{n^2 v_1^2}{4\sigma^2 \omega^2} \right)^{-\frac{1}{2}}$$

is smaller than v_1 and they arrive to the receiver much later than signals we are interested in.

The sets of poles given by (5.11b) are

$$\pm 2\kappa_n = \pm \left[\frac{\omega^2}{v_1^2} + (n + \frac{1}{2} + \gamma)^2 / 4\sigma^2 \right]^{\frac{1}{2}} \quad (5.13)$$

At low frequencies when γ is real the poles lie on the real axis "beyond" the branch points $\pm \frac{\omega}{v_1}$ on the lower Riemann sheet (Fig. 5.6b). The zero frequency position is

$$\pm 2\kappa_n^0 = \pm \frac{n+1}{2\sigma} \quad (5.14)$$

As frequency increases they move towards the branch points.

At frequency ω^*

$$\omega^* = \frac{v_1}{4\sigma} \sec \theta_c \quad (5.15)$$

they are in position.

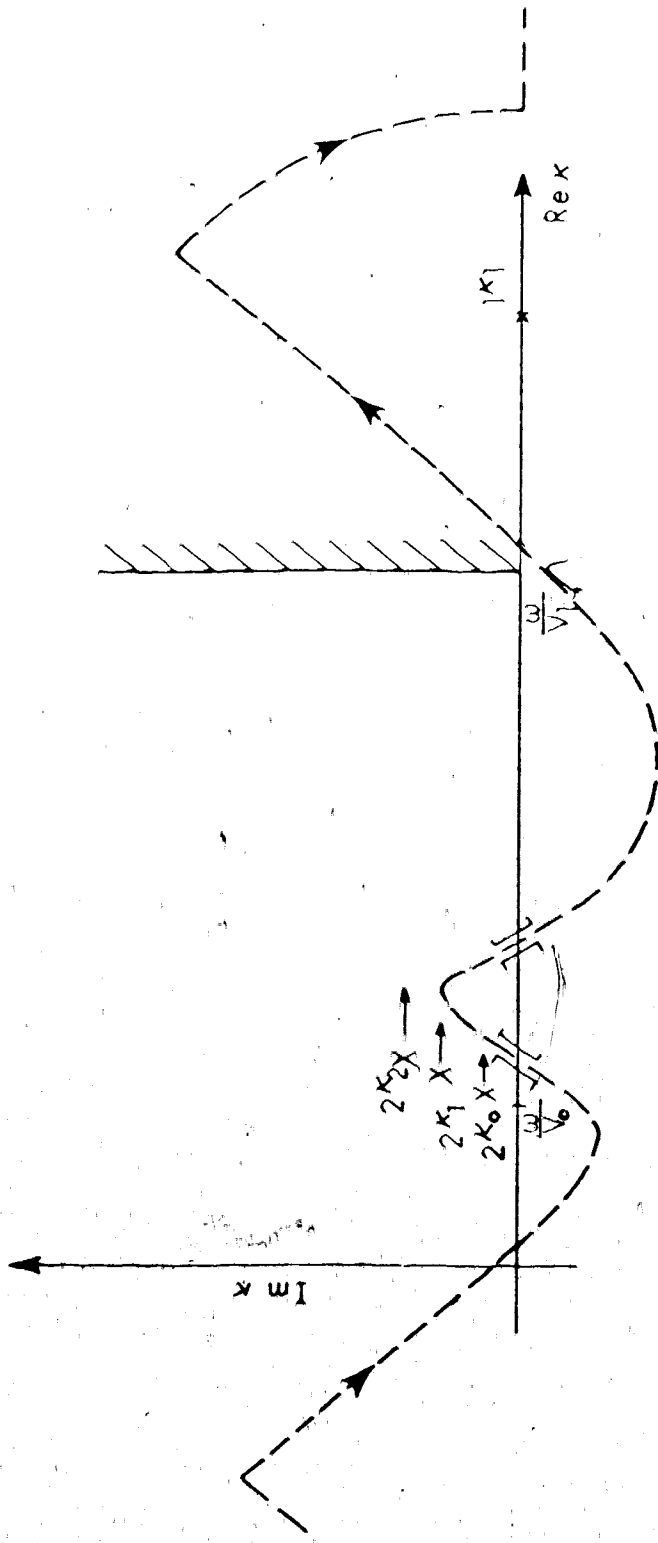


Figure 5.5a The high frequency positions of the poles λ_k , $n=0,1,2$ on the top Riemann sheet of the complex x plane. The arrows show the direction of the movement of the poles as frequency decreases. The saddle points and the distorted contour are also indicated.

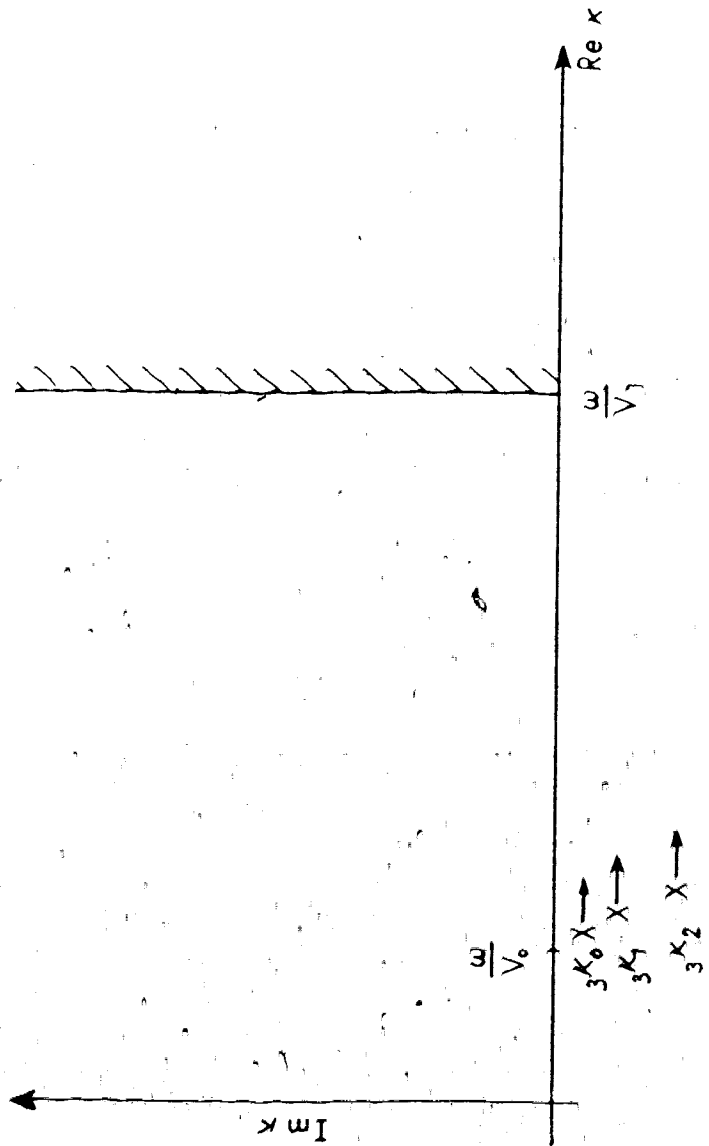


Figure 5.5b The high frequency positions of the poles $3^k X$, $n=0, 1, 2$ on the bottom Riemann sheet of the complex k plane. The arrows indicate the movement of the poles as frequency decreases.

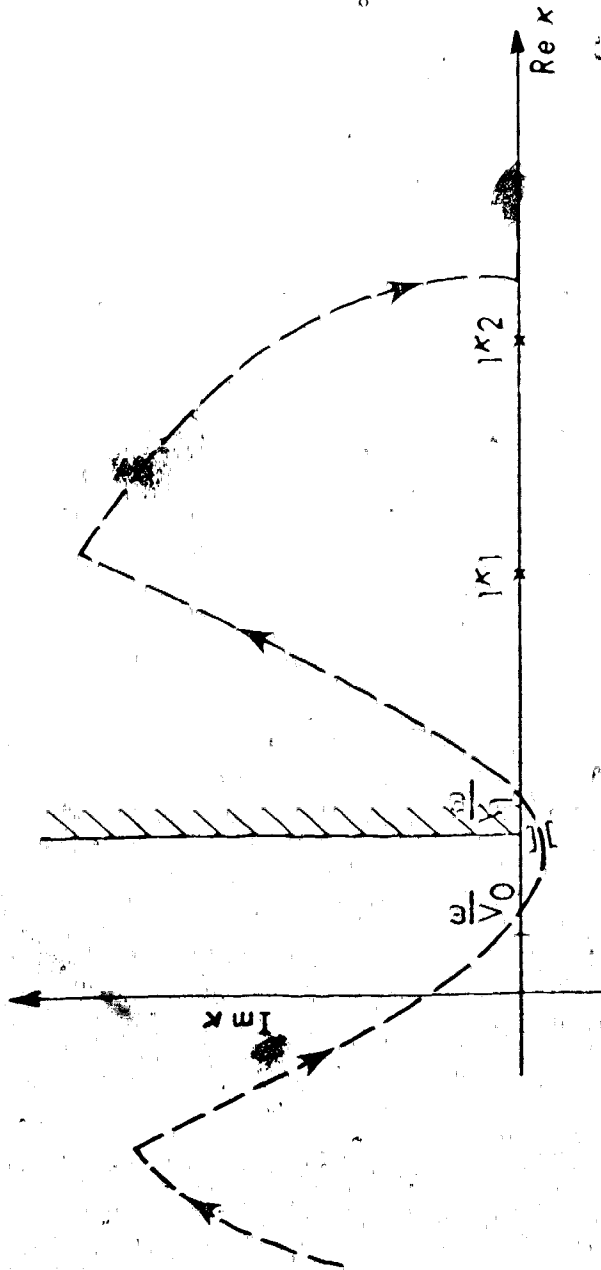


Figure 5.6a The poles' positions on the top Riemann sheet of the complex x plane for low frequencies. The distorted contour of integration is also shown.

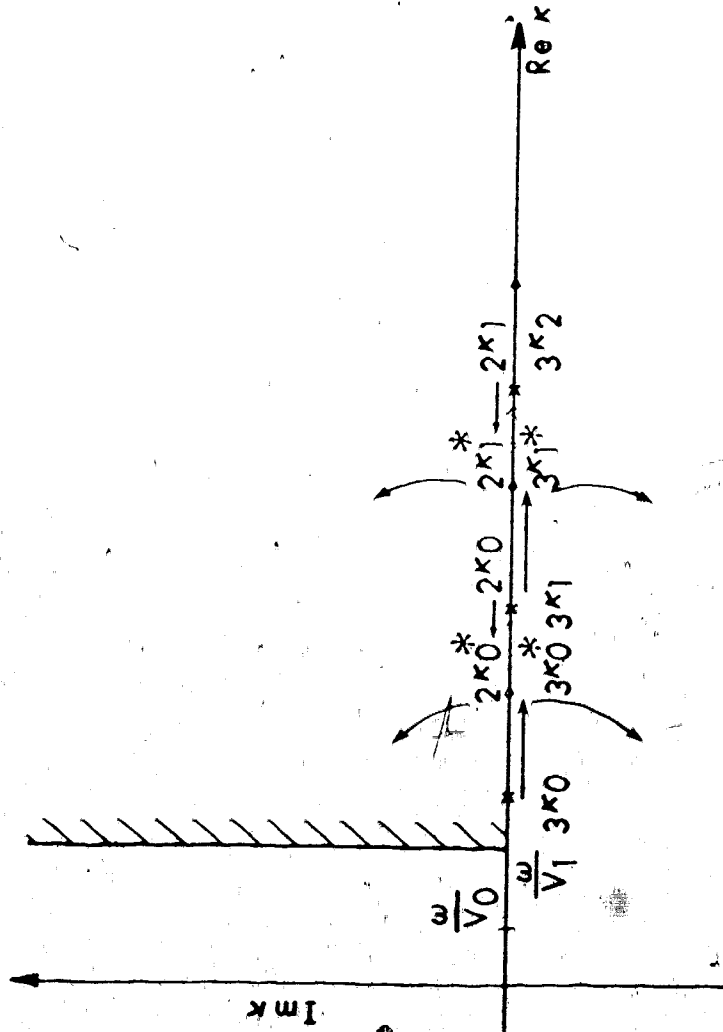


Figure 5.6b The poles' positions on the bottom Riemann sheet of the complex k plane for low frequencies. The arrows indicate the direction of the movement of the poles as frequency increases.

$$\pm \frac{1}{2} \kappa_n^* = \pm \left[\frac{\omega^2}{v_1^2} + (n + \frac{1}{2})^2 / 4\sigma^2 \right]^{\frac{1}{2}} \quad (5.16)$$

and they leave the real axis. As frequency increases they move anticlockwise in the first and third quadrants of the lower Riemann sheet, their real part decreasing in absolute value and imaginary part increasing in absolute value. They reach the branch cut where $|\operatorname{Re} \kappa_n| \sim \frac{\omega}{v_1}$ and pass onto the top Riemann sheet. Then they continue to move towards the high frequency position where they slow down and "settle" at

$$\pm \frac{1}{2} \kappa_n = \pm \left[\frac{\omega^2}{v_0^2} + \left\{ (n + \frac{1}{2})^2 + \frac{1}{4} \right\} / 4\sigma^2 + 1 - (n + \frac{1}{2}) \frac{S_c}{4\sigma^2} (\cos^2 \theta_c - \frac{1}{4S^2})^{\frac{1}{2}} \right]^{\frac{1}{2}} \quad (5.17)$$

(Fig. 5.5a). The complex poles on the top Riemann sheet contribute to signals propagating with phase velocity between v_1 and v_0 and are important in the evaluation of the response integral. Only the poles in the first quadrant contribute, however, as they are close to the steepest descent path. Further discussion of the behaviour of the reflection coefficient in the neighbourhood of these poles is left to the next section.

The two sets of poles given by (5.11c) are

$$\pm \frac{3}{2} \kappa_n = \pm \left[\frac{\omega^2}{v_1^2} + (n + \frac{1}{2} \pm \gamma)^2 / 4\sigma^2 \right]^{\frac{1}{2}} \quad (5.18)$$

and they lie on the lower Riemann sheet. Their zero frequency positions are

$$\pm 3^{\kappa_n^0} = \pm \frac{n}{2\sigma} \quad (5.19)$$

As frequency increases the poles move along the real axis away from the branch points. As $\omega = \omega^*$ they reach the position $2^{\kappa_n^*}$ and coalesce with the set of poles 2^{κ_n} (5.13). They leave the real axis in the direction opposite to that of 2^{κ_n} and move clockwise in the second and fourth quadrants of the lower Riemann sheet. (Fig. 5.6b). As high frequency limit is approached, their movement slows down and they settle at positions

$$\pm 3^{\kappa_n} = \pm \left[\frac{\omega^2}{v_0^2} + [(n+\frac{1}{2})^2 + \frac{1}{4}] \cdot \frac{1}{4\sigma^2} - 1(n+\frac{1}{2}) \frac{S}{4\sigma^2} (\cos^2 \theta_c - \frac{1}{4S^2})^{\frac{1}{2}} \right]^{\frac{1}{2}} \quad (5.20)$$

(Fig. 5.5b). The poles $3^{\kappa_n^0}$, being on the bottom sheet, have no effect on the reflection coefficient and no signals arise from their contribution.

5.2 The response integral

The rays most effected by the velocity reversal are those emerging at angles close to critical angle θ_c . The response integral (2.22) for the velocity reversal where density is constant is

$$P(\omega, r, z_r) = \frac{1}{4} P_S(\omega) \int_{-\infty}^{+\infty} R(z_S, z_r, \kappa) H_0^{(1)}(\kappa r) \frac{\kappa}{q_S} d\kappa \quad (5.21)$$

where $R(z_S, z_r, \kappa)$ is the reflection coefficient given by (5.2). At high frequencies the same method of evaluation can be used as that used previously for the monotonic velocity transition (see Section 4.3). The reflection coefficient can be approximated by the WKBJ reflection coefficient (4.17) and its phase is

$$\phi(\kappa) = 2\alpha q_1 \log \frac{4\alpha^2 q_1^2}{((\frac{1}{2} - 2i\sigma q_1)^2 - \gamma^2)} - i\gamma \log \frac{(\frac{1}{2} - 2i\sigma q_1 + \gamma)(\frac{1}{2} - \gamma)}{(\frac{1}{2} - 2i\sigma q_1 - \gamma)(\frac{1}{2} + \gamma)} - q_S z_S - q_r z_r \quad (5.22)$$

The point of stationary phase of the integrand κ^* is given by the condition

$$r + \frac{d\phi}{d\kappa} = 0 \quad (5.23)$$

where

5.2 The response integral

The rays most effected by the velocity reversal are those emerging at angles close to critical angle θ_c . The response integral (2.22) for the velocity reversal where density is constant is

$$P(\omega, r, \zeta_r) = \frac{1}{4} P_S(\omega) \int_{-\infty}^{+\infty} R(\zeta_s, \zeta_r, \kappa) H_0^{(1)}(\kappa r) \frac{\kappa}{q_s} d\kappa \quad (5.21)$$

where $R(\zeta_s, \zeta_r, \kappa)$ is the reflection coefficient given by (5.2). At high frequencies the same method of evaluation can be used as that used previously for the monotonic velocity transition (see Section 4.3). The reflection coefficient can be approximated by the WKBJ reflection coefficient (4.17) and its phase is

$$\phi(\kappa) = 2\sigma q_1 \log \frac{4\sigma^2 q_1^2}{((\frac{1}{2} - 2i\sigma q_1)^2 - \gamma^2)} - i\gamma \log \frac{(\frac{1}{2} - 2i\sigma q_1 + \gamma)(\frac{1}{2} - \gamma)}{(\frac{1}{2} - 2i\sigma q_1 - \gamma)(\frac{1}{2} + \gamma)} - q_s \zeta_s - q_r \zeta_r \quad (5.22)$$

The point of stationary phase of the integrand κ^* is given by the condition

$$r + \frac{d\phi}{d\kappa} = 0 \quad (5.23)$$

where

$$\frac{d\phi}{d\kappa} = -2\sigma \frac{\kappa}{q_1} \log \frac{4\sigma^2 q_1^2}{((\frac{1}{2} - 2i\sigma q_1)^2 - \gamma^2)} - \frac{2\sigma\kappa(\frac{1}{2} - 2i\sigma q_1)}{q_1((\frac{1}{2} - 2i\sigma q_1)^2 - \gamma^2)} +$$

$$+ \frac{\kappa}{q_s} \zeta_s + \frac{\kappa}{q_r} \zeta_r \quad (5.24)$$

The equation (5.23) must be solved numerically for complex κ . This gives two saddle points very close to the real κ axis between $\kappa_0 = \frac{\omega}{v_0}$ and $\kappa_1 = \frac{\omega}{v_1}$ if the horizontal distance is greater than λ_C . There are two arrivals at these distances (Fig. 5.1) which at high frequencies are represented by two aforementioned saddle points. The saddle point close to $\frac{\omega}{v_0}$ represents the ray close to the critical ray and is most affected by the velocity reversal while the other represents the ray reflected by the large velocity gradient (Fig. 5.5a).

The amplitude at the saddle point κ^* is proportional to

$$\left| \frac{dr}{d\kappa} \right|_{\kappa^*}^{-1/2} = \left| \frac{d^2\phi}{d\kappa^2} \right|_{\kappa^*}^{-1/2} \quad (5.25)$$

where

$$\frac{d^2\phi}{d\kappa^2} = -\frac{\omega^2}{v_1^2} \frac{2\sigma}{q_1} \left(\log \frac{4\sigma^2 q_1^2}{((\frac{1}{2} - 2i\sigma q_1)^2 - \gamma^2)} + \frac{(\frac{1}{2} - 2i\sigma q_1)}{((\frac{1}{2} - 2i\sigma q_1)^2 - \gamma^2)} \right) + \frac{4\sigma\kappa^2}{q_1} +$$

$$+ \frac{16\sigma^3 \kappa^2}{q_1((\frac{1}{2} - 2i\sigma q_1)^2 - \gamma^2)} + \frac{8i\sigma^2 \kappa^2 (\frac{1}{2} - 2i\sigma q_1)^2}{((\frac{1}{2} - 2i\sigma q_1)^2 - \gamma^2)^2} + \frac{\omega^2}{v_s^2} \frac{\zeta_s}{q_s} + \frac{\omega^2}{v_r^2} \frac{\zeta_r}{q_r} \quad (5.26)$$

At high frequencies the saddle point approximation gives the response

$$P(\omega, r, t_r) = \frac{P_s(\omega)}{2\sqrt{2\pi}} \frac{\kappa^{*1/2} e^{i\kappa^* r + i\phi(\kappa^*)}}{q_s \left\{ r \cdot \frac{dr}{d\kappa} \Big|_{\kappa^*} \right\}^{1/2}} \quad (5.27)$$

for the wave propagating along the reversal. The saddle point approximation for the reflected wave is

$$P(\omega, r, t_r) = -i \frac{P_s(\omega)}{2\sqrt{2\pi}} \frac{\kappa^{*1/2} e^{i\kappa^* r + i\phi(\kappa^*)}}{q_s \left\{ -r \cdot \frac{dr}{d\kappa} \Big|_{\kappa^*} \right\}^{1/2}} \quad (5.28)$$

The geometrical arrival time is given by

$$T = \frac{1}{\omega} \operatorname{Re}\{\kappa^* r + \phi(\kappa^*)\} \quad (5.29)$$

The second order saddle point approximation fails near the caustic C (Figure 5.1). In its vicinity the same treatment as that described in detail in Section 4.3 can be used to obtain the high frequency approximation in terms of Airy function. The behaviour in the caustic region was investigated in Chapter 4 while in this chapter the attention is concentrated on the effect of the velocity maximum on the wave propagation. As the angle of emergence $\theta_1 > \theta_c$ approaches the critical angle the ray travels further in the region of the reversal and its

amplitude decays. The saddle point which is the approximation of this ray at high frequencies approaches the zeroth pole in the string, 2^{κ_n} (5.13). The contribution from the integration through the saddle point becomes equivalent to that of the residue of the zeroth pole (Fig. 5.7). The amplitude given by the residue of the zeroth order pole decays exponentially when r is large (Appendix C).

$$P(\omega, r, \zeta_r) \approx \frac{P_s(\omega)}{40} \frac{q_{10}}{q_{s0}} \frac{e}{\sqrt{2^{\kappa_0} r}} \cdot e^{i 2^{\kappa_0} r + i \frac{\pi}{4} - i q_{s0} \zeta_s - i q_{r0} \zeta_r} \cdot e^{\frac{1}{2} r \log \frac{(\frac{1}{2} + \gamma)^2}{-2\gamma} + 2\gamma \log \frac{(\frac{1}{2} - \gamma)}{2\gamma}} \quad (5.30)$$

where $q_{p0} = \left(\frac{\omega^2}{v_1^2} - 2^{\kappa_0} \right)^{\frac{1}{2}}$ for $p = 1, s$ or r

The decay rate of the signal is given by the imaginary part of the zeroth pole. To first order in frequency

$$\text{Im } 2^{\kappa_n} \approx (n + \frac{1}{2}) \frac{v_0}{v_1} \frac{1}{2\sigma} \left(\left(1 - \frac{v_0^2}{v_1^2} \right) - \frac{1}{4S^2} \right)^{\frac{1}{2}} \quad (5.31)$$

Thus the decay rate at high frequencies is independent of frequency. The dashed line in Figure 5.8 represents the residue evaluation of the response integral (5.21). When the numerical integration was computed for this signal separately, the amplitude curves coincided with this line at frequencies $\omega \geq 8$ for distances $X = r \geq 700$ km.

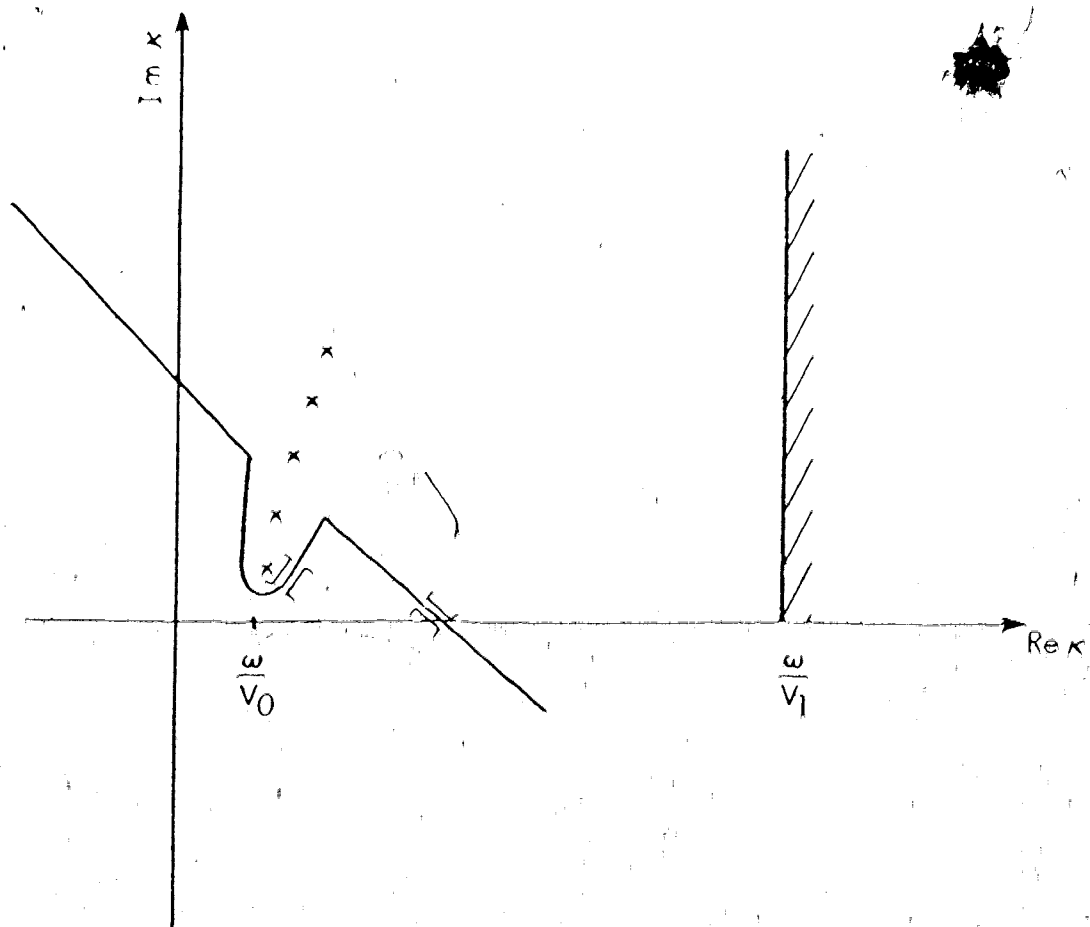


Figure 5.7 The steepest descent path in the complex κ plane for large horizontal distances. The crosses indicate the poles κ_n , $n=0, 1, 2, 3, 4$.

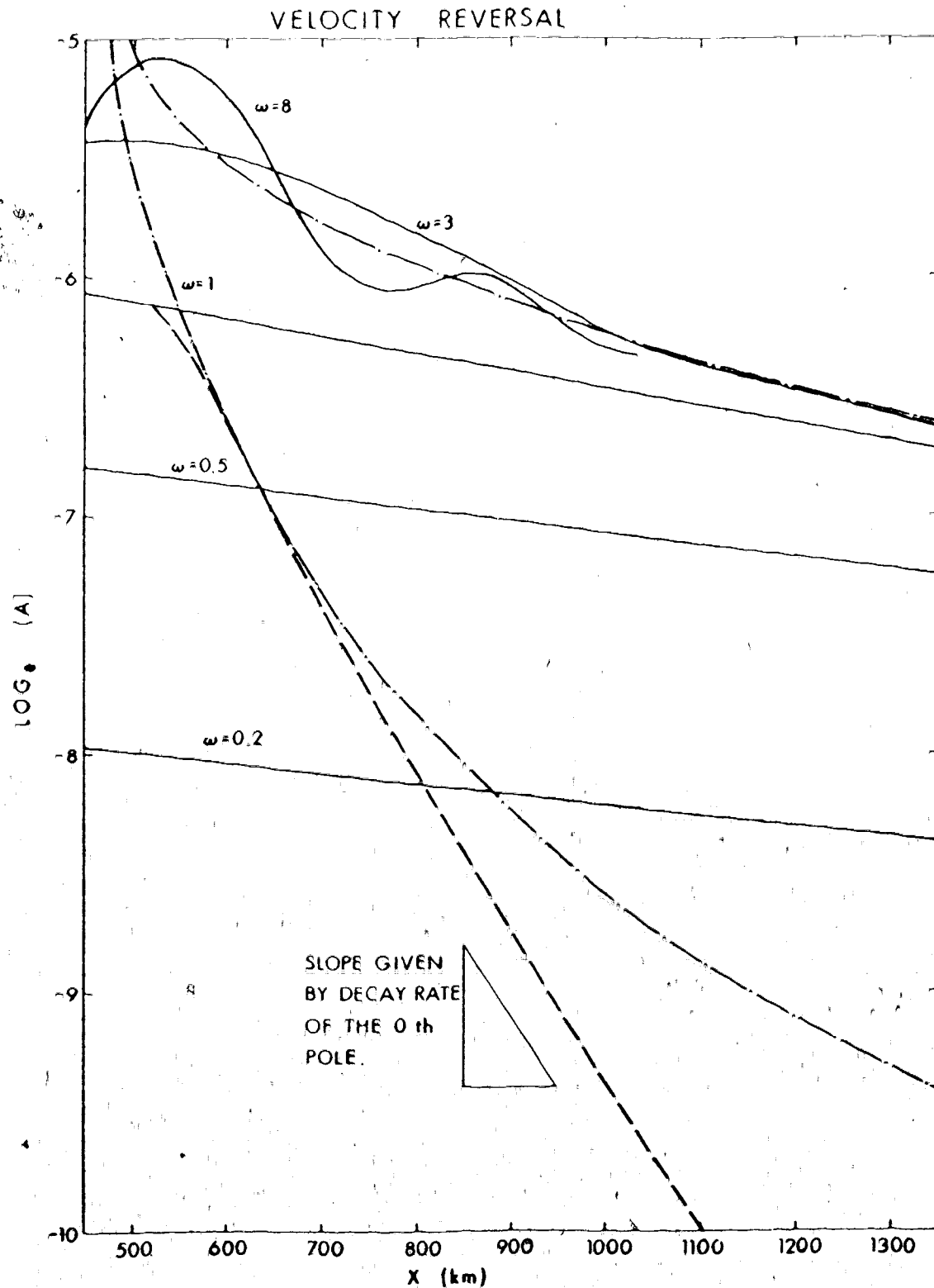


Figure 5.8 The amplitude curves evaluated numerically for different frequencies (full lines). The geometrical amplitudes from the saddle point evaluation (chained lines) and the residue of the zeroth pole (broken line) are also indicated.

Chapman (1969) studied the decay rate of rays effected by the parabolic velocity reversal (5.8). Then the reflection coefficient has poles at

$$k_n = \frac{\omega}{v_0} + i \left| \frac{v_0''}{v_0} \right|^{\frac{1}{2}} (n + \frac{1}{2}) \quad (5.32)$$

and the decay of the low order poles

$$\sim e^{-r \left| \frac{v_0''}{v_0} \right|^{\frac{1}{2}} (n + \frac{1}{2})}$$

also independent of frequency. Both profiles have the same curvature at the maximum if

$$v_0'' = - \frac{1}{v_0} \frac{v_0^2}{4\sigma^2} \left(\frac{v_0}{v_1} - 1 \right) \quad (5.33)$$

and the decay of the amplitudes with growing distance is identical then. This result could be anticipated as these rays are effected mainly by the velocity structure at the maximum. Chapman (personal communication) showed, that the geometrical amplitude given by $\left| r \frac{dr}{dK} \right|^{-\frac{1}{2}}$ reduces to the same exponential decay as that given by the zeroth order pole.

It can be said that due to the rapid decay of the amplitudes a "shadow" is observed. Although the signals are present their amplitude is so small that they cannot be detected. Thus the "shadow" caused by the velocity reversal is very different from the real shadow caused by an interface when no rays

propagate beyond the shadow boundary.

The signals near a real shadow caused by an interface are diffracted signals grazing the interface. These diffracted signals propagate along the interface and emerge at distances beyond the shadow boundary given by the grazing ray and, therefore, blur the shadow boundary. Their contribution is obtained from the residues at the poles of the coefficient of reflection from the interface. Duwalo and Jacobs (1959) found the approximate positions of the low order poles for a model of a fluid sphere in a homogeneous medium. Their result (in spherical coordinates R, θ, ϕ)

$$v_p = k_\alpha R_c \left(1 + \frac{1}{2}(4p + c)\right)^{2/3} \left(\frac{3\pi}{4k_\alpha R_c}\right)^{2/3} e^{i\frac{\pi}{3}}$$

gives a decay constant proportional to $\omega^{1/3}$. (v is the wavenumber in θ direction i.e. equivalent to K in our case; R_c is the radius of the sphere and $k_\alpha = \frac{\omega}{\alpha(R_c)}$ is the wavenumber at the surface of the sphere.) The position of poles is slightly modified if a layered or inhomogeneous medium is assumed (Phinney and Alexander, 1966, 1969, respectively) but the asymptotic frequency dependence remains unchanged. The constant c depends on the boundary conditions and for the models just mentioned $|c| \leq 1$. It is, however, rather difficult to find c analytically. Chapman (1969) also gives useful approximate expressions for positions of poles when

the parabolic velocity reversal lies near an interface. Then the decay rate depends on the relative position of the interface and the reversal and on the frequency range considered.

The diffracted signals propagating along the interface or velocity reversal are mathematically given by contribution from poles of the reflection coefficient. The discontinuity on the travel-time curve due to the shadow can only be interpreted correctly when the amplitudes are analysed. The frequency dependent amplitude decay is basically different from the frequency independent decay due to the reversal.

At short distances the evaluation of the integral by method of residues is not valid (Appendix C) and the high frequency approximation is given by (5.27) indicated by the chained line in Figure 5.8. This can be called the "illuminated" region in analogy to the case of an interface shadow for which the residue evaluation is not valid either before the shadow boundary. The region when the saddle point evaluation (5.27) is not a good approximation due to the poles' influence, and the high frequency approximation is given by residues (5.30), can be considered a "shadow". As frequency decreases the poles' positions become frequency dependent and both approximations become invalid and the response integral must be evaluated numerically. Its values are shown in Figure 5.8 in dependence on range $r = X$. The

oscillatory character of the total amplitude for $\omega = 8$ is given by the interference of the two waves arriving at the receiver almost together near the cusp C (Fig. 5.1). The amplitude oscillates around the geometrical values (5.28) of the wave reflected by the velocity gradient. These waves form the reversed branch of the travel-time curve in Figure 5.1 and are much stronger than the waves propagating along the reversal whose geometrical amplitude at large ranges is given by the pole's contribution (5.30). These come to the receiver earlier than the reflected waves and form the forward branch CD. All the amplitudes for frequencies larger than $\omega = 8$ oscillate around the geometrical value of the reflected wave. For frequencies $\omega < 3$ the total amplitude is smaller than the geometrical value and decreases rather rapidly with frequency. The transmission of the energy through the velocity barrier increases at low frequencies and the amount of reflection decreases.

The results of this chapter indicate that "diffraction" at velocity reversals depends entirely on the velocity structure near the maximum. The "shadow" is caused by large geometrical spreading along the ray path. Using the geometrical ray theory, Chapman (personal communication) has shown that its growth is exponential. This is confirmed by the results of the full wave theory presented in this section. The

equivalence of the parabolic and "sech²" profiles is a very encouraging conclusion as it gives us a tool for investigation of shadow caused by more complex structures. Provided the "sech²" profile has the same curvature as the part of the complicated velocity structure that causes the shadow, the amplitude decay should be equivalent.

5.3 Synthetic seismograms

The parameters of the Model II which was used to compute the amplitude curves in Figure 5.8 are:

$$\begin{aligned}
 v_1 &= v_2 = 7.83 \text{ km/s} \\
 v_0 &= 8.05 \text{ km/s} \\
 \sigma &= 10 \\
 z_0 &= 35 \text{ km} & z_s = z_r = 0 \text{ km} \\
 \rho &= \text{constant}
 \end{aligned}
 \tag{5.34}$$

The velocities were chosen close to velocities at the top of the low velocity zone in the Earth's mantle.

Theoretical seismograms in Figures 5.9 and 5.10 were computed using the method described in Section 4.4. First the response integral (5.21) was calculated by numerical contour integration for 8 frequencies ranging from $\omega = .5$ rad/sec to $\omega = 30$ rad/sec. From $\omega = 60$ rad/sec to $\omega = 110$ rad/sec the high frequency approximations were used. For the reflected

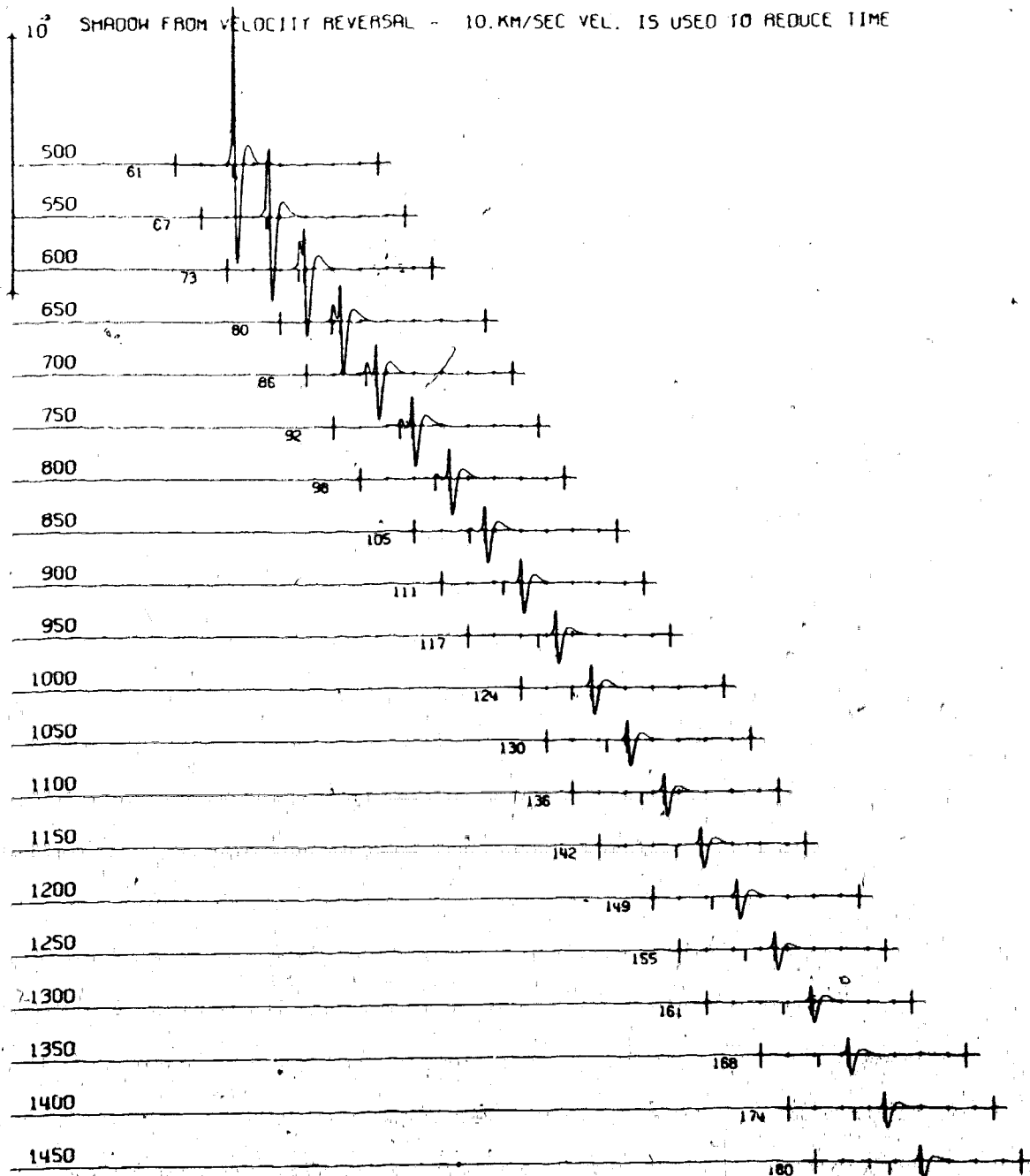


Figure 5.9 The synthetic seismograms for the Model II normalized with respect to the Airy phase amplitude at $X = 500$ km. Marks on the time scale are every second and the geometrical arrival times are indicated by longer vertical marks.

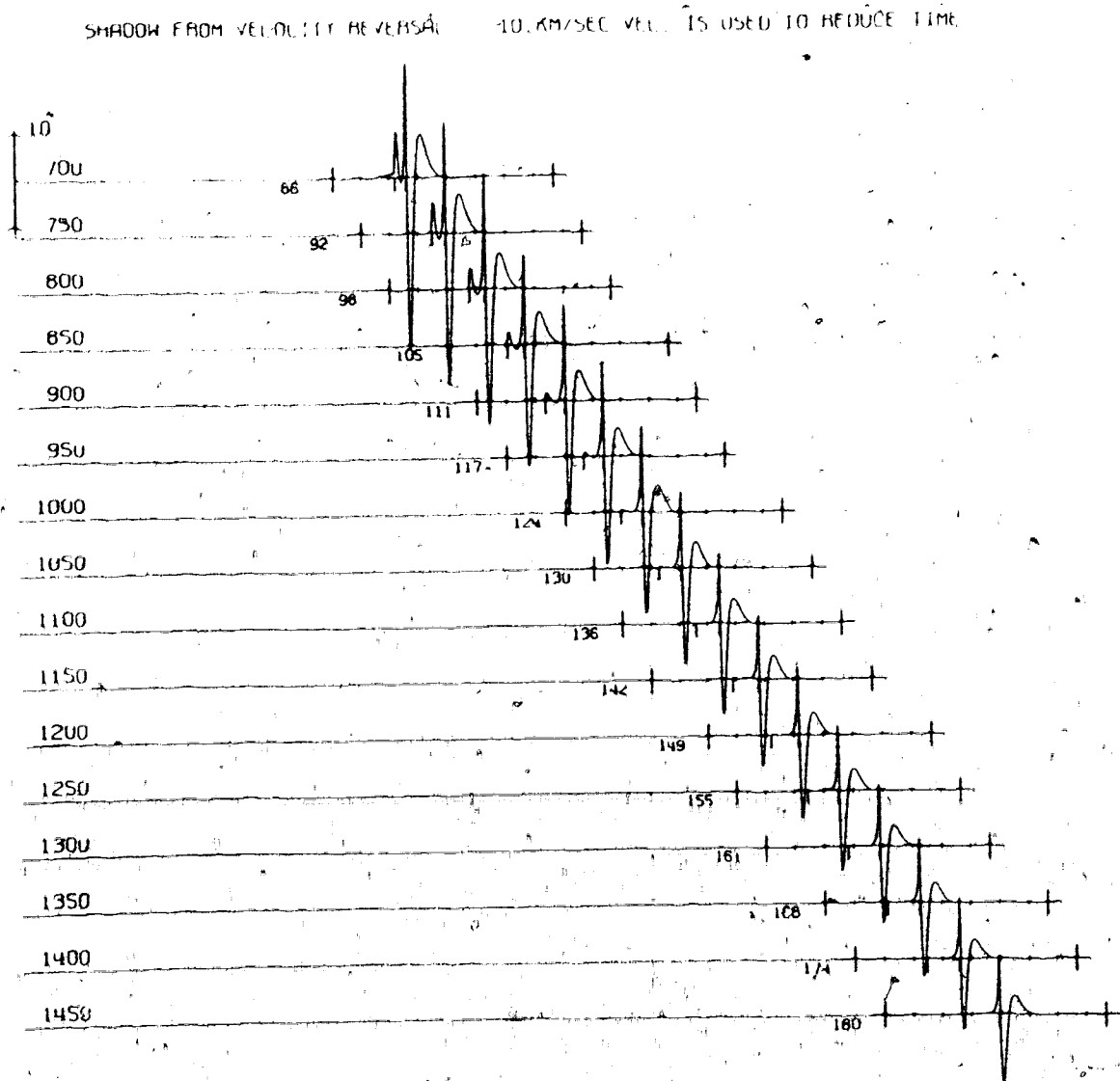


Figure 5.10 The synthetic seismograms for the Model II normalized with respect to the amplitude at $X = 700$ km. (Time scale as in Figure 5.9.)

wave (5.28) was calculated for all distances. The amplitude of the "diffracted" wave (or wave propagating along the reversal) was approximated by (5.27) when $r = x < 650$ km and by (5.30) when $r = x > 650$ km. 17 spectral values were interpolated using cubic spline to obtain the complete spectrum (Section 4.4). The unit step function source $P_s(t) = H(t)$ and the transfer function of a seismometer given by (4.59) was assumed. Their convolution gives the spectrum in Figure 4.23 and the response of the seismometer to $P_s(t)$ is in Figure 4.24.

The synthetic seismograms in Figures 5.9 and 5.10 show clearly the rapid decay of the first arriving wave that propagates along the maximum. The seismograms in Figure 5.9 are normalized with respect to the maximum amplitude at $x = 500$ km given by the Airy phase due to caustic C in Figure 5.1. The marks on the time scale are every second and the geometrical arrivals are marked by longer vertical marks. The first arrival at $x = 900$ km is negligible when normalized with respect to the amplitude at the caustic. For greater distances the first arriving signal cannot be seen. The same seismograms but normalized with respect to the amplitude at $x = 700$ km are shown in Figure 5.10. The second arrivals are the waves reflected at the velocity gradient and are much stronger. At large distances only these can be observed.

CHAPTER 6 CONVERGENCE OF THE RAY EXPANSION

Theoretical seismograms presented in this thesis were computed from exact Epstein's solutions (3.20) of the wave equation (Epstein, 1930). One question arises immediately: what would the seismograms look like if the Epstein profiles were replaced by a stratified medium consisting of homogeneous layers. The last has been studied extensively by many authors (Thomson, 1950; Haskell, 1953; Brekhovskikh, 1960; Gilbert and Backus, 1966; Müller, 1968, 1969; Hron, F. and Kanasewich, 197 as it represents the simplest approach to studies of wave propagation within the Earth. Cisternas et al. (1973) showed that the exact solution of this problem, represented by Thomson-Haskell matrices can be expressed as infinite series whose terms can be physically interpreted as rays. Each ray is represented by a product of reflection and transmission coefficients at the interfaces on its path. These are independent of frequency and Cagniard-de Hoop can be applied to obtain the solutions in the time domain for each ray (Cagniard, 1962; de Hoop, 1960). If the contribution from all rays in the "complete" ray expansion given by Cisternas et al. (1973) were evaluated and added to give the exact response of the medium, enormous amount of computing time would be required even for a small number of layers. Thus only the most important rays, i.e. those of maximum amplitude, are usually included

and the rest of the series is neglected. The use of the "partial" ray expansion is only justified if the ray series is convergent. The convergence, while assumed, has never been proved analytically, and the reason probably is that it is rather difficult. Some of the problems encountered when attempting to prove the convergence of the ray series as well as a proof in one special case are discussed in Section 6.3.

The wave equation can be integrated numerically for the continuous velocity profile and for the layered medium. The solution to the first problem is equivalent to the analytic solution obtained by Epstein while the other is equivalent to the complete ray expansion. The errors introduced by the approximation of the continuous model by layered medium are studied in Section 6.2. We also study the partial ray expansion that includes only the once reflected rays and investigate the error arising from neglecting rays with more reflections.

6.1 Fundamental solution

Equations of motion (2.4) and the constitutive relation for pressure (2.3) can be written in the form

$$\frac{d}{dz} \begin{pmatrix} u \\ z \\ P \end{pmatrix} = \begin{pmatrix} 0 & -\frac{Q^2}{\omega^2 \rho(z)} \\ \rho \omega^2 & 0 \end{pmatrix} \begin{pmatrix} u \\ z \\ P \end{pmatrix} \quad (6.1)$$

after the transformations with respect to time t and r .

The equations (6.1) can be written in the matrix form

$$\frac{d\underline{V}(z)}{dz} = \underline{M} \underline{V}(z) \quad (6.2)$$

and the solution of such an equation is given by

$$\underline{V}(z) = \underline{P}(z, z_0) \underline{V}(z_0) \quad (6.3)$$

where $\underline{P}(z, z_0)$ is so-called propagator, introduced to seismology by Gilbert and Backus (1966). It is a fundamental matrix such that $\underline{P}(z_0, z_0) = \underline{I}$ (identity matrix) and it can be found from

$$\underline{P}(z, z_0) = \underline{F}(z) \underline{F}^{-1}(z_0) \quad (6.4)$$

where $\underline{F}(z)$ is any fundamental matrix. A fundamental matrix is a non-singular solution of (6.2). Gilbert and Backus (1966) stated that formally

$$\underline{P}(z, z_0) = \exp \int_{z_0}^z \underline{M}(\xi) d\xi \quad (6.5)$$

which is applicable particularly if $\underline{M}(\xi)$ is independent of z . Thus, if we assume a medium of homogeneous layers (Fig. 6.1) and choose an intermediate point ξ_1 in i -th layer

$$\underline{M}(z) = \underline{M}(\xi_1), \quad z_{i-1} < z < z_i \quad (6.6)$$

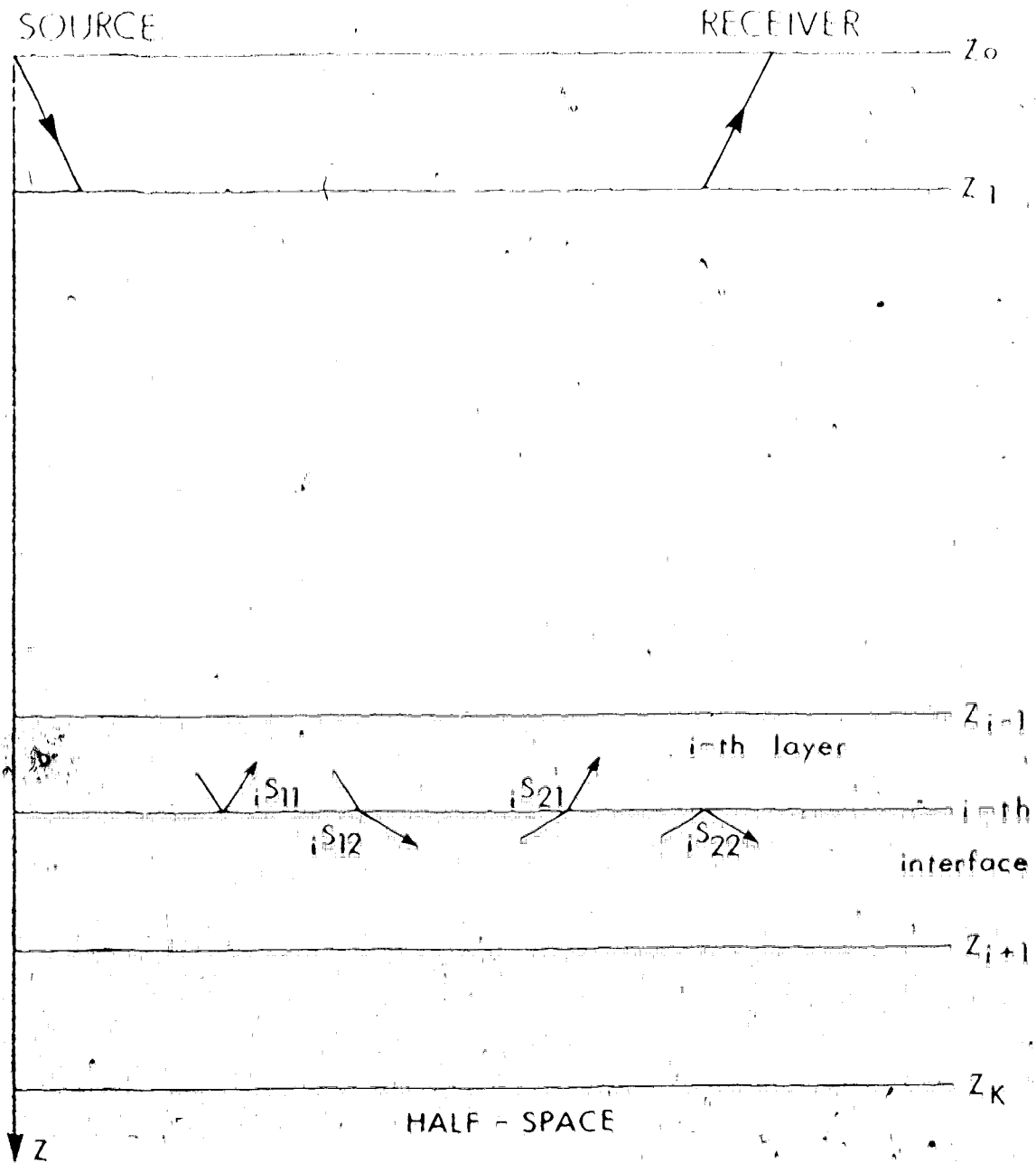


Figure 6.1 The stratified medium of homogeneous layers.

The propagator (6.5) is

$$P(z_1, z_{1-1}) = e^{\underline{M}_1 d_1} \quad (6.7)$$

where $\underline{M}_1 = \underline{M}(\xi_1)$ and $d_1 = z_1 - z_{1-1}$. We denote \underline{N} a matrix of eigenvectors of \underline{M} , i.e.

$$\underline{M} \cdot \underline{N} = \underline{N} \cdot \underline{B}^{(0)} \quad (6.8)$$

where $\underline{B}^{(0)}$ is a diagonal matrix of eigenvalues (we use the notation introduced by Chapman (1973)). The columns of \underline{N} are plane wave solutions and the elements of $\underline{B}^{(0)}$

$$\underline{B}^{(0)} = \underline{N}^{-1} \cdot \underline{M} \cdot \underline{N} \quad (6.9)$$

are their wavenumbers. We denote $\underline{N}_1 = \underline{N}(\xi_1)$ and $\underline{B}_1^{(0)} = \underline{B}^{(0)}(\xi_1)$ where 1 corresponds to the 1-th homogeneous layer. The propagation in the 1-th layer is given by

$$P(z_1, z_{1-1}) = e^{\underline{M}_1 d_1} = \underline{I} + \underline{M}_1 d_1 + \frac{\underline{M}_1^2 d_1^2}{2!} + \dots = \underline{N}_1 e^{\underline{B}_1^{(0)} d_1} \underline{N}_1^{-1} \quad (6.10)$$

since $\underline{M}_1^k = \underline{N}_1 \cdot \underline{B}_1^{(0)k} \cdot \underline{N}_1^{-1}$

Thus the solution at the 1-th layer can be written

$$\underline{V}(z_1) = \underline{N}_1 e^{\underline{B}_1^{(0)} d_1} \underline{N}_1^{-1} \cdot \underline{V}(z_{1-1}) \quad (6.11)$$

and the physical interpretation is evident: N_1^{-1} resolves the displacement and stress at $z = z_{1-1}$ into plane wave components $e^{\sum_{i=1}^{N_1} d_i^{(o)}}$ multiplies each component by its phase across the i -th layer and N_1 recombines the plane waves into displacement and stress at $z = z_1$. The total propagator across the layered medium was given by Gilbert and Backus (1966)

$$P_{\sum_{i=1}^K}(z_K, z_0) = \prod_{i=1}^K P_{\sum_{i=1}^K}(z_i, z_{i-1}) \quad (6.12)$$

Therefore it contains products

$$Z_{\sum_{i=1}^K} = \prod_{i=1}^{N_1-1} N_i \quad (6.13)$$

which represent the transfer function of the i -th interface.

The vector of amplitudes of individual waves at the $(i-1)$ -th interface is

$$X_{\sum_{i=1}^K}(z_{i-1}) = \prod_{i=1}^{N_1-1} V_{\sum_{i=1}^K}(z_{i-1}) \quad (6.14)$$

while the vector of complete solutions in terms of plane waves including phase function in the i -th layer is

$$\underline{X}_1(z) = e^{\sum_{i=1}^{N_1} d_i^{(o)}(z-z_{i-1})} \underline{X}_{\sum_{i=1}^K}(z_{i-1}) \quad (6.15)$$

The reflection-transmission problem at the i -th interface is a solution of

$$\underline{v}(z_1 - 0) = \underline{v}(z_1 + 0) \quad (6.16)$$

i. e.
$$\underline{N}_1 \underline{X}_1(z_1) = \underline{N}_{1+1} \underline{X}_{1+1}(z_1)$$

There will be as many possible reflection and transmission problems as there are columns of \underline{N} (see Figure 3.5 in Chapter 3 for acoustic case). Thus, the reflection-transmission problem can be solved using matrices at each interface, which, of course, is nothing new because it represents the Thomson-Haskell method, developed twenty years ago (Thomson, 1950; Haskell, 1953). Thus the Thomson-Haskell matrix method is equivalent to finding the propagator $\underline{P}(z_K, z_0)$

$$\underline{P}(z_K, z_0) = \underline{N}_K e^{B^{(0)}_K d_K} \underset{z_{K-1}}{\dots} \underset{z_2}{\dots} e^{B^{(0)}_2 d_2} \underset{z_1}{\dots} e^{B^{(0)}_1 d_1} \underline{N}_1^{-1} \quad (6.17)$$

and
$$\underline{v}(z_K) = \underline{P}(z_K, z_0) \underline{v}(z_0) \quad (6.18)$$

Cisternas et al. (1973) showed that if a vector \underline{X} is formed of all vectors \underline{X}_i , $i = 1, 2, \dots, K$, the reflection-transmission problem in a layered medium can be written in the following form

$$\underline{X} = \underline{\Omega} \underline{X} + \underline{X}_0 \quad (6.19)$$

where \underline{X}_0 is the source term. This can be expanded into infinite series

$$\underline{X} = \sum_{\lambda=0}^{\infty} \Omega^{\lambda} \underline{X}_0 \quad (6.20)$$

and Cisternas et al. (1973) verified that terms in this power series represent physical rays. This is an important conclusion because it gives a new interpretation to the Thomson-Haskell matrix solution which is a complete solution of (6.2).

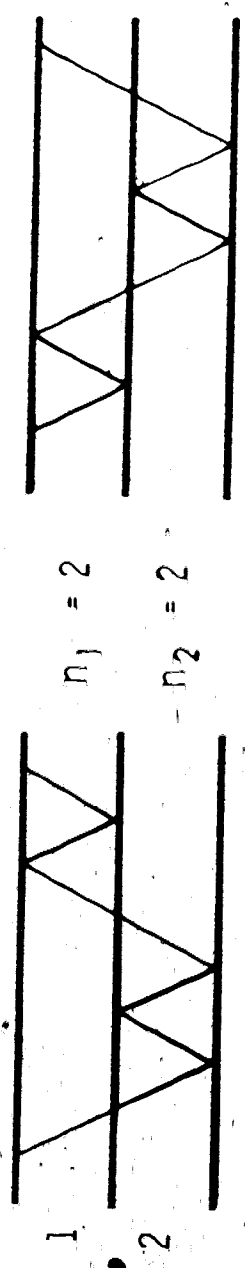
Hron, F. (1972) showed how to generate unconverted rays in such layered medium and the formulae he obtained determine all rays possible in the layered medium. He introduced to seismology so-called "kinematic" and "dynamic analogues" in order to describe groups of rays with identical properties. The waves which travel in the layered medium along different paths but with identical travel-time curves (Fig. 6.2) are kinematically equivalent and thus called "kinematic analogues". Their total number N_k depends on the half-number of segments in each layer n_i (Hron, F., 1971)

$$N_k(n_1, \dots, n_J) = \prod_{i=1}^{J-1} C_{n_{i+1}}^{n_i + n_{i+1} - 1} \quad (6.21)$$

where

$$C_{n_i}^{n_i + n_{i+1} - 1} = \frac{(n_i + n_{i+1} - 1)!}{n_i! (n_{i+1} - 1)!}$$

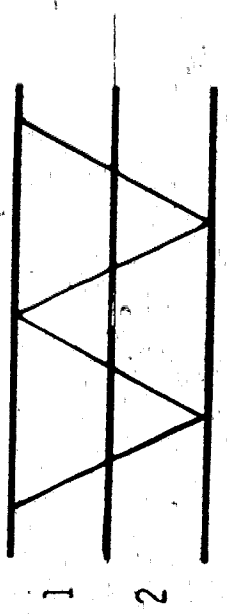
KINEMATIC GROUP



$$n_1 = 2$$

$$n_2 = 2$$

$$J = 2$$



1

2

$$N_k(2, 2) = C_2^3 = 3$$

Numbers of kinematic analogues $N_k(n_1, \dots, n_J) = \prod_{i=1}^{J-1} C_{n_{i+1}}^{n_i+1} - 1$

1

Figure 6.2

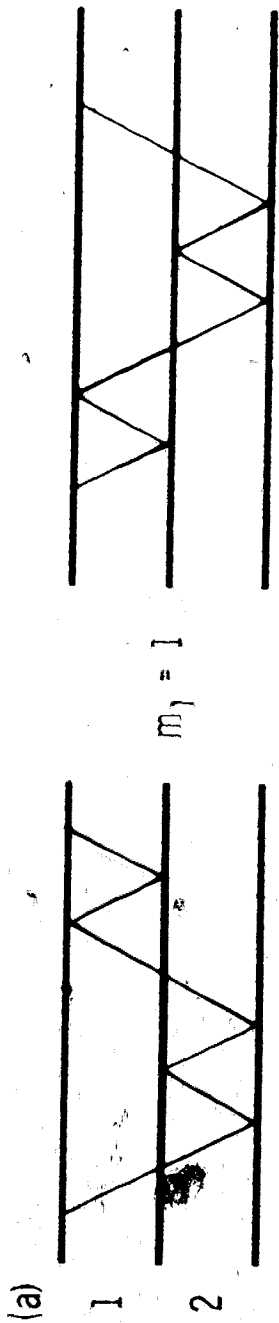
are combination numbers. The group of kinematic analogues consists of several subgroups of waves which have identical amplitudes. These are called groups of "dynamic analogues" (Fig. 6.3) and the number of waves within each group depends on the number of reflections m_i at each interface:

$$N_d(n_1, \dots, n_J; m_1, \dots, m_{J-1}) = \prod_{i=1}^{J-1} C_{m_i}^{n_i} C_{v_i-1}^{n_{i+1}-1} \quad (6.22)$$

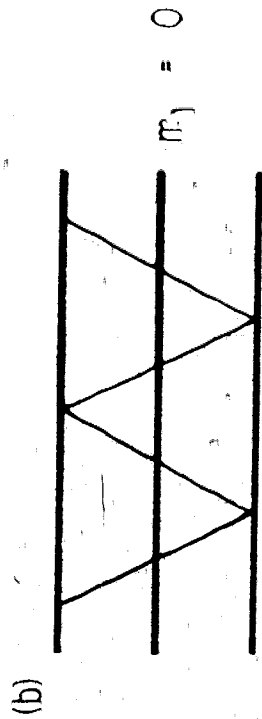
where $v_i = n_i - m_i$ is the number of transmissions through the i -th interface (Hron, F., 1971). The amplitude of the whole group of dynamic analogues called sometimes "total dynamic effect of the group" is evaluated as a product of the amplitude of one dynamic analogue and the number N_d . This saves a great deal of computations where the theoretical seismograms are calculated.

Based on results by Hron, F. (1972), Chapman (personal communication) showed that the complete unconverted ray expansion in the medium consisting of K homogeneous layers overlaying a homogeneous half-space (Figure 6.1) is given by the expression in Figure 6.4. Although this expansion is basically equivalent to that of Cisternas et al. its terms can be interpreted more easily than the complicated products of matrices in the series (6.20). The time transformation given by the Cagniard-de Hoop method is (HelMBERGER, 1968)

DYNAMIC GROUPS



$$N_d(2, 2; 1) = C_1^2 C_0^1 = 2$$



$$N_d(2, 2; 0) = C_0^2 C_1^1 = 1$$

Numbers of dynamic analogues $N_d(n_1, \dots, n_J; m_1, \dots, m_{J-1}) = \prod_{i=1}^{J-1} C_{m_i}^{n_i} C_{n_i - m_i - 1}^{n_{i+1} - 1}$

Figure 6.3

COMPLETE UNCONVERTED RAY EXPANSION

$$\begin{aligned}
 & \sum_{j=1}^{\infty} \sum_{i=1}^{2n_j} n_j v_i^{d_i} \\
 & \sum_{j=1}^{n_1-1} \sum_{i=1}^{n_{j-1}-1} \sum_{k=1}^{m_1} \left(s_{12}^{i s_{21}} \right)^{m_i} \left(s_{22}^{i s_{21}} \right)^{n_{i+1}-v_i} \\
 & m_1 = \max(0, n_1 - n_2) \\
 & \vdots \\
 & m_{j-1} = \max(0, n_{j-1} - n_j)
 \end{aligned}$$

Kinematic Group

Multiplicity

Dynamic Group

Figure 6.4

$$\tau = p r + \sum_{i=1}^J 2n_i n_{v_i} d_i \quad (6.23)$$

and the term

$$\sum_{m_1 = \max(0, n_1 - n_2)}^{n_1 - 1} \dots \sum_{m_{J-1} = \max(0, n_{J-1} - n_J)}^{n_{J-1} - 1} \prod_{i=1}^{J-1} C_{m_i}^{n_i} C_{v_i - 1}^{n_{i+1} - 1} S_{11}^{m_i} (S_{12} S_{21})^{v_i} S_{22}^{n_{i+1} - v_i} \quad (6.24)$$

represents the total amplitude of all rays with identical arrival time τ . S_{11} and S_{22} are the coefficients of reflection from the top and bottom of the i -th interface, respectively. S_{12} and S_{21} are the coefficients of transmission through the i -th interface in positive and negative z direction, respectively (Figure 6.1).

In practise only the "partial" ray expansion is used, which means that for given number of layers K only a finite number of kinematic groups is considered, and within these only the dynamic groups with significant dynamic effect are taken into account (Hron, F. and Kanasewich, 1971; Müller, 1970; Gilbert and HelMBERGER, 1972). The partial

ray expansion may be viewed as an approximate solution of (6.2) that does not satisfy exactly the boundary conditions at each interface.

The equation (6.2) can be solved numerically for both models, the Epstein monotonic transition and a stratified medium of homogeneous layers. The first yields the exact solutions (3.20) and the other will give the complete ray expansion in Figure 6.4 which should converge to the first one as the layer thickness decreases. The partial ray expansion can be obtained adding rays with certain number of reflections at each interface. The behaviour of the solutions with respect to the layer thicknesses is studied in the next section.

6.2 The numerical solution of the wave equation

The components of the vector $\underline{V}(z)$ and the wave numbers κ and Q are complex functions and, therefore, equation (6.2) represents four equations. The equation (6.2) can be numerically integrated step by step as $Q = Q(z)$ is a known function. Many numerical methods exist for integration of systems such as (6.1). A very efficient method by Bulirsch and Stoer (1966) was used to obtain the solution $\underline{V}(z)$. For this method, the initial values must be known and the accuracy of the integration depends on their accuracy.

In our problem it is not difficult to determine the initial values as in regions far above or far below the anomalous region centered around $z=z_m$ the plane wave solutions are valid (see Chapters 2 and 3).

For the monotonic velocity increase given by

$$v(\zeta) = \left(\frac{1}{2} + \frac{1}{2} e^{\zeta/\sigma} \right)^{-1/2} \cdot \left(1 + e^{\zeta/\sigma} \right)^{1/2}, \quad (6.25)$$

where $\zeta = (z-z_m)$ for $\rho = \text{const}$, according to (2.14), the vertical wavenumber is

$$Q(\zeta) = \left(\frac{\omega^2}{v^2(\zeta)} - \kappa^2 \right)^{1/2} \quad (6.26)$$

Above the turning point of a ray, ζ_T , two travelling solutions should be present while below the turning point only the exponentially decaying solution is valid. From this, the initial values for the integration can be set as:

$$\underline{v}(\zeta_B) = \begin{bmatrix} \text{Re } u_\zeta(\zeta_B) \\ \text{Im } u_\zeta(\zeta_B) \\ \text{Re } P(\zeta_B) \\ \text{Im } P(\zeta_B) \end{bmatrix} = \begin{bmatrix} \frac{\text{Im } Q(\zeta)}{\rho \omega^2} \\ 0 \\ 1 \\ 0 \end{bmatrix} = \text{Im } Q(\zeta_B) \cdot \zeta_B \quad (6.27)$$

where $\text{Re } Q(\zeta_B) \approx 0$, $\text{Im } Q(\zeta_B) = \left(\kappa^2 - \frac{\omega^2}{v^2(\zeta_B)} \right)^{1/2}$ at $\zeta_B \gg \zeta_T$.

ϵ remains constant and represents the parameter of the ray whose turning point is at ζ_T (4.24). After several tests of the program it was found that the initial values should be taken at the depth ζ_B which is approximately four wavelengths below the transition. This seems to be an optimum depth with respect to the accuracy of the results and the computing time required to calculate them.

It is evident from the initial values (6.23) and the matrix \underline{M} in (6.1) that the numerical solution $\underline{V}(\zeta)$ of (6.2) remains real for all ζ . Thus above the turning point it represents a standing wave rather than travelling waves we would like to study. Analogously to (6.14) these solutions can be obtained from the matrix \underline{N}^{-1}

$$\underline{X}(\zeta) = \underline{N}^{-1} \underline{V}(\zeta) \quad (6.28)$$

The matrix of eigenvectors \underline{N} is given by

$$\underline{N}(\zeta) = \begin{pmatrix} \frac{1Q(\zeta)}{\rho\omega^2} & -\frac{1Q(\zeta)}{\rho\omega^2} \\ 1 & 1 \end{pmatrix} \quad (6.29)$$

and the vector $\underline{X}(\zeta)$ is formed by the solutions representing the waves travelling in the positive (X_+) and negative (X_-) ζ -direction:

$$X(\zeta) = \begin{pmatrix} X_+ \\ X_- \end{pmatrix} \quad (6.30)$$

The inverse matrix \underline{N}^{-1} is

$$\underline{N}^{-1}(\zeta) = \begin{pmatrix} -\frac{1\rho\omega^2}{2Q(\zeta)} & \frac{1}{2} \\ \frac{1\rho\omega^2}{2Q(\zeta)} & \frac{1}{2} \end{pmatrix} \quad (6.31)$$

and from (6.1) we obtain

$$\begin{aligned} X_+ &= \frac{1}{2}P - \frac{1\rho\omega^2}{2Q} u_\zeta \\ X_- &= \frac{1}{2}P + \frac{1\rho\omega^2}{2Q} u_\zeta \end{aligned} \quad (6.32)$$

where u_ζ and P are components of $\underline{V}(\zeta)$ determined by the numerical integration. The reflection coefficient being the ratio of the upgoing and the downgoing waves is

$$R = e^{i2\beta} \quad (6.33)$$

where

$$\beta = \arctan \frac{\rho\omega^2 u_\zeta}{QP}$$

The numerical solutions of (6.1) for Model IV (4.50) when $\zeta_B = 2$ km, $\omega = 100$ rad/sec, $\sin \theta_1 = .887965$ and the relative error of the integration is less than $\epsilon = 10^{-5}$, are

denoted X_+ and X_- . These are compared with numerical solutions of (6.1) for a stratified medium of homogeneous layers which are denoted ${}_L X_+$ and ${}_L X_-$. The last represent the complete ray expansion in Figure 6.4 and should be better approximations of X_+ and X_- as number of layers increases. The layered medium is obtained from the continuous velocity Model IV (4.50) by dividing it into equal steps in velocity δv . The modulus of X_+ is compared at the point ζ_T and at the turning point ζ_T to the modulus of the complete ray expansion ${}_L X_-$. The point ζ_T lies 20 km above the center of the transition i.e. at the same level as the source and receiver for synthetic seismograms in Chapter 4. The percentage error

$$\epsilon = 100 \cdot \frac{|X_+| - |{}_L X_+|}{|X_+|}$$

for Model IV, $\omega = 100$ rad/sec and $\lambda = .5$ km is given in Table 6.1. It is evident that at this frequency the results for both models become equivalent only if the number of layers is very large. The percentage errors at both points are less than 2% if the number of layers is greater than 400. That is such a great number of layers that if the Cagniard-de Hoop method were used to evaluate the synthetic seismograms it would consume enormous amount of computing time. Thus we can

THE PERCENTAGE ERROR OF THE COMPLETE RAY EXPANSION
FOR MODEL IV AND $\omega = 100$ rad/sec

Number of Layers K	Error at $l_r = 20$ km e [%]	Error at l_T e [%]
3	99.98	99.98
4	98.96	99.12
5	95.14	95.11
7	84.12	83.81
10	68.44	67.95
15	50.05	50.11
20	38.63	39.81
30	26.18	26.99
40	19.84	20.41
50	16.05	16.34
60	13.50	13.58
70	11.66	11.78
80	10.24	10.27
90	9.108	9.091
100	8.186	8.144
120	6.766	6.83
140	5.730	5.703
160	4.946	4.940
180	4.336	4.347
200	3.853	3.963
250	3.005	3.102
300	2.465	2.591
350	2.095	2.178
400	1.828	1.870
450	1.625	1.672
500	1.465	1.479

again appreciate the value of the exact solution (3.20) from which we were able to compute the exact synthetic seismograms without running into the aforementioned difficulty. Müller (1970) computed theoretical seismograms for a linear transition 1 km thick with velocities $v_1 = 6.4$ km/s, $v_2 = 8.2$ km/s and densities $\rho_1 = 3.0$ g/cm³ and $\rho_2 = 3.3$ g/cm³. He found that the seismograms at epicentral distance of 150 km for the linear transition are equivalent to seismograms computed for a layered medium with 240 layers. The transition in our Model IV (4.50) is thicker and continuous and the ratio $\frac{v_1}{v_2} = .82$ is greater. Thus the first guess on the basis of Müller's conclusion is that the number of layers necessary for a good approximation of Model IV will be even greater. These qualitative estimates are rigorously justified by our quantitative results presented in Table 6.1.

We have already mentioned that the synthetic seismograms if evaluated by Cagniard-de Hoop method require a great deal of computing time. That is why only the most important rays i.e. rays whose amplitude are the largest, are considered, when the computation of the synthetic seismogram is performed. The amplitude is dependent on number of reflections and transmissions the ray suffers on its path from the source to the receiver. We will study the convergence of the ray expansion analytically in the next section. In this section,

however, we would like to demonstrate some of the weaknesses that the partial ray expansion can have. The accuracy of the partial ray expansion depends on the correct choice of rays that contribute most to the amplitude. Such choice is often biased by the personal judgement of the authors - usually the rays that suffer only one reflection are considered to be of greatest importance. The rays with multiple reflections are considered to be weaker. We shall try to point out that this is not always valid and that also other than the rays with one reflection must be taken into account if we want to obtain a meaningful result. To demonstrate the nature of the approximation given by rays with only one reflection a program was written which adds all contributions of once-reflected rays (Fig. 6.5).

The contribution pertinent to the ray reflected at the L -th interface is

$$X_p(L) = {}_L S_{11} \cdot X_0 \prod_{i=1}^{L-1} {}_i S_{12} {}_i S_{21} e^{i\omega G(\zeta)} \quad (6.34)$$

where X_0 is the amplitude at the point ζ .

$${}_i S_{12} = {}_i S_{21} = \frac{2\sqrt{Q_i \cdot Q_{i+1}}}{Q_i + Q_{i+1}}$$

are transmission coefficients across the i -th interface

$${}_L S_{11} = \frac{Q_L - Q_{L+1}}{Q_L + Q_{L+1}}$$

is the coefficient of reflection from the L -th interface

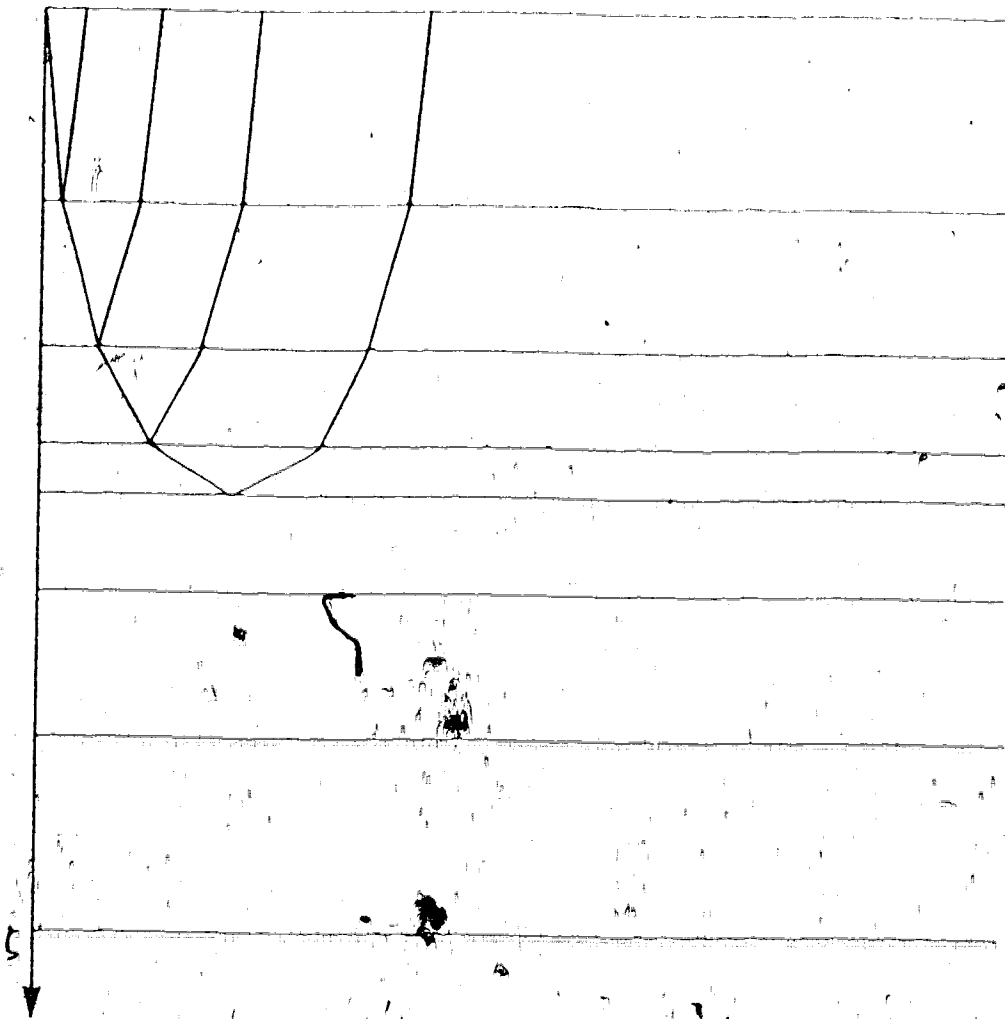


Figure 6.5 Plane waves propagating in the layered medium.

$\Omega_1 = \omega \left(\frac{1}{v_1^2} - p^2 \right)^{1/2}$ and $p = p_0 = \text{constant}$ are vertical and horizontal wavenumbers in the i -th layer, respectively.

$G(\ell)$ is a phase gain attributed to the ray path covered by the ray on its way down from point ℓ_S to the reflecting interface and up from the reflecting interface to the receiver.

The continuous velocity profile from Model IV was divided into homogeneous layers in the same manner as when the complete ray expansion was studied, i.e. into equal steps in velocity. The amplitude at the point $\ell_S = \ell_T$ was set equal to the exact value X_+ at $\ell_S = \ell_T$ (20 km above the center of the transition). At each interface the contributions of rays reflected once at interfaces below were added to form the amplitude of the wave going upwards. Such addition depends on frequency and layer thicknesses and we observe an interference phenomenon. Thus the returning wave has varying amplitude which depends on frequency and the number of layers. Thus we cannot compare this value in any way to the complete ray expansion result or to the result for the continuous velocity profile. We can, however, compare the amplitudes at the turning point of the ray ℓ_T of the downgoing wave which represents the first term in the ray series in Figure 6.4. The percentage error of this partial ray expansion

$$\epsilon = 100 \cdot \frac{|X_+| - |P X_+|}{|X_+|}$$

evaluated for the same parameters as in the previous example is displayed in Table 6.2 as a function of number of layers K . We see that the error does not decrease with the number of layers but remains rather large $\sim 14\%$. We can plot the absolute values of the percentage errors for the complete ray expansion and the partial ray expansion (Figure 6.6). The shaded area between the two curves can be interpreted as the difference due to the contribution of multiple reflected rays in this steady state case. The situation is slightly different if response to an impulsive source is investigated, especially for the first arrivals. Several authors showed that in this case once reflected rays give sufficiently accurate results (see, for example, HelMBERGER, 1968). For later arrivals the situation is different and multiply reflected rays must be taken into account. Müller (1970) computed theoretical seismograms for media consisting of homogeneous layers using rays with different number of reflections. He showed that only minor differences exist between the seismograms which include rays with only one reflection and those which include rays with three or five reflections, provided the medium has "moderate" number of layers (10-15 in his case).

THE PERCENTAGE ERROR OF THE PARTIAL RAY
EXPANSION FOR MODEL IV AND $\omega = 100$ rad/sec

Number of Layers K	Error at L_T ϵ [%]
3	15.79
4	-3.618
5	2.608
7	-4.987
10	-5.475
15	-8.532
20	-10.15
30	-11.83
40	-12.69
50	-13.22
60	-13.58
70	-11.74
80	-12.18
90	-12.52
100	-12.79
120	-13.21
140	-13.52
160	-13.75
180	-13.93
200	-13.32
250	-13.72
300	-13.49
350	-13.76
400	-13.96
450	-13.78
500	-13.94

Table 6.2

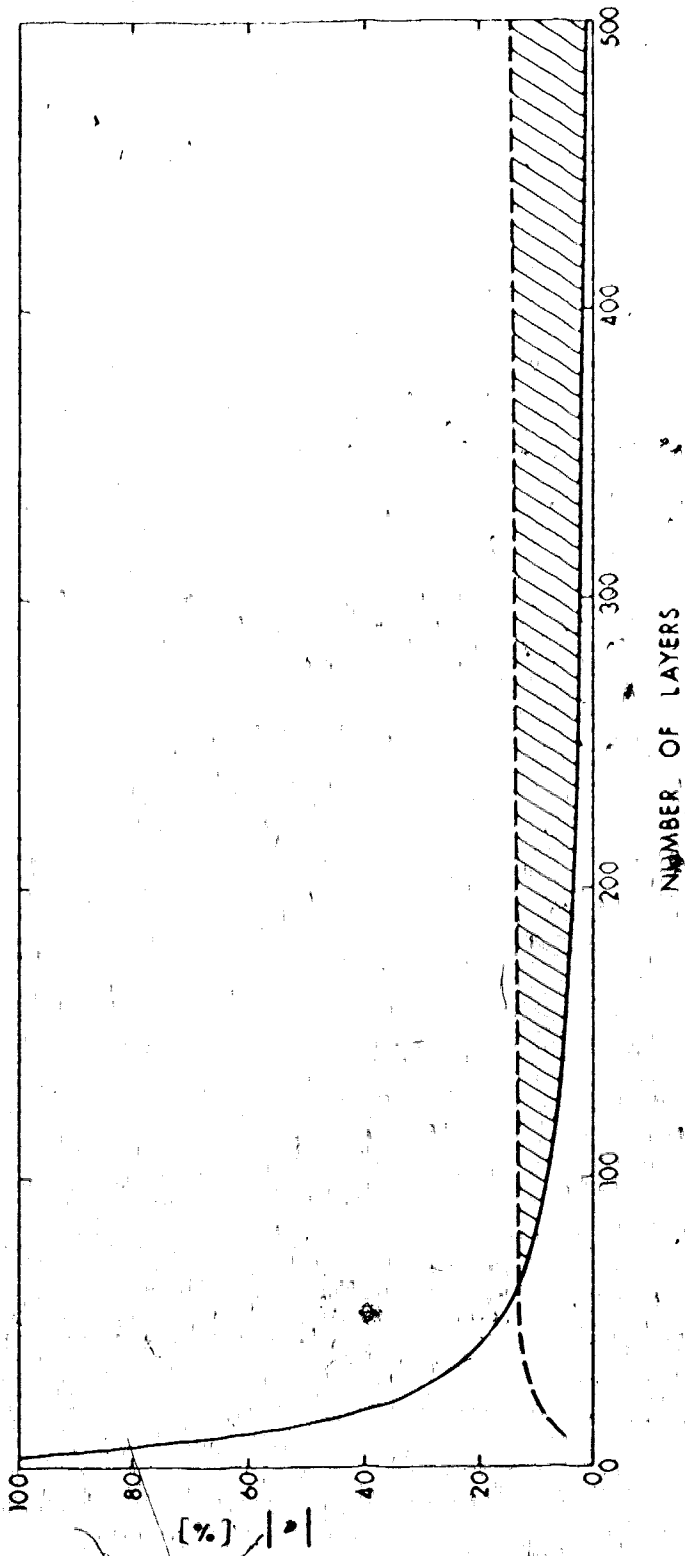


Figure 6.6 Percentage error of the complete and partial ray expansions (full line and dashed line, respectively).

Nevertheless, for media with greater number of layers, the multiply reflected rays cannot be neglected. Waddington (1973) also showed that considerable differences exist between the seismograms which include only once reflected rays and those which include multiply reflected rays.

The purpose of this study was to demonstrate the nature of the approximations of the solution for continuous velocity transition by complete or partial ray expansions. It was shown that the error in the complete ray expansion with respect to the exact solution is due to the bad approximation of the continuous model by layered medium when number of layers is small. The main source of the error in the partial ray expansion is in the choice of rays that take part in the partial ray expansion. With increasing number of layers the number of rays with three or five reflections grows considerably and their contribution plays a significant role in evaluation of the amplitude.

6.3 Convergence of the ray expansion

In any ray expansion the amplitude of rays decrease with increasing number of reflections and refractions. This justifies the use of partial ray expansion in practise. The decrease in amplitude of one dynamic analogue may, however, be compensated by their number in the dynamic group. The

total dynamic effect of the group of dynamic analogues depends on their number in the group N_d (6.12) and on the amplitude of the dynamic analogue. In order to study the behaviour of the total dynamic effect the problem will be simplified by assuming only vertical or near vertical reflections. The reflection and transmission coefficients at the i -th interface are

$$\begin{aligned} {}_i S_{11} &= -{}_i S_{22} = \frac{Q_i - Q_{i+1}}{Q_i + Q_{i+1}} \\ {}_i S_{12} &= {}_i S_{21} = \frac{2\sqrt{Q_i - Q_{i+1}}}{Q_i + Q_{i+1}} \end{aligned} \quad (6.35)$$

where

$$Q_i = \left(\frac{\omega^2}{2v_i} - \kappa^2 \right)^{1/2}$$

In the case of near vertical reflections they become

$$\begin{aligned} {}_i S_{11} &= -{}_i S_{22} = \frac{\delta v_i}{v_{i+1}} \\ {}_i S_{12} &= {}_i S_{21} = 1 = \frac{(\delta v_i)^2}{v_{i+1}^2} \end{aligned} \quad (6.36)$$

for

$$\frac{\delta v}{v_{i+1}} \ll 1$$

It is assumed that at the free surface $z = z_0$ (Figure 6.1) the reflection coefficient ${}_0 S_{22} = -1$. The layers are

chosen in such a way that the reflection and transmission are constant (i.e. the indices in (6.36) can be omitted). Thus the amplitude of a dynamic analogue depends only on the total number of reflections and does not depend on their distribution on the interfaces. The number of reflections at each interface is subject to conditions

$$\max(0, n_1 - n_{j+1}) \leq m_j \leq n_j - 1 \quad j = 1, \dots, J-1 \quad (6.37)$$

implied by (6.24). In analogy with the dynamic analogue characterized by number of reflections at each interface, the dynamic analogue characterized by total number of reflections can be called a "generalized dynamic analogue". This is an important simplification which allows us to rewrite the total amplitude (6.24) of the group of kinematic analogues arriving at time (6.23)

$$T = \prod_{i=1}^J 2n_i n_{i+1} d_i$$

in the following form

$$\sum_{M=M_{\min}}^{M_{\max}} A_m \mathcal{N}(N; M) = \sum_{M=M_{\min}}^{M_{\max}} A_m \quad (6.38)$$

M is the total number of reflections along the ray path

$$M = \sum_{i=1}^{J-1} m_i + \sum_{i=1}^{J-1} (n_i - n_{i+1}) + n_J + n_1 - 1 = 2M + 2n_J - 1 \quad (6.39)$$

M is the total number of reflections from above the interfaces $i = 1, \dots, J-1$

$$M = \sum_{i=1}^{J-1} m_i \quad (6.40)$$

Every kinematic analogue (6.23) has total number of segments equal to

$$2N = 2 \sum_{i=1}^J n_i \quad (6.41)$$

where n_i is the half-number of segments in each layer. The minimum number of reflections from above the interfaces $i = 1, \dots, J-1$ is given by

$$M_{\min} = \sum_{i=1}^{J-1} \max(0, n_i - n_{i+1}) \quad (6.42)$$

The maximum number of reflections from above the interfaces $i = 1, \dots, J-1$ is given by

$$M_{\max} = \sum_{i=1}^{J-1} (n_i - 1) = N - n_J - J + 1 \quad (6.43)$$

The total dynamic effect of groups of generalized dynamic analogues is denoted A_{mp} and the number of generalized ana-

logues in the group is $\mathcal{N}(N, M)$.

$$\int \mathcal{M} = \Lambda \mathcal{M} \mathcal{N}(N, M) \quad (6.44)$$

where

$$\Lambda \mathcal{M} = (-1)^{M+n_{J-1}} \binom{\delta v}{2v} \mathcal{M}^{J-1-n_1} \quad (6.45)$$

is the amplitude of the generalized dynamic analogue characterized by \mathcal{M} reflections. Thus the total amplitude of all rays (or all kinematic analogues) arriving at time t is the sum (6.38) of total dynamic effects of groups of generalized dynamic analogues. $\mathcal{N}(N, M)$ is the total number of generalized dynamic analogues in the group of generalized dynamic analogues with \mathcal{M} reflections.

$$\mathcal{N}(N, M) = \sum_{k=1}^{K_M} N_d(n_1, m_1(k)) \quad (6.46)$$

and the summation is over all possible distributions of M reflections into $J-1$ layers so that in the i -th layer the number of reflections satisfies the condition (6.37).

$N_d(n_1, m_1(k))$ is the number of dynamic analogues in the group, where number of reflections m_1 at i -th interface is given by k -th distribution of M . The number of distributions of M reflections into $J-1$ layers, subject to condition (6.37) is denoted by K_M . To determine this we must solve the problem of determination of the number of distinct ways in which M

balls can be distributed into $J-1$ different pockets allowing at most I_i balls in i -th pocket ($i = 1, \dots, J-1$).

$$I_i = n_i - 1 - \text{Max}(0, n_i - n_{i+1}) \quad (6.47)$$

Eisen (1969; p. 96) gives the solution to a simpler problem of distinct distributions of M balls into $J-1$ pockets allowing at most I balls per pocket. Then the number of these distributions is given by a simple recurrent formula

$$K_M = K(M; J-1, I) = \sum_{\ell=0}^I K(M-\ell; J-2, I) \quad (6.48)$$

and its results are displayed in Table 6.3 for the case of maximum number of balls allowed per pocket being $I = 3$.

By convention

$$K(0; 0; I) = 1 \quad \text{and} \quad K(M; 0, I) = 0 \quad \text{for } M \neq 0 \quad (6.49)$$

The formula (6.48) can be generalized for the case, when the maximum number of balls allowed per pocket is different for different pockets. Generally, we can write

$$K_M = K(M; J-1, I) = K(M; I_1, I_2, \dots, I_{J-1}) \quad (6.50)$$

for $I_i = I, i = 1, \dots, J-1$ and generate the recurrent formula analogously to that in (6.48):

THE NUMBER OF DISTINCT WAYS IN WHICH M-BALLS CAN BE
 DISTRIBUTED INTO J-1 POCKETS ALLOWING AT
 MOST 3 BALLS PER POCKET

$M \backslash J-1$	0	1	2	3	4	5	6	7	8	9
0	1									
1	1	1	1	1						
2	1	2	3	4	3	2	1			
3	1	3	6	10	12	12	10	6	3	1
4	1	4	10	20	31	40	44	40	31	20

Table 6.3 (from Eisen, 1969, p. 97)

$$K_M = K(M; I_1, I_2, \dots, I_{J-1}) = \sum_{\ell=0}^{I_1} K(M-\ell; I_2, \dots, I_{J-1}) \quad (6.51)$$

i.e. if the first pocket contains ℓ balls, where $\ell = 1$ or $2 \dots$ or I_1 , the remaining $M-\ell$ balls can be distributed into $J-2$ remaining pockets in $K(M-\ell; I_2, \dots, I_{J-1})$ ways. Table 6.4 gives the numbers of distributions for $I_1 = 2, I_2 = 3, I_3 = 2, I_4 = 4$. The initial values remain the same as in (6.49).

For every distribution of N , given by $n_i, i = 1, 2, \dots, J$, i.e. for every kinematic analogue, each of the distributions $k, k=1, \dots, K_M$ of M reflections represents a group of dynamic analogues $N_d(n_i, m_1(k))$. Thus

$$\sum_{M=M_{\min}}^{M_{\max}} K_M = \text{number of all groups of dynamic analogues}$$

When investigating Table 6.4 we see, that every row has a maximum for

$$M = \frac{M_{\max}}{2} \quad (6.52)$$

rounded up or down if M is odd. The fraction rounded down is denoted

$$\widehat{M} = \left(\frac{M_{\max}}{2} \right) \quad (6.53)$$

THE NUMBER OF DISTINCT WAYS IN WHICH M BALLS CAN BE DISTRIBUTED INTO $J-1$ POCKETS ALLOWING AT MOST 2 BALLS IN THE FIRST AND THIRD POCKETS, 3 BALLS IN THE SECOND POCKET AND 4 BALLS IN THE FOURTH POCKET

$J-1 \backslash M$	0	1	2	3	4	5	6	7	8	9	
0	1										
$I_{1,2} = 2$	1	1	1								
$I_{2,3} = 3$	2	1	2	3	3	2	1				
$I_{3,2} = 2$	3	1	3	6	8	8	6	3	1		
$I_{4,4} = 4$	4	1	4	10	18	26	31	31	26	18	10

Table 6.4

After studying the Table 6.3 it can be seen that the numbers of distribution K_M , $M = M_{\min}, \dots, M_{\max}$ in each row must always be smaller than the maximum in the previous row added $I + 1$ times. Thus for $J \geq 2$

$$K_M \leq K_{M'} \leq (I+1)^{J-2}, M = M_{\min}, \dots, M_{\max} \quad (6.54)$$

In the general case when the number of balls in the pockets is not equal for all pockets the numbers of distribution K_M can be bounded by

$$K_M \leq [\text{Max}(I_j, j=1, \dots, J-1)]^{J-2}, M = M_{\min}, \dots, M_{\max} \quad (6.55)$$

Every group of generalized dynamic analogues contains one group of dynamic analogues with maximum number of analogues for given M . We will denote this number of dynamic analogues by $M^N_d(n_1, m_1(k))$ and we can write an upper limit for $\mathcal{N}(N, M)$ as follows:

$$\mathcal{N}(N, M) \leq [\text{Max}(I_j, j=1, \dots, J-1)]^{J-2} \cdot M^N_d(n_1, m_1(k)) \quad (6.56)$$

To find the "most powerful" group of dynamic analogues

$M^N_d(n_1, m_1(k))$ is analytically very difficult since from (6.22)

$$N_d(n_1, m_1(k)) = \prod_{i=1}^{J-1} C_{m_i}^{n_i} C_{n_i - m_i - 1}^{n_{i+1} - 1}$$

where $M = \sum_{i=1}^{J-1} m_i$ and $m_i(k)$ is given by the k -th distribution of M , subject to the restriction (6.37). We were not able to find an analytic way of determining $M_d^n(n_1, m_1(k))$. Obviously, an upper limit to (6.22) can be given by

$$M_d^n(n_1, m_1(k)) \leq \left(C_{\frac{n}{2}}^n \cdot C_{\frac{n-1}{2}}^{n-1} \right)^{J-1} \quad (6.57)$$

where $n = \text{Max}(n_1, 1, \dots, J-1)$. This overestimates $M_d^n(n_1, m_1(k))$ but we do not know a better way at this moment. The number of generalized dynamic analogues in a group with $|||$ reflections is bounded by

$$||| (N, M) \leq \frac{1}{n-1} ((n-1) \left(C_{\frac{n}{2}}^n \cdot C_{\frac{n-1}{2}}^{n-1} \right)^{J-1}) \quad (6.58)$$

and total dynamic effect of the group of generalized dynamic analogues is

$$|A_m| \leq |A_{|||}| \cdot \frac{1}{n-1} ((n-1) \left(C_{\frac{n}{2}}^n \cdot C_{\frac{n-1}{2}}^{n-1} \right)^{J-1}) \quad (6.59)$$

Thus if we can prove that the upper limit of A_m tends to zero faster than $(M_{\max} - M_{\min})^{-1}$ as $n \rightarrow \infty$, the convergence of the partial ray expansion has been proved.

For large values of n the Stirling's approximation (C.11) can be used to approximate $C_{\frac{n}{2}}^n$ and $C_{\frac{n-1}{2}}^{n-1}$ in (6.57). Then

$$C_{\frac{n}{2}}^n \cdot C_{\frac{n}{2}-1}^{n-1} \sim \left\{ \frac{e}{\pi} 2^{2n} \cdot \frac{1}{n+1} \cdot \left(\frac{n+1}{n+2} \right)^{n+1} \right\}^{J-1} \quad \text{for } n \text{ even} \quad (6.60)$$

$$C_{\frac{n}{2}}^n \cdot C_{\frac{n}{2}-1}^{n-1} \sim \left\{ \frac{e}{\pi} 2^{2n} \cdot \frac{1}{n+1} \cdot \left(\frac{n}{n+1} \right)^{n+1} \right\}^{J-1} \quad \text{for } n \text{ odd}$$

The only estimate we could find for the amplitude of one generalized dynamic analog $A_{\mathcal{M}}$ from (6.44) is

$$|A_{\mathcal{M}}| = \left(\frac{\delta v}{2v} \right)^{\mathcal{M} + 1 - n_1} \left(\frac{\delta v}{2v} \right)^{2n_J - n_1} \quad (6.61)$$

If we substitute (6.60) and (6.61) into (6.59), we see that the upper limit of $|A_{\mathcal{M}}|$ grows with n . Thus all the estimates were too rough to yield a useful result.

Many attempts have been made to find a finer estimate and prove the convergence in the general case, but all with no success. The convergence was proved only for one special group of kinematic analogues which is the group of kinematic analogues with uniform distribution of segments into the layers (Fig. 6.7). The symmetry of the problem introduces symmetry into the "most powerful" group of dynamic analogues $M_d(n_1, m_1(k))$ which, in the general case, had to be introduced artificially (see Eq. 6.57). This, as we shall see, is an important property and allows us to give more realistic estimates to all the factors that contribute to the

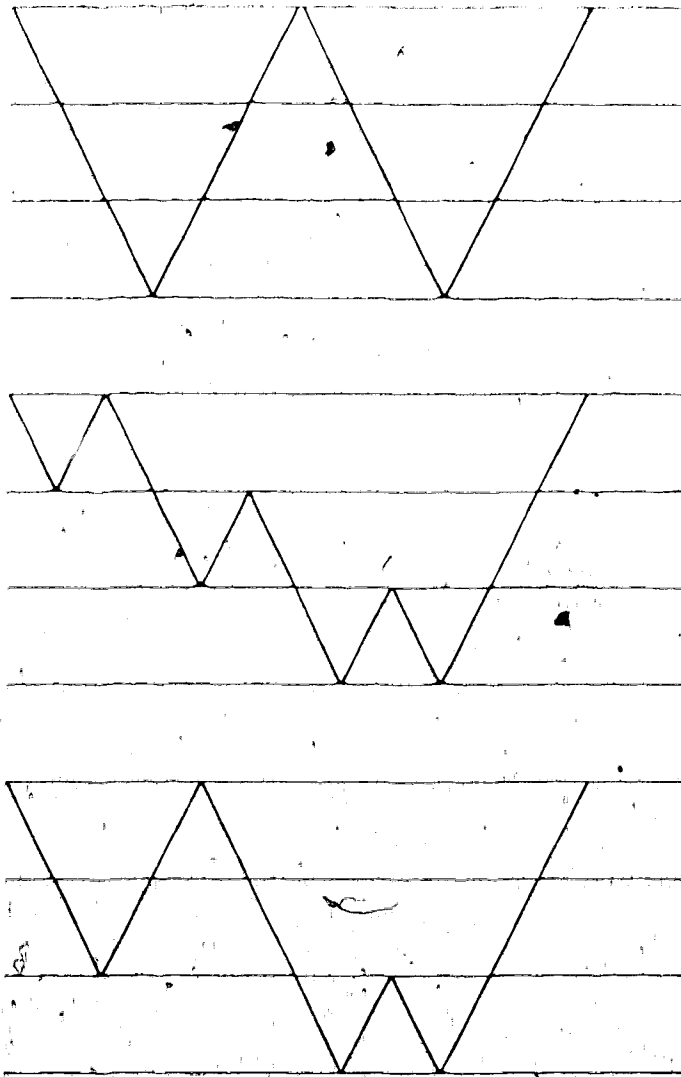


Figure 6.7 Some of the dynamic analogues in the group of kinematic analogues $N_K(2, 2)$.

total dynamic effect of the group of generalized dynamic analogues.

We will denote n a half-number of segments in each layer. Thus

$$N = n \cdot J, \quad M_{\min} = 0, \quad M_{\max} = (J-1) \cdot (n-1) \quad (6.62)$$

and $0 \leq m_1 \leq n-1$

If $M = \sum_{i=1}^{J-1} m_i$, then the recurrent formula (6.48) for the numbers of distributions of M into $J-1$ layers is valid if 1 is replaced by $n-1$. The "most powerful" group of dynamic analogues is that with number of reflections m_1 being equal to $(\frac{n}{2})$ (fraction rounded down). Thus the number of generalized analogues with M reflections can be estimated by

$$\mathcal{N}^n(N, M) \leq K_{\bar{M}} \cdot M^N / (n; (\frac{n}{2}))^{J-1} = \bar{\mathcal{N}}^n(N, \bar{M}) \quad (6.63)$$

where

$$\bar{\mathcal{N}}^n(N, \bar{M}) = \frac{1}{n-1} \left\{ \frac{e}{\pi} 2^{2n} \frac{n-1}{n+1} \left(\frac{n+1}{n+2} \right)^{n+1} \right\}^{J-1} \quad \text{for } n \text{ even} \quad (6.64)$$

$$\bar{\mathcal{N}}^n(N, \bar{M}) \approx \frac{1}{n-1} \left\{ \frac{e}{\pi} 2^{2n} \frac{n-1}{n} \left(\frac{n}{n+1} \right)^{n+1} \right\}^{J-1} \quad \text{for } n \text{ odd}$$

After a considerable amount of algebra it can be shown that $\mathcal{N}^n(N, M)$ has maximum at \bar{M} and the function is diagrammatically drawn in Figure 6.8.

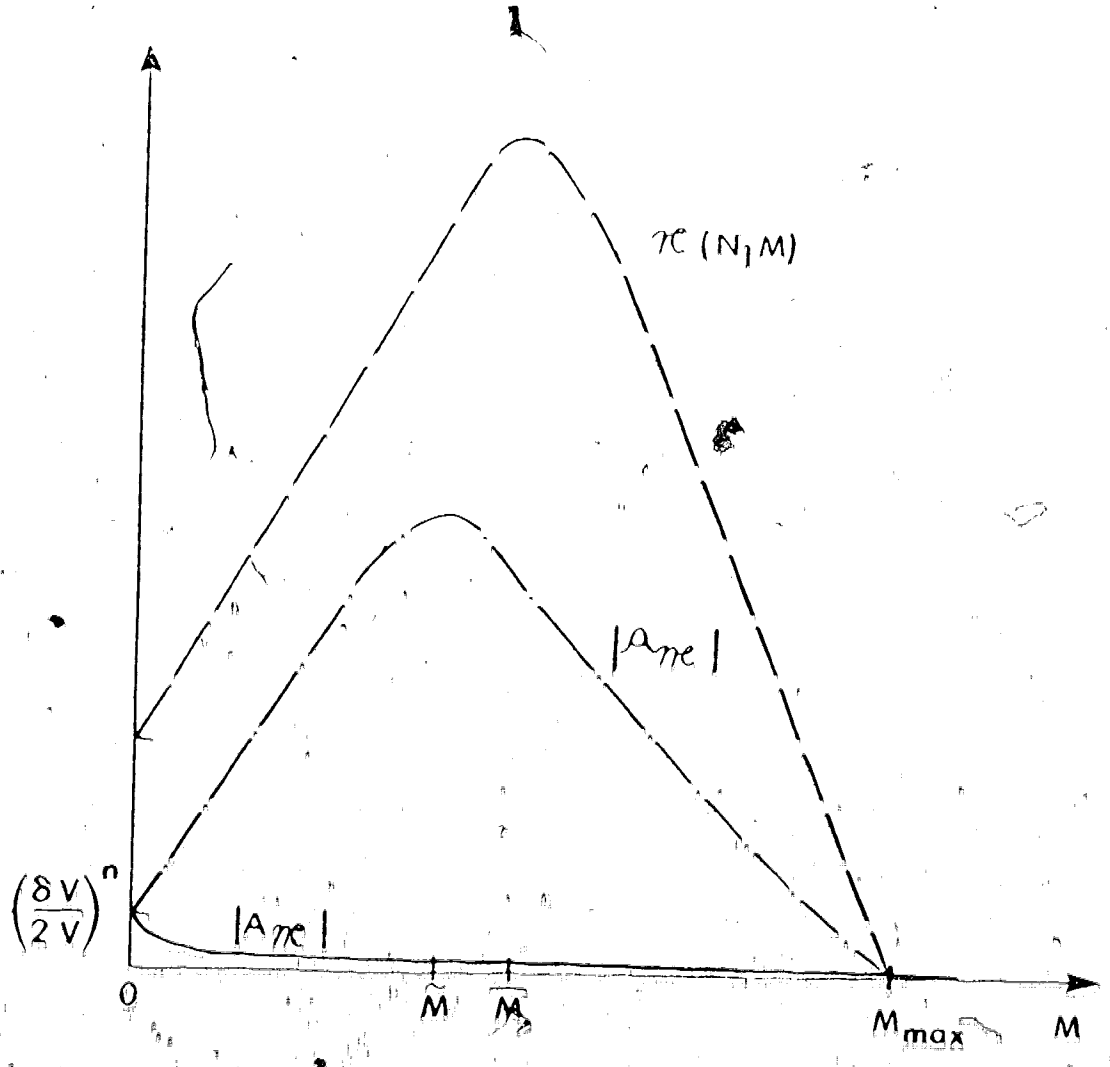


Figure 6.8 Schematic diagram of the behaviour of the amplitude $|A_m|$ of generalized dynamic analogues, of the number of generalized dynamic analogues $K(N, M)$, and of the total dynamic effect $|A_T|$. The scales along the ordinate are different for all three functions. The only purpose is to show the approximate shape of those functions.

The amplitude of the generalized analogue characterized by $\overline{M} = M_{\max} + 2n - 1$ reflections can be estimated for all n (both even and odd) as

$$|A_{\overline{M}}| = \left(\frac{\delta v}{2v}\right)^{\overline{M}} = \left(\frac{\delta v}{2v}\right)^{(n-1)(J-1)+1} \quad (6.65)$$

The upper estimate of the dynamic effect pertaining to the group of generalized dynamic analogues with \overline{M} reflections is

$$|A_{\overline{M}}| \leq |A_{\overline{M}}| \cdot \overline{M}(N, M) \quad (6.66)$$

and for $\frac{\delta v}{v} < \frac{1}{2}$ we can write

$$\lim_{n \rightarrow \infty} |A_{\overline{M}}| = 0 \quad (6.67)$$

So far we have proved that the total dynamic effect pertinent to the most numerous or "most powerful" group of generalized dynamic analogues decreases with increasing half-number of segments n . But this group is only one of their total number $M_{\max} + 1$ and represents only one term in the series (6.38). The next step is to show that any of the $M_{\max} + 1$ groups of generalized dynamic analogues decreases with increasing n . If \overline{M} is the point where $|A_{\overline{M}}|$ has its maximum i.e.

$$\left. \frac{d|A_{\overline{M}}|}{dM} \right|_{\overline{M}} = 0 \quad (6.68)$$

We are able to find its position with respect to \bar{M} :

$$\frac{d|A_{\mathcal{M}}|}{dM} = \mathcal{H}(N, M) \frac{d|A_{\mathcal{M}}|}{dM} + |A_{\mathcal{M}}| \cdot \frac{d\mathcal{H}(N, M)}{dM} \quad (6.69)$$

where

$$\frac{d|A_{\mathcal{M}}|}{dM} = \left(\frac{\delta v}{2v}\right)^{\mathcal{M}+1-n} \cdot 2 \log\left(\frac{\delta v}{2v}\right) < 0 \quad \text{for } M > 0 \quad (6.70)$$

and

$$\frac{d\mathcal{H}(N, M)}{dM} \begin{cases} > 0 & \text{for } M < \bar{M} \\ = 0 & \text{for } M = \bar{M} \\ < 0 & \text{for } M > \bar{M} \end{cases} \quad (6.71)$$

Therefore $M < \bar{M}$ (i.e. $\tilde{\mathcal{M}} = 2(M+n)-1 < \bar{\mathcal{M}}$) and the behaviour of $|A_{\mathcal{M}}|$ and $\mathcal{H}(N, M)$ as functions of M is diagrammatically drawn in Figure 6.8. The derivative

$$\frac{d|A_{\mathcal{M}}|}{dM} \rightarrow 0 \quad \text{as } n \rightarrow \infty \quad (6.72)$$

and therefore $\bar{M} \rightarrow \bar{M}$ as $n \rightarrow \infty$ and the maximum of $|A_{\mathcal{M}}|$ approaches to the maximum of $\mathcal{H}(N, M)$. So we can say that for any $\epsilon > 0$ real, there exists M_0 such that for any $M > M_0$ the following relation is valid

$$|A_{\mathcal{M}}| \leq |A_{\mathcal{M}_0}| + \epsilon \quad (6.73)$$

where $\mathcal{M} = 2(M+n)-1$ and $\mathcal{M}_0 = 2(M_0+n)-1$. Our objective is to investigate the convergence of the partial ray expansion when the amplitude of individual events is estimated by

$$U_n = \sum_{M=0}^{M_{\max}} A_m \tilde{m} \{ (N, M) \} \quad N = n - J, \quad \tilde{m} = 2M + 2n - 1 \quad (6.74)$$

If we use for the upper limit of U_n

$$|U_n| \leq M_{\max} \cdot |A_{\tilde{m}}| \quad (6.75)$$

where $M_{\max} = (n-1)(J-1)$ and $\tilde{m} = 2M + 2n - 1$ we can prove that

$$\lim_{n \rightarrow \infty} |U_n| = 0$$

and therefore also

$$\lim_{n \rightarrow \infty} U_n = 0$$

Thus we have proved the convergence of the partial ray series which consist only of kinematic analogues with uniform distribution of segments into individual layers. We hope that the procedure showed the enormous difficulties encountered in the attempt to prove the convergence generally. It looks that the decision about significance of contribution from different groups of dynamic analogues must be done numerically for individual cases. We have not found any theoretical criterion according to which the ray series can be terminated at certain points with assurance that the remainder is negligible.

CONCLUSIONS

In this thesis the non-geometrical effects of the wave propagation from a point source in the Epstein medium were studied. The response of the medium in the frequency domain was expressed as an integral in the complex plane of the horizontal wavenumber. The integrand contained the source strength and the reflection coefficient that describes the change of the wave on its path from the source to the receiver. The reflection coefficient for Epstein medium is an analytic function and the integration was performed both analytically and numerically. The analytic evaluation is an asymptotic one valid only at high frequencies. The numerical integration can be performed for any frequency needed for the determination of the spectrum used to synthesize the seismograms. The approach used here to study acoustic waves in fluid media is well suited to SH waves in elastic media. In principle it can also be applied to investigation of P-SV waves in elastic media provided a suitable potential representation is employed that results in the decoupling of P and SV waves at high frequencies.

The behaviour of the response integral in the vicinity of caustics shows large amplitude decay at high frequencies. The amplitudes are much stronger at low frequencies which is the result of stronger partial reflection for longer wavelengths. In the region before the caustic that is the

illuminated region, the oscillation of amplitude due to the interference of two arriving waves is observed. The maximum amplitude is shifted from the geometrical endpoint into the illuminated region. For narrow transitions the behaviour near the caustic changes to critical point behaviour characterized by interference of the totally reflected wave and the head wave. The partial reflection is stronger and more like the sub-critical reflection from a sharp velocity increase. It is evident that the effect of finite dimensions of the transition layer on partially reflected wave and the head wave grows with increasing thickness. The dependence of the head wave amplitude changes with increasing thickness from $\frac{1}{\omega}$ to 1 and should be useful for the interpretation of data when the transition thickness is determined.

For transitions with velocity reversal the amplitude of the wave propagating along the reversal decays exponentially with distance. The "shadow" caused by this amplitude decrease is frequency independent which is quite different from a "true" shadow. The amplitude decay into the shadow caused by a sudden velocity decrease depends on $\exp(-a\omega^{1/3})$. Therefore when interpretation is done these phenomena can be used to distinguish between these two cases which on the travel-time curves have very similar characteristics.

The exact solutions for Epstein velocity profiles can be compared with approximate solutions for layered media. When the continuous Epstein structure is replaced by a layered medium, a procedure often used in seismology to find approximate solutions for inhomogeneous media, the error arising from this approximation can be estimated. This approximation, which depends on the number of layers and the wavelength of propagating waves, is good only if a very large number of layers is used. With the computers available at the present time, it is impossible to compute the synthetic seismograms by Cagniard-de Hoop technique for that many layers. Therefore we must be satisfied with less accurate approximations of the medium. But even for a small number of layers further approximations are made by considering waves that contribute most to the total amplitude and neglecting the rest. The study of the partial ray expansion shows that not only the once reflected waves are significant but that multiply reflected waves often contribute significantly as well. Their contribution grows with growing number of layers and unless they are included in the evaluation of the amplitude the results are inconclusive.

BIBLIOGRAPHY

- Abramowitz, M. and Stegun, I. A., 1965, Handbook of Mathematical Functions, Dover Publications, Inc., New York.
- Airy, G. B., 1838, On Intensity of Light in the Neighbourhood of a Caustic, Cambridge Phil. Trans. 6, 379-401.
- Alexander, S. S. and Phinney, R. A., 1966, A Study of the Core-Mantle Boundary Using P-Waves Diffracted by the Earth's Core, J. Geophys. Res. 71, 5943-5958.
- Barnes, E. W., 1908, A New Development of the Theory of Hypergeometric Functions, Proc. Lond. Math. Soc. (2) 6, 141-177.
- Bolt, B. A., 1970, PdP and PKiKP Waves and Diffracted PcP Waves, Geophys. J. R. Astr. Soc. 20, 367-382.
- Bolt, B. A., 1972, The Density Distribution Near the Base of the Mantle and Near the Earth's Center, Phys. Earth Planet. Interiors 5, 301-311.
- Brekhovskikh, L. M., 1960, Waves in Layered Media, Academic Press, Inc., New York.
- Budden, K. G., 1961, Radio Waves in the Ionosphere, Cambridge University Press, Cambridge.
- Bulirsch, R. and Stoer, J., 1966, Numerical Treatment of Ordinary Differential Equations by Extrapolation methods, Numerische Mathematik 8, 1-13.
- Bullen, K. E., 1963, An Introduction to the Theory of Seismology, Third Edition, Cambridge University Press, Cambridge.
- Cagniard, L., 1939, Réflexion et Réfraction des Ondes Seismiques Progressive, Gauthier-Villars, Paris.
- Cagniard, L., 1962, Reflection and Refraction of Progressive Seismic Waves, McGraw-Hill Book Company, Inc., New York.

- Cervený, V., 1962, On the Length of the Interference Zone of a Reflected and Head Wave Beyond the Critical Point and on the Amplitude of Head Waves, *Studia Geophys. et Geod.* 6, 49-64.
- Cervený, V. and Ravindra, R., 1971, Theory of Seismic Head Waves, University of Toronto Press, Toronto.
- Chapman, C. H., 1969, Seismic Wave Diffraction Theory, Ph.D. Thesis, Cambridge University.
- Chapman, C. H. and Phinney, R. A., 1970, Diffraction of P Waves by the Core and an Inhomogeneous Mantle, *Geophys. J. R. Astr. Soc.* 21, 185-205.
- Chapman, C. H., 1972, Lamb's Problem and Comments on the Paper 'On Leaking Modes' by Usha Gupta, *Pure Appl. Geophys.* 94, 233-247.
- Chapman, C. H. and Phinney, R. A., 1972, Diffracted Seismic Signals and Their Numerical Solution, Methods in Computational Physics, Vol. 12, 165-230, Academic Press, New York.
- Chapman, C. H., 1973, The Earth Flattening Transformation in Body Wave Theory, *Geophys. J. R. Astr. Soc.*, in press.
- Chessell, C. I., 1971, The Numerical Calculation of Reflection and Transmission Coefficients for Thin Highly Ionized Layers Including the Effect of the Earth's Magnetic Field, *J. Atmosph. Terr. Phys.* 33, 1515-1532.
- Chester, C., Friedman, B. and Ursell, F., 1957, An Extension of the Method of Steepest Descent, *Proc. Camb. Phil. Soc.* 53, 599-611.
- Cisternas, A., Betancourt, C. and Leiva, A., 1973, Body Waves in a "Real Earth", Part 1, *Bull. Seismol. Soc. Am.* 63, 145-156.
- Cooley, J. W. and Tukey, J. W., 1965, An Algorithm for the Machine Calculation of Complex Fourier Series, *Math. of Comput.* 19, 297-301.
- Copson, E. T., 1935, An Introduction to the Theory of Functions of a Complex Variable, Oxford University Press.

- Duwallo, C. and Jacobs, J. A., 1959, Effects of a Liquid Core on the Propagation of Seismic Waves, *Can. J. Phys.* 37, 109-128.
- Eisen, M., 1969, Elementary Combinational Analysis, Gordon and Breach Science Publishers, Inc., New York.
- Epstein, P. S., 1930, Reflection of Waves in an Inhomogeneous Absorbing Medium, *Proc. Nat. Acad. Sci. Wash.* 16, 627-637.
- Erdelyi, A., Magnus, W., Oberhettinger, F. and Tricomi, F. G., 1953, Higher Transcendental Functions, Vol. 1, Bateman Manuscript Project, McGraw-Hill Book Company, Inc., New York.
- Ewing, W. M., Jardetsky, W. S. and Press, F., 1957, Elastic Waves in Layered Media, McGraw-Hill Book Company, Inc., New York.
- Fuchs, K. and Müller, G., 1971, Computation of Synthetic Seismograms with the Reflectivity Method and Comparison with Observations, *Geophys. J. R. Astr. Soc.* 23, 417-433.
- Gilbert, F. and Laster, S. J., 1962, Excitation and Propagation of Pulses on an Interface, *Bull. Seismol. Soc. Am.* 52, 299-319.
- Gilbert, F., 1964, Propagation of Transient Beaking Modes in a Stratified Elastic Wave-guide, *Rev. Geophys.* 2, 123-153.
- Gilbert, F. and Backus, G. E., 1966, Propagation Matrices in Elastic Wave and Vibration Problems, *Geophys.* 31, 326-332.
- Gilbert, F. and Helmberger, D. V., 1972, Generalised Ray Theory for a Layered Sphere, *Geophys. J. R. Astr. Soc.* 27, 57-80.
- Gupta, R. N., 1966, Reflection of Elastic Waves from a Linear Transition Layer, *Bull. Seismol. Soc. Am.* 56, 511-526.
- Gutenberg, B., 1958, Velocity of Seismic Waves in the Earth's Mantle, *Trans. Am. Geophys. Union* 39, 486-489.

- Haskell, N. A., 1953, The Dispersion of Surface Waves on Multilayered Media, Bull. Seismol. Soc. Am. 43, 17-34.
- Heading, J., 1962, An Introduction to Phase-Integral Methods; Methuen's Monographs on Physical Subjects, John Wiley and Sons, Inc., New York.
- HelMBERGER, D. V., 1968, The Crust-Mantle Transition in the Bering Sea, Bull. Seismol. Soc. Am. 58, 179-214.
- HelMBERGER, D. V. and Wiggins, R. A., 1971, Upper Mantle Structure of the Midwestern United States, J. Geophys. Res. 76, 3229-3245.
- HelMBERGER, D. V., 1972, Numerical Seismograms of Long Period Body Waves from 17° to 40°, Bull. Seismol. Soc. Am., in press.
- Hill, D. P., 1971, High Frequency Wave Propagation in the Earth: Theory and Observation, Ph.D. Thesis, California Institute of Technology.
- Hill, D. P., 1972, An Earth Flattening Transformation for Waves from a Point Source, Bull. Seismol. Soc. Am. 62, 1195-1210.
- Hoop, A. T., De, 1960, A Modification of Cagniard's Method for Solving Seismic Pulse Problems, Appl. Sci. Res. B8, 349-356.
- Hron, F., 1971, Criteria for Selection of Phases in Synthetic Seismograms for Layered Media, Bull. Seismol. Soc. Am. 61, 765-779.
- Hron, F. and Kanasevich, E. R., 1971, Synthetic Seismograms for Deep Seismic Sounding Studies Using Asymptotic Ray Theory, Bull. Seismol. Soc. Am. 61, 1169-1200.
- Hron, F., 1972, Numerical Methods of Ray Generation in Multilayered Media, Methods in Computational Physics, Vol. 12, 1-34.
- Jackson, J. D., 1972, Classical Electrodynamics, John Wiley and Sons, Inc., New York.

- Jeffreys, H., 1939, The Times of Core Waves, Mon. Not. R. Astr. Soc., Geophys. Suppl. 4, 548-561.
- Jeffreys, H. and Bullen, K. E., 1940, Seismological Tables, Brit. Ass. Adv. Sci., London.
- Johnson, L. R., 1967, Array Measurements of P Velocity in The Upper Mantle, J. Geophys. Res. 72, 6309-6325.
- Julian, B. R. and Anderson, D. L., 1968, Travel Times, Apparent Velocities and Amplitudes of Body Waves, Bull. Seismol. Soc. Am. 58, 339-366.
- Knopoff, L. and Gilbert, F., 1961, Diffraction of Elastic Waves by the Core of the Earth, Bull. Seismol. Soc. Am., 51, 35-49.
- Kuki, H., 1972, Algorithm 421, Complex Gamma Function with Error Control [S14], Comm. ACM 15, 271-272.
- Lamb, H., 1904, On the Propagation of Tremors over the Surface of an Elastic Solid, Phil. Trans. Roy. Soc. London, Ser A, 203, 1-42.
- Lang, R. H. and Shmoys, J., 1968, Lateral Wave on a Symmetrical Epstein Transition, J. Appl. Phys. 39, 1670-1680.
- Lee, W. H. K., 1962, Padé Power Series Approximation for Gamma Function, unpublished UCSD manuscript.
- Lucas Jr., C. W. and Terrill, C. W., 1971, Algorithm 404, Complex Gamma Function [S14], Comm. ACM 14, 48-49.
- Merzer, A. M., 1971, Head Waves from Different Transition Layers, Geophys. J. R. Astr. Soc. 24, 77-95.
- Morse, P. M. and Feshbach, H., 1953, Methods of Theoretical Physics, McGraw-Hill Book Company, Inc., New York.
- Müller, G., 1968, Theoretical Seismograms for Some Types of Point-Sources in Layered Media, Part I: Theory, Z. Geophys. 34, 15-35.
- Müller, G., 1969, Theoretical Seismograms for Some Types of Point-Sources in Layered Media, Part II: Single Force and Dipole Sources of Arbitrary Orientation, Z. Geophys. 35, 347-371.

- Müller, G., 1970, Exact Ray Theory and its Application to the Reflection of Elastic Waves from Vertically Inhomogeneous Media, *Geophys. J. R. Astr. Soc.* 21, 261-283.
- Müller, G., 1971, Approximate Treatment of Elastic Body Waves in Media with Spherical Symmetry, *Geophys. J. R. Astr. Soc.* 23, 435-449.
- Nakamura, Y., 1964, Head Waves from a Linear Transition Layer in a Liquid, *J. Geophys. Res.* 69, 4349-4354.
- Northover, F. H., 1962, Reflection of Electromagnetic Waves from Thin Ionized Caseous Layers, *J. Res. NBS* 66D, 73-80.
- Pekeris, C. L., 1948, Theory of Propagation of Explosive Sound in Shallow Water, *Geol. Soc. Am. Mem.* 27, 43-70.
- Phinney, R. A., 1961, Leaking Modes in the Crustal Waveguide, 1, The Oceanic PL Wave, *J. Geophys. Res.* 66, 1445-1469.
- Phinney, R. A. and Alexander, S. S., 1966, P Wave Diffraction Theory and the Structure of the Core Mantle Boundary, *J. Geophys. Res.* 71, 5959-5975.
- Phinney, R. A. and Cathles, L. M., 1969, Diffraction of P by the Core: A Study of Long Period Amplitudes Near the Edge of the Shadow, *J. Geophys. Res.* 74, 1556-1574.
- Phinney, R. A. and Alexander, S. S., 1969, The Effect on a Velocity Gradient at the Base of the Mantle on Diffracted P Waves in the Shadow, *J. Geophys. Res.* 74, 4967-4971.
- Phinney, R. A., 1970, Reflection of Acoustic Waves from a Continuously Varying Interfacial Region, *Rev. Geophys. Space Phys.* 8, 517-532.
- Rawer, K., 1939, Elektrische Wellen in einem geschichteten Medium, *Ann. Physik* 35, 385-416.
- Richards, P. G., 1970, A Contribution of the Theory of High Frequency Elastic Waves, with Applications to the Shadow Boundary of the Earth's Core, Ph.D. Thesis, California Institute of Technology.

- Richards, P. G., 1971, Potentials for Elastic Displacement in Spherically Symmetric Media, *J. Acoust. Soc. Am.* 150, 188-197.
- Richards, P. G., 1973, Calculation of Body Waves for Caustics and Tunnelling in Core Phases, *Geophys. J. R. Astr. Soc.*, in press.
- Rydbeck, O. E. H., 1943, The Reflection of Electromagnetic Waves from a Parabolic Ionized Layer, *Phil. Mag.* 34, 342-348.
- Scholte, J. G. J., 1956, On Seismic Waves in a Spherical Earth, *Kon. Ned. Meteorol. Inst. Publ.* 65, 9-55.
- Teng, T. and Richards, P. G., 1969, Diffracted P, SV and SH Waves and Their Shadow Boundary Shifts, *J. Geophys. Res.* 74, 1537-1555.
- Thomson, W. T., 1950, Transmission of Elastic Waves Through a Stratified Solid Medium, *J. Appl. Phys.* 21, 89-93.
- Waddington, E., 1973, Numerical Seismograms by the Cagniard-de Hoop Method for Core Diffraction Problems, M.Sc. Thesis, University of Alberta.
- Wang, C., 1972, A Simple Earth Model, *J. Geophys. Res.* 77, 4318-4329.
- Ward, R. W., 1973, Response of Transition Zones to Nearby Sources, *Geophys. J. R. Astr. Soc.*, in press.
- Yanovskaya, T. B., 1966, Approximate Methods in Elastic Wave Theory, unpublished manuscript, Dept. of Appl. Math. and Theor. Phys., Cambridge University.

APPENDIX A TRANSCENDENTAL FUNCTIONS

This appendix contains details about some properties of the hypergeometric and Airy functions frequently used in this thesis. The results are stated for reference purposes and their justification is not included.

A.1 Hypergeometric functions

The formulae in this section are taken from Erdelyi et al. (1953, Chapter 2), Copson (1935, Chapter 10) and Abramowitz and Stegun (1965, p. 556).

The hypergeometric function

$$F(a, b; c; \xi) = \sum_{n=0}^{\infty} \frac{(a)_n (b)_n}{(c)_n} \frac{\xi^n}{n!} \quad \text{A.1.1}$$

where

$$(a)_n = \frac{\Gamma(a+n)}{\Gamma(a)}$$

is a solution of the hypergeometric equation

$$\xi(1-\xi) \frac{d^2\phi}{d\xi^2} + \{c-(a+b+1)\xi\} \frac{d\phi}{d\xi} - ab\phi = 0 \quad \text{A.1.2}$$

The equation A.1.2 has three regular singularities at $\xi_1 = 0$, $\xi_2 = 1$ and $\xi_3 = \infty$. Copson (1935, p. 237) shows that a second order differential equation with regular singularities has two independent solutions in terms of series. These series are

convergent in certain regions near the regular singularities.

For equation A.1.2 the series solutions are:

$$\text{at } \xi_1 = 0 \quad \Phi_1 = F(a, b; c; \xi)$$

$$\Phi_2 = (-\xi)^{1-c} F(a-c+1, b-c+1; 2-c; \xi)$$

$$\text{at } \xi = 1 \quad \Phi_3 = F(a, b; a+b+1-c; 1-\xi)$$

$$\Phi_4 = (1-\xi)^{c-a-b} F(c-b, c-a; c-a-b+1; 1-\xi)$$

$$\text{at } \xi = \infty \quad \Phi_5 = (-\xi)^{-b} F(b, b-c+1; b-a+1; \xi^{-1})$$

$$\Phi_6 = (-\xi)^{-a} F(a, a-c+1; a-b+1; \xi^{-1})$$

A.1.3

The hypergeometric function $\Phi_1 = F(a, b; c; \xi)$ is defined by the series solution in region $|\xi| < 1$ and by the analytic continuation for $|\xi| > 1$. It is regular for $|\xi| < 1$ and we shall see from its analytic continuation that it has two branch points at $\xi_2 = 1$ and $\xi_3 = \infty$.

The analytic continuation is possible due to the fact, that regions of convergence around each singularity have common regions through which the line of continuation can be drawn. At the same time, an integral solution was found by

Barnes (1908) which is valid everywhere in ξ plane with exception of the singularities ξ_1 , ξ_2 and ξ_3 :

$$I_B(\xi) = \frac{\Gamma}{2\pi i} \int_{-1-i\infty}^{1-i\infty} \frac{\Gamma(a+s)\Gamma(b+s)\Gamma(-s)}{\Gamma(c+s)} (-\xi)^s ds \quad A.1.4$$

The evaluation of this integral in different regions of ξ plane which correspond to the regions of convergence around the singularities gives the correct analytic continuation for every solution in A.1.3. By contour integration in the complex s plane along curve C_1 (Fig. A.1) we get for $|\xi| < 1$.

$$I_B(\xi) = \frac{\Gamma(a)\Gamma(b)}{\Gamma(c)} \cdot F(a, b; c; \xi) \quad A.1.5$$

(Copson, 1935; p. 254). C_1 avoids all poles of the integrand in A.1.4 except those of $\Gamma(-s)$.

For $|\xi| > 0$ the integration in the complex s plane is performed along curve C_2 which avoids all poles of $\Gamma(-s)$. Thus we get

$$I_B(\xi) = \frac{\Gamma(b-a)\Gamma(a)}{\Gamma(c-a)} (-\xi)^{-a} F(a, a-c+1; a-b+1; \xi^{-1}) + \frac{\Gamma(a-b)\Gamma(b)}{\Gamma(c-b)} (-\xi)^{-b} F(a, b-c+1; b-a+1; \xi^{-1})$$

A.1.6

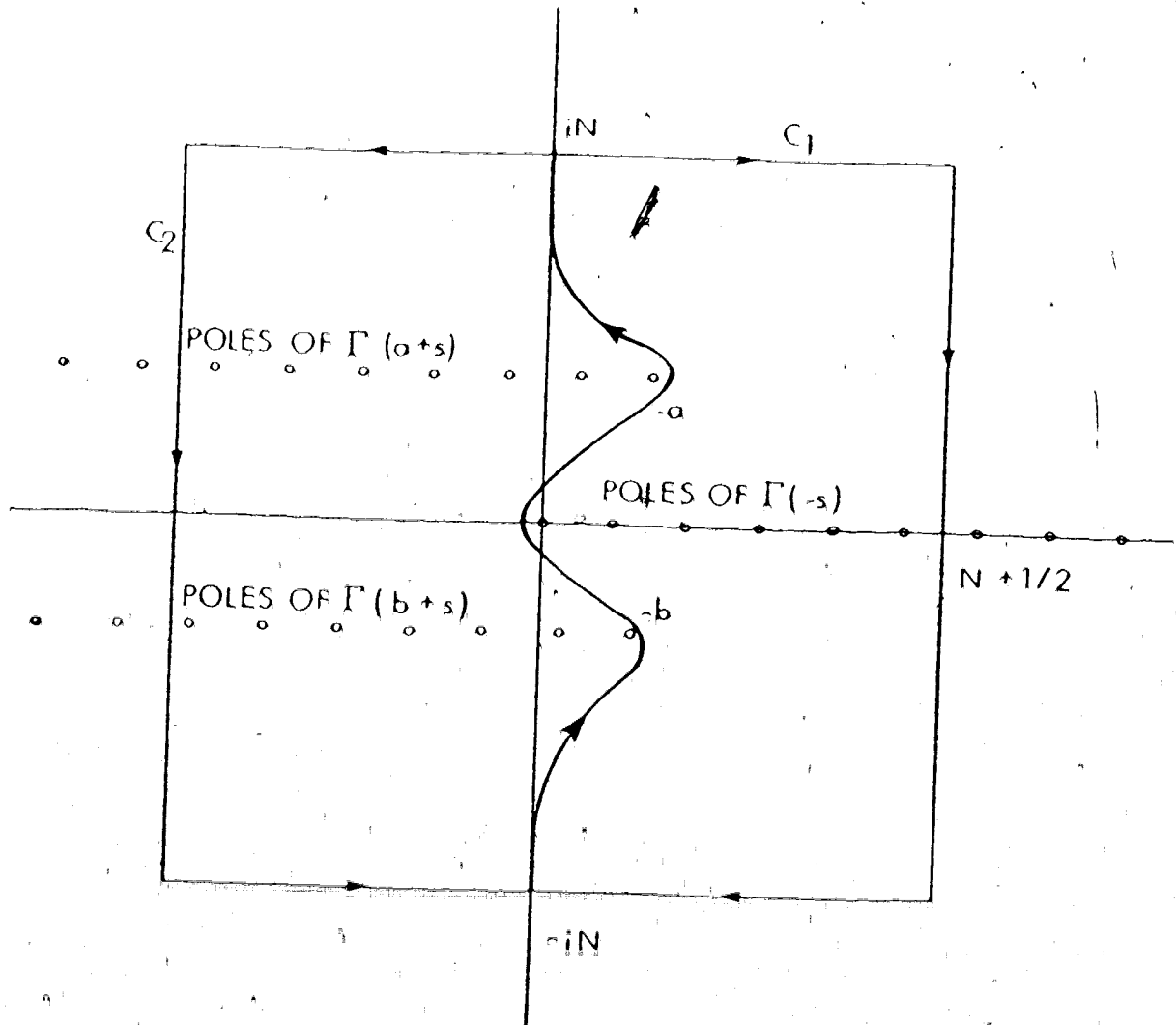


Figure A.1 The complex s plane showing contour for Barnes integral.

for $|\xi| > 1$. The formula

$$\phi_1 = \frac{\Gamma(a-b)\Gamma(c)}{\Gamma(c-b)\Gamma(a)} \phi_5 + \frac{\Gamma(b-a)\Gamma(c)}{\Gamma(c-a)\Gamma(b)} \phi_6 \quad \text{A.1.7}$$

gives the correct analytic continuation of ϕ_1 . It defines the hypergeometric function ϕ_1 for $|\xi| > 1$. Similar formulae can be obtained for all hypergeometric functions A.1.3.

The method of analytic continuation is well demonstrated through matrix notation. If $1\underline{\phi}$ denotes a column vector of solutions convergent around ξ_1 and $1j\underline{A}$ a matrix of analytic continuation from region ξ_1 to region ξ_j , we can write

$$1\underline{\phi} = 1j\underline{A} 1\underline{\phi} \quad 1, j = 1, 2, 3 \quad \text{A.1.8}$$

$$1\underline{\phi} = \begin{pmatrix} \phi_1 \\ \phi_2 \end{pmatrix}, \quad 2\underline{\phi} = \begin{pmatrix} \phi_3 \\ \phi_4 \end{pmatrix}, \quad 3\underline{\phi} = \begin{pmatrix} \phi_5 \\ \phi_6 \end{pmatrix} \quad \text{A.1.9}$$

The following expression demonstrates the analytic continuation of $1\underline{\phi}$ throughout the entire ξ plane;

$$1\underline{\phi} = 12\underline{A} 2\underline{\phi} = 12\underline{A} \cdot 23\underline{A} 3\underline{\phi} = 13\underline{A} 3\underline{\phi} \quad \text{A.1.10}$$

It is easy to realize that $13\underline{A}^{-1} = 31\underline{A}$. The elements of the matrices of analytic continuation can be found from the connection formulae between different solutions which are

listed in Erdelyi et al. (1953, p. 106). We are interested mainly in matrix ${}_{31}\underline{A}$ which is

$${}_{31}\underline{A} = \begin{pmatrix} A_{51} & A_{52} \\ A_{61} & A_{62} \end{pmatrix} = \begin{pmatrix} \frac{\Gamma(1-c)\Gamma(1+b-a)}{\Gamma(1-a)\Gamma(1+b-c)} & \frac{\Gamma(c-1)\Gamma(1+b-a)}{\Gamma(c-a)\Gamma(b)} \\ \frac{\Gamma(1-c)\Gamma(1+a-b)}{\Gamma(1-b)\Gamma(1+a-c)} & \frac{\Gamma(c-1)\Gamma(1+a-b)}{\Gamma(c-b)\Gamma(a)} \end{pmatrix}$$

A.1.11

The indices of the elements of the matrix are due to the components of the vectors they are connecting:

$${}_{3}\underline{\Phi} = \begin{pmatrix} \Phi_5 \\ \Phi_6 \end{pmatrix} = \begin{pmatrix} A_{51} & A_{52} \\ A_{61} & A_{62} \end{pmatrix} \begin{pmatrix} \Phi_1 \\ \Phi_2 \end{pmatrix} = {}_{31}\underline{A} \underline{1}\underline{\Phi} \quad \text{A.1.12}$$

This may seem redundant but for use in Chapter 3 it proves useful. Similarly, for matrix ${}_{13}\underline{A}$ we have

$${}_{13}\underline{A} = \begin{pmatrix} A_{15} & A_{16} \\ A_{25} & A_{26} \end{pmatrix} = \begin{pmatrix} A_{62} & -A_{52} \\ -A_{61} & A_{51} \end{pmatrix} = \frac{1}{\det {}_{31}\underline{A}} \quad \text{A.1.13}$$

where $\det {}_{31}\underline{A} = \frac{a-b}{c-1} = (\det {}_{13}\underline{A})^{-1}$

A.2 Airy functions and Stokes phenomenon

The results and formulae presented in this appendix are taken from Budden (1961, Chapter 15) and Abramowitz and Stegun (1965, p. 446).

Solutions to the differential equation

$$\frac{d^2 w}{d\chi^2} - \chi w = 0 \quad \text{A.2.1}$$

are Airy functions $Ai(\chi)$, $Bi(\chi)$ or $Ai(\chi e^{\pm \frac{2\pi i}{3}})$ or any linear combination. The following linear relation connects them

$$\begin{pmatrix} Ai(\chi) \\ Bi(\chi) \end{pmatrix} = \underline{M} \begin{pmatrix} Ai(\chi e^{\frac{2\pi i}{3}}) \\ Ai(\chi e^{-\frac{2\pi i}{3}}) \end{pmatrix} \quad \text{A.2.2}$$

The elements of the matrix are given by Abramowitz and Stegun (1965, p. 446)

$$\underline{M} = \begin{pmatrix} e^{-\frac{\pi i}{3}} & e^{\frac{\pi i}{3}} \\ e^{\frac{\pi i}{6}} & e^{-\frac{\pi i}{6}} \end{pmatrix} \quad \text{A.2.3}$$

For real $\chi < 0$, $Ai(\chi)$ and $Bi(\chi)$ represent oscillatory solutions which in wave propagation can be thought of as standing waves.

For $\chi > 0$ real, $Ai(\chi)$ is exponentially decaying while $Bi(\chi)$ grows exponentially (Fig. A.2). This is evident from their

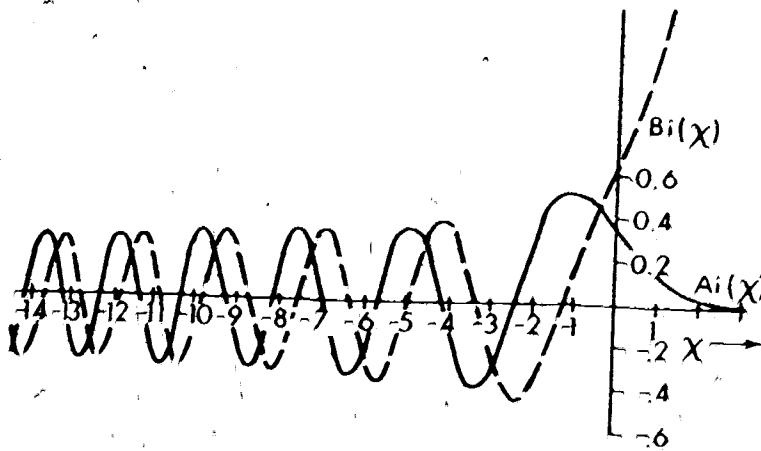


Figure A.2 Airy functions $Ai(x)$, $Bi(x)$ for real values of x . (Budden, 1961; p. 290).

asymptotic expressions which are in fact linear combinations of the WKBJ solutions to A.2.1:

$$A_1(\chi) = \frac{1}{2}\pi^{-\frac{1}{2}} \chi^{-\frac{1}{2}} e^{-\frac{2}{3}\chi^{3/2}} \quad |\arg \chi| < \pi$$

$$A_1(\chi) = \pi^{-\frac{1}{2}} |\chi|^{-\frac{1}{2}} \sin\left(\frac{2}{3}|\chi|^{3/2} + \frac{\pi}{4}\right) \quad |\arg(-\chi)| < \frac{2}{3}\pi$$

A.2.4

From this we get asymptotic formulae for $A_1(\chi e^{\pm \frac{2\pi i}{3}})$ on the negative real χ axis in the form:

$$A_1(\chi e^{\pm \frac{2\pi i}{3}}) = \frac{1}{2}\pi^{-\frac{1}{2}} |\chi|^{-\frac{1}{2}} e^{\pm \frac{\pi i}{12}} e^{\pm \frac{2}{3}|\chi|^{3/2}} \quad |\arg \chi| < \pi$$

A.2.5

Thus in application to wave propagation $A_1(\chi e^{\pm \frac{2\pi i}{3}})$ represents a wave travelling in positive χ direction while $A_1(\chi e^{-\frac{2\pi i}{3}})$ is a wave travelling in negative χ direction.

The asymptotic behaviour of the function $A_1(\chi)$ is described in different regions of the χ plane by different linear combinations of the WKBJ solutions. This property of the asymptotic approximations to the solutions of the differential equations is called "Stokes phenomenon". The WKBJ solutions of A.2.1 are

$$w = \chi^{-\frac{1}{2}} e^{\pm \frac{2}{3}\chi^{3/2}} \quad |\chi| \gg \frac{1}{2} \quad \text{A.2.6}$$

They are in fact the second order saddle point contributions of the integrand in Airy integral (Fig. A.3)

$$A_1(\chi) = \frac{1}{2\pi i} \int_{C_1} e^{-\frac{1}{3}y^3 + \chi y} dy \quad A.2.7$$

Two saddle points at $y = \pm \chi^{1/2}$ give the contributions

$$\frac{1}{2} \pi^{-1/2} \chi^{-1/2} e^{\pm \frac{2}{3} \chi^{3/2}}$$

which differ from the WKB solutions A.2.6 only by constant factors. On the lines $\arg \chi = 0, \frac{2\pi}{3}, -\frac{2\pi}{3}$ the exponents in A.2.6 are purely real. These lines are called the Stokes lines and one solution always exponentially grows with $|\chi|$ increasing and we call this the dominant solution. The other decays and is called the subdominant solution. On the lines $\arg \chi = \frac{\pi}{3}, \pi, -\frac{\pi}{3}$ the exponent in A.2.6 is purely imaginary, the solutions have equal moduli and have an oscillatory character. We call these lines the anti-Stokes lines. The region between two anti-Stokes lines are called the Stokes regions where both solutions are present - the dominant and the subdominant. If we evaluate the Airy integral A.2.7 and $|\arg \chi| < \frac{2\pi}{3}$ the contour C_1 passes only through one saddle point $y = \chi^{1/2}$ (Fig. A.4.a). For $|\arg \chi| = \frac{2\pi}{3}$ the second saddle point contribution must be considered too as C_1 passes through

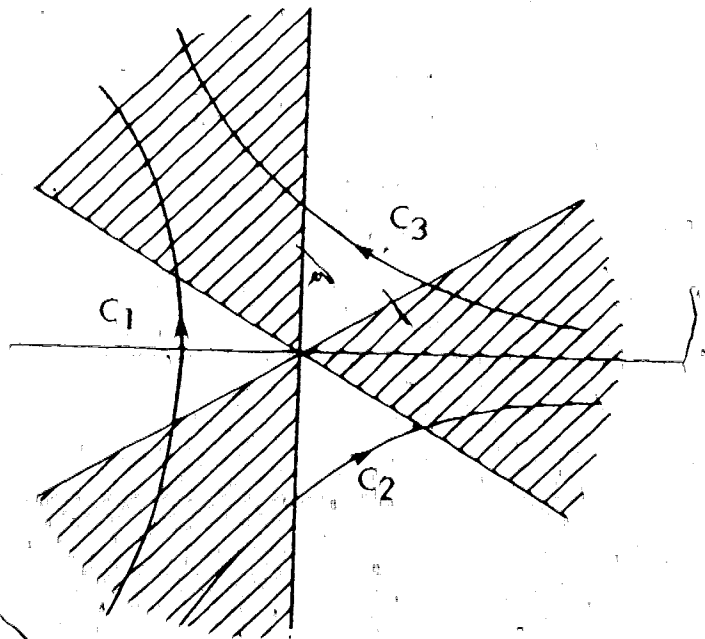
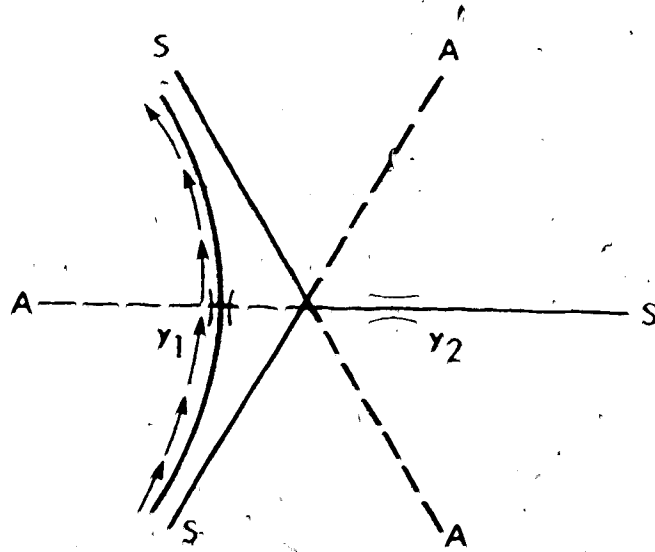
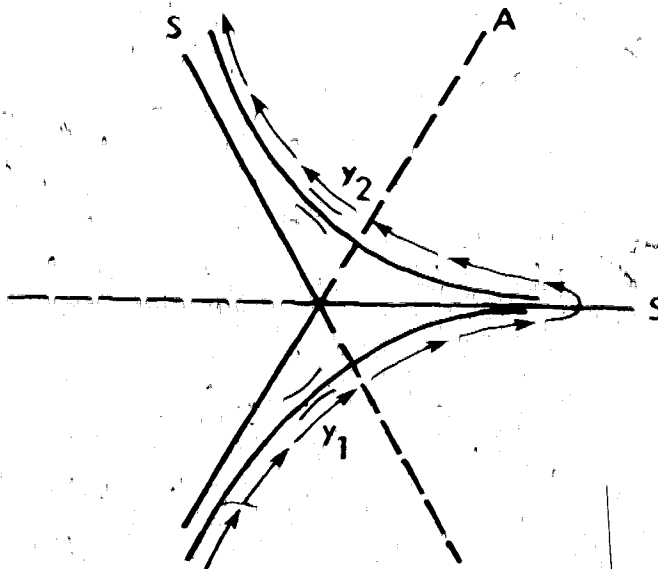


Figure A.3 The complex y plane. The curve C_1 can be distorted to coincide with the contours $C_2 + C_3$. The ends of contours must be restricted to the shaded regions. (Budden, 1961; p. 289).



a)



b)

Figure A.4 Complex y plane with Stokes lines (S) and anti-Stokes lines (A) of the Airy functions. The position of saddle points y_1 , y_2 changes with $\arg \chi$ in $\text{Ai}(\chi)$. Arrows show the path of integration (a) for $\arg \chi = 0$, (b) for $\arg \chi = \pi$ (Budden, 1961; p. 303 and 307).

both saddles $y = \pm \chi^{1/2}$ (Fig. A.4.b). This is why the Stokes phenomenon occurs. On the Stokes lines the error introduced by the saddle point method of evaluation of the integral is greater than the subdominant term obtained from the contribution of the other saddle point. This is why we can neglect the subdominant term on the Stokes lines and express the asymptotic approximation only as one WKBJ solution. The detailed study of the Stokes phenomena for all four Airy functions can be found in Budden (1961, p. 294). The Stokes diagram in Fig. A.5 shows the asymptotic behaviour of $A_1(\chi)$ and $B_1(\chi)$ in dependence on $\arg \chi$. For any argument a line inside the circle means the subdominant term is present and a line outside the circle means the dominant term is present.

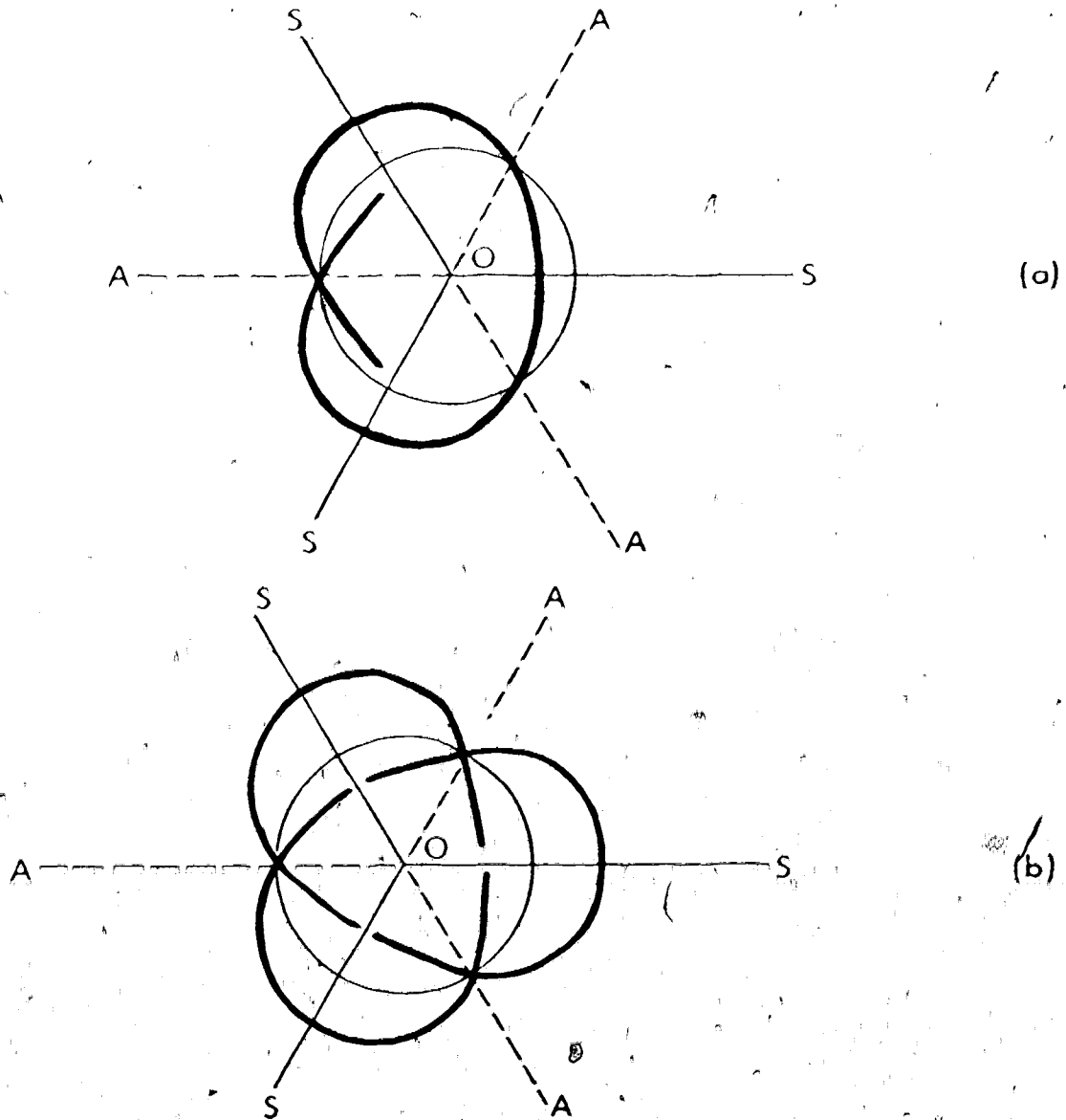


Figure A.5 Stokes diagram for the functions
(a) $A_1(\chi)$, (b) $B_1(\chi)$. (Budden, 1961;
p. 294).

APPENDIX B VALIDITY OF THE REFLECTION COEFFICIENT

The reflection coefficient for Epstein velocity transitions was found in Chapter 3. From (3.16) we get

$$R(\beta_s) = \frac{\Gamma(c-1)\Gamma(1-a)\Gamma(1+b-c)}{\Gamma(c-a)\Gamma(b)\Gamma(1-c)} \cdot \frac{F(a-c+1, b-c+1; 2-c; -e^{\beta_s})}{F(a, b; c; -e^{\beta_s})} e^{-(c-1)\beta_s} \quad (B.1)$$

for $\beta_r = \beta_s \ll 0$. This is only valid when the leading term in the hypergeometric series is considered i.e. far from the transition region. The remaining terms are dependent on frequency and thickness, since from (3.18) for ρ constant

$$c-1 = 2l\sigma q_1 = 1 \text{ S } \cos \theta_1$$

$$a-b = 2l\sigma q_2 = 1 \text{ S } \left(\frac{v_1^2}{v_2^2} - \sin^2 \theta_1 \right)^{1/2}$$

$$a+b-c = \pm (1 + 16\sigma^2 (q_0^2 - \frac{1}{2}(q_1^2 + q_2^2)))$$

For monotonic velocity transition, $a+b-c = \pm 1$. First we show that the sign in the third equation is arbitrary and does not effect the results. We introduce new variables

$$a-b = 2\alpha$$

$$a+b = 2\beta \quad \text{where} \quad \beta = c \pm \frac{1}{2} \quad (B.2)$$

and the reflection coefficient becomes

$$R(\beta_s) = \left\{ \frac{\Gamma(c-1)\Gamma(1-\alpha-\frac{c}{2}+\frac{1}{2})\Gamma(1-\alpha-\frac{c}{2}+\frac{1}{2})}{\Gamma(1-c)\Gamma(-\alpha+\frac{c}{2}+\frac{1}{2})\Gamma(-\alpha+\frac{c}{2}+\frac{1}{2})} \right\} \cdot \left\{ \frac{F(1+\alpha-\frac{c}{2}+\frac{1}{2}, 1-\alpha-\frac{c}{2}+\frac{1}{2}; 2-c; -e^{\beta_s})}{F(\alpha+\frac{c}{2}+\frac{1}{2}, -\alpha+\frac{c}{2}+\frac{1}{2}; c; -e^{\beta_s})} \right\}$$

(B.3)

The term in the first curly brackets is evidently invariable to the change of sign. It remains to prove that

$$\frac{F(g, h; 2-c; -e^{\beta_s})}{F(-h, -g; c; -e^{\beta_s})} = \frac{F(g+1, h+1; 2-c; -e^{\beta_s})}{F(-h+1, -g+1; c; -e^{\beta_s})} \quad (\text{B.4})$$

where

$$g = \alpha - \frac{c}{2} + \frac{1}{2} \quad \text{and} \quad h = \alpha - \frac{c}{2} + \frac{1}{2}$$

From Abramowitz and Stegun (1965) formula 15.2.14 we get that the L.H.S. of the equation (B.4) is equal to

$$\text{L.H.S.} = \frac{h F(g, h+1; 2-c; -e^{\beta_s}) - g F(g+1, h; 2-c; -e^{\beta_s})}{h F(-h+1, -g; c; -e^{\beta_s}) - g F(-h, -g+1; c; -e^{\beta_s})}$$

(B.5)

From formula 15.2.19 of Abramowitz and Stegun (1965) we get that the R.H.S. of (B.4) is equal to (B.5). Thus the expression (B.3) is invariable with respect to the change of sign. To assess the validity of the reflection coefficient in (B.1) we must evaluate the absolute values of the second terms in the hypergeometric series:

$$F(a, b; c; -e^{z_s}) = 1 - \frac{ab}{c} e^{z_s} + o(e^{2z_s})$$

$$F(a+1-c, b+1-c; 2-c; -e^{z_s}) = 1 - \frac{(a+1-c)(b+1-c)}{2-c} e^{z_s} + o(e^{2z_s})$$

$$\Delta_1 = \left| \frac{ab}{c} \right| = \left| \frac{(a+1-c)(b+1-c)}{2-c} \right| = \frac{1}{2} S^2 \left(1 - \frac{v_1^2}{2} \right) (1 + S^2 \cos^2 \theta_1)^{-\frac{1}{2}}$$

for $v_1 \leq v_2$. Thus the condition for validity of the reflection coefficient (B.1) is

$$|z_s| \gg \log \Delta_1 \quad (B.6)$$

Where $z_r \neq z_s$, the same condition applies to z_r concurrently.

The transmission coefficient (3.17) for $z_t = |z_s|$ is

$$T(z_t) = \frac{\Gamma(1-a)\Gamma(1+b-c)}{\Gamma(1+b-a)\Gamma(1-c)} \cdot \frac{F(b, b-c+1; b-a+1; -e^{-z_t})}{F(a, b; c; -e^{-z_t})} e^{\frac{c-1}{2} z_t + \frac{a-b}{2} z_t}$$

(B.7)

and

$$F(b, b-c+1; b-a+1; -e^{-\beta t}) = 1 - \frac{b(b-c+1)}{b-a+1} e^{-\beta t} + o(e^{-2\beta t})$$

The transmission coefficient is valid if

$$|\beta t| \gg \log \Lambda_1 > \log \Lambda_2 \quad (\text{B.8})$$

where

$$\Lambda_2 = \left| \frac{b(b-c+1)}{b-a+1} \right| = \frac{1}{2} S^2 \left(1 - \frac{v^2}{2} \right) \left(1 + S^2 \left(\frac{v^2}{2} - \sin^2 \theta_1 \right) \right)^{-\frac{1}{2}}$$

For $|\beta t| \gg \beta t$ the condition (B.6) applies as well.

The condition (B.6) is satisfied for models (4.49), (4.50), (4.51) and (5.34) in the frequency range used in this thesis:

APPENDIX C CONVERGENCE OF THE RESPONSE INTEGRALS

To evaluate the response integral (2.22) we must evaluate the inverse Bessel transform

$$P(\omega, r, \zeta_r) = \frac{1}{2} \cdot \frac{\rho_o}{\rho_s} P_s(\omega) \int_0^{\infty} R(\zeta_s, \zeta_r, \kappa) J_0(\kappa r) \frac{\kappa}{q_s} d\kappa \quad (C.1)$$

where $R(\zeta_s, \zeta_r, \kappa)$ is given by (4.2) or (5.2). If we use the following properties of the Bessel functions

$$\begin{aligned} J_\lambda(\kappa r) &= \frac{1}{2} [H_\lambda^{(1)}(\kappa r) + H_\lambda^{(2)}(\kappa r)] \\ H_0^{(1)}(\kappa r) &= -H_0^{(2)}(-\kappa r) \end{aligned} \quad (C.2)$$

the response integral (C.1) becomes

$$P(\omega, r, \zeta_r) = \frac{1}{4} \cdot \frac{\rho_o}{\rho_s} P_s(\omega) \int_{-\infty}^{+\infty} R(\zeta_s, \zeta_r, \kappa) H_0^{(1)}(\kappa r) \frac{\kappa}{q_s} d\kappa \quad (C.3)$$

The integrand in (C.3) is a multivalued function due to vertical wavenumber q . The complex κ plane consists of different Riemann surfaces given by different values of the square roots. The passage from one Riemann surface at a branch cut which is defined as any line connecting two branch points

often via infinity. Its choice is arbitrary, depending on the problem solved. The contour of integration along the real axis can be moved into any suitable position, provided it starts and ends on the same Riemann sheet, and, at the same time, the contributions from any singularities enclosed or crossed are taken into account.

For the velocity reversal the reflection coefficient is given by (5.2)

$$R(\zeta_s, \zeta_r, \kappa) = - \frac{\Gamma(1+2i\sigma q_1)}{\Gamma(1-2i\sigma q_1)} \frac{\Gamma(\frac{1}{2}-2i\sigma q_1-\gamma)\Gamma(\frac{1}{2}-2i\sigma q_1+\gamma)}{\Gamma(\frac{1}{2}-\gamma)\Gamma(\frac{1}{2}+\gamma)} e^{-1(q_s \zeta_s + q_r \zeta_r)}$$

and the contour of integration in (C.3) can be moved to position in Figure 5.5 which is the steepest descent path. There are no poles in the first quadrant beyond the branch cut nor in the second. Only the poles $\pm i\kappa_n$ (5.12) on the real axis exist and the contour is taken initially above these.

The contribution along the arcs tends to zero as their radius grows to infinite values. For κ large the asymptotic expression for the reflection coefficient (5.22) may be used:

$$R(\zeta_s, \zeta_r, \kappa) \sim e^{i\phi(\kappa)}$$

where

$$\begin{aligned} \phi(\kappa) = & -q_s \zeta_s - q_r \zeta_r + 2\sigma q_1 \log \frac{4\sigma^2 q_1^2}{(\frac{1}{2}-2i\sigma q_1)^2 - \gamma^2} \\ & - i\gamma \log \frac{(\frac{1}{2}-2i\sigma q_1+\gamma)(\frac{1}{2}-\gamma)}{(\frac{1}{2}-2i\sigma q_1-\gamma)(\frac{1}{2}+\gamma)} \end{aligned}$$

For large argument the asymptotic expression for $H_0^{(1)}(\kappa r)$ is used

$$H_0^{(1)}(\kappa r) \sim \sqrt{\frac{2}{\pi \kappa r}} \cdot e^{i\kappa r - i\frac{\pi}{4}} \quad (C.4)$$

(formula 9.2.3 in Abramowitz and Stegun, 1965).

(1) If $\kappa = \text{Re} \kappa + i \text{Im} \kappa$ and $\text{Re} \kappa \rightarrow +\infty$ while $\text{Im} \kappa = 0$ we can do the following estimates:

$$\begin{aligned} \left| \frac{\kappa}{q_s} \right| &\sim 1 \\ H_0^{(1)}(\kappa r) &\sim |\kappa|^{-\frac{1}{2}} \rightarrow 0 \end{aligned} \quad (C.5)$$

and the reflection coefficient

$$|R(\zeta_s, \zeta_r, \kappa)| \sim e^{\zeta_s \text{Im} q_s + \zeta_r \text{Im} q_r} \rightarrow 0 \quad (C.6)$$

since $\text{Im} q_s > 0$, $\text{Im} q_r > 0$, $\zeta_s < 0$ and $\zeta_r < 0$.

(2) If $\text{Im} \kappa \rightarrow +\infty$ and $\text{Re} \kappa \rightarrow 0$ or $\text{Re} \kappa \rightarrow +\frac{\omega}{v_1}$, the following estimates can be made:

$$\begin{aligned} \left| \frac{\kappa}{q_s} \right| &\sim 1 \\ |H_0^{(1)}(\kappa r)| &\sim e^{-r \text{Im} \kappa} \cdot |\kappa|^{-\frac{1}{2}} \rightarrow 0 \end{aligned} \quad (C.7)$$

and

$$|R(\zeta_s, \zeta_r, \kappa)| \sim e^{-2\pi \sigma \text{Re} q_1} \rightarrow 0 \quad (C.8)$$

because $\text{Re} q_1 > 0$.

h

This proves that the contributions due to integration along the arcs can be neglected. Thus for the velocity reversal the main contribution to the response integral (C.3) is from the integration along the steepest descent path in Figures 5.5 and 5.6.

At high frequencies where the saddle point approximation is valid the saddle point close to $\frac{\omega}{v_0}$ represents wave effected most by the velocity reversal as was explained in Chapter 5. This saddle point approaches the pole 2^{κ_0} (5.13), (5.17) and is influenced by it. The integration contour can be moved so that it passes between the j -th and $(j+1)$ -th pole of the string 2^{κ_n} if we include their contribution. The residue contribution of the reflection coefficient at the j -th pole is

$$2\pi i \operatorname{Res} [R(\zeta_r, \zeta_r, 2^{\kappa_j})] = \frac{\pi \cos^2 \pi \gamma}{\sigma \sin 2\pi \gamma} (-1)^j \frac{q_{1j}}{2^{\kappa_j}} \frac{(j+\frac{1}{2}+\gamma)\Gamma^2(j+\frac{1}{2}+\gamma)}{\Gamma(j+1)\Gamma(j+1+2\gamma)} e^{-i(q_{sj}\zeta_s + q_{rj}\zeta_r)} \quad (C.9)$$

The remaining term in the integrand is

$$|H_o^{(1)}(2^{\kappa_j r}) \frac{2^{\kappa_j}}{q_{sj}}| \sim \sqrt{\frac{2|2^{\kappa_j}|}{\pi r}} \frac{1}{|q_{sj}|} e^{-r \operatorname{Im} 2^{\kappa_j}} \quad (C.10)$$

and $q_{pj} = \left(\frac{\omega^2}{v_p^2} - 2^{\kappa_j}\right)^{1/2}$ for $p = 1, s$ or r .

The residue series whose terms are (C.9) is not convergent. This becomes evident if the Stirling approximation for the gamma function is used

$$\Gamma(z) \sim (2\pi)^{-1/2} e^{-z} z^{z-1/2} \quad z \rightarrow \infty, \quad |\arg z| < \pi \quad (\text{C.11})$$

(formula 6.1.37 in Abramowitz and Stegun, 1965). Then

$$\frac{(j+\frac{1}{2}+\gamma)\Gamma^2(j+\frac{1}{2}+\gamma)}{\Gamma(j+1)\Gamma(j+1+2\gamma)} \sim e^{-1+\frac{1}{2}\log \frac{(j+1+2\gamma)(j+1)}{(j+\frac{1}{2}+\gamma)^2} + j \log \frac{(j+\frac{1}{2}+\gamma)^2}{(j+\frac{1}{2}+2\gamma)(j+1)}}$$

$$\sim e^{2\gamma \log \frac{(j+\frac{1}{2}+\gamma)}{(j+1+2\gamma)}} \rightarrow \infty \text{ as } j \rightarrow \infty$$

The term

$$\left| e^{-1(q_{sj}\zeta_s + q_{rj}\zeta_r)} \right| \sim e^{\zeta_s \text{Im } q_{sj} + \zeta_r \text{Im } q_{rj}} \rightarrow \infty$$

because $\text{Im } q_{sj} < 0$, $\text{Im } q_{rj} < 0$, $\zeta_s < 0$, $\zeta_r < 0$. Only if the exponential decay of the Hankel function due to distance overcomes the exponential growth of the reflection coefficient, the residue series will decrease for poles up to certain order. This happens at large distances r and then, only the zeroth pole is important and the rest can be neglected. It is not possible, however, to write the response as a complete residue series; we can only include the low order poles, say k , whose contribu-

tion decreases as order increases. The residue series forms an asymptotic series. That means the contour passes between k -th and $(k+1)$ -th poles. The remainder of the contour integration is of the same order of magnitude as the residue contribution of the $(k+1)$ -th pole. If the higher order poles were included the integral would increase in magnitude. The order k when the series should be terminated depends on distance: as range increases k also increases. This is due to the rapid decay given by distance between the poles

$$r = \text{Im}(2^{\kappa_{k+1}} - 2^{\kappa_k}) \gg 1 \quad (\text{C.12})$$

In such cases only the zeroth order pole need be considered.

If the residue of the zeroth order pole given by

$$|2\pi i \text{Res } R(\zeta_s, \zeta_r, 2^{\kappa_0})| \approx \left(\frac{\pi}{2}\right)^{\frac{1}{2}} \frac{1}{\sigma} \left|\frac{q_{10}}{2^{\kappa_0}}\right| e^{\zeta_s \text{Im} q_{s0} + \zeta_r \text{Im} q_{r0} + \frac{1}{2} \log \frac{\frac{1}{2} + \bar{\gamma}^2}{2\bar{\gamma}}}$$

$$\text{where } \gamma = 1 - \bar{\gamma} \quad (\text{C.13})$$

is of comparable modulus as the exponential term from $H_0^{(1)}(\kappa r)$ (C.10), the residue of the first pole contribution

$$|2\pi i \text{Res } R(\zeta_s, \zeta_r, 2^{\kappa_1})| \approx \left(\frac{\pi}{2}\right)^{\frac{1}{2}} \frac{1}{\sigma} \left|\frac{q_{11}}{2^{\kappa_1}}\right| e^{2 + \zeta_s \text{Im} q_{s1} + \zeta_r \text{Im} q_{r1} + \frac{1}{2} \log \frac{(\frac{1}{2} + \bar{\gamma}^2)(\frac{9}{4} + \bar{\gamma}^2)^2}{8(1+4\bar{\gamma})^{3/2}} + 2\bar{\gamma} \arctan 2\bar{\gamma} - \bar{\gamma} \arctan \frac{\bar{\gamma}}{2 - \frac{3}{4}}}$$

$$(\text{C.14})$$

is greater and the residue series grows from the very beginning. This happens in the "illuminated" region and the integral cannot be evaluated by method of residues.

For monotonic velocity transition the reflection coefficient in (C.3) is given by (4.2). The steepest descent path is shown in Figures 4.8 and 4.9. The integrand tends to zero in the second quadrant of complex κ plane and also in the first quadrant beyond the branch cut of q_1 . This can be proved in the same way as that used above in the case of velocity reversal (Eqs. (C.5), (C.6), (C.7) and (C.8)) provided we take the approximate reflection coefficient (4.17). The steepest descent path in Figure 4.8 ends in the valley above the real axis and if the original contour was deformed in this direction it would cross the branch cut. Thus we should return along the branch cut and then the contour can end anywhere in the first quadrant beyond the branch cut. The steepest descent path in Figure 4.9 leads in the valley in the third quadrant. The contour cannot be distorted to end in the third quadrant as the integrand does not decay there with $|\kappa|$ growing. Again the integration should return to the real axis or first quadrant.

APPENDIX D ALGORITHMS FOR SPECIAL FUNCTIONS NEEDED FOR
EVALUATION OF THE RESPONSE INTEGRAL

D.1 Complex gamma function

An algorithm for evaluation of the complex gamma function and its logarithm had to be developed in order to evaluate the reflection coefficient (3.22). At the time when this work had begun no standard program was available and we will describe here the algorithm developed for use in our computations. Since then, several algorithms appeared in literature as, for example, Algorithm 404, Complex gamma function, by Lucas and Terill (1971) and Algorithm 421, Complex gamma function with error control by Kuki (1972).

The inverse gamma function $\frac{1}{\Gamma(z)}$ and the logarithm $\log_e(\Gamma(z))$ for z complex were computed using the following methods:

$$\Gamma(z^*) = \Gamma^*(z) \quad (D.1.1)$$

(formula 6.1.23 from Abramowitz and Stegun, 1965, henceforth referred to as Ref. 1) is used to restrict the argument into the first and second quadrants of the complex z plane

$$\Gamma(z) = \frac{1}{z} \Gamma(z + 1) \quad (D.1.2)$$

(6.1.15 in Ref. 1) is used to move the argument into the first quadrant so that

$$(a) \operatorname{Re}(z) \geq 0 \quad \text{if} \quad \operatorname{Im}(z) \leq 2$$

$$(b) \operatorname{Re}(z) \geq 10 \quad \text{if} \quad \operatorname{Im}(z) > 2$$

The asymptotic formula is used to evaluate the $\log_e \Gamma(z)$ if $\operatorname{Re}(z) \geq 10$:

$$\log_e \Gamma(z) \sim (z - \frac{1}{2}) \log_e z - z + \frac{1}{2} \log_e (2\pi) + \frac{1}{12z} - \frac{1}{360z^3}$$

(D.1.3)

(6.1.41 in Ref. 1). If $\operatorname{Re}(z) < 10$ the following relations are used to restrict the argument so that $0 \leq \operatorname{Re}(z) \leq 1$ and $0 < \operatorname{Im}(z) \leq 0$. The Gauss multiplication formula

$$\log_e \Gamma(nz) = \frac{1}{2}(1-n) \log_e (2\pi) + (nz - \frac{1}{2}) \log_e n + \sum_{k=0}^{n-1} \log_e \Gamma(z + \frac{k}{n})$$

(D.1.4)

(6.1.20 in Ref. 1) is used if $1 < \operatorname{Im}(z) \leq 2$ to reduce to $0 < \operatorname{Im}(z) \leq 1$.

$$\Gamma(z) = (z-1)\Gamma(z-1) \quad (\text{D.1.5})$$

(6.1.15 in Ref. 1) is used if $\operatorname{Re}(z) > 1$, $0 < \operatorname{Im}(z) \leq 1$ to reduce to $0 \leq \operatorname{Re}(z) \leq 1$. Then Padé power series determined by Lee (1962) is used to evaluate the inverse gamma function

$$\frac{1}{\Gamma(z)} = \frac{\sum_{i=1}^{\infty} a_i z^i}{\sum_{i=0}^{\infty} b_i z^i} \quad (\text{D.1.6})$$

for $0 \leq \text{Re}(z) \leq 1$, $0 \leq \text{Im}(z) \leq 1$. This is too accurate for an IBM 360/65 computer and some simpler series could be employed to improve the efficiency.

The Fortran IV subroutines are used for real arguments after they were shifted to positive values performing step (D.1.2) above.

When compared to Table 6.7 in Ref. 1 the results are accurate to 1 part in 10^5 .

D.2 Hankel function of the zeroth order

An algorithm for evaluation of the Hankel function $H_0^{(1)}(z)$ for z complex was developed. It uses the Hankel's asymptotic expansion for $|z| > 5$ and the ascending series for $|z| \leq 5$.

From formula (9.2.7), (9.2.9) and (9.2.10) in Abramowitz and Stegun (1965, from now on Ref. 1) we obtain the following asymptotic expansion for the Hankel function $H_0^{(1)}(z)$ which is used if $|z| > 5$:

$$H_0^{(1)}(z) = \left(\frac{2}{\pi z}\right)^{1/2} (P(0, z) + iQ(0, z)) e^{iz - i\frac{\pi}{4}} \quad (\text{D.2.1})$$

where

$$P(0, z) \sim \sum_{k=0}^{\infty} (-1)^k \frac{[(4k-1)!!]^2}{(2k)!(8z)^{2k}} \quad (\text{D.2.2})$$

and

$$Q(0, z) = \sum_{k=0}^{\infty} (-1)^k \frac{[(4k+1)!!!]^2}{(2k+1)! (8z)^{2k+1}} \quad (D.2.3)$$

where

$$(4k-1)!!! = \pi^{-1/2} 2^{2k} \Gamma(2k+1/2), \quad (2k)!! = \Gamma(2k+1)$$

Terms up to $k = 3$ are included in the computations. For small values of $|z|$ the following method is used:

$$H_0^{(1)}(z) = J_0(z) + i Y_0(z) \quad (D.2.4)$$

where according to (9.1.12) and (9.1.13) in Ref. 1

$$J_0(z) = \sum_{k=0}^{\infty} \frac{(-1)^k (z/2)^{2k}}{(k!)^2} \quad (D.2.5)$$

and

$$Y_0(z) = \frac{2}{\pi} \{ [\ln(z/2) + \gamma] J_0(z) - \sum_{k=1}^{\infty} \left(\sum_{n=1}^k \frac{1}{n} \right) \frac{(-1)^k (z/2)^{2k}}{(k!)^2} \} \quad (D.2.6)$$

γ is the Euler's constant. The first four terms are used for $0 < |z| < 1.5$ then next three terms are added if $1.5 < |z| < 3$, and for $3 < |z| < 5$ another three terms are added.

When compared to Table 9.1 in Ref. 1 the results are accurate to 1 part in 10^5 .